

**NASA  
Technical  
Memorandum**

NASA TM-108390

**IMAGING THE SUN IN HARD X-RAYS  
USING FOURIER TELESCOPES**

By J.W. Campbell

Space Science Laboratory  
Science and Engineering Directorate

January 1993

(NASA-TM-108390) IMAGING THE SUN  
IN HARD X-RAYS USING FOURIER  
TELESCOPES (NASA) 277 0

13-12-93

13-12-93

63/34 0139615



National Aeronautics and  
Space Administration

George C. Marshall Space Flight Center

1N-89  
139615  
P.277



REPORT DOCUMENTATION PAGE			Form Approved OMB No. 0704-0188	
Public reporting burden for this collection of information is estimated to average 1 hour per response, including the time for reviewing instructions, searching existing data sources, gathering and maintaining the data needed, and completing and reviewing the collection of information. Send comments regarding this burden estimate or any other aspect of this collection of information, including suggestions for reducing this burden, to Washington Headquarters Services, Directorate for Information Operations and Reports, 1215 Jefferson Davis Highway, Suite 1204, Arlington, VA 22202-4302, and to the Office of Management and Budget, Paperwork Reduction Project (0704-0188), Washington, DC 20503.				
1. AGENCY USE ONLY (Leave blank)	2. REPORT DATE January 1993	3. REPORT TYPE AND DATES COVERED NASA Technical Memorandum		
4. TITLE AND SUBTITLE Imaging the Sun in Hard X-Rays Using Fourier Telescopes			5. FUNDING NUMBERS	
6. AUTHOR(S) J. W. Campbell				
7. PERFORMING ORGANIZATION NAME(S) AND ADDRESS(ES) George C. Marshall Space Flight Center Marshall Space Flight Center, AL 35812			8. PERFORMING ORGANIZATION REPORT NUMBER	
9. SPONSORING/MONITORING AGENCY NAME(S) AND ADDRESS(ES) National Aeronautics and Space Administration Washington, D.C. 20546			10. SPONSORING/MONITORING AGENCY REPORT NUMBER NASA TM - 108390	
11. SUPPLEMENTARY NOTES Prepared by Space Science Laboratory, Science & Engineering Directorate.				
12a. DISTRIBUTION/AVAILABILITY STATEMENT Unclassified -Unlimited			12b. DISTRIBUTION CODE	
<p>13. ABSTRACT (Maximum 200 words) For several years, solar flares have been observed with a variety of instruments confirming that tremendous amounts of energy are locally stored in the solar magnetic field and then rapidly released during the life of the flare. In concert with observations, theorists have attempted to describe the means by which these energetic events occur and evolve. In an attempt to explain the ambiguities regarding hard x-ray emission from flares, two competing theories have emerged and have stood the test of time. One theory describes the flare in terms of nonthermal, electron beam injection into a thick target while the other uses a thermal approach. Both theories provide results which are reasonably consistent with current observations; but to date, none have been able to provide conclusive evidence as to the validity of either model. This is principally due to the short physical time scales and small size scales involved. So far, the averaging effects of observations taken over large time and size scales have tended to mask the differences. Imaging on short time scales (i.e., 1 sec) and/or small size scales (i.e., 1 arc sec) should give definitive answers to these questions. In order to test whether a realistic telescope can indeed discriminate between models, we construct model sources based upon the thermal and the nonthermal models and calculate the emission as a function of time and energy in the range from 10 to 100 keV. In addition, we construct model telescopes representing both the spatial modulation collimator (SMC) and the rotating modulation collimator (RMC) techniques of observation using random photon counting statistics. With these two types of telescopes we numerically simulate the instrument response to the above two model flares to see if there are distinct x-ray signatures which may be discernable. We find that theoretical descriptions of the primary models of solar flares do indeed predict different hard x-ray signatures for 1 sec time scales and at 1-5 arc sec spatial resolution. However, these distinguishing signatures can best be observed early in the impulsive phase and from a position perpendicular to the plane of the loop. Furthermore, we find that Fourier telescopes with reasonable and currently attainable design characteristics can image these signatures and that given the same sensitive areas and short temporal integration times relative to source evolution (i.e., 1 sec), the RMC and the SMC will both provide about the same performance. The ability to image is strongly dependent upon the intensity of the specific loop being observed. Specifically, for 1 sec temporal integration times, for 10 keV energy bins, and for complex sources, the intensity threshold is found to be <math>0.2 \text{ photon cm}^{-2} \text{ sec}^{-1} \text{ keV}^{-1}</math> per <math>4 \times 4 \text{ arc sec}</math> telescope resolution cell at the Earth. For intensities greater than this threshold, clear imaging can be accomplished using our Fourier telescope. However, this is only true for intensities which are within a factor of 10 of the brightest intensity in its immediate vicinity as the dynamic range of the telescope was found to be on the order of 10:1. This limitation has been found to play a role in imaging emission profiles of both models in that weak spatial features are suppressed by brighter ones. Also, we find that the telescope is tolerant to random noise on the detector and that imaging performance is surprisingly resistant to twist (i.e., rotation of the grids with respect to one another) less than 2 arc min in magnitude. Actual fields of view of the telescopes are much less (i.e., 1:4) than the geometric fields of view; however, full Sun coverage is achievable for telescopes using reasonable parameters. In summary, we find that Fourier telescopes are promising approaches for hard x-ray imaging of the Sun and should serve to provide significant insight into the physical processes at work in flares.</p>				
14. SUBJECT TERMS X-Rays, Sun, Fourier Telescope, X-Ray Optics, X-Ray Imaging			15. NUMBER OF PAGES 277	
			16. PRICE CODE NTIS	
17. SECURITY CLASSIFICATION OF REPORT Unclassified	18. SECURITY CLASSIFICATION OF THIS PAGE Unclassified	19. SECURITY CLASSIFICATION OF ABSTRACT Unclassified	20. LIMITATION OF ABSTRACT Unlimited	



## TABLE OF CONTENTS

I. Introduction . . . . .	1
A. Research Objectives . . . . .	5
B. Flare Background . . . . .	9
C. X-ray Imaging Background . . . . .	23
D. Research Approach . . . . .	24
II. Model N-T Hard X-ray Emission . . . . .	28
A. Introduction . . . . .	28
B. Emission as a Function of Time, Position, and Energy	35
C. Summary . . . . .	38
III. Model T Hard X-ray Emission . . . . .	45
A. Introduction . . . . .	45
B. Emission Characteristics . . . . .	51
C. Summary . . . . .	73
IV. The Fourier Telescope . . . . .	79
A. Introduction . . . . .	79
B. Theory . . . . .	83
C. The Astronomical Imaging Processing System (AIPS)	94
D. Potential Engineering Constraints . . . . .	102
E. Summary . . . . .	107

<b>V. The Spatial Modulation Collimator . . . . .</b>	<b>109</b>
A. Introduction . . . . .	109
B. Theory . . . . .	115
C. Results . . . . .	117
D. Summary and Conclusions . . . . .	126
<b>VI. The Rotating Modulation Collimator . . . . .</b>	<b>129</b>
A. Introduction . . . . .	129
B. Theory . . . . .	129
C. Results . . . . .	136
D. Summary . . . . .	143
<b>VII. Fourier Images of Synthetic Flare Profiles . . . . .</b>	<b>148</b>
<b>VIII. Summary and Conclusions . . . . .</b>	<b>158</b>
A. Conclusions . . . . .	158
B. Optimization Recommendations For The Future	161
C. Recommendations for Future Research . . . .	162
<b>Appendix A. Model T Code . . . . .</b>	<b>169</b>
<b>Appendix B. Model N-T Codes . . . . .</b>	<b>181</b>
<b>Appendix C. Spatial Modulation Collimator Codes . .</b>	<b>204</b>
<b>Appendix D. Rotating Modulation Collimator Codes .</b>	<b>233</b>
<b>References . . . . .</b>	<b>258</b>

## LIST OF FIGURES

Figure	Page
1.1 The Heidi Concept . . . . .	3
1.2 The HESP Concept . . . . .	4
1.3 The LUNAR P/OF . . . . .	6
1.4 Fourier Telescope Concept for Shuttle Platform . . .	7
1.5 A Fourier Telescope for a Free Flying Satellite . . .	8
1.6 Typical Microwave and Hard X-ray Emissions . . . .	9
1.7 Selected Emission Lines and Hard X-ray Emission . .	12
1.8 Time Dependence of a Typical Hard X-ray Burst . .	14
1.9 M Class Flare in H-alpha . . . . .	16
1.10 Hard X-ray Spectra for Four Different Events . . .	19
1.11 Model N-T and Model T . . . . .	20
1.12 HXIS Hard X-ray Images . . . . .	22
1.13 A Dirty Image of a Typical Astrophysical Source . .	25
1.14 The CLEAN Image . . . . .	26
2.1 Model N-T Concept . . . . .	29
2.2 Density Versus Loop Position . . . . .	33

2.3	Thermal Emission Profile at 10 keV . . . . .	36
2.4	Thermal Emission Profile at 40 keV . . . . .	37
2.5	Nonthermal Emission Profile at 10 keV . . . . .	39
2.6	Total Emission Profile at 10 keV . . . . .	40
2.7	Total Emission Profile at 40 keV . . . . .	41
2.8	Total Emission Profile at 70 keV . . . . .	42
2.9	Total Emission Profile at 100 keV . . . . .	43
3.1	Model T Concept . . . . .	46
3.2	Electron and Ion Distribution Functions . . . . .	48
3.3	Marginal Stability Analog . . . . .	50
3.4	Model T Kernel Temperature as a Function of Time .	54
3.5	Maxwellian Cooling Over Time . . . . .	56
3.6	Relaxation to Maxwellian Distribution . . . . .	58
3.7	Dimensionless Differences . . . . .	60
3.8	Hybrid Distribution . . . . .	69
3.9	Model T Velocity Comparison . . . . .	70
3.10	Model T Emission Profile at 10 keV . . . . .	74
3.11	Model T Emission Profile at 40 keV . . . . .	75
3.12	Model T Emission Profile at 70 keV . . . . .	76
3.13	Model T Emission Profile at 100 keV . . . . .	77
4.1	Basic Fourier Telescope Geometry . . . . .	81
4.2	Basic Fourier Telescope Imaging Concept . . . . .	82



4.3	A Basic Radiotelescope . . . . .	86
4.4	A Typical Interferometer Response . . . . .	87
4.5	AIPS Cookbook Cover . . . . .	95
4.6	Palmer Results . . . . .	98
4.7	AIPS Contour of Palmer Results . . . . .	99
4.8	AIPS 3-D of Palmer Results . . . . .	100
4.9	AIPS Grey of Palmer Results . . . . .	101
4.10	Tungsten Throughput . . . . .	104
4.11	Aluminum Throughput . . . . .	105
4.12	BATSE Detector and SMC Imaging Thresholds . . . . .	106
5.1	SMC Fourier Plane Coverage . . . . .	110
5.2	SMC Upper Grid . . . . .	112
5.3	SMC Lower Grid . . . . .	113
5.4	SMC Moire Fringes for Point Source at 20" . . . . .	114
5.5	SMC Numerical Model . . . . .	118
5.6	SMC and RMC Flare Model . . . . .	119
5.7	SMC Dirty Image of Loop . . . . .	120
5.8	SMC Clean Image of Loop . . . . .	121
5.9	SMC Point Spread Function (Beam) . . . . .	123
5.10	SMC Full Sun Field of View Demonstrated . . . . .	124
5.11	SMC Twist . . . . .	125

5.12	Dynamic Range Illustrated . . . . .	127
6.1	RMC Ray Trace Model . . . . .	130
6.2	RMC Sawtooth . . . . .	131
6.3	Grid Pair Maxima and Minima . . . . .	134
6.4	RMC Ray Trace Compressed Sawtooth . . . . .	135
6.5	RMC Simulation Model . . . . .	138
6.6	RMC Real and Imaginary Photon Sawtooths . . . . .	139
6.7	RMC Cleaned Loop . . . . .	140
6.8	RMC Point Spread Function (Beam) . . . . .	141
6.9	RMC Beam 3-D Representation . . . . .	142
6.10	RMC Rotated Loop . . . . .	144
6.11	RMC Footpoint Image . . . . .	145
6.12	RMC Twist . . . . .	146
7.1	Model N-T Intensity Profiles . . . . .	149
7.2	Model T Intensity Profiles . . . . .	151
7.3	Model N-T Hard X-ray Images at 10 keV . . . . .	152
7.4	Model T Hard X-ray Images at 10 keV . . . . .	154
7.5	Model N-T and Model T Hard X-ray Images at 40 keV . . . . .	155
7.6	Model N-T and Model T Hard X-ray Images at 100 keV . . . . .	156
8.1	The Fourier Spiral (Transparency) . . . . .	164

<b>8.2 The Fourier Spiral (Opaque)</b>	<b>165</b>
<b>8.3 The Fourier Transform of Four Point Sources</b>	<b>166</b>
<b>8.4 Four Fresnel Spiral Equivalent Point Sources</b>	<b>167</b>

## **LIST OF TABLES**

<b>Table</b>	<b>Page</b>
<b>5.1 Our SMC Compared to YOHKOH and HESP . . .</b>	<b>116</b>
<b>5.2 Our RMC Compared to YOHKOH and HESP . .</b>	<b>137</b>

## List of Symbols

- $\alpha$  - normal angle of incidence to grid pair
- $c_s$  - ion-acoustic speed
- $d$  - grid separation
- $D_{new}$  - dimensionless difference
- $D_{old}$  - dimensionless difference
- $E_o$  - electron energy
- $\epsilon$  - photon energy
- $F_l$  - beam flux
- $F_o$  - electron spectrum
- $F(v, t)$  - electron distribution
- $f(v, t)$  - normalized electron distribution
- $g(t)$  - variation of electron beam in time
- $Im$  - imaginary value of Fourier component
- $I_{th}$  - thermal intensity
- $J$  - cumulative intensity
- $j(x)$  - normalized cumulative intensity
- $k$  - Boltzmann constant
- $L$  - length of kernel
- $m_e$  - electron mass

$m_i$  - proton mass  
 $N$  - column depth  
 $N_1$  - number collisions defining upper limit of bulk Maxwellian  
 $N(\nu, t)$  - number of collisions for a given time  
 $\nu$  - collision frequency  
 $P$  - period of grid pair  
 $\phi$  rotational angle of RMC  
 $\phi_{max}$  - RMC angle which produces maximum detector intensity  
 $\phi_{min}$  - RMC angle which produces minimum detector intensity  
 $Q_{ms}$  - heat flux corresponding to marginal stability  
 $Re$  - real value of Fourier component  
 $R(t)$  - radio telescope response function  
 $s$  - slit plus slat width  
 $\sigma_k$  - Kramer cross section  
 $T_e$  - electron temperature  
 $T_i$  - ion temperature  
 $t_c$  - Spitzer collision time  
 $u$  - coordinate axis in Fourier plane  
 $v_e$  - thermal speed  
 $v_{crit}$  - critical velocity for electron distribution  
 $v_1$  - velocity defining upper limit of bulk Maxwellian  
 $v_2$  - velocity defining lower limit of collisionless flux  
 $v_{lco}$  - lower cutoff velocity escaping flux

$v_{max}$  - maximum velocity of escaping flux

$V_1$  - voltage from radio telescope signal

$V_2$  - voltage from radio telescope signal

$V$  - visibility function

$v$  - coordinate axis in Fourier plane





## I. INTRODUCTION

For many years the properties of hard x-ray sources in solar flares have been studied in order to gain greater insight into the underlying processes causing these highly energetic events. To date, temporal, spectral, and polarization measurements have failed to provide unambiguous information on the processes responsible for accelerating protons and electrons. There are a variety of reasons for this, foremost among which is the limited temporal and/or spatial resolution available. (Tandberg-Hanssen and Emslie, 1988).

High resolution spatial observations show great potential for advancing our knowledge of the hard x-ray production mechanism since for the first time our ability to measure spatial structure approaches temporal and spatial resolution scales of physical interest (e.g., the collisional stopping length of a high-energy electron in the corona; Campbell, Davis, and Emslie, 1991).

Unfortunately, hard x-rays ( $\epsilon > 10$  keV) cannot be imaged by conventional methods such as lenses or mirrors. In addition, the usefulness of grazing incidence telescopes in this energy regime is limited due to the stringent requirements imposed on the smoothness of the optics, the physical sizes necessary for a reasonable collecting area, and the unreasonably long focal lengths which would be required. On the other hand, images can be obtained in a number of ways from absorptive grids or masks made from *high Z* materials such as tungsten.

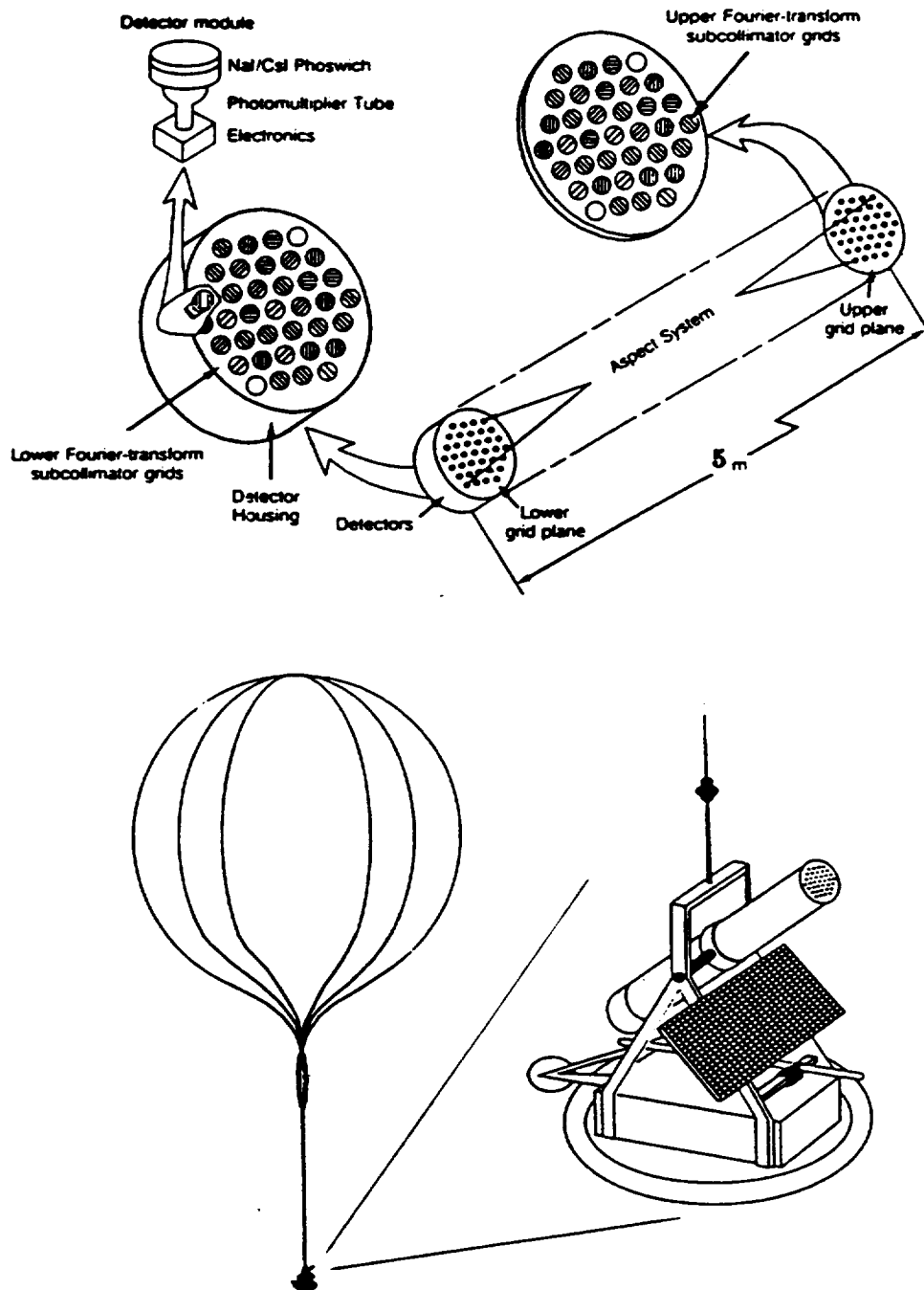
One popular approach in the astrophysics community has been coded aperture telescopes (Murphy, 1990). These instruments use a multiple pinhole mask to produce a pattern which is the correlation function of the source image with the pinhole array. The source image can be recovered by inverting the correlation integral. Unfortunately, while this instrument allows 50% quantum throughput, practical limitations to its spatial resolution (i.e.,  $\cong 25$  arc seconds based in part on attainable detector pixel sizes) make it marginal for use in imaging flares.

Another type of instrument, the Fourier telescope (see Chapter IV), offers in principle much better resolution but the throughput will be reduced to 25%. These instruments work by measuring the intensity distribution in Fourier space and then either (a) numerically recomposing the components or (b) “back projecting” the detector response onto the sky to provide an image (Murphy, 1990).

Essentially the concept involves sampling selected two-dimensional Fourier components from a wavefront emitted by the source. Each component may be visualized as a single point on a common complex surface. By measuring a surprisingly small number of components over a sufficiently large spatial frequency spectrum, this Fourier surface may be approximated. An inverse Fourier transform of this surface function then yields a noisy or a *dirty* image (using terminology taken from radio astronomy). This description is aesthetically correct, for when viewing a typical *dirty* image, the processing artifacts can make the picture very difficult for the eye to understand. Techniques taken from radio astronomy such as the *maximum entropy* and the *clean* methods can be used to suppress these artifacts and produce a more meaningful image (Campbell et al., 1991a). This will be discussed in greater detail in Chapter IV.

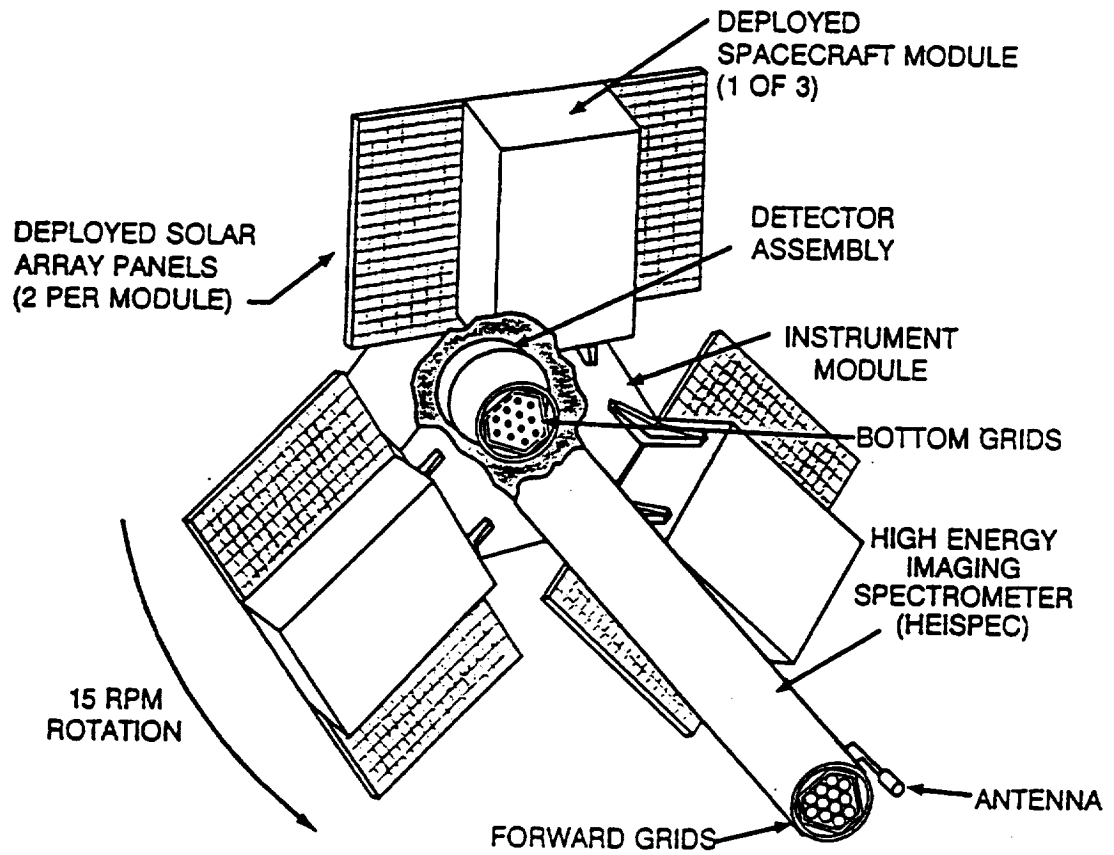
Several Fourier telescope concepts have been developed to study solar flares. They include the High Energy Imaging Device (HEIDI), an imaging experiment for the Max '91 balloon program planned for a 1992 launch (Figure 1.1); the Japanese Solar-A Hard X-ray Telescope on the YOHKOH satellite launched in August 1991; the High Energy and Spectroscopy (HEISPEC) investigation which is proposed as the key component of the High Energy Solar Physics (HESP) mission (Figure 1.2) scheduled for the next solar maximum; and the lunar Pinhole/Occluder Facility (P/OF). These instruments are expected to be able to provide full Sun coverage within the instrument field of view with resolutions approaching 1 arc second.

Figure 1.3 illustrates the lunar P/OF. This is an innovative idea which takes



**Figure 1.1: The HEIDI Concept**

A conceptual sketch of HEIDI, a hard x-ray imaging system mounted upon a balloon platform. The grid plane separation distance is 5 meters.



**Figure 1.2: The HESP Concept**

A conceptual sketch of HESP, a hard x-ray imaging system mounted upon a free flying satellite platform. In this case the grid planes would be separated by 5 meters.

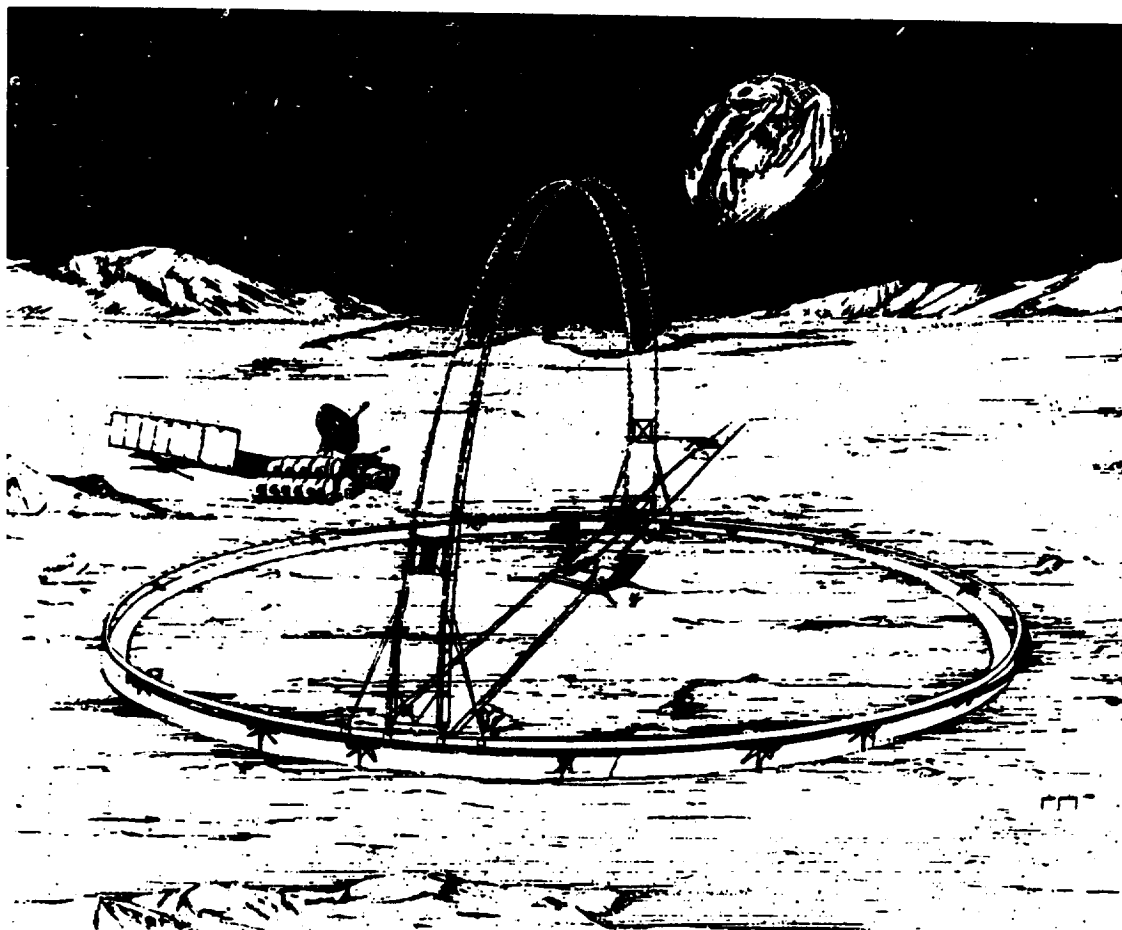
advantage of the relatively weak gravity of the moon to construct a large extended telescope structure for obtaining high resolution hard x-ray images. The larger ring rotates in the horizontal plane a full  $360^\circ$  while the small upper grid tray is free to move in a constrained path along the larger ring through a  $180^\circ$  extent. The pedestal at the center also supports a lower grid tray which is moved independently so as to maintain a parallel orientation and alignment with the upper one. This allows the observatory to track a point in the lunar sky (e.g., a solar flare) to within the accuracy of the pointing system (Campbell et al., 1991b).

Figure 1.4 illustrates another concept in which a Fourier telescope (or a redundant coded aperture) is deployed from the shuttle. In this concept, the successful heritage of actual shuttle experiments employing extended truss structures in microgravity would be exploited. During launch, the truss structure would be stored in a cannister within the shuttle bay. Once on orbit, the truss would be extended to its full length (e.g., 100 feet) and stabilized using small, microthrust nozzles in conjunction with a laser feedback system for control stability and pointing accuracy. For a Fourier telescope, one grid plane would be mounted at the top of the boom with the lower grid plane, detector arrays, and electronics mounted in the bay.

Figure 1.5 illustrates how a free flying Fourier telescope could be employed using extendable boom technology. Another approach would be to use an extendable tube to separate grid planes. The free flyer is probably the most cost effective of the options considered here in that it holds the potential for providing maximum science return for several years for a relatively moderate price.

## **A. Research Objectives**

The primary objective of this research is to derive the hard x-ray emission as a function of time, energy, and loop position for two prominent solar flare models found in the literature and here denoted the Model T and the Model N-T. Once



**Figure 1.3: The LUNAR P/OF**

A conceptual sketch of the lunar P/OF, a hard x-ray imaging system as part of a lunar-based facility. This concept would take advantage of the reduced gravity with an innovative pointing and tracking design.

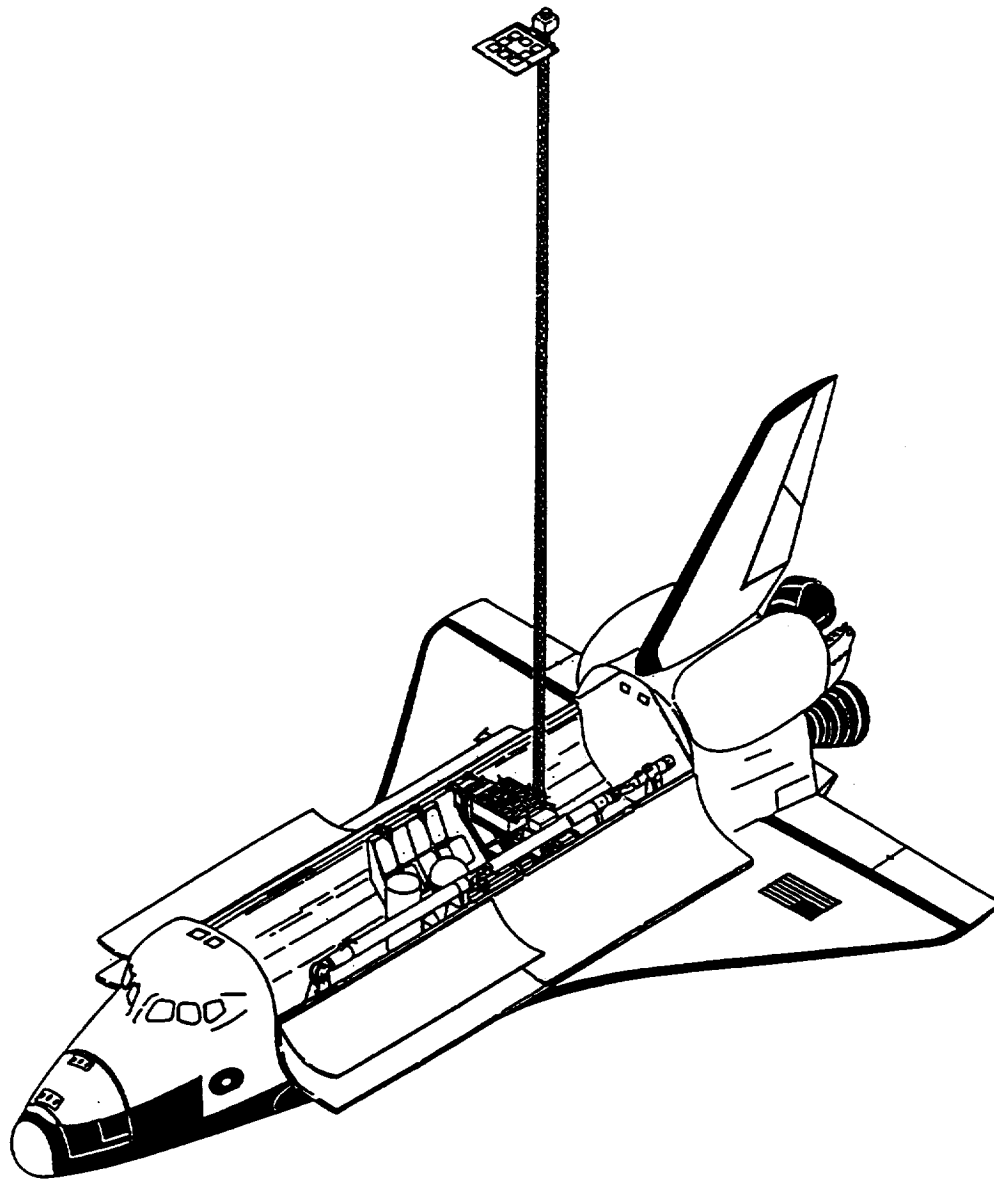


**Figure 1.4: Fourier Telescopes Concept For Shuttle Platform**

A conceptual sketch of the a shuttle oriented Fourier telescope design. This concept would use an extendable, stabilized boom.

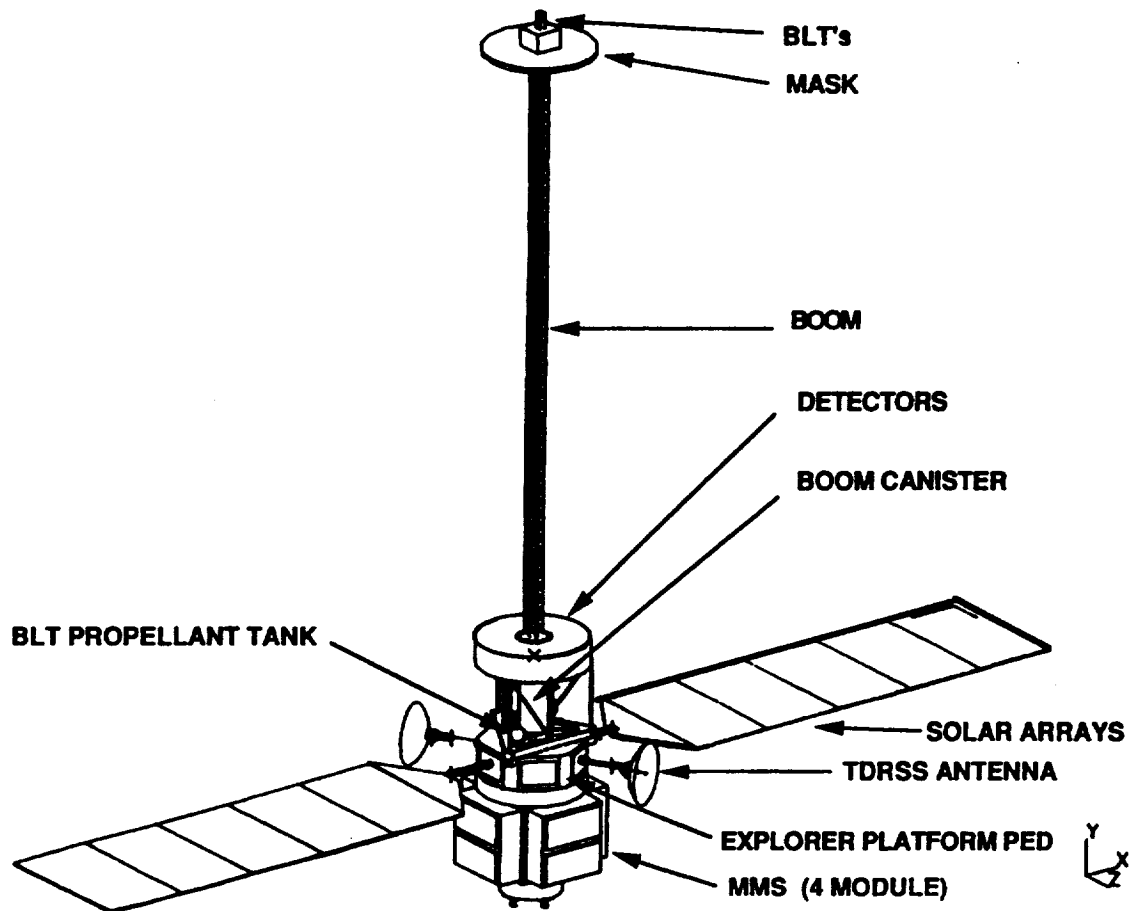


**Figure 1.5: A Fourier Telescope For A Free Flying Satellite**



the hard x-ray emission profiles are obtained, distinguishing signatures may be identified. This will be discussed in detail in Chapters II and III.

The next step will be to construct two numerical models representing the two basic classes of Fourier telescopes, a Spatial Modulation Collimator (SMC) and a Rotating Modulation Collimator (RMC). Each will view the previously obtained profiles to determine over what energy range, and at what integration times, good images can be obtained. Chapters V and VI will discuss these telescopes in detail. In addition, various instrument- related questions will be addressed such as low flux level, effective field of view, twist, and noise capabilities and limitations.

## B. Flare Background

The Sun's atmosphere consists of four regions each defined by different characteristics. The lowest is called the **photosphere** and is mostly what we observe when we look at the Sun in visible light. It is (relative to the other layers) dense and opaque and on the order of 500 km in thickness. Temperatures in this region are on the order of 6000 K and densities are  $10^{17} \text{ cm}^{-3}$ .

Above the photosphere lies the **chromosphere**, which is relatively more transparent and about 2500 km thick. Temperatures are on the order of 5000 K and densities are typically  $10^{12} \text{ cm}^{-3}$ . Above the chromosphere lies the **transition region** which is on the order of 200 km thick in the quiet Sun. In a flare, this thickness may decrease to less than 1 km. In this region, the temperature rises rapidly approaching  $10^6 \text{ K}$  at the bottom of the next region which is called the **corona**. The corona may extend out for thousands of kilometers and is characterized by relatively high temperatures and low densities (i.e.,  $\leq 10^9 \text{ cm}^{-3}$ ). In a flare, the density within the corona may increase to  $10^{11} \text{ cm}^{-3}$ .

Flares occur primarily in active regions on the Sun. These active regions extend vertically from deep photospheric levels through the chromosphere and the

transition region high into the corona. They exhibit much higher magnetic field strengths (i.e., 100-1500 G) than the surrounding quiet regions (1-10 G). Soft x-ray observations from Skylab showed that to a large extent the active solar plasma is contained in loops that exist on scales from the smallest 1 arc second diameter bipolar loops emerging from below the photosphere to enormous coronal loops and arches spanning distances of a solar radius or more.

A typical flare evolutionary sequence starts with precursors, such as gradual soft x-ray brightenings, which lead into an impulsive phase which, in turn, is followed by a gradual phase and then by a decay. It is during the impulsive phase that most of the energy which has slowly been built up and stored in the local magnetic field during the pre-flare period is suddenly released. Observations show this phase to be characterized by intense, rapidly fluctuating bursts of high-energy radiation, such as hard x-rays and  $\gamma$ -rays; bursts of accelerated electrons and protons; and plasma and bulk fluid acceleration.

There are also associated emissions at other energies, such as EUV and optical, generated as a result of the thermal response of the atmosphere to this phase. Figure 1.6 compares microwave and hard x-ray signatures for impulsive flares, establishing the simultaneity between the two. Since the microwaves are produced by the gyrosynchrotron radiation from the hot electrons spiraling around magnetic field lines in the loop, this figure illustrates the importance of complementary measurements and the importance of microwaves as a diagnostic tool. Figure 1.7 shows the relationship between two emission lines and hard x-rays for a selected flare and illustrates the importance of complementary x-ray and UV observations. In particular, UV observations can provide information about preheating processes prior to the impulsive hard x-ray bursts. These figures also are examples of the impulsive phase of a flare.

In order to produce hard x-ray and  $\gamma$ -ray bursts, the basic flare mechanism

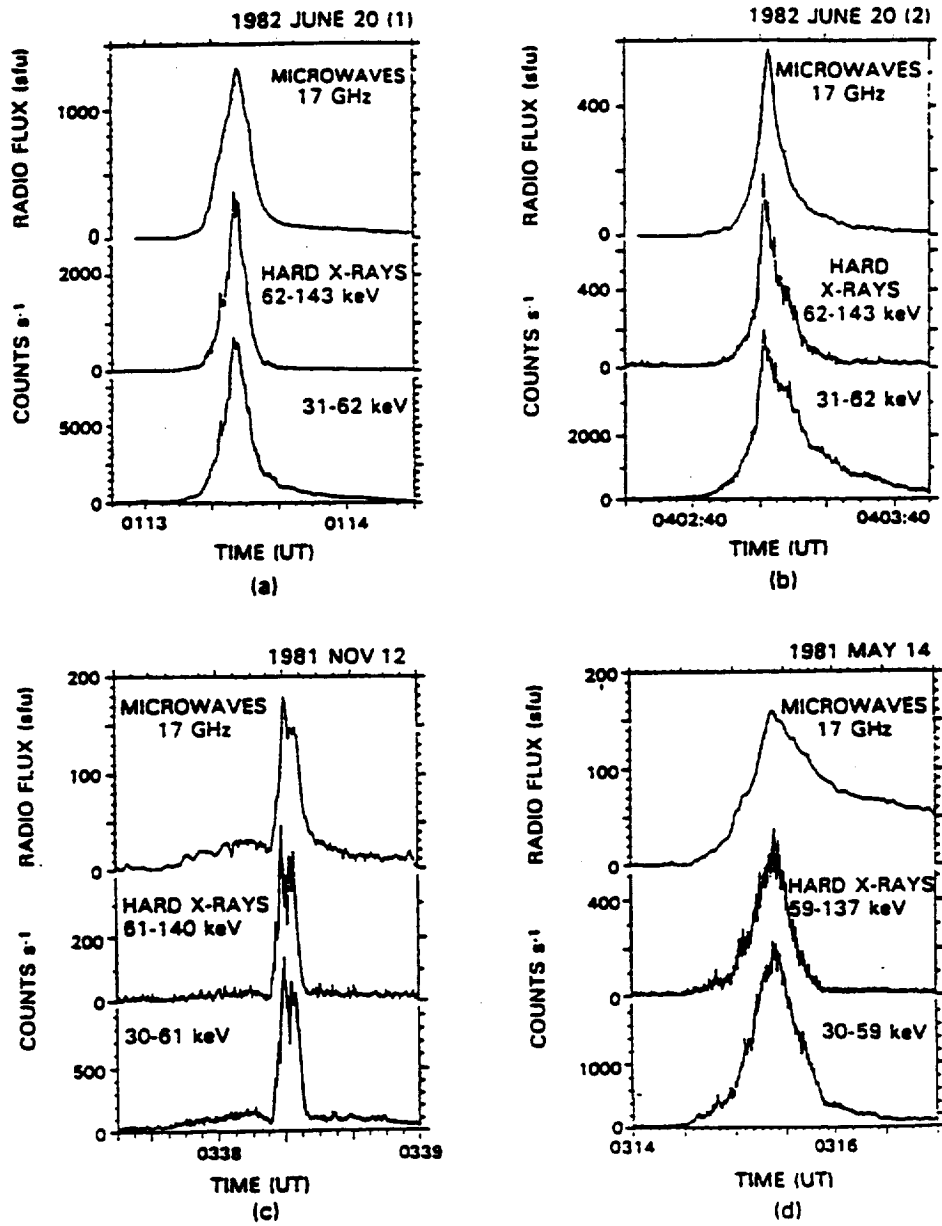
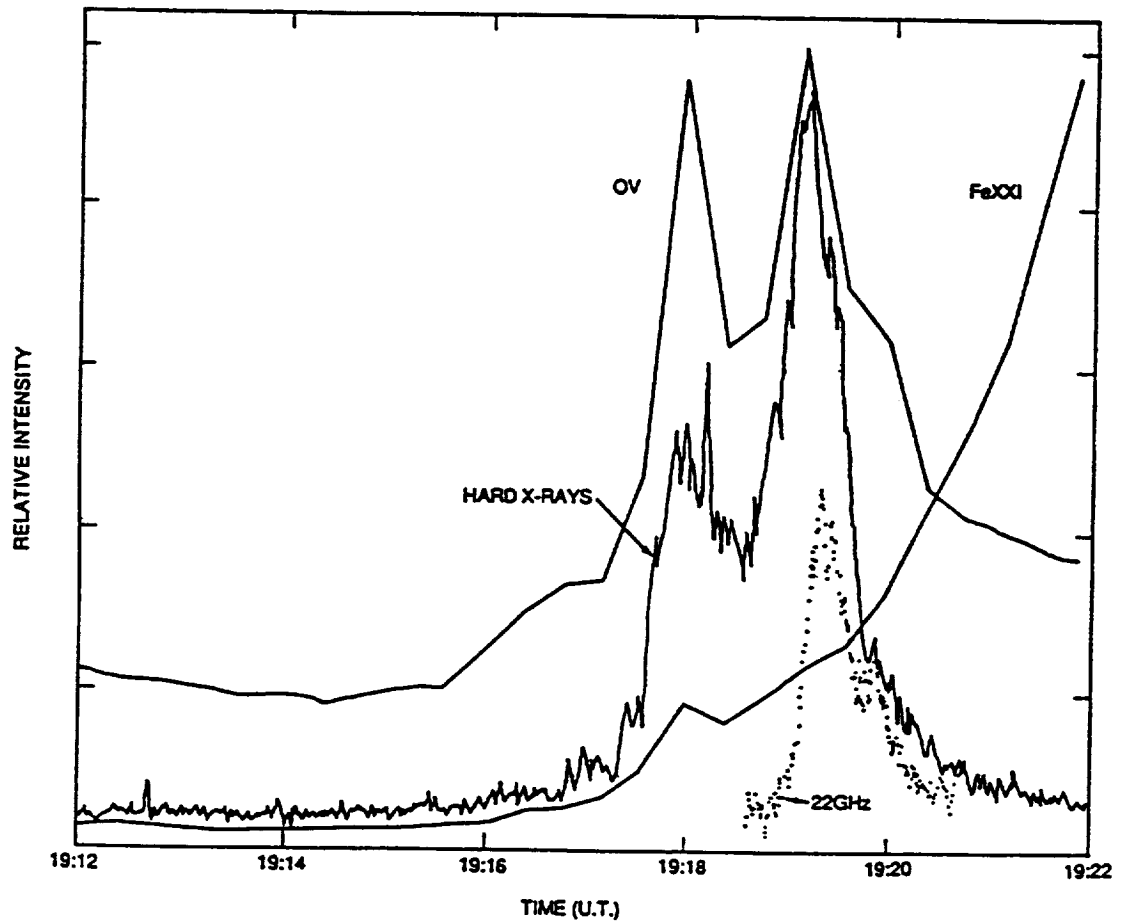


Figure 1.6: Typical Microwave And Hard X-ray Emissions

These observations indicate that both the microwave and hard x-ray emissions from the impulsive phase of the flare occur simultaneously (Kosugi, Dennis, and Kai, 1988).



**Figure 1.7: Selected Emission Lines And Hard X-ray Emission**

This shows the behaviour of two ultraviolet (oxygen and iron) lines overlaid on the impulsive phase x-ray and microwave emissions. The UV lines should be a good impulsive phase diagnostic since it provides information about preheating processes in the flare prior to the onset of the impulsive phase. This illustrates the importance of hard x-ray and UV complementary observations. Time profiles are from the impulsive phase of a flare observed on November 1, 1980 (from Tandberg-Hanssen and Emslie, 1984).

must be capable of accelerating large quantities of particles, both electrons and protons. This particle acceleration is also implied by centimeter microwave bursts and energetic proton streams. Microwave bursts, while relatively low in energy compared to the hard x-ray bursts, provide significant insight into the processes at work. Proton streams at the Earth typically have a power law shape (van Hollebeke et al., 1975). The accelerating mechanism is unknown and continues to receive a great deal of attention from the scientific community.

Hard x-ray emission in flares can range from the simple isolated bursts with a total duration of several seconds to extended bursts lasting up to  $10^3$  sec, such as the great flare of August 4, 1972 (Hoyng et al., 1976). Figure 1.8 illustrates a hard x-ray burst time profile and indicates that the same mechanism produces photons over a the range from 28-111 keV. In addition, the rapid falloff of intensity as a function of energy is shown. Other observations have extended this idea to even higher wavelengths. This figure also indicates that this flare is composed of several events occurring somewhat sequentially in time.

Simple bursts are characterized by a few loops sharing common footpoints while extended bursts are characterized by arcades of loops extending over the size scale of an active region (i.e., 1 arc minute). In both cases, strongly sheared, magnetic field lines running almost parallel to the neutral line, occur in this region. One scenario for energy release involves a long filament or strand of solar plasma several arc seconds long erupting into the tangle of stressed loops triggering an energy release in one or more. As individual loops are triggered they in turn trigger adjacent loops with some time delay. The flare then becomes a complicated cascade of sequentially triggered loops or elementary bursts.

Figure 1.9 shows an *M class* flare observed by the author at the Marshall Space Flight Center Solar Magnetograph Observatory in H-alpha and illustrates the complexity of these events when observed in H-alpha. Clearly, complementary

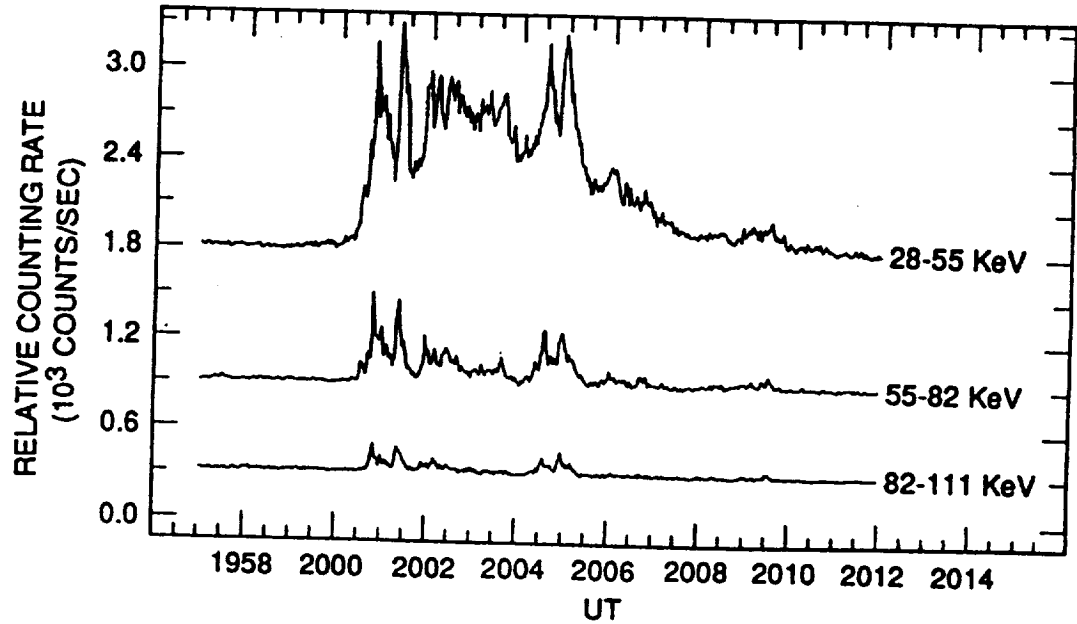


**Figure 1.8: Time Dependence Of A Typical Hard X-ray Burst**

This shows the simultaneity in three different energy bins of hard x-rays from 28 to 111 keV indicating that the same mechanism produces the x-ray photons over these energies. In addition, the rapid decrease in intensity as a function of energy is shown. (from Kane et al., 1979b).

observations will be helpful in providing greater insight.

Peterson and Winckler first detected hard x-rays from solar flares in 1959 using a balloon observatory. Since that time, space and ground-based instruments have expanded the observational data base across the electromagnetic spectrum including hard x-rays presumably produced by bremsstrahlung. X-ray emission by bremsstrahlung (*braking radiation*) is simply described as photon generation due to the large angle collision and the subsequent deceleration of an energetic electron with an ion in which the electron remains free.

Understanding hard x-rays is extremely important to understanding the overall physical processes occurring in the flare since they may be directly related to the dominant energy release processes occurring during the event. For example, bremsstrahlung resulting from electron beam deceleration in a thick target (see Chapter II) is extremely inefficient ( $\cong 10^5$  erg of electron energy is needed to produce  $\cong 1$  erg of x-ray energy; Tandberg-Hanssen and Emslie, 1988). Consequently, extremely high limits are placed on the minimum required energy in the release.

Not only is the energy required in such a model large, it must be in the low entropy form of directed, accelerated particles rather than a high entropy release in the form of bulk heat (Smith, 1980). Thus, an unambiguous verification of the nonthermal model would provide tremendous insight into the energy release process and its demands on the magnetic field.

These constraints make attractive a model in which the bremsstrahlung producing electrons do not interact with cooler electrons thereby allowing a more efficient conversion of their energy into x-rays. Such a model could in principle reduce the number of electrons required at the beginning of the release (Tandberg-Hanssen and Emslie, 1988).

Such a *thermal* model, the **Model T**, may be pictured simply as a hot mass of plasma with temperatures sufficiently large that



**Figure 1.9: M Class Flare In H-Alpha**

This indicates the complexity of even moderately sized flares as seen in H-alpha. The flare was observed by the author on June 1, 1991 at the Marshall Space Flight Center Solar Magnetograph Observatory.



$$kT \approx \epsilon \approx 10 \text{ keV}$$

whence

$$T \approx 10^8 \text{ K}.$$

However, one runs into difficulties with this picture as well. Kahler (1971a,b) pointed out that at the  $10^8 \text{ K}$  and upward temperatures required of such a thermal hard x-ray source, conductive cooling (using classical relationships; Spitzer, 1962) would be so efficient that a supply of energy even larger than that required for a nonthermal model would need to be provided for the observed duration of the burst. He further pointed out that it would be exceedingly difficult to confine such a hot plasma because of the very long collisional mean free paths

$$\lambda \approx \frac{2 \times 10^4 T^2}{n} \approx \frac{10^{20}}{n} \geq 10^9 \text{ cm}$$

of the electrons and the consequent high probability of escape.

Brown et al. (1979) showed, however, that collective plasma processes can significantly alter the physics of such sources. A very large electrical current would be generated as a result of the electrons streaming out of the source into the surrounding cooler plasma. The electric field set up by the resulting charge separation would accelerate ambient electrons into a reverse current with a velocity relative to the background ion distribution sufficiently large that ion-acoustic waves would be generated. These waves would be turbulent in nature and would tend to form into a barrier region which would reduce the mean free path of the electrons resulting in more effective confinement (Brown, Melrose, and Spicer, 1979).

The turbulent containment region would quickly evolve to a marginally stable state (Manheimer, 1977) in which the escape of the most energetic electrons would

be balanced by a return current just sufficient to maintain the barrier. The region containing the turbulence would be relatively thin (i.e., on the order of 1 km) and would move along the loop at the ion sound speed driven by the temperature gradient. Chapter III will discuss this in more detail.

Unfortunately, both of these models predict similar hard x-ray spectral signatures (Brown and Emslie, 1987; Emslie and Machado, 1987; Emslie, 1989). For example, Figure 1.10 shows an example of the hard x-ray spectra for four typical flares spanning a range from 10 to 100 keV (Kane et al., 1979b). These curves may be fitted by a power law, however this is not necessarily a unique mathematical solution. The fact that these observations alone are insufficient to distinguish between models serves as a motivation to move toward high resolution, imaging telescopes which can resolve directly the evolution of hard x-ray sources in flares in order to distinguish between these scenarios.

As shown in Figure 1.11, Model N-T can be qualitatively characterized by an initial *footpoint* structure, which subsequently evolves into a filled loop. Chapter II will discuss this in greater detail. By contrast, Model T initially exhibits a bright central region in addition to footpoint emission formed by high energy electron escaping from the central region. This central region grows and gradually fills the loop. Chapter III will discuss this in greater detail. These two different spatial emission signatures may provide the basis for a discriminating test between the two models through imaging (Emslie, 1981).

However, this probably will only be true at the beginning of the impulsive phase. At the end of the impulsive phase (typically 30-60 sec), the loop should become uniformly filled in either case and if viewed at this time would probably offer little insight into the mechanism at work. In addition, since the impulsive phase itself is composed of many elemental flare bursts, it may prove necessary to image the first one as subsequent bursts may overlap and obscure signatures.

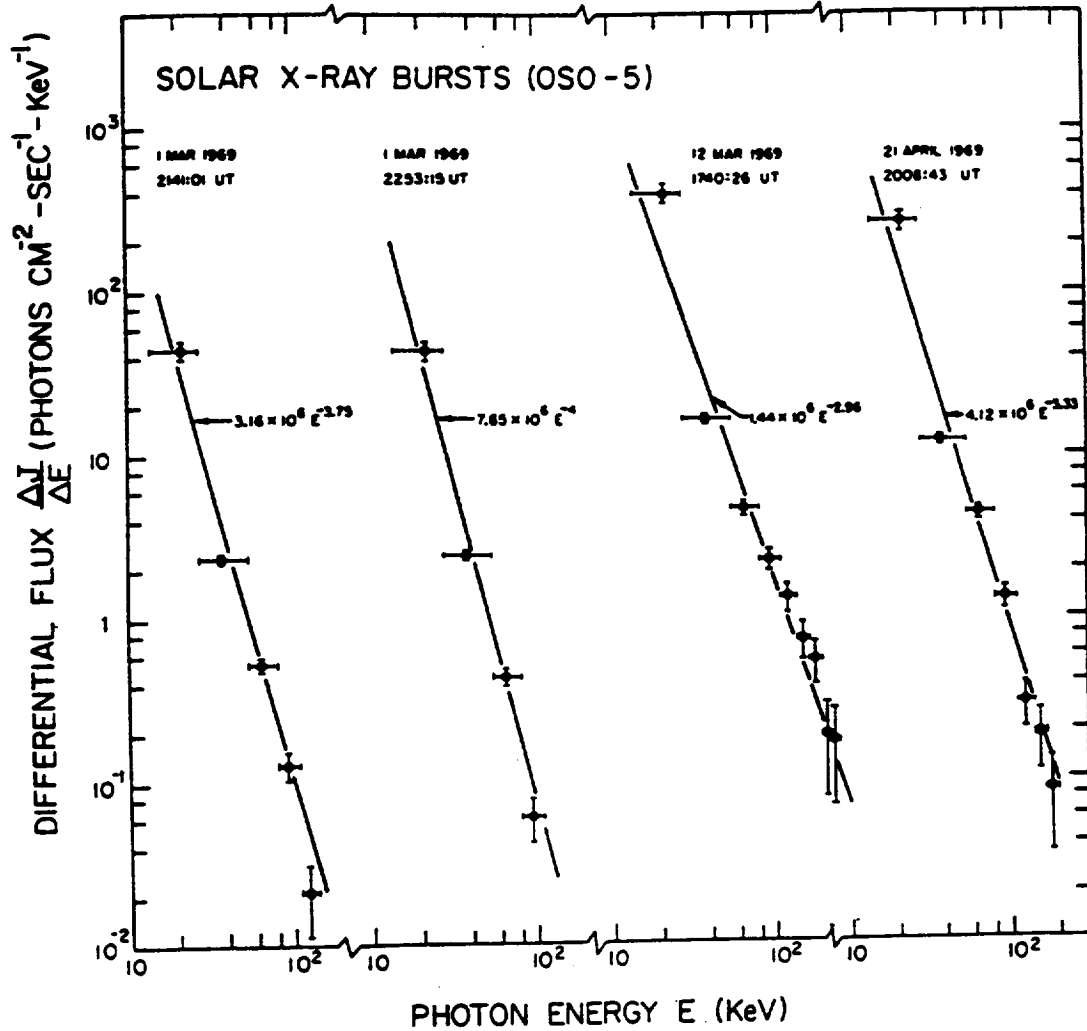


**Figure 1.10: Hard X-ray Spectra For Four Different Events**

This shows four typical observations spanning a spectral range from 10 to 100 keV (Kane et al., 1979b). Note that each observation can be fitted by a power law; however, this may not be a unique solution. These observations alone are not sufficient to provide an unambiguous determination of impulsive phase processes.

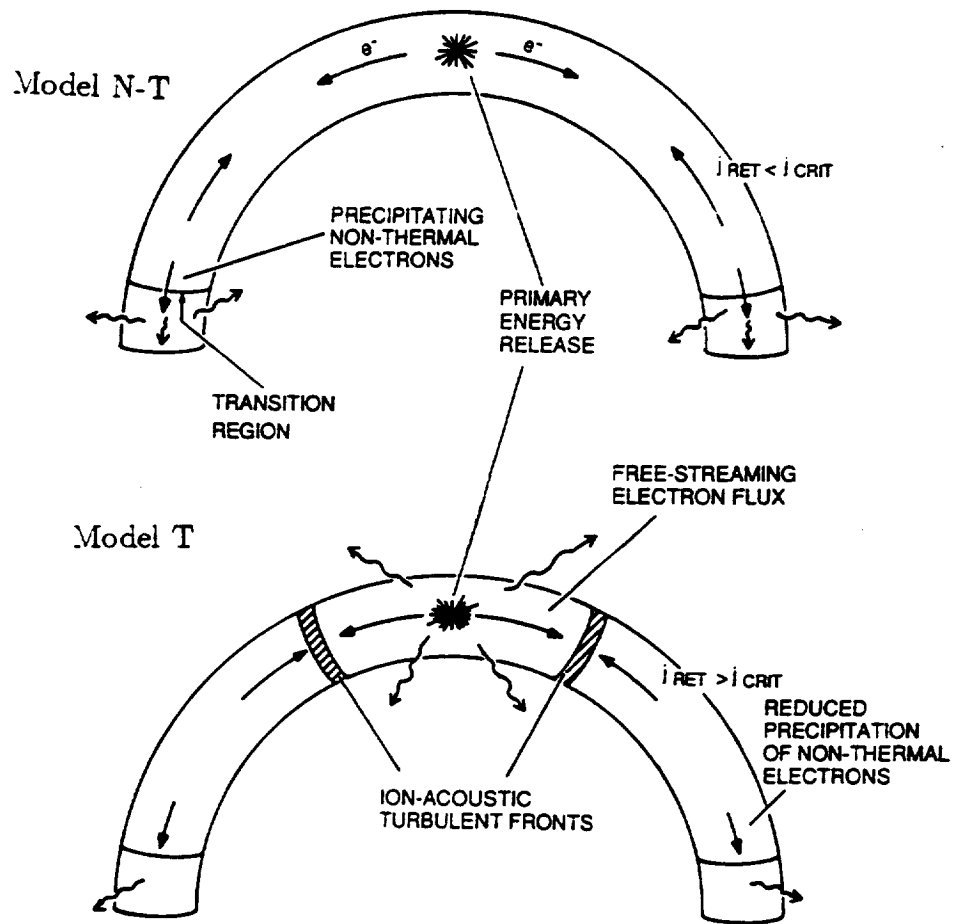


**Figure 1.11: Model N-T And Model T**

These show expected dominant emission points based on a qualitative understanding of the Model T and the Model N-T (graphics from Tandberg-Hanssen and Emslie, 1988). Quantitatively, the emission profiles as a function of time, energy, and loop position must be developed and then viewed by a Fourier telescope to determine if any differences in the resulting images at a particular time and energy are possible.

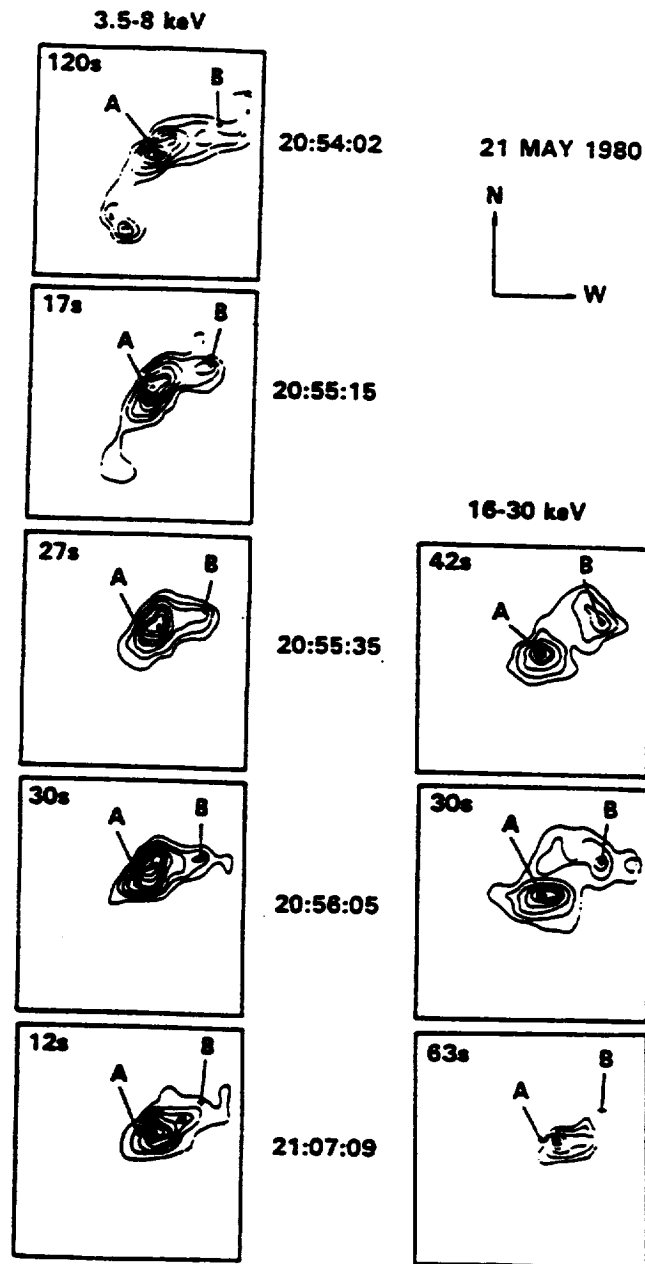
Direct imaging of hard x-ray sources in solar flares has only been accomplished fairly recently with the Hard X-Ray Imaging Spectrometer (HXIS) instrument on the Solar Maximum Mission (SMM) spacecraft and with the Solar X-Ray Telescope (SXT) onboard the Hinotori satellite. Hoyng et al. (1981) reported images in the energy range 16-30 keV which change from a double footpoint structure early in the event to a more amorphous structure later. The Japanese free flyer, YOHKOH, is presently making observations; however, the data have not been reduced yet.

Figure 1.12 shows HXIS hard x-ray images of a flare on May 21, 1980 (Antonucci et al., 1982), which are somewhat ambiguous, due to the limited temporal and spatial resolution of the instrument among other reasons. However, these and other HXIS hard x-ray images indicating the existence of footpoints as sources do not sufficiently discriminate between the Model T and the Model N-T. In fact, due to low count rates and the correspondingly large integration times necessary to achieve a statistically significant image, and to telemetry limitations (MacKinnon, Brown, and Hayward, 1985), the HXIS data has in general done little to alleviate the uncertainty between the two models (Brown and Emslie, 1988; Emslie, 1983). More statistically significant hard x-ray imaging data, at significantly higher photon energies and with higher resolution, are vitally needed to provide better descriptions of these processes.

The spatial resolution required to understand the physical processes at work in the flare may be calculated as follows. From Emslie and Machado (1987), the energy of the incident electron may be related to the column depth to which it penetrates a thick target by

$$E^2 = E_o^2 - 2KN \quad (1.1)$$

where  $E$  is the electron energy at particular column depth,  $N = \int ndz$ ,  $K = 2.8 \times 10^{-18} \text{ cm}^2 \text{ keV}^{-1}$ , and  $n$  is the electron density. We can estimate the depth



**Figure 1.12: HXIS Hard X-ray Images**

This illustrates images of a flare in hard x-rays taken on May 21, 1980 (Antonucci et al., 1982). Although the resolution is somewhat limited, footpoints seem to be indicated.

an electron will penetrate into the chromosphere from

$$z \cong \frac{E_o^2 - E^2}{2Kn}. \quad (1.2)$$

Taking  $E_o = 20$  keV and  $E = 10$  keV (the threshold for production of a 10 keV photon), we find with  $n = 10^{11} \text{ cm}^{-3}$ ,

$$z \cong \frac{5 \times 10^{19}}{10^{11}} \text{ km} \cong 7 \text{ arc second}. \quad (1.3)$$

Therefore, in order to follow the degradation of the electron energy, a spatial solution substantially better than 7 arc seconds is required. Hence, the minimum requirements suggested by this analysis for imaging telescopes are spatial resolutions on the order of 1-4 arc second.

Sub arc second resolution may be desirable in the next generation of instruments to further characterize these processes. Similarly, from considerations of collisional stopping times, and loop transit times for a typical loop 1 arc second in cross sectional diameter and 20 arc seconds in loop diameter, temporal resolutions on the order of 1-5 seconds are desirable (LaRosa, 1990).

### C. X-Ray Imaging Background

A Fourier-transform telescope typically consists of a set of subcollimators each of which modulate incoming photons onto an associated detector array providing a measurement of a Fourier component. Image making in hard x-rays can be shown (Chapter IV) to correspond to that in the radio frequency regime in that the data are basically now in the same form as those from a radio telescope. Also, it can be brought into the Astronomical Image Processing System (AIPS), hitherto used for radio images and processed with the algorithms therein. Refer to Chapter IV for a more detailed discussion.

AIPS, developed and maintained by the National Radio Astronomy Observatory (NRAO), is widely accepted today in the radio astronomy community (Mertz, 1989). It is a highly sophisticated VMS overlay software system which requires over 180,000 blocks of VAX disk space to run. At its core is a multitude of software routines which allows the user to bring Flexible Image Transport System (FITS) data into the AIPS operating system; (Greisen, 1986; Greisen and Harten, 1981) fast Fourier transform the data to form a dirty map; clean the dirty map to form an image using several different, optional algorithms; and then display the image in a number of different ways. Peripheral software offers the user a number of options with which to enhance an image in a number of different ways. Chapter IV will discuss this in greater detail.

One major advantage in using AIPS is that it allows a “dirty” image to be cleaned several different ways. Two of the most widely used are the CLEAN algorithm and the Maximum Entropy Method (MEM). Figure 1.13 shows an example of a dirty image of an astrophysical source emitting in the radiofrequency regime. Although many artifacts are present, the trained observer will expect a real source or sources at the center of the symmetrical pattern. The shape and intensity of the source is basically unknown. Figure 1.14 shows the true image after the CLEAN algorithm was applied. Here, the source, a radio emitting galaxy, is revealed much more clearly.

One of the strengths of a numerical model is that a dirty image can be cleaned conveniently using both techniques and then the images compared. In addition, artifacts which might be introduced by approximations in the techniques will become apparent and will serve as useful supporting information for handling real data.

## **D. Research Approach**

We used the wealth of literature relating to both Model T and Model N-T



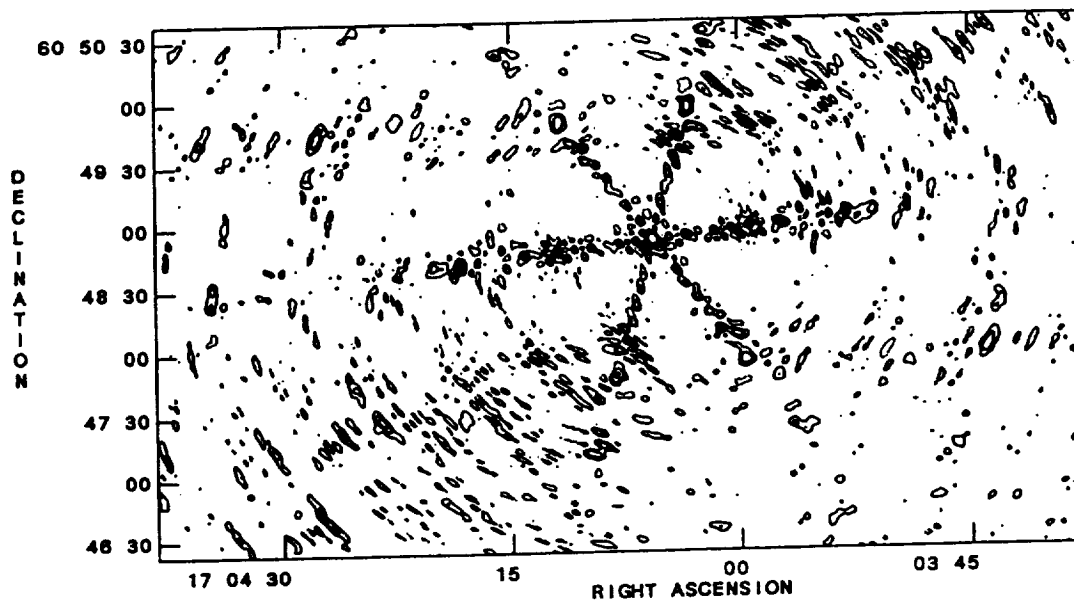


**Figure 1.13: A Dirty Image Of A Typical Astrophysical Source**

The trained observer will expect to find a source at the center of the symmetrical region. However, this dirty image alone is not sufficient to show accurately the shape and intensity of the source.

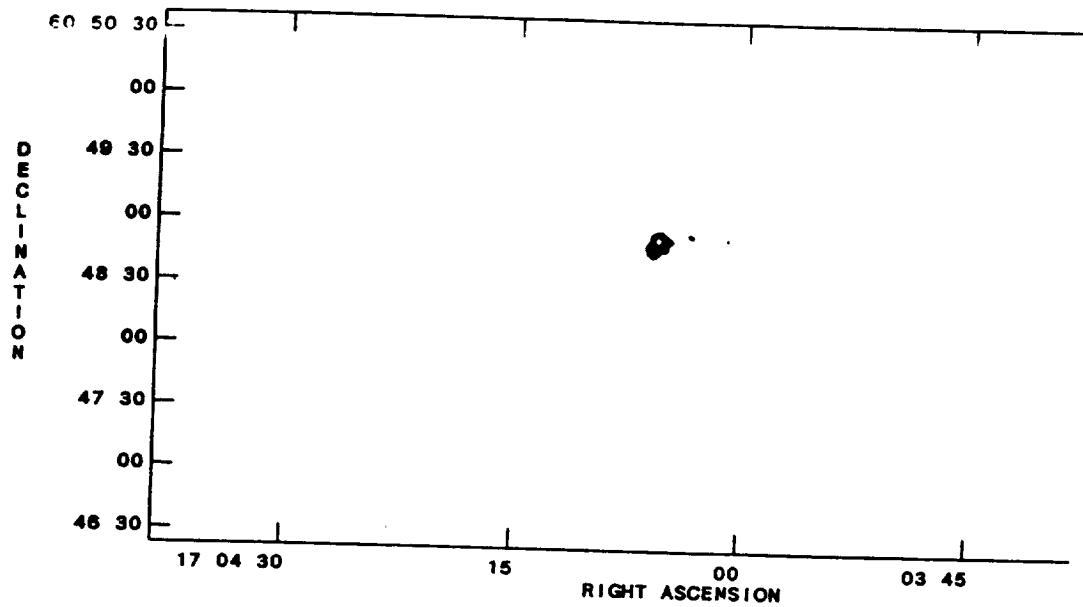


**Figure 1.14: The Clean Image**

The CLEAN algorithm was applied to generate this *cleaned* image. When comparing the quality of this image with its *dirty* image, the power of this image reconstruction algorithm becomes truly evident

to describe quantitatively the hard x-ray emission as a function of time, energy, and loop position (Chapters II and III). The emission profiles for each model are then examined for distinctive signatures and used to construct *synthetic* flares to be viewed by the model telescopes.

Using random photon counting techniques, SMC and RMC models were constructed to *view* Model T and Model N-T flare profiles and AIPS was modified and calibrated to reconstruct images from the telescope x-ray optics output. Comparison of the images at similar times and energies should provide a basis for judging the ability of a given telescope to resolve the distinctive features of a synthetic event.

In addition, various instrumental questions were addressed such as the effects of low signal levels, random noise on the detector, twist, etc. The end-to-end set of software including those codes which generated synthetic flares, those codes which represented the operation of the telescope, those codes which developed the appropriate detector responses, and those codes in AIPS were designated the Marshall Space Flight Center Hard X-ray Imaging Simulations (MAHXIS). See Appendices A - D for examples.

## II. MODEL N-T HARD X-RAY EMISSION

### A. INTRODUCTION

As mentioned in the introduction, there are two prevalent, competing theories (Model T and Model N-T) for explaining hard x-ray emission from solar flares (e.g., Campbell et al., 1990; Brown, 1974; Emslie and Vlahos, 1980; Tandberg-Hanssen and Emslie, 1988). The purpose of this chapter is to describe quantitatively the Model N-T hard x-ray emission as a function of time, energy, and loop position. This will be compared with the Model T profiles to be discussed in Chapter III to determine if any differences exist between the two. These profiles will then be viewed numerically (Chapter VII) through a Fourier telescope model to determine if in fact the differences will be evident in the hard x-ray images.

Figure 2.1 illustrates the Model N-T concept. A beam of electrons is injected at the apex of the loop. These electrons travel down the legs of the loop and impact the denser chromosphere in the footpoints. Since the bulk of the interactions in this region are Coulomb collisions, the plasma is heated rapidly which increases the pressure locally. This increase in pressure forces material to migrate up the legs of the loop until it reaches the apex after which point it simply piles up in the loop, increasing the density. This migration leads to substantial increases in temperature and in density in the loop. As the density increases, more and more interactions between beam electrons and the ambient plasma cause additional heating and also result in nonthermal bremsstrahlung emission. The hot plasma in the loop eventually reaches a temperature in which thermal emission becomes significant at hard x-ray energies.

The *Model N-T* exhibits both thermal and nonthermal characteristics. The distinction between thermal and nonthermal bremsstrahlung used in this context is as follows: if the emission is produced by interactions within a population of

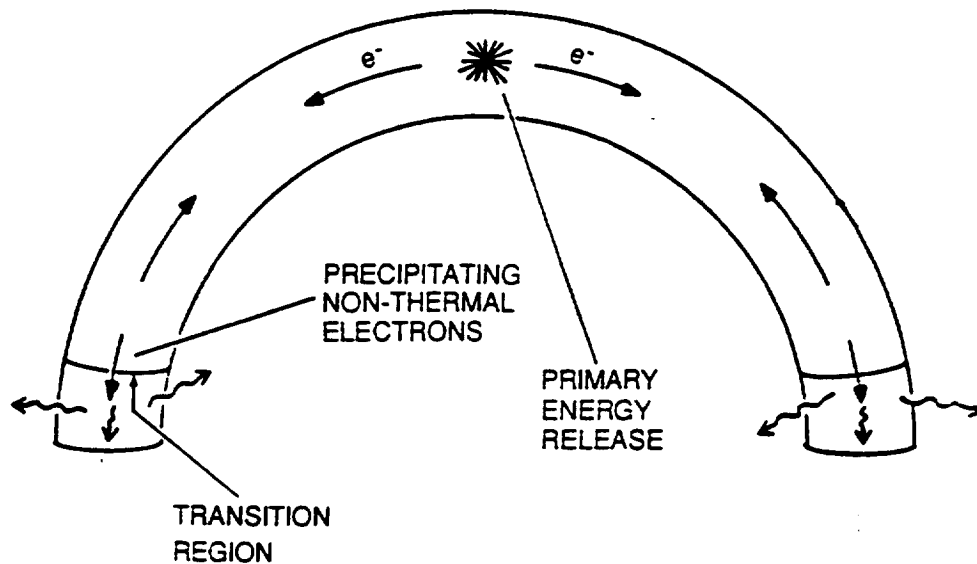


**Figure 2.1: Model N-T Concept**

A beam of electrons is injected at the apex of the loop (graphics from Tandberg-Hanssen and Emslie, 1988). These electrons travel down the legs of the loop and impact the denser chromosphere in the footpoints. Since the bulk of the interactions in this region are Coulomb collisions, the plasma is heated rapidly which increases the pressure locally. This increase in pressure results in the migration of material up and *down* the legs of the loop. Both nonthermal and thermal emission occur throughout the loop at lower energies.

particles roughly distributed according to a Maxwellian then we say the process is **thermal** in nature. On the other hand, if the population forms a separate high-energy component at energies much greater than the bulk of the population then we define it as **nonthermal**.

Brown and Emslie (1987) calculated the spatial structure and temporal evolution of the hard x-ray emission of both nonthermal and thermal components during the impulsive phase of an electron-heated (Model N-T) solar flare based on hydrodynamic simulations by Nagai and Emslie (1984) and Emslie and Nagai (1985).

Recently, Mariska, Emslie, and Li (1989) carried out a series of numerical simulations which more completely describe the response of the solar atmosphere to heating by a nonthermal electron beam. In this work, the electron beam is injected at the apex of the loop and the beam electrons have an energy spectrum of the form

$$F_0(E_0, t) = F_0(E_0)g(t) \quad (2.1)$$

$$= \frac{4(\delta - 2)F_1g(t)}{(\delta + 2)E_c^2} \left[ \frac{E_0}{E_c} \right]^2 \quad (2.2)$$

if

$$E_0 \leq E_c$$

or

$$F_0(E_0, t) = \frac{4(\delta - 2)F_1g(t)}{(\delta + 2)E_c^2} \left[ \frac{E_0}{E_c} \right]^{-\delta} \quad (2.3)$$

if

$$E_0 \geq E_c.$$

Here  $F_l$  is the injected flux ( $\text{erg cm}^{-2} \text{s}^{-1}$ ),  $E_c$  is a low-energy *inflection point*,  $\delta$  is the spectral index,  $E_0$  is the electron energy in keV, and  $g(t)$  is a triangular time profile given by

$$g(t) = \frac{t}{30} \quad (2.4)$$

for

$$0 \leq t \leq 30 \text{ s}$$

or

$$g(t) = 2 - \frac{t}{30} \quad (2.5)$$

for

$$30 \leq t \leq 60 \text{ s}.$$

The low-energy form of the electron energy spectrum (equation 2.2) gives a much smoother variation of heat input with depth than that corresponding to an electron spectrum with a sharp low-energy cutoff (see e.g., Nagai and Emslie, 1984) and is primarily used to permit a more efficient and rapid numerical solution of the hydrodynamic equations. Its use does not change, however, the power-law spectral shape of hard x-ray bursts at photon energies ( $\epsilon > E_c$ ) and thus is still consistent with observations (Figure 1.10).

Figure 2.2 shows the results for the density in the model from 10 to 30 seconds. At 10 seconds into the flare, bulk material motion can be observed moving up from the footpoints. At 20 seconds the material has almost reached the apex of the loop, and at 30 seconds the material is piling up in the legs of the loop. The change in density from 20 to 30 seconds produces some interesting spatial structure for the

emission at 10 keV (Figure 2.6) since both the thermal and nonthermal emission are directly affected by changes in density at this energy which will be discussed later.

Now, following Emslie and Machado (1987), the integrated nonthermal hard x-ray yield from column depth 0 to  $N$  ( $N = \int n dz$ ) in photons  $\text{cm}^{-2} \text{s}^{-1} \text{keV}^{-1}$  may be written as

$$J(\epsilon, N) = \int_0^N I(\epsilon, N') dN' \quad (2.6)$$

$$= \frac{\kappa}{\epsilon} \int_{N'=0}^N dN' \int_{E_0^*}^{\infty} \frac{F_0(E_0)}{(E_0^2 - 2KN)^{\frac{1}{2}}} dE_0 \quad (2.7)$$

where

$$E_0^* = (\epsilon^2 + 2KN)^{\frac{1}{2}} \quad (2.8)$$

and

$$K = 2\pi e^4 \Lambda \quad (2.9)$$

is the coefficient of the variation of energy with column depth due to Coulomb collisions and is defined in Tandberg-Hanssen and Emslie (1988).  $\Lambda$  is the Coulomb logarithm. From Brown (1971) and Li and Emslie (1987), the cumulative intensity  $J(\epsilon, N)$  may be written as

$$J(\epsilon, N) = \frac{A}{(\delta + 2)(\delta - 1)} F_l g(t) E_c^{\delta-2} \epsilon^{1-\delta} j(x; y) \quad (2.10)$$

in units of photons  $\text{cm}^{-2} \text{s}^{-1} \text{keV}^{-1}$  at the Sun, where

$$A = 4 \times 1.6 \times 10^{-9} \frac{\kappa}{K} = 1140 \text{ erg}^{-1}. \quad (2.11)$$



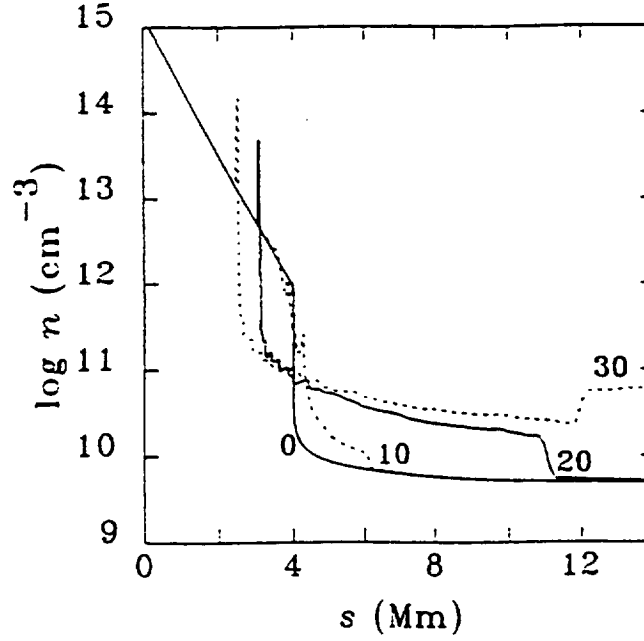


**Figure 2.2: Density Versus Loop Position**

This shows the density results from the Mariska, Emslie, and Li (1989) hydrodynamic simulation as a function of loop position for a family of times. The beam heats the material in the footpoints and the bulk motion from the footpoints toward the top of the loop can be seen. At 30 seconds, the front has reached the top and material starts piling up. This causes approximately an order of magnitude increase in the density from 20 to 30 seconds at the apex.

The dimensionless quantities

$$x = \frac{2KN}{\epsilon^2} \quad (2.12)$$

and  $j$  are functions of both the dimensionless column density  $x$  and  $y = \frac{\epsilon}{E_c}$ . These are shown graphically for various forms of  $F_0(E_0)$  by Li and Emslie (1990), and Emslie and Machado (1986).

As a result of Coulomb collisions of the beam electrons with the ambient electrons in the target, the electron temperature in the flare loop can rise to  $10 - 100 \times 10^6$  K (Mariska, Emslie, and Li, 1989), adequate to produce significant hard x-ray emission, especially at lower energies ( $\epsilon \leq 10 \text{ keV}$ ). This additional “secondary” thermal bremsstrahlung yield from a segment of the loop is (Allen, 1973; Culhane and Acton, 1970)

$$\Delta J(\epsilon) = 1.2 \times 10^{-11} \left( \frac{n^2 l}{\epsilon T^{\frac{1}{2}}} \right) \exp\left(\frac{-\epsilon}{kT}\right) \quad (2.13)$$

in photons  $\text{cm}^{-2} \text{ s}^{-1} \text{ keV}^{-1}$  at the Sun,  $n$ ,  $T$ , and  $l$  are the density, temperature, and the length of the segment.

A given  $\Delta J$  (whether due to nonthermal or thermal emission) produces a certain number of counts on a detector in low-Earth orbit can be obtained from

$$C = C_T \Delta J (\text{counts } \text{s}^{-1}), \quad (2.14)$$

where

$$C_T = \sigma \left( \frac{A}{4\pi R^2} \right) \Delta \epsilon, \quad (2.15)$$

and  $A$  is the flare area,  $R = 1 \text{ AU}$ ,  $\sigma$  is the effective detector area, and  $\Delta \epsilon$  is the effective energy width of the observation bin.

This equation assumes an ideal detector which is equally responsive to photons of any energy within the selected bin. In reality, above 100 keV detector quantum efficiency tends to decrease dramatically as one goes higher in energy; thus, it is desirable to take energy bins as small as possible to compensate for this effect. Also, the detector response characteristic may change over time. Real-world detector constraints will be discussed in greater detail in Chapter IV.

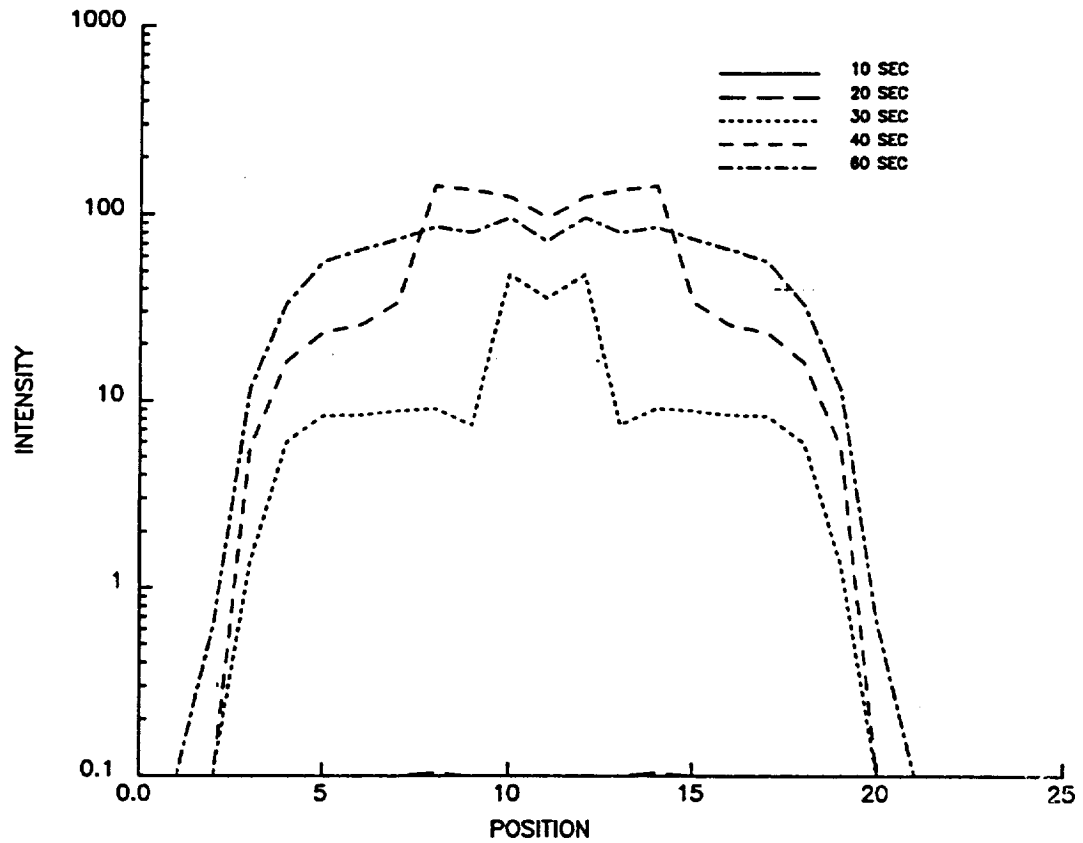
In the following section the total hard x-ray bremsstrahlung emission as a function of energy, time, and position along the loop is presented. The beam parameters have the following values:  $F_l = 10^{11} \text{ erg cm}^{-2} \text{ s}^{-1}$ ,  $E_c = 15 \text{ keV}$ , and  $\delta = 6$ .

## B. EMISSION AS A FUNCTION OF TIME, POSITION, AND ENERGY

The following series of plots illustrate the predicted emission from model N-T at the Earth. This, as discussed previously, will be composed of both thermal and nonthermal components. However, since our telescopes cannot, of course, distinguish how an x-ray photon was created we simply look at the total emission signature. The following plots will show the intensity at the Earth in photons  $\text{cm}^{-2} \text{ sec}^{-1} \text{ keV}^{-1}$  for a given loop pixel.

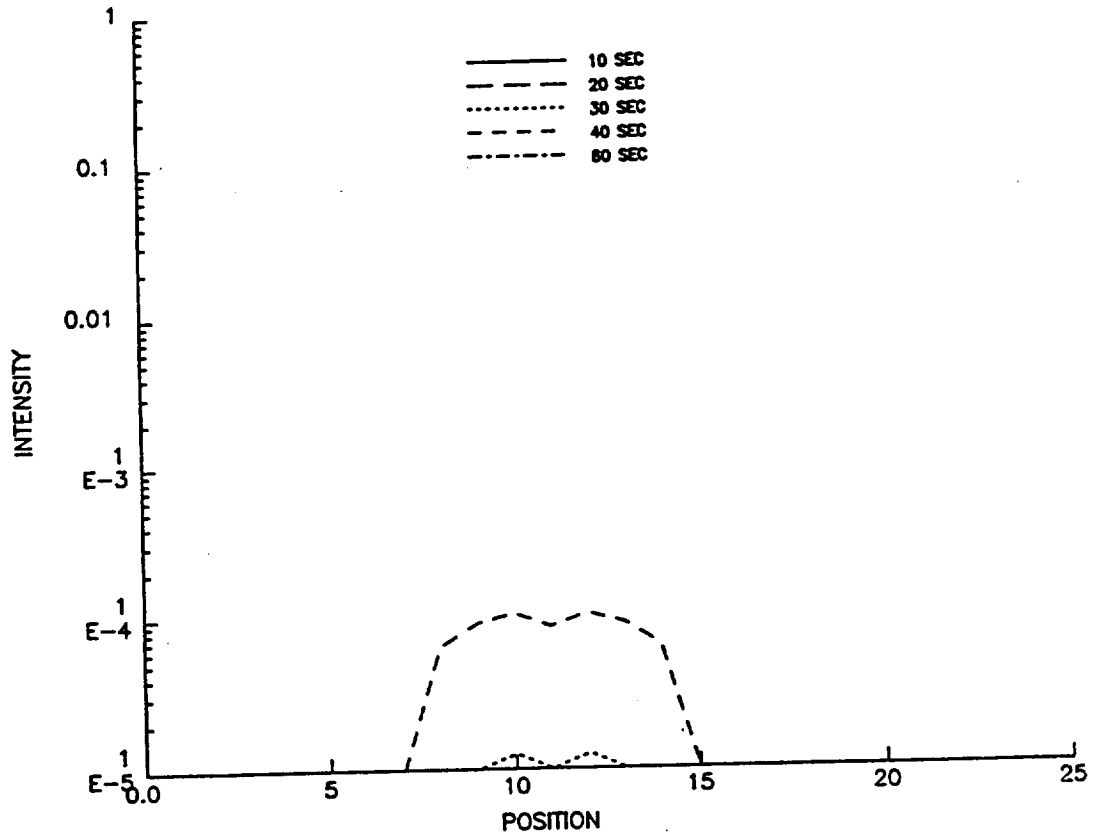
The first two plots (Figures 2.3 and 2.4) show the predicted spatial distribution of the emission due to thermal effects only for a given family of times (10, 20, 30, 40, 60 seconds), for photon energies at 10 and 40 keV, respectively. As one would expect, the decrease in thermal emission from 10 to 40 keV is extremely large. At 40 keV and higher there is no significant emission being produced by thermal bremsstrahlung. This is to be expected from the relatively low temperatures ( $kT < 10 \text{ keV}$ ) found in the loop at this time (equation 2.13).

Figure 2.5 shows the predicted emission profile of the flare at 10 keV due to nonthermal emission alone for the same family of times mentioned above. While



**Figure 2.3: Thermal Emission Profile at 10 keV**

This shows the Model N-T thermal emission component only. The thermal emission starts increasing between 20 and 30 seconds, corresponding to the arrival of bulk material from the footpoints, and remains high throughout the rest of the event. At 60 seconds, the beam has shut off and only the emission from the filled loop remains.



**Figure 2.4: Thermal Emission Profile at 40 keV**

The maximum temperatures in the loop ( $\cong 2 \times 10^7$  K) are not high enough to produce significant thermal emission at 40 keV. Hence nearly all the significant emission from Model N-T at energies from 40-100 keV is nonthermal.

most of the emission occurs in the footpoints, significant emission is also produced higher in the loop. Corresponding to the large density increase at the top of the loop from 20 to 30 seconds is a substantial increase in the total emission from the apex of the loop. The beam heats this material producing some nonthermal emission while an order of magnitude additional thermal emission is produced by the heated plasma. This is to be expected since the thermal bremsstrahlung is inherently a more efficient process (Chapter I). At 60 seconds (beam shutoff), only a filled loop remains.

Figures 2.6 through 2.9 show the combined emission at the aforementioned times for 10, 40, 70, and 100 keV photons, respectively. The footpoint region is heated rapidly by the beam and the corresponding increase in local pressure produces both upward and downward mass motions. This appears in Figure 2.2 as a shift in the high density region downward and is similarly reflected in the emission by a corresponding shift in the peak intensity from one pixel to the next lower one.

As stated before, the emission, seen in Figures 2.7-2.9, at 40-100 keV is non-thermal; and the profile signature is one of relatively bright footpoints with less bright pixels in the upper part of the flare loop.

### C. SUMMARY

The emission as a function of time, energy, and loop position of the Model N-T has been determined quantitatively. The predominant hard x-ray signature predicted by this model is one of twin footpoints early in time at low energies and at all times at higher energies. The telescope will image both thermal and nonthermal components together; thus, the total profile must be used as input for the Fourier telescopes, the SMC and the RMC, discussed in Chapters V and VI. How well these telescopes can image the predicted profiles will be discussed in Chapter VII.

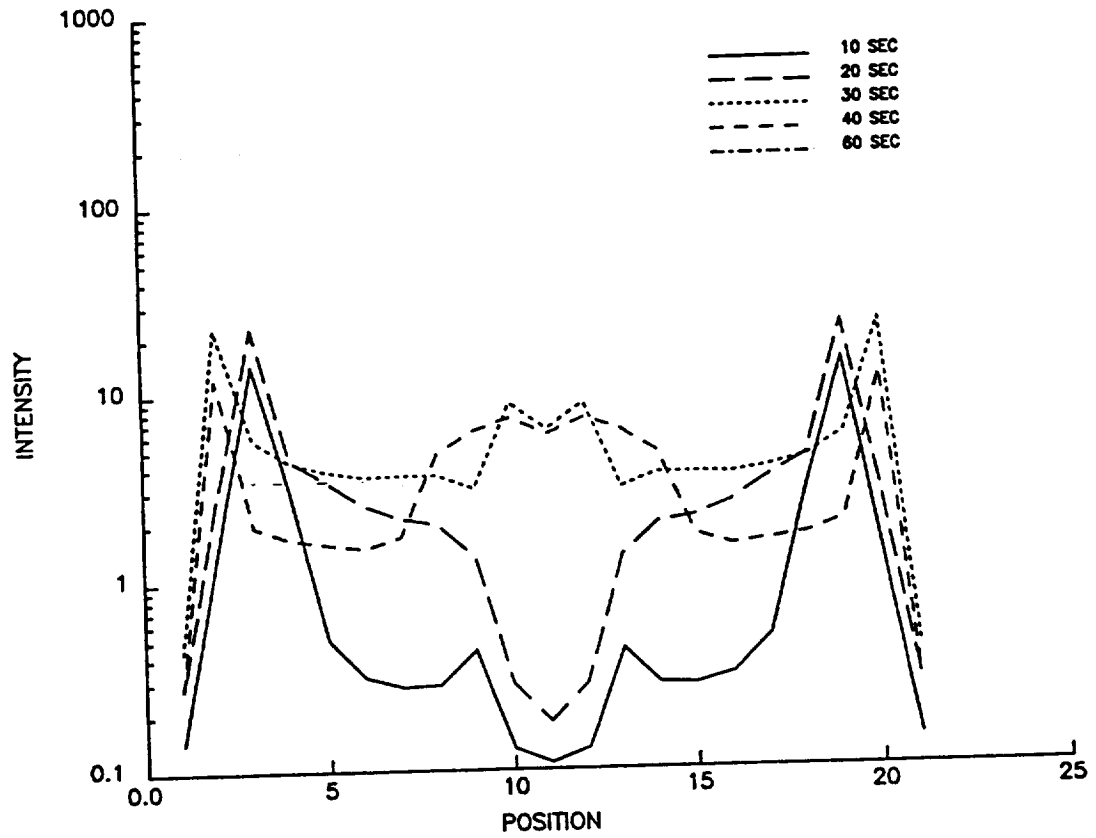


**Figure 2.5: Nonthermal Emission Profile at 10 keV**

Clearly, emission from the footpoints is dominant in the loop from 0-20 seconds and remains at significant levels until beam cutoff at 60 seconds. However, significant emission is also produced higher in the loop especially after those times in which the density has greatly increased.

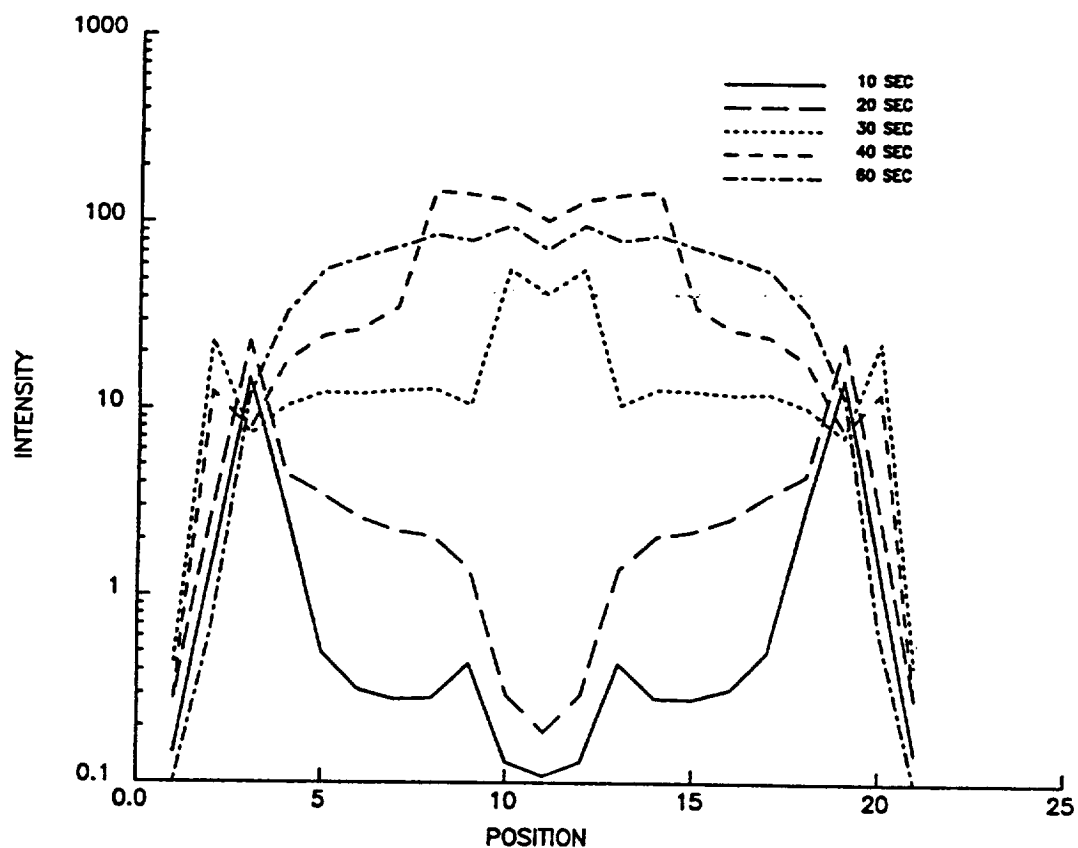


**Figure 2.6: Total Emission Profile at 10 keV**

This shows the Model N-T total emission profile. These combined thermal and nonthermal profiles will serve as input to the telescope models (Chapter VII) The movement in time of the footpoint peaks corresponds to mass motions up and *down* the loop resulting from increased local pressure in the region.



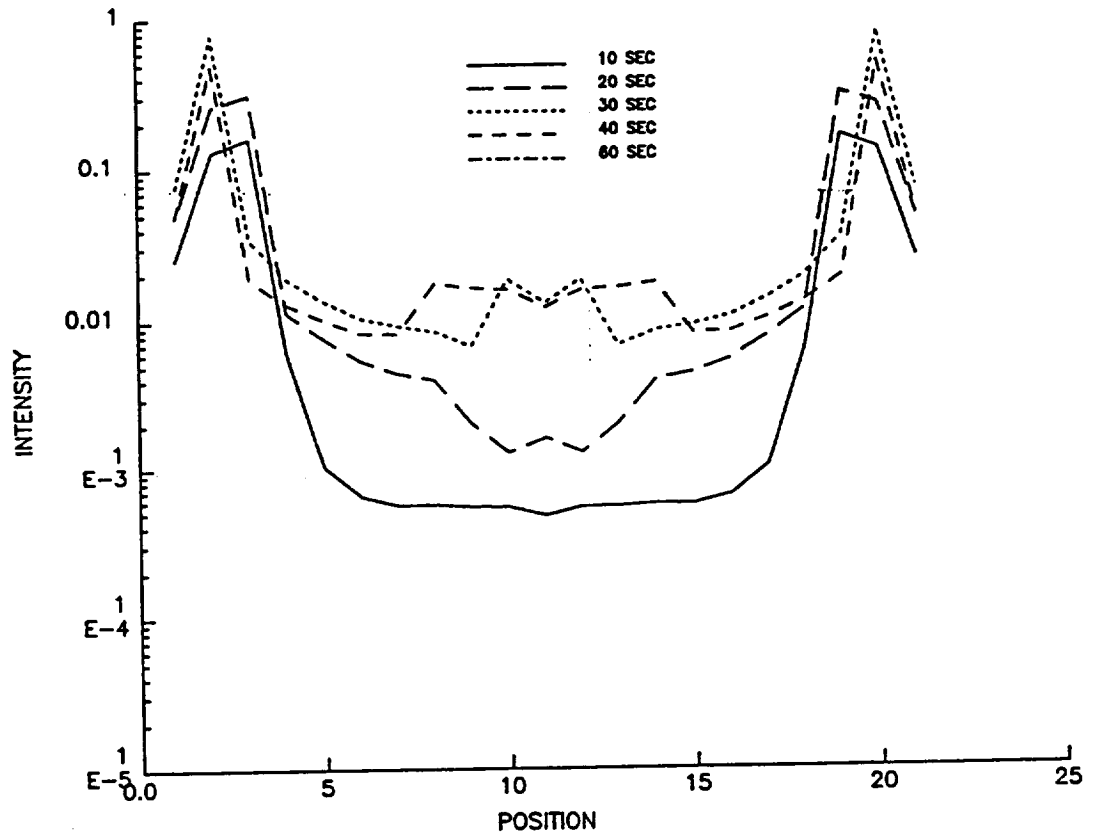


**Figure 2.7: Total Emission Profile at 40 keV**

This shows the Model N-T total emission profile. These combined thermal and nonthermal profiles will serve as input to the telescope models (Chapter VII). The movement in time of the footpoint peaks corresponds to mass motions both up and down the loop due to increased local pressure in the region. As expected, the total intensity is significantly reduced at 40 keV relative to that at 10 keV and is predominantly nonthermal.

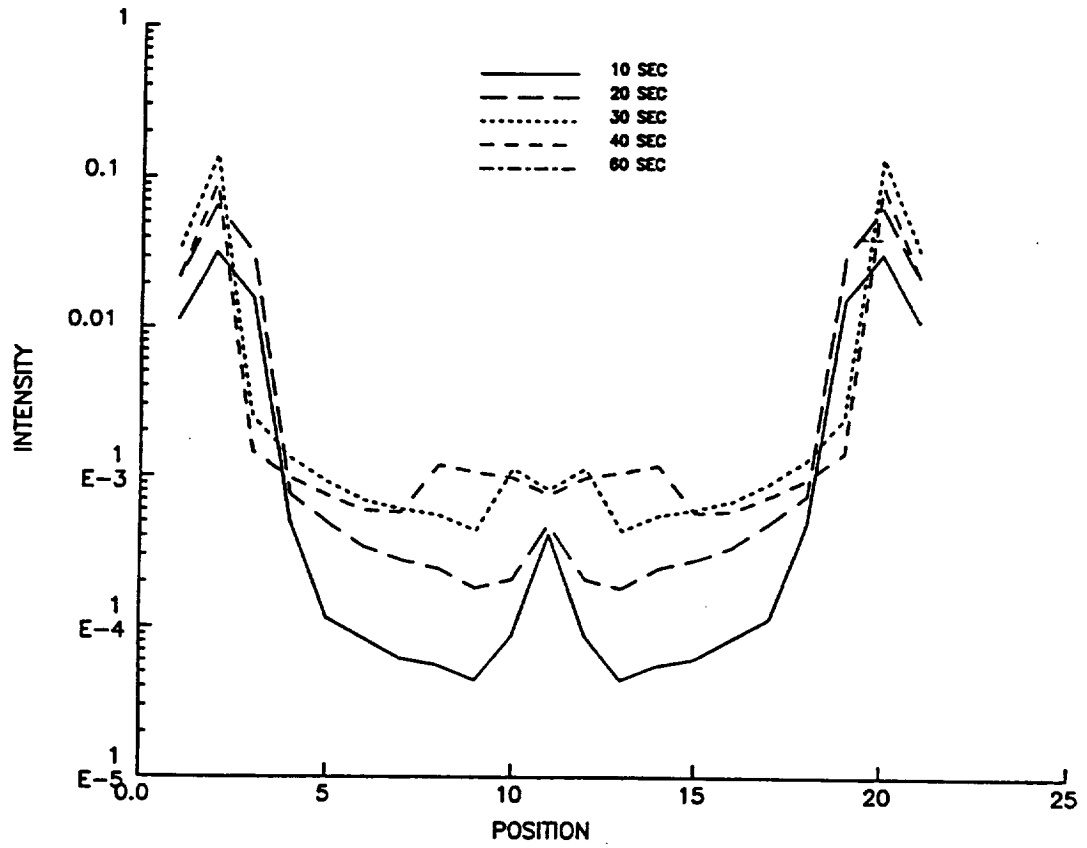


**Figure 2.8: Total Emission Profile at 70 keV**

This shows the Model N-T total emission profile. As expected, the total intensity is even more reduced at 70 keV (Figures 2.6 and 2.7) and is predominantly nonthermal.

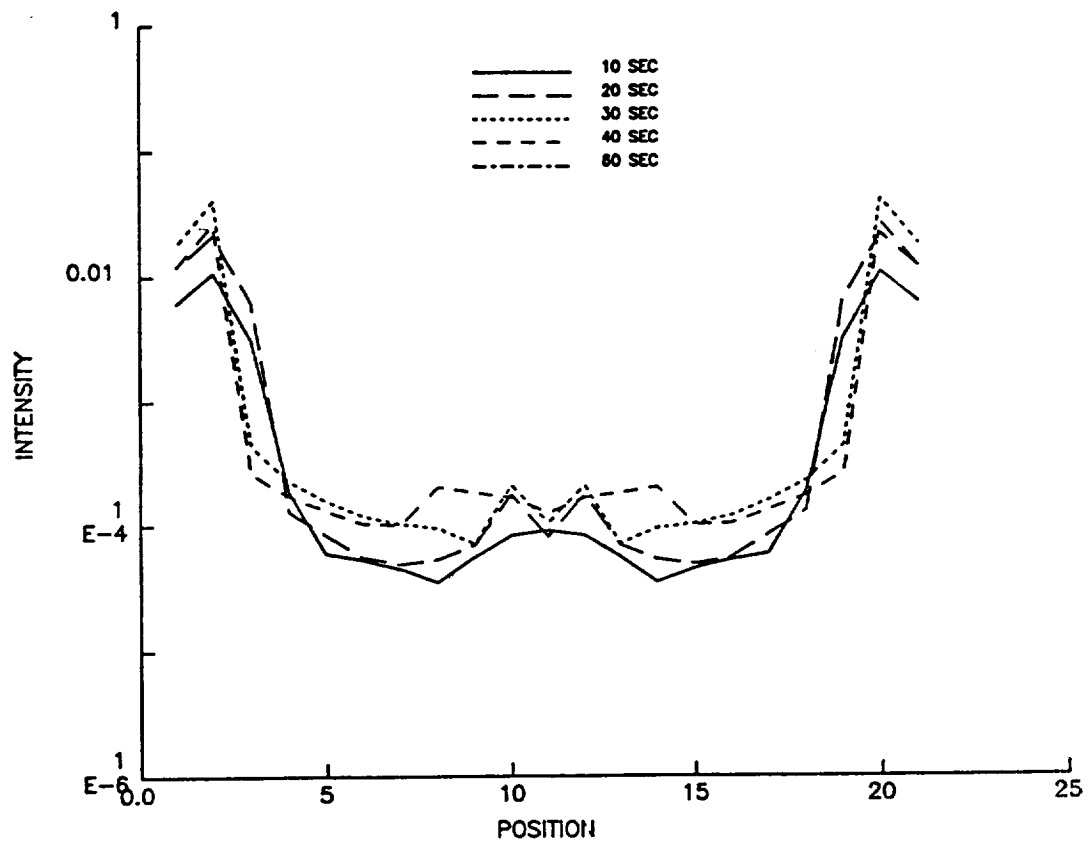


**Figure 2.9: Total Emission Profile at 100 keV**

This shows the Model N-T total emission profile. As expected, the total intensity is significantly reduced at 100 keV relative to that at 70 keV (Figure 2.8) and is predominantly nonthermal.

Clearly, the Model N-T evolves rapidly over a period of a few seconds. The bright footpoints spatially occupy 1-3 arc second each and should be observable by a telescope with  $\cong 4$  arc second resolution such as ours. While the footpoints persist in this model for several seconds, having 1 second integration times would still be desirable as the 10 keV case evolves significantly from a bright footpoint structure to a predominant central peak and then to a filled loop.

### III. MODEL T HARD X-RAY EMISSION

#### A. INTRODUCTION

Chapter II discussed the quantitative development of the Model N-T hard x-ray emission as a function of time, loop position, and energy. This chapter will present the Model T concept and determine analytically its associated emission characteristics. Once the emission profiles for this model are obtained, they can be compared with those in Chapter II to determine if those for each of the two models are sufficiently distinct to afford an observational test. Chapter VII will discuss Fourier telescope image differences between the two models.

The Model T concept is one of an extremely hot mass of plasma created in a coronal loop such that the thermal electrons have sufficient energy to produce bremsstrahlung at hard x-ray energies through large-angle scattering off ambient protons (Chubb et al., 1966). Based in part on fusion research, Brown et al. (1979) describe an improvement to this basic idea. Initially, the electrons in a small region of the loop near its apex are heated rapidly. The heating mechanism and rate are assumed to be such that only the electrons would be heated appreciably leaving the ions at essentially their preflare ( $\cong 10^6$  K) temperature.

A large electrical current is generated by the hot electrons streaming outward from the relatively small, initial source volume down the legs of the flare loop containing cooler plasma. The electric field established by a combination of inductive and charge separation effects accelerates ambient electrons into a reverse current which quickly exceeds the ion-sound velocity in the plasma, thus generating ion-acoustic waves (Figure 3.1).

A brief discussion of the physics of ion-acoustic waves follows (Krall and Trivelpiece, 1973; Chen, 1974). In the absence of ordinary collisions within a plasma, ions can still transmit momentum to each other through the intermediary

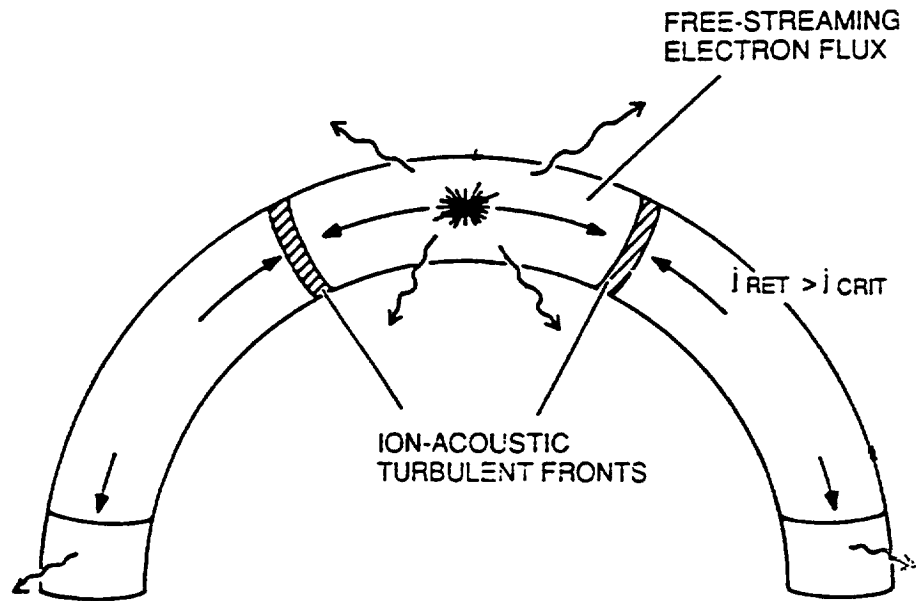


**Figure 3.1: Model T Concept**

The electrons in a relatively small region at the apex of the loop are heated to  $2 \times 10^8$  K. The hot electrons begin streaming away down the legs of the loop inducing a return current exceeding the ion-acoustic speed which leads to ion-acoustic turbulence. The waves form a marginally stable, moving barrier which contains most of hot electrons. The most energetic ones escape and serve to maintain the marginal stability condition. Thermal emission is produced in the kernel while nonthermal emission is produced outside the kernel and in the footpoints.

of an electric field carried by mobile electrons. These form regions of compression and rarefaction, just as in an ordinary sound wave. Compressed regions tend to expand into the rarefactions. This happens because (i) thermal effects tend to spread out the ions and (ii) the ion bunches are positively charged and tend to disperse because of the resulting electric field. Once in motion, the ions in the bunches tend to overshoot equilibrium because of their relatively large inertia. This naturally leads to an oscillation in which the compressions and rarefactions are regenerated to form an ion-acoustic wave.

Ion-acoustic waves occur due to the interaction of both the electron and ion components within the plasma. These waves are strongly affected by Landau damping and hence only created in any strength when  $T_e \gg T_i$ . If one considers the classic surfboard analogy (Chen, 1974) in which surfboards (electrons) slower than the (ion) wave gain energy from the wave while surfboards faster than the wave lose energy to the wave, then the importance of the electron temperature being higher than that of the ions becomes evident as this spreads out the electron distribution and damps the wave more slowly.

Figure 3.2 illustrates the two distributions at the beginning of the event near the top of the loop in the Model T. The hot electron distribution is skewed representing a return current moving through the ambient, colder ions. The threshold for instability is reached when the bulk velocity of the backward-streaming electrons exceeds the ion-acoustic speed.

Rapid isotropization of ion-sound waves occurs through scattering on the ambient particles, and the resulting ion-sound turbulence in turn scatters the hot electrons. This turbulence in effect forms a moving *barrier* in which the electrons have a reduced mean free path. Thus, most of the hot electrons in the kernel are reflected while only the ones possessing the highest energies (i.e., greatest mean free paths) pass through. This passage of the *highest* energy electrons is vital to

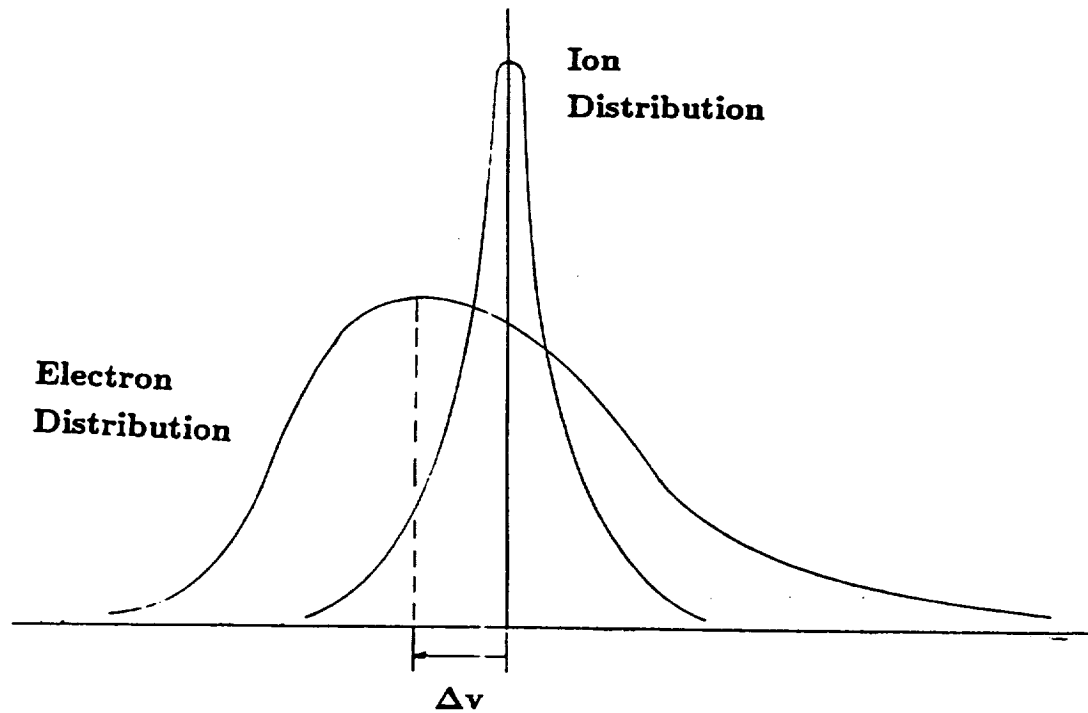


**Figure 3.2: Electron and Ion Distribution Functions**

This shows the cold ion and hot electron distributions near the top of the loop at the beginning of the event in the Model T concept. The electron distribution at low velocities is skewed reflecting a return current. When the bulk velocity of this return current exceeds the ion-acoustic speed, an ion-acoustic instability is excited leading to ion-acoustic turbulence.



maintaining the *marginal stability* of the barrier throughout its movement from the apex to the footpoints corresponding to the flare's impulsive phase.

Marginal stability in this context may be illustrated by considering two perturbations. In the first case, the level of acoustic wave turbulence is increased slightly. This causes the hot plasma to be contained more efficiently reducing the escape current and the return current and hence the level of acoustic wave turbulence. In the second case, the level of turbulence is decreased slightly. This reduces the effectiveness of containment and allows the current to increase. The return current then increases restoring the level of turbulence to its original value.

A simple analog of marginal stability is presented in Figure 3.3. In this analog, a system comprised of hose pipes, movable barrier, and bucket are arranged as shown in the figure. The hose pipes have their nozzles adjusted so that the water flow rate through each one varies. The system is placed in equilibrium by placing the barrier so that the fastest streams of water clear the top of the barrier to be collected in the bucket. A drain hole is punched in the bottom of the bucket. Some water clears the barrier and is collected by the bucket adding to its weight. Thus, the barrier is maintained at its equilibrium height balanced between the pull of gravity and the spring force.

If the barrier is pushed down slightly, more water goes to the bucket, which gets heavier and pulls the barrier back up again. If the barrier is pushed upward slightly, less water gets over the top and the bucket gets lighter thus allowing the spring to pull the barrier back down again. Finally, we note that if the fastest hose is turned off, then the bucket gets lighter allowing the spring to pull the barrier down slightly to allow additional water over the top thus maintaining equilibrium.

Returning to the solar case, two barriers would form, one in each leg of the loop and would move apart down the legs of the loop at about the ion-

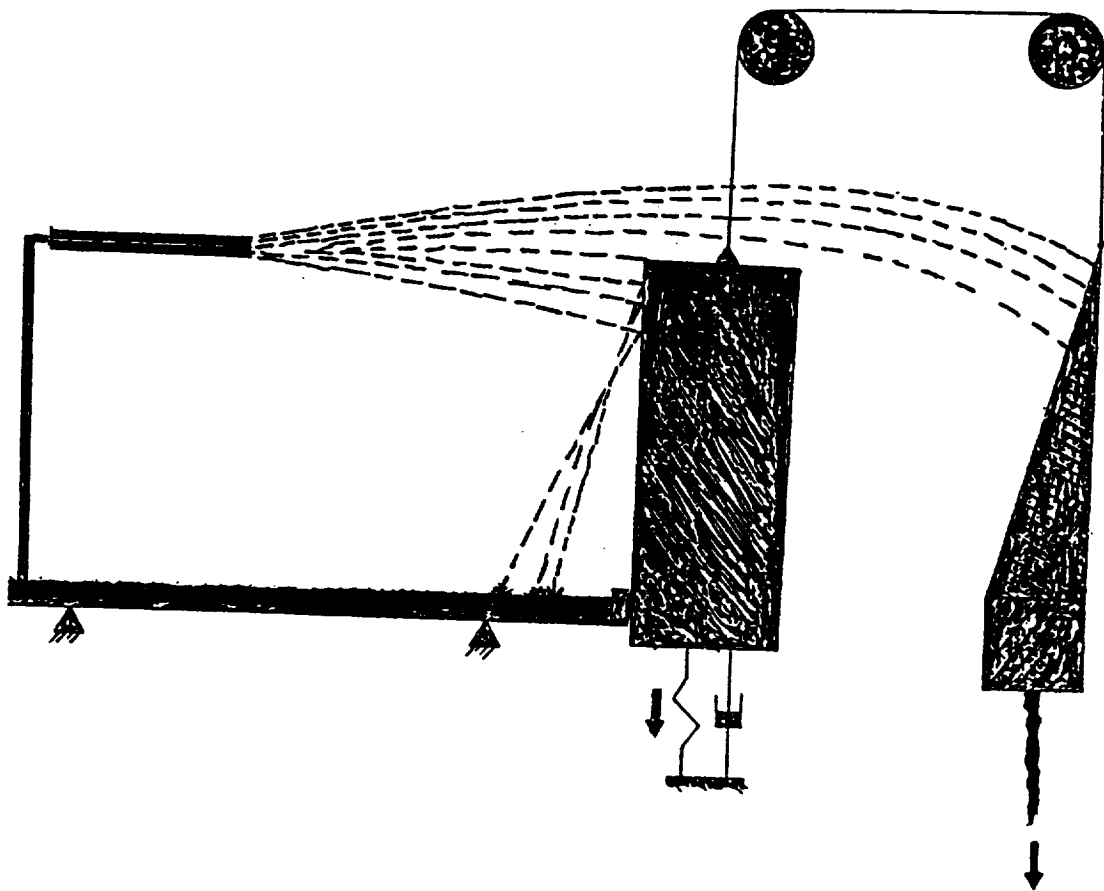


**Figure 3.3: Marginal Stability Analog**

This shows streams of water projected at a barrier supported by a bucket and pulley system. Some of the water gets over the top of the barrier into the bucket but flows out through a hole in the bottom. The system can be designed to be initially in equilibrium. If a high velocity stream is turned off, the barrier will drop down a bit to maintain equilibrium.

sound speed. The region in between would contain a hot *kernel* of expanding plasma. Brown et al. (1979) stated that these barriers would be relatively thin (on the order of 0.13 km). Other authors (Smith and Brown, 1980) have revised this estimate upward somewhat; nevertheless, all agree that the thickness of the barriers is relatively small compared to the overall length of the loop and therefore not resolvable.

Electron and ion densities would remain roughly constant over the loop to within 10-20 % (Smith and Lilliquist, 1979). This may be visualized simplistically as a weather front in our own atmosphere. There is relatively little change in the total density through the front, yet, as it moves, the temperature at a particular location may change significantly. The predominant loss of energy would be in the form of an *anomalous* heat flux carried by the escaping tail electrons,  $Q = n_e m_e v_e^2 c_s$ .

## B. EMISSION CHARACTERISTICS

The aim of this chapter is to describe the Model T hard x-ray emission. Once the emission in time and energy is known, one can then turn to the telescope simulations to determine at which times and at which energies this hard x-ray model would provide a discernable and characteristic signature to the observer.

While it is not necessary to rework here the details of the internal processes which form and maintain the barrier, it is necessary to note that it is permeable first to the highest energy *available* electrons. This happens because only the highest energy particles have sufficient energy (i.e., long enough mean-free-paths) to diffuse all the way through the barrier region (Brown et al., 1979). Another important implication is that a collisionless flux stream which is not energetic enough to escape early in time will have another chance later simply because it

would then represent the highest *available* energy. In the meantime, however, it is reflected by the barrier.

Within the kernel, hard x-rays are produced by thermal bremsstrahlung. In the footpoints and to some extent in the legs of the loop, a thick target, non-thermal description is more appropriate since we have a distribution of electrons with energies  $E \gg kT$  impacting the relatively cool, lower corona and chromosphere. While there are many initial conditions that could be chosen to quantify the treatment, the ones used here form a typical case.

The *Model T* basic description is restated as follows. The initial electron distribution is a Maxwellian at  $2 \times 10^8$  K. The initial kernel length is  $10^8$  cm bounded by relatively thin regions of confining ion-acoustic turbulence. The centroid of the initial kernel is taken to occur at the apex of the loop. An unknown mechanism heats the electrons initially and is assumed to have little effect on the more massive ions (i.e.,  $T_e \gg T_i$ ). Electron and ion number densities are taken as constant at  $10^{11} \text{ cm}^{-3}$  throughout the impulsive phase (Smith and Lilliequest, 1979). The loop geometry is a semi-torus with a  $\cong 1$  arc second cross section and an overall loop diameter of  $\cong 20$  arc second. The speed of the turbulent acoustic wavefronts is taken to be the local ion-acoustic speed (Brown et al., 1979).

Given these assumptions, we are now in a position to determine  $T_e$ , the temperature of electrons inside the kernel, and  $L$ , the length of the kernel as functions of time. Assuming energy losses from the kernel to be relatively small, conservation of energy may be used to write

$$LT_e \cong L_o T_o. \quad (3.1)$$

The source length  $L$  increases at the local sound speed,  $c_s$ ,

$$c_s = \left( \frac{kT_e}{m_i} \right)^{\frac{1}{2}} \quad (3.2)$$

on each side; thus

$$\frac{dL}{dt} = 2\sqrt{\frac{kT_e}{m_i}}, \quad (3.3)$$

which by (3.1) may be written as

$$\frac{dL}{dt} = 2\sqrt{\frac{kL_oT_o}{m_iL}}. \quad (3.4)$$

Integrating, we obtain

$$L(t) = L_o \left[ 1 + \frac{3}{L_o} \sqrt{\frac{kT_o}{m_i}} t \right]^{\frac{2}{3}}. \quad (3.5)$$

Using equation (3.1) again, the electron temperature as a function of time may now be written as

$$T_e(t) = T_o \left[ 1 + \frac{3}{L_o} \sqrt{\frac{kT_o}{m_i}} t \right]^{-\frac{2}{3}}. \quad (3.6)$$

Numerically, for  $L_o = 10^8$  cm and  $T_o = 2 \times 10^8$  K, the time for the barrier to reach the footpoints (i.e., the length of the impulsive phase) is 28.5 seconds which is consistent with typical observations for the duration of the impulsive phase (Tandberg-Hanssen and Emslie, 1988). The final temperature is  $8.6 \times 10^6$  K is sufficiently large compared to the preflare temperature (on the order of  $10^6$  K) that equation (3.1) is a valid approximation (Figure 3.4).

The aforementioned discussion is concerned with the bulk behavior of the distribution; however, the high-energy tail of the electron distribution must also be taken into account as it will be responsible for any emission in the footpoints of the loop. From Spitzer (1962), the collision time,  $t_c$ , may be written as

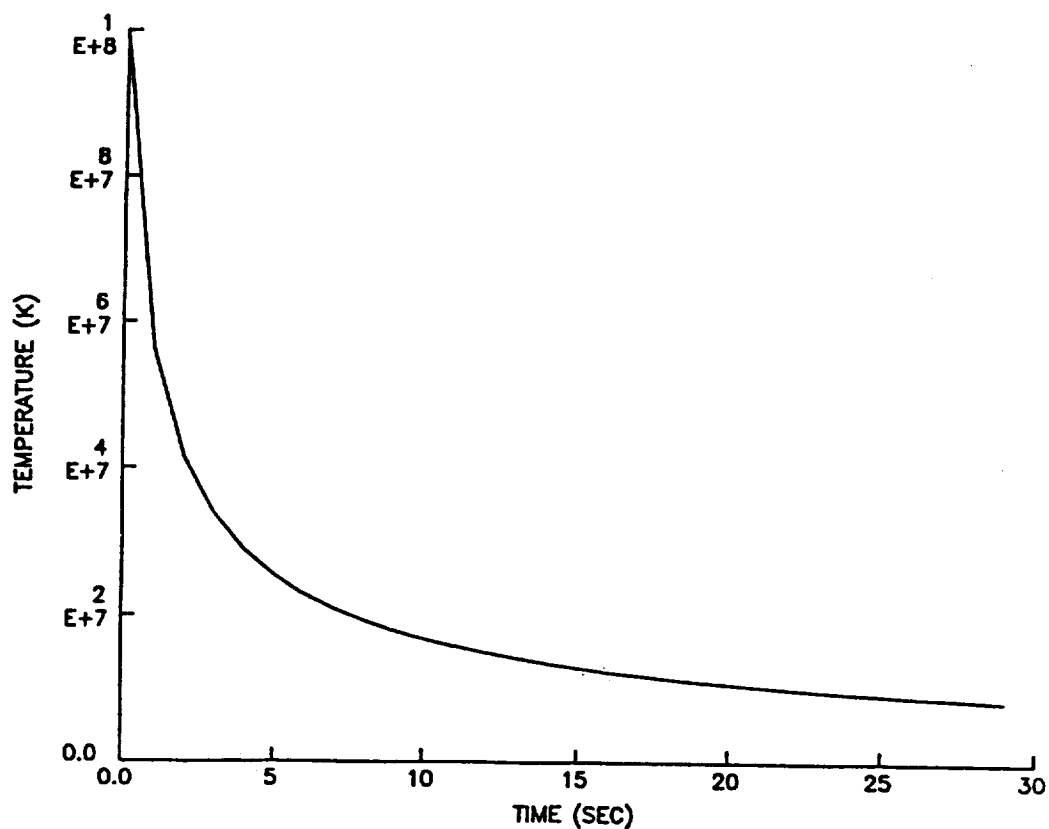


**Figure 3.4: Model T Kernel Temperature As A Function Of Time**

This shows the evolution of the bulk temperature of the expanding kernel as a function of time. It cools very rapidly early in the event and then slows exponentially for the later portion of the event. One would expect from this behavior that the high-energy emission will come early in time.

$$t_c = \frac{.266T^{\frac{3}{2}}}{n \ln \Lambda}, \quad (3.7)$$

where  $\ln \Lambda$  is the Coulomb logarithm, which for solar conditions may be taken as a constant ( $\ln \Lambda = 20$ ; Spitzer, 1962). Since the self collision time,  $t_c$ , for the electrons is short ( $\approx 10^{-1}$  s) relative to the characteristic expansion and cooling time of the kernel ( $\approx 30$  s), one expects the kernel for the bulk of the electron distribution to be Maxwellian (Figure 3.5). However, early in the impulsive phase one would expect the *tail* of the distribution to be non-Maxwellian (Kahler, 1971a, b). Since the initial Maxwellian tail is essentially collisionless over the length of the kernel at that time, one would expect it to persist for some finite time while the bulk of the distribution follows a relaxing Maxwellian throughout the event.

In this regard, MacDonald et al. (1957) discuss the behavior of a system of particles relaxing through Coulomb forces from an extreme initial distribution to a final Maxwellian. By treating the problem with dimensionless parameters (e.g., dimensionless velocity  $\xi$ ), the results are applicable to a distribution at any temperature. As a specific example, they chose an initial distribution in the form of a displaced Gaussian and provided a few curves at different times, including in particular the one for the distribution after a relaxation time of  $5.9t_c$ . At this time, the relaxing distribution approximated a Maxwellian except in the tail. The temperature used to calculate the collision time was that associated with the fully relaxed distribution.

This specific example may be generalized to be applicable to our situation by defining the dimensionless differences

$$D_{old} = \frac{h_i - h}{h_i - h_M} \quad (3.8)$$

and

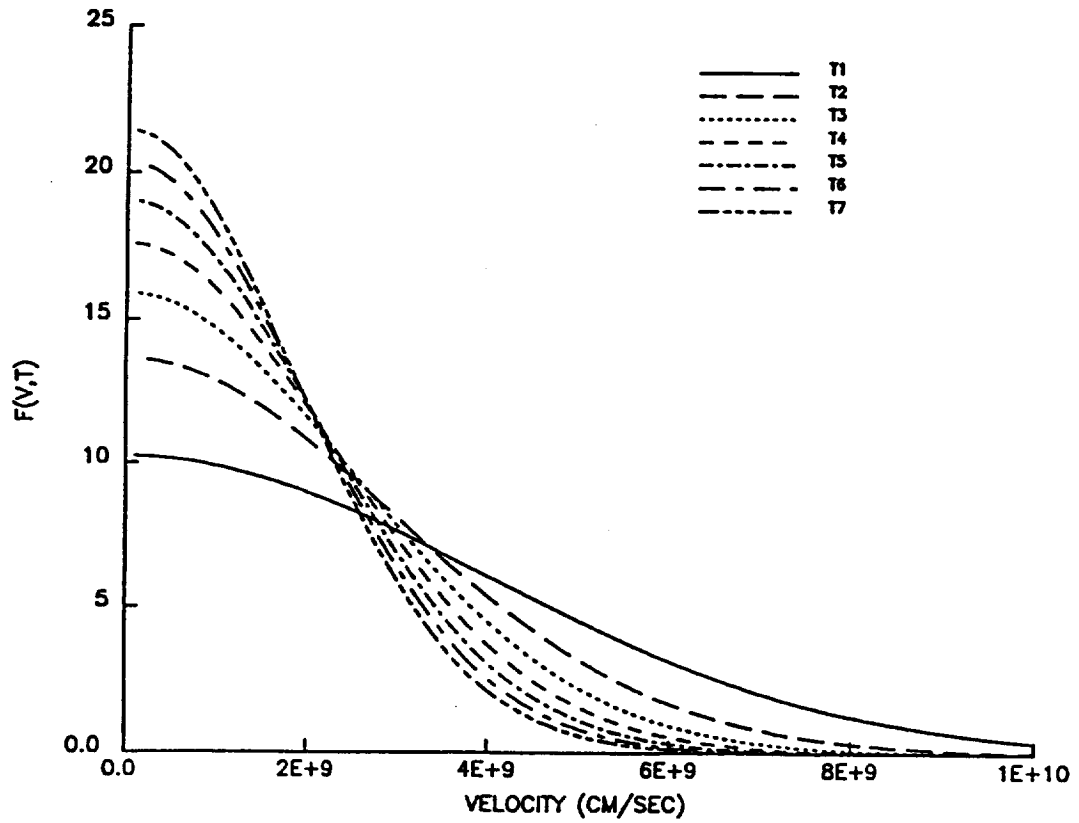


**Figure 3.5: Maxwellian Cooling Over Time**

The kernel cools slowly enough that the bulk of the distribution will follow the evolution of a cooling Maxwellian distribution. However, the tail of the distribution will not necessarily be Maxwellian.



$$D_{new} = \frac{h - h_M}{h_i - h_M} \quad (3.9)$$

representing the difference between the initial, final, and Maxwellian distributions as a function of velocity ( $D_{old} + D_{new} = 1$ ). Here  $h$  is the distribution after a relaxation time of  $5.9 t_c$ ,  $h_M$  is the fully relaxed Maxwellian, and  $h_i$  is the initial distribution (Figure 3.6).

Except in the region where  $h_i \approx h_M$  at  $\xi = 0.25$  (Figure 3.6),  $D_{old}$  and  $D_{new}$  are expected to apply to a more general class of problem such as ours. If we plot  $D_{old}$  and  $D_{new}$  (Figure 3.7) against the dimensionless velocity, we find that  $D_{new} \cong 0$  over the bulk of the distribution and then begins to rapidly grow as one approaches the tail of the distribution. Unfortunately, not enough data are provided to determine a similar departure from the initial distribution. Now, a velocity may be selected ( $D_{new} = 0.01$ ) as the cutoff at which the relaxing distribution is defined to be no longer Maxwellian. This point on the MacDonald et al. (1957) curves corresponds to

$$\xi_1 = 0.31 \quad (3.10)$$

at time

$$t = 5.9 t_c \quad (3.11),$$

where

$$\xi = 0.335 v \left( \frac{m}{3kT_e} \right)^{\frac{1}{2}} \quad (3.12)$$

is the dimensionless velocity used by MacDonald et al. (1957),  $T_e$  is the temperature associated with the new distribution,  $k$  is the Boltzmann constant, and  $m$  is the electron mass. Equation (3.12) can be inverted to provide the velocity in cm

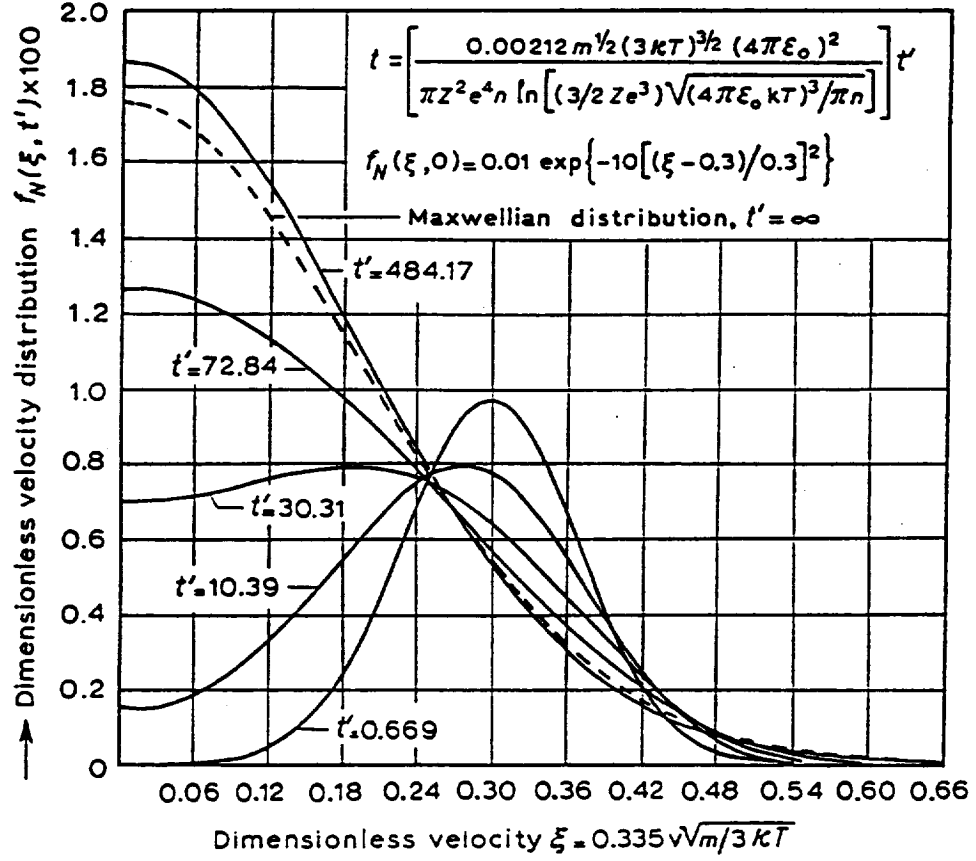


**Figure 3.6: Relaxation To Maxwellian Distribution**

This shows the initial, dimensionless Gaussian distribution and four later times as it relaxes toward a final Maxwellian. Note that for the dimensionless time 484.17 (i.e.,  $5.9 t_c$ ), the curve closely approximates that of a Maxwellian for lower values of  $\xi$  (MacDonald et al., 1957).

$s^{-1}$  which defines the edge of the Maxwellian bulk distribution in phase space,  $v_1$ . We also have sufficient information at this point to derive an expression for the temperature of the bulk distribution corresponding to  $5.9 t_c$  and hence  $v_e$  at that time.

From equation (3.6),

$$t(T) = \frac{1}{3} \sqrt{\frac{m_i}{L_o k T_o}} \left[ \left( \frac{L_o T_o}{T_e} \right)^{\frac{3}{2}} - L_o^{\frac{3}{2}} \right]. \quad (3.13)$$

Setting  $t = 5.9 t_c$ , the time used by McDonald et al. (1957), we find, using equation (3.7) and the substitution

$$x = T_e^{\frac{3}{2}} \quad (3.14)$$

that equation (3.13) may be written in the form of a quadratic equation

$$ax^2 + bx + c = 0 \quad (3.15)$$

where

$$a = 5.9 \times \frac{0.266}{n \ln \Lambda} \quad (3.16)$$

$$b = \frac{1}{3} \sqrt{\frac{m_i}{L_o k T_o}} L_o^{\frac{3}{2}}, \quad (3.17)$$

and

$$c = -\frac{1}{3} \sqrt{\frac{m_i}{L_o k T_o}} (L_o T_o)^{\frac{3}{2}}. \quad (3.18)$$

Hence, equation (3.15) can be solved to yield  $T_e$  at the time corresponding to the MacDonald et al. (1957) results on which Figure 3.6 is based. This also will allow a determination of the rms velocity,

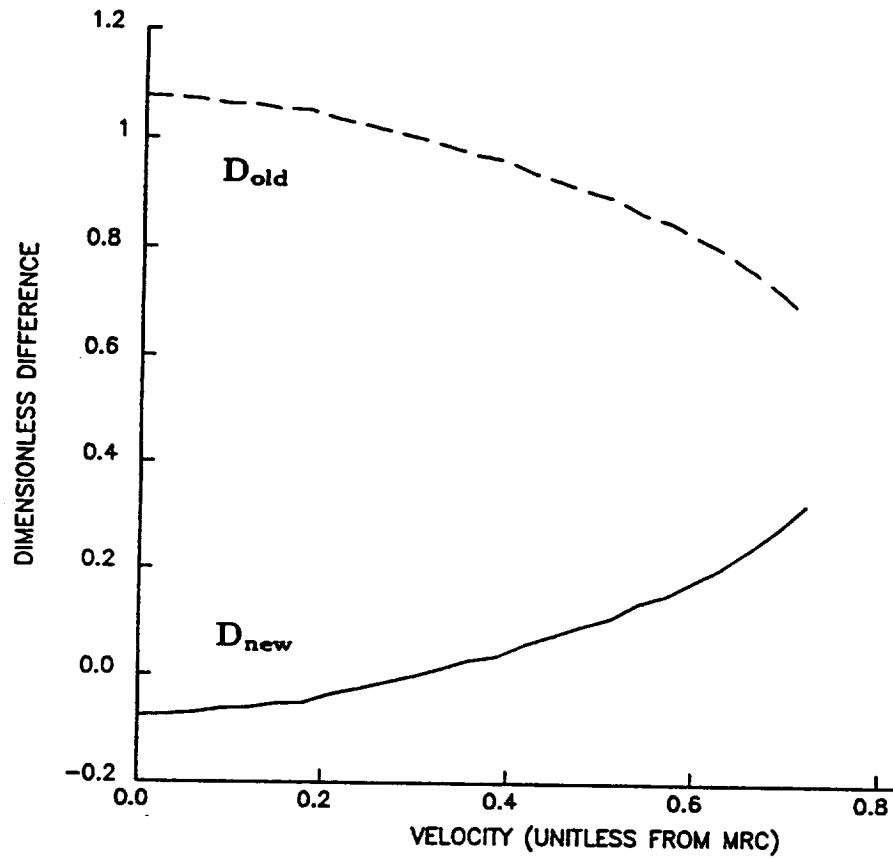


**Figure 3.7: Dimensionless Differences**

This shows a comparison of the dimensionless differences,  $D_{new}$  and  $D_{old}$  obtained from the curves provided by McDonald et al. (1957). The point at which  $D_{new}$  exceeds 0.01 was chosen as the cutoff for the bulk Maxwellian. This corresponds to a dimensionless velocity of  $\xi = 0.31$  at  $5.9 t_c$ . Clearly, above this cutoff,  $D_{new}$  begins to diverge from a Maxwellian rapidly.

$$v_e = \left( \frac{kT_e}{m_e} \right)^{\frac{1}{2}}. \quad (3.19)$$

The dependence of collision frequency on velocity may be used to describe fully the electron distribution as a function of time throughout the event. We define  $v_{crit}$  as the velocity at which the number of collisions occurring during a particular elapsed time corresponds to 1 ( $N(v, t) = 1$ ). Spitzer (1962) describes *one collision* as the summed effect of many grazing encounters by a particular particle until a  $90^\circ$  change in direction has been accomplished. Clearly, at velocities less than  $v_1$ , defined by equations (3.10) and (3.12), enough of these collisions have occurred for the bulk distribution to be Maxwellian. We therefore expect this velocity to satisfy the relationship  $v_1 < v_{crit}$ . Similarly, at a higher velocity,  $v_2 > v_{crit}$ , the distribution must resemble the initial distribution as beyond that point collisions are not occurring quickly enough to change the character of the distribution in this region of phase space.

Now, the number of collisions at a given velocity,  $N$ , is given by

$$N(v, t) = \nu t \quad (3.20)$$

where  $t$  is the time and  $\nu(v)$  is the collision frequency associated with a given velocity. The collision frequency varies with velocity as

$$\nu = \frac{v_e^3 \nu_e}{v^3} \quad (3.21)$$

where  $\nu_e = t_c^{-1}$  is the collision frequency associated with the rms velocity,  $v_e$ .

Substituting for  $\nu$  in equation (3.20) we find

$$N = \frac{tv_e^3}{t_c v^3}. \quad (3.22)$$

Substituting the value of  $v_1 = \left(\frac{0.31\sqrt{3}}{0.335}\right)v_e$  [from equations (3.10) and (3.12)] for  $v$ , and the value of  $t = 5.9t_c$  from equation (3.11) provides the number of collisions required to define the boundary ( $D_{new} = 0.01$ ) in phase space of the Maxwellian bulk distribution. This is

$$N_1 = 5.9 \left[ \frac{0.335}{0.31\sqrt{3}} \right]^3 \cong 1.4, \quad (3.23)$$

and indicates that only a relatively small number of Spitzer collisions are needed to thermalize an initially non-Maxwellian bulk distribution. Since  $v_1 \cong t^{\frac{1}{3}}$  (equation 3.22), and  $v_1 = \left(\frac{0.31\sqrt{3}}{0.335}\right)v_e$  at  $t = 5.9t_c$ , we obtain an expression for  $v_1$  as a function of time;

$$v_1 \cong 0.9 \left( \frac{t}{t_c} \right)^{\frac{1}{3}} v_e. \quad (3.24)$$

Substituting we find that

$$v_1 \cong (7 \times 10^9) t^{\frac{1}{3}}. \quad (3.25)$$

This finding agrees with MacDonald et al. (1957) who found that the rate of expansion of the edge of the Maxwellian bulk distribution in phase space is independent of temperature.

Now, for  $N = 1, v = v_{crit}$ , and we have

$$\frac{t}{t_c} = \left( \frac{v_{crit}}{v_e} \right)^3. \quad (3.26)$$

At  $t = 5.9 t_c$ , we therefore find that

$$v_{crit} = (5.9)^{\frac{1}{3}} v_e \cong 1.8 v_e \quad (3.27)$$

and from equation (3.24) at the same time,

$$v_1 \cong 0.9(5.9)^{\frac{1}{3}} v_e \cong 1.6 v_e \quad (3.28)$$

Now, in the absence of information from MacDonald et al. (1957) for the high energy part of the distribution, the number of collisions,  $N_2$ , beyond which the distribution remains that of the initial condition is not well known. However, we observe that  $v_1 < v_{crit} < v_2$  and that by assuming symmetry in the difference curves shown in Figure 3.7, we derive

$$2v_{crit} = v_1 + v_2 \quad (3.29)$$

and

$$N_2 = [(2N_{crit})^{\frac{1}{3}} - N_1]^3 \cong 0.7. \quad (3.30)$$

Also, the corresponding velocity at  $5.9 t_c$  will be

$$v_2 \cong 1.1(5.9)^{\frac{1}{3}} v_e \cong 2.0 v_e. \quad (3.31)$$

Thus, for velocities,  $v < v_1$ , the distribution is a relaxed Maxwellian at the new  $T$  and for  $v > v_2$  the distribution is represented by the initial condition. The middle region is relatively small in extent and may be interpolated by a cubic spline which matches endpoints and first and second derivatives.

Previous authors have assumed all escaping electrons to disappear from the kernel instantaneously. Clearly, however, since  $L \cong 10^8$  cm, these collisionless electrons will not all arrive at the front instantaneously but rather will replenish the front electrons continuously during some finite time interval. We will now treat this replenishment more correctly in order to better understand its role in the event. We start with the anomalous heat flux equation from Brown et al. (1979) to calculate the lower cutoff velocity of the escaping electrons,  $v_{lco}$ , at a

given time. Knowing the velocity as a function of time is the key to describing the escaping flux traveling to the footpoints. We write the heat flux as

$$Q = \int_{v_{lco}}^{v_{max}} F(v, t) v^3 dv \quad (3.32)$$

where  $F(v, t)$  is the electron distribution.

Now, for marginal stability,

$$Q_{ms} = \frac{3}{2} n m_e v_e^2 c_s \quad (3.33)$$

Hence,

$$\frac{3}{2} n m_e v_e^2 c_s = \int_{v_{lco}}^{v_{max}} v^3 F(v, t) dv \quad (3.34)$$

where both  $v_{max}$  and  $v_{lco}$  are functions of time.

For the initial condition, we have  $v_{max}(t) = v_{maxo} = \infty$ . Solving for the first  $v_{lco}$  we find that

$$\int_{v_{lco}}^{v_{max}=\infty} v^3 f dv = \frac{3}{2} v_e^2 c_s m_e = \frac{3}{2} \frac{(kT)^{\frac{3}{2}}}{m_i^{\frac{1}{2}}} \quad (3.35)$$

where

$$f(v, 0) = \left( \frac{m_e}{2\pi kT} \right)^{\frac{1}{2}} \exp\left(-\frac{v^2}{2v_e^2}\right). \quad (3.36)$$

Evaluating the integral I, we obtain,

$$I = \frac{1}{2} \left( \frac{m_e}{2\pi kT} \right)^{\frac{1}{2}} \exp\left(-\frac{m_e}{2kT} v_{lco}^2\right) \left[ \left( \frac{2kT}{m_e} \right)^2 + \left( \frac{2kT}{m_e} \right) v_{lco}^2 \right]. \quad (3.37)$$

Setting this result equal to  $\frac{3}{2} \frac{(kT)^{\frac{3}{2}}}{m_i^{\frac{1}{2}}}$  leads to the equation



$$c_2 + v_{lco}^2 = 3c_1 \exp\left(\frac{v_{lco}^2}{c_2}\right) \quad (3.38)$$

where  $c_1$  and  $c_2$  are constants;

$$c_1 = \left(\frac{9\pi m_e}{2m_i}\right)^{\frac{1}{2}} kT, \quad (3.39)$$

and

$$c_2 = \frac{2kT}{m_e}. \quad (3.40)$$

Solving, we find that

$$v_{lco} \cong 2.6v_e, \quad (3.41)$$

in agreement with Brown et al. (1979).

While this works for the Maxwellian initial condition, we would not expect it to be valid for our distribution at later times since  $v_{max}$  will become finite as the highest energy electrons escape. For later times consider the following: the collisionless flux may be modeled as a series of differential flux streams  $i$ , with velocities between  $v_i$  and  $v_i + dv$ . These streams are continuously striking the front and either (a) passing through to maintain the marginally stable turbulence (if  $v > v_{lco}$ ) or (b) being reflected if  $v < v_{lco}$ . As soon as the highest velocity stream departs, a new, slower stream must begin its departure for the system to continue to satisfy the marginal stability condition. The velocity of this new stream will correspond to a new  $v_{lco}$ . In the limit, this becomes a continuous process with  $v_{lco}$  decreasing at a slower rate than  $v_{max}$  as the density increases at lower velocities.

Finding  $v_{lco}$  and  $v_{max}$  as functions of time is a tedious numerical exercise. However, it turns out that analytical solutions may be obtained for the set of

discrete times at which a given  $v_{lco}$  subsequently becomes the relevant  $v_{max}$ . This idea will be discussed in greater detail in the following paragraphs.

The time,

$$t_o = \frac{L(t)}{v_{lco}}, \quad (3.42)$$

at which a  $v_{lco}$  flux stream becomes a  $v_{max}$  stream is just equal to the time it takes the last electron in the  $v_{lco}$  flux stream to travel from the other end of the kernel to the moving front and escape. In other words, the  $v_{lco}$  stream becomes, momentarily, just before the last electrons pass through the front a  $v_{max}$  itself. Using this key idea we can calculate a progression of  $v_{lco}$ 's as a function of time in the following manner. Knowing  $v_{max}$  initial, we first calculate the kernel length,  $L(t)$ , at which time the last electron in the escaping flux stream reaches the front. This gives us a time,  $\frac{L}{v_{max}}$ , at which the next  $v_{lco}$  begins its departure from the kernel. Calculating the time of transit of the last electron in this flux stream provides the time at which this  $v_{lco}$  becomes a  $v_{max}$  itself. Thus, using this step by step approach we may calculate a sequence of  $v_{lco}$  's exactly.

To calculate the length of the kernel when  $v_{lco}(t = t_{n-1})$  becomes  $v_{max}$  we write

$$L_n = \left( 3\sqrt{\frac{kL_oT_o}{m_i}}t_n + L_o^{\frac{3}{2}} \right)^{\frac{2}{3}} \quad (3.43)$$

where  $t_n$  is the specific time at which the last electron in the flux stream departs and the time when the particle reaches the moving front is

$$t_n = t_{n-1} + \frac{L_n}{v_{lco}}. \quad (3.44)$$

Substituting, we obtain

$$L_n = \left[ 3\sqrt{\frac{kL_oT_o}{m_i}} \left( t_{n-1} + \frac{L_n}{v_{lco}} \right) + L_o^{\frac{3}{2}} \right]^{\frac{2}{3}} \quad (3.45)$$

and

$$L_n^{\frac{3}{2}} = 3\sqrt{\frac{kL_oT_o}{m_i}} t_{n-1} + 3\sqrt{\frac{kL_oT_o}{m_i}} \frac{L_n}{v_{lco}} + L_o^{\frac{3}{2}}. \quad (3.46)$$

This takes the form ( $x = L^{\frac{1}{2}}$ ),

$$x^3 + ax^2 + b = 0 \quad (3.47)$$

where

$$a = -3\sqrt{\frac{kL_oT_o}{m_i}} \frac{1}{v_{lco}} \quad (3.48)$$

and

$$b = -3\sqrt{\frac{kL_oT_o}{m_i}} t_{n-1} - L_o^{\frac{3}{2}}. \quad (3.49)$$

Taking the only real root, we find that

$$L_n^{\frac{1}{2}} = -\frac{a}{3} + \frac{a^2}{9} \left( -\frac{a^3}{27} - \frac{b}{2} + \sqrt{\frac{a^3b}{27} + \frac{b^2}{4}} \right)^{-\frac{1}{3}} \\ + \left( \frac{-a^3}{27} - \frac{b}{2} + \sqrt{\frac{a^3b}{27} + \frac{b^2}{4}} \right)^{\frac{1}{3}}. \quad (3.50)$$

Now, this value can be used in equation (3.44) to calculate the time at which the electron reaches the barrier.

Using the marginal flux condition, the new  $v_{lco}$  can be calculated from

$$I = a_2 \int_{v_{lco}}^{v_{max}} v^3 \exp(-b_2 v^2) dv \quad (3.51)$$

$$= a_2 \left( \frac{\left( -\frac{1}{2b_2^2} \right) - \left( \frac{v^2}{2b_2} \right)}{e^{b_2 v^2}} \right) \Big|_{v_{lco}}^{v_{max}} \quad (3.52)$$

$$= \left( \frac{-\frac{a_2}{2b_2^2} - \frac{a_2 v_{max}^2}{2b_2}}{e^{b_2 v_{max}^2}} \right) + \left( \frac{\frac{a_2}{2b_2^2} + \frac{a_2 v_{lco}^2}{2b_2}}{e^{b_2 v_{lco}^2}} \right) \quad (3.53)$$

where  $a_2 = \left( \frac{m_e}{2\pi kT} \right)^{\frac{1}{2}}$  and  $b_2 = \frac{1}{2v_e}$ .

Also, we know that

$$I = \frac{3}{2} m_e v_e^2 c_s \quad (3.54)$$

giving

$$\frac{3}{2} m_e v_e^2 c_s + \left( \frac{\frac{a_2}{2b_2^2} + \frac{a_2 v_{max}^2}{2b_2}}{e^{b_2 v_{max}^2}} \right) = \left( \frac{\frac{a_2}{2b_2^2} + \frac{a_2 v_{lco}^2}{2b_2}}{e^{b_2 v_{lco}^2}} \right) \quad (3.55)$$

This can be solved to give a new  $v_{lco}$ . As stated before, by setting each  $v_{lco}$  as a  $v_{max}$  for the next step, the problem may be solved exactly at these times for any number of iterations. Appendix B includes the code which accomplishes these calculations.

The initial condition flux rapidly departs. In other words,  $v_{lco}$  decreases rapidly while  $v_1$ , the edge of thermal bulk distribution in phase space, is increasing rapidly (Figure 3.8). At time  $\cong 1.4$  seconds the two curves intersect (Figure 3.9) implying that by this time the high-energy, initial condition electrons have escaped to the tail and that the kernel is completely thermalized.

Thus, the MacDonald et al. (1957) analysis, while informative, is only needed to deal with the first second or so of the event. The front is maintained thereafter by new high-energy electrons created by the *pumping* action of the collisional distribution. Hence  $v_{lco} \cong 2.6 v_e(t)$  may be used to describe the period of time  $t > 1.4$  seconds.

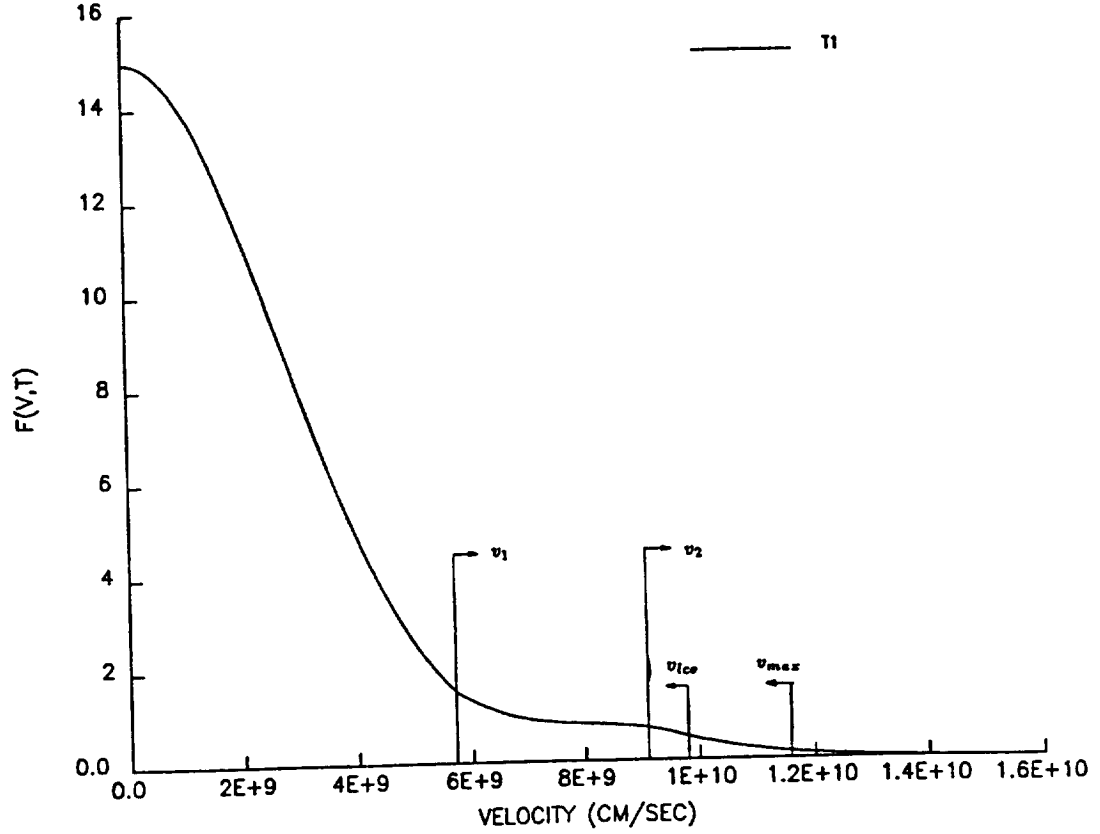


**Figure 3.8: Hybrid Distribution**

This shows an example of the a distribution constructed from a Maxwellian kernel, a Maxwellian tail from a hotter distribution, and a spline linking function. It represents the distribution in the Model T kernel early in the event. Region I bounded at the higher velocities by  $v_1$  is a cooling Maxwellian, region III is the collisionless tail remaining from the initial distribution, and region II, bounded at the higher end by  $v_2$ , is a mixture of both. All flux streams above  $v_{lco}$  are escaping and all flux streams above  $v_{max}$  have already departed.

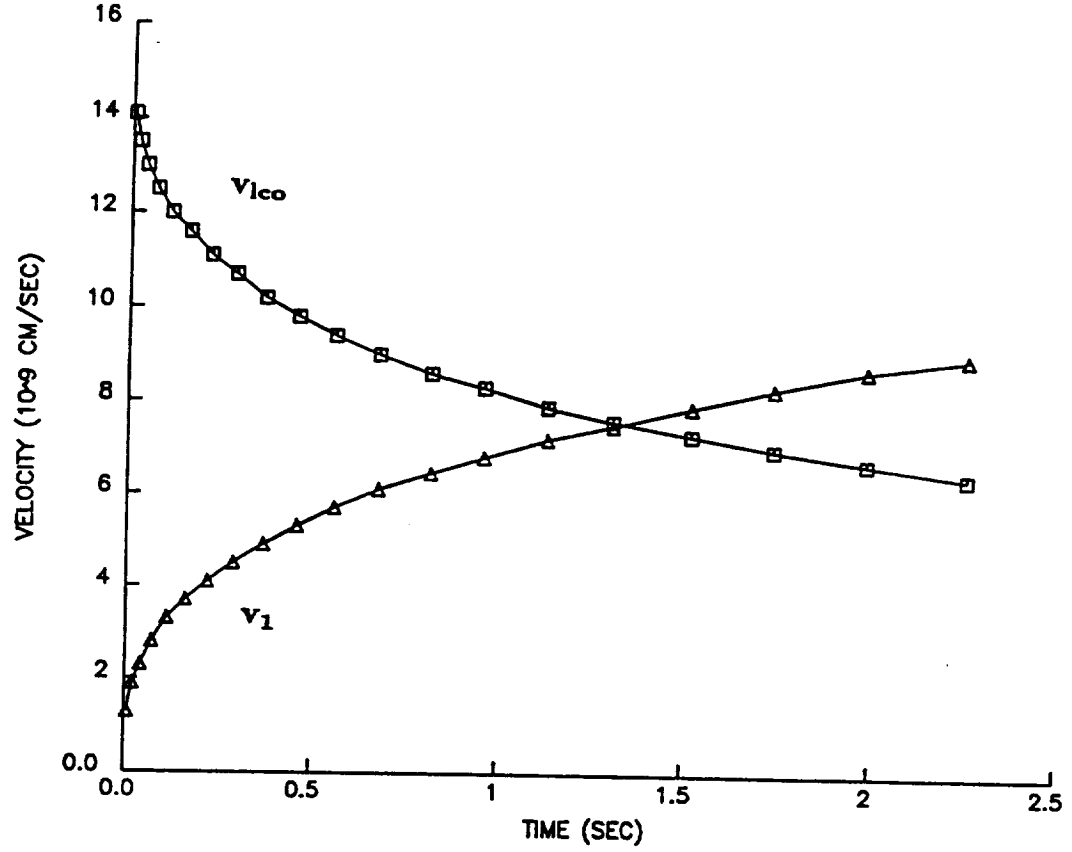


**Figure 3.9: Model T Velocity Comparison**

This shows the evolution of  $v_{lco}$ , the lower boundary of the flux escaping through the ion-acoustic fronts, and  $v_1$ , the upper boundary of the Maxwellian bulk distribution as a function of time. Clearly, the overlap occurring between 1 and 2 seconds into the event suggests that at this point the kernel electron distribution has become entirely Maxwellian.

We now have reached the point in the development such that the electron distribution is known as a function of time for the entire event. Now using this distribution, both the thermal and nonthermal hard x-ray emission may be calculated for Model T. We use the Kramer cross section as a good approximation to the more rigorous Bethe-Heitler cross section (Li and Emslie, 1990; Emslie and Machado, 1987),

$$\sigma_K(\epsilon, E) = \frac{\kappa}{\epsilon E} \quad (3.56)$$

where

$$\kappa = 7.9 \times 10^{-25} \bar{Z}^2 \quad (3.57)$$

and

$$\bar{Z}^2 = 1.4, \quad (3.58)$$

the mean square atomic number for solar abundances (Allen, 1973; Emslie et al., 1986a; and Tandberg-Hanssen and Emslie, 1988).

Now, from Tandberg-Hanssen and Emslie (1988), the Maxwellian may be written as (electrons  $\text{cm}^{-3}$   $\text{erg}^{-1}$ )

$$f(E) = \frac{2n_e}{\pi^{\frac{1}{2}}(kT)^{\frac{3}{2}}} E^{\frac{1}{2}} e^{-\frac{E}{kT}} \quad (3.59)$$

and the thermal emission at the Earth in photons  $\text{cm}^{-2} \text{keV}^{-1} \text{s}^{-1}$  may be found from

$$I_{th}(\epsilon) = \frac{2n_e}{4\pi R^2} \int_{\epsilon}^{\infty} f_E(E) v(E) \sigma_K(\epsilon, E) dE, \quad (3.60)$$

where R is the mean distance from the Earth to the Sun.

This integral may be used to calculate the thermal bremsstrahlung from the bulk Maxwellian and the cubic spline regimes by integration from  $\epsilon$  to  $\epsilon_1 = \frac{1}{2}mv_1^2$  using a Maxwellian  $f(E)$  summed with an integration from  $v_1$  to  $v_2$  using a cubic spline  $f(E)$ . In a similar fashion, after 1 second, the thermal emission from the kernel may be found using a Maxwellian truncated at  $2.6 v_e$ .

To illustrate this further, the intensity at the Earth due to a truncated Maxwellian for  $\epsilon < \alpha$  is (photons  $\text{cm}^{-2} \text{keV}^{-1} \text{s}^{-1}$ ),

$$I_{th}(\epsilon) = (9.55 \times 10^{-13}) \frac{n^2 l A}{\epsilon T^{1/2} R^2} \left[ e^{-\frac{\epsilon}{kT}} - e^{-\frac{\alpha}{kT}} \right] \quad (3.61)$$

where  $\alpha = 3.38 m_e v_e^2$ ,  $l$  is the pixel length,  $R$  is the mean distance from the Earth to the Sun, and  $A$  is the flare cross sectional area. For  $\epsilon > \alpha$ , we have

$$I_{th} = 0. \quad (3.62)$$

For the nonthermal emission, we follow the approach used in Chapter II with the difference that the injection point ( $N = 0$ ) will now correspond to the time-varying edge of the kernel. For a Maxwellian tail (Brown and Emslie, 1988), we have

$$F(E_o) = \frac{2^{\frac{3}{2}}}{(\pi m_e)^{\frac{1}{2}}} \frac{n_e E_o}{(kT)^{\frac{3}{2}}} e^{-\frac{E_o}{kT}} \quad (3.63)$$

in electrons  $\text{cm}^{-2} \text{s}^{-1} \text{erg}^{-1}$ .

Using equation (3.63), the cumulative intensity may now be found numerically from (Appendix B)

$$J(\epsilon, N) = \frac{\kappa}{\epsilon} \int_{N'=0}^N \int_b^{\infty} \frac{F(E_o)}{(E_o^2 - 2KN)^{1/2}} dE_o dN' \quad (3.64)$$

where  $b = \max[E_c, (\epsilon^2 + 2KN)^{\frac{1}{2}}]$  and  $E_c = 3.38 m_e v_e^2$ .



The nonthermal emission in photons  $\text{cm}^{-2} \text{s}^{-1} \text{keV}^{-1}$  for the  $i$ 'th pixel may be found from

$$I_i(\epsilon) = J(\epsilon, N_i) - J(\epsilon, N_{i-1}). \quad (3.65)$$

Figures 3.10-3.13 show the results of this analysis for photon energies equal to 10, 40, 70, and 100 keV, respectively. At 10 keV (Figure 3.10), the apex is extremely bright with weaker emission from the footpoints. The effect of the growing, cooling kernel can be seen in the emission as well. Some nonthermal emission is found between the kernel and the footpoints but is dominated by the kernel and footpoint emission.

As one goes higher in energy, the emission from the apex decreases much faster than that in the footpoints until at 40 keV (Figure 3.11) the apex and footpoints are emitting roughly the same flux at  $t = 0$ . At 70 keV (Figure 3.12) and 100 keV (Figure 3.13), the apex is still visible but the emission from all sources is greatly reduced from that at lower energies. Indeed, at higher energies the Model T mimics the emission profiles of the Model N-T discussed in Chapter II.

### C. SUMMARY

This chapter developed the Model T quantitatively to provide emission profiles as functions of time, energy, and loop position. By examining the results of this model and comparing them with the Model N-T from Chapter II we immediately ascertained that differences in the emission profiles of the two models were indeed present at lower energies. At higher energies, the Model T profiles began to mimic those of the Model N-T.

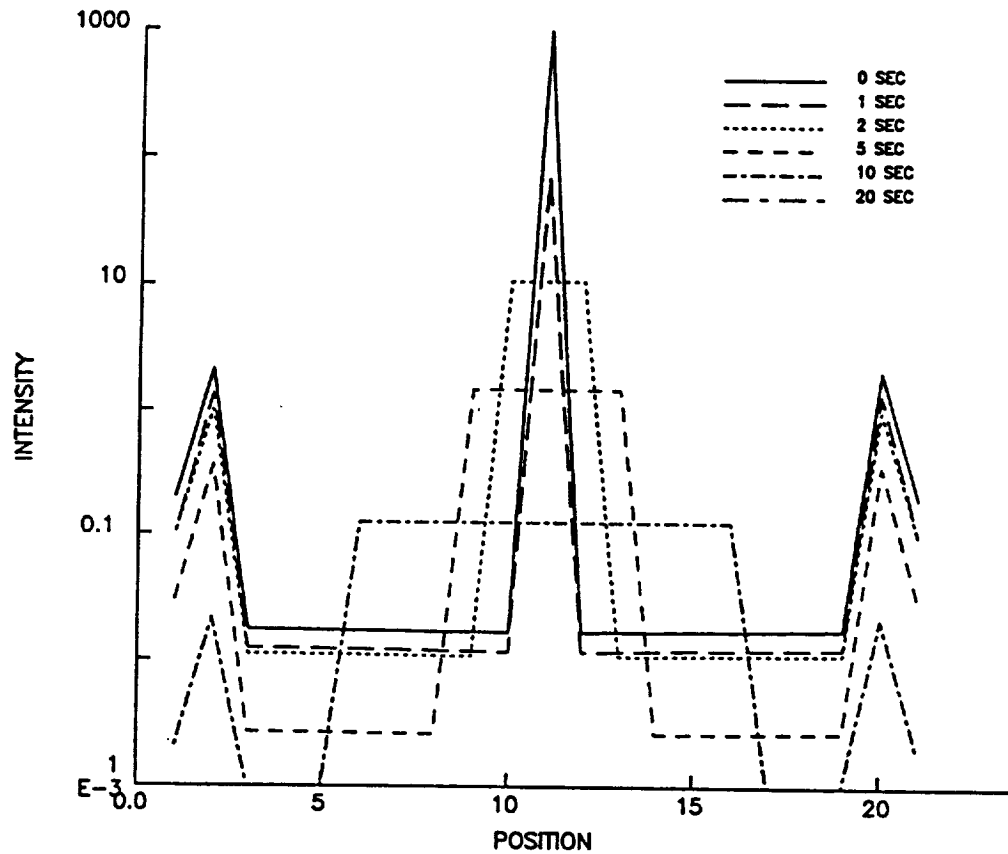


**Figure 3.10: Model T Emission Profile At 10 keV**

This shows the emission for 21 pixels composing the loop. Early in time the bright central pixel is dominant. As the kernel expands and cools, the central pixel emission decreases while that of adjoining pixels increase. In general, the overall signature is much different from that of the Model N-T at the same energy.

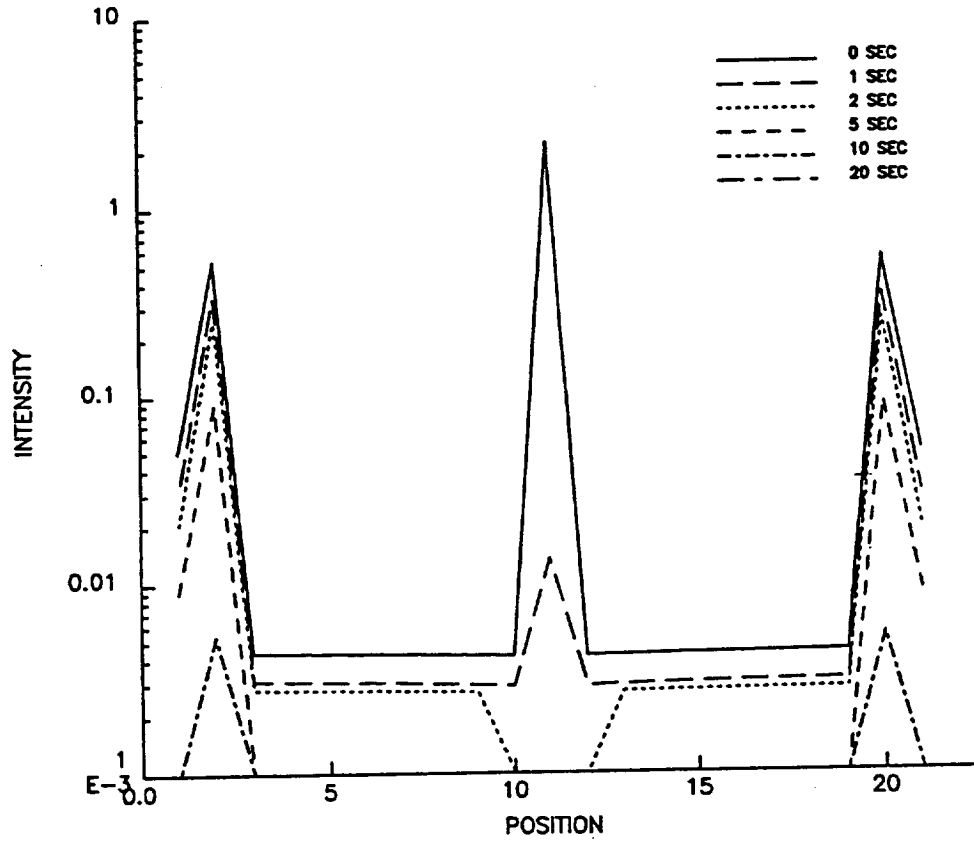


**Figure 3.11: Model T Emission Profile At 40 keV**

This shows the emission for 21 pixels composing the loop. In this profile early in time, the central pixel is as bright as the footpoint pixel. Due to the rapid cooling of the kernel, the emission from both pixels decreases rapidly. In general, after one second, this signature begins to look much like that of the Model N-T at the same energy.

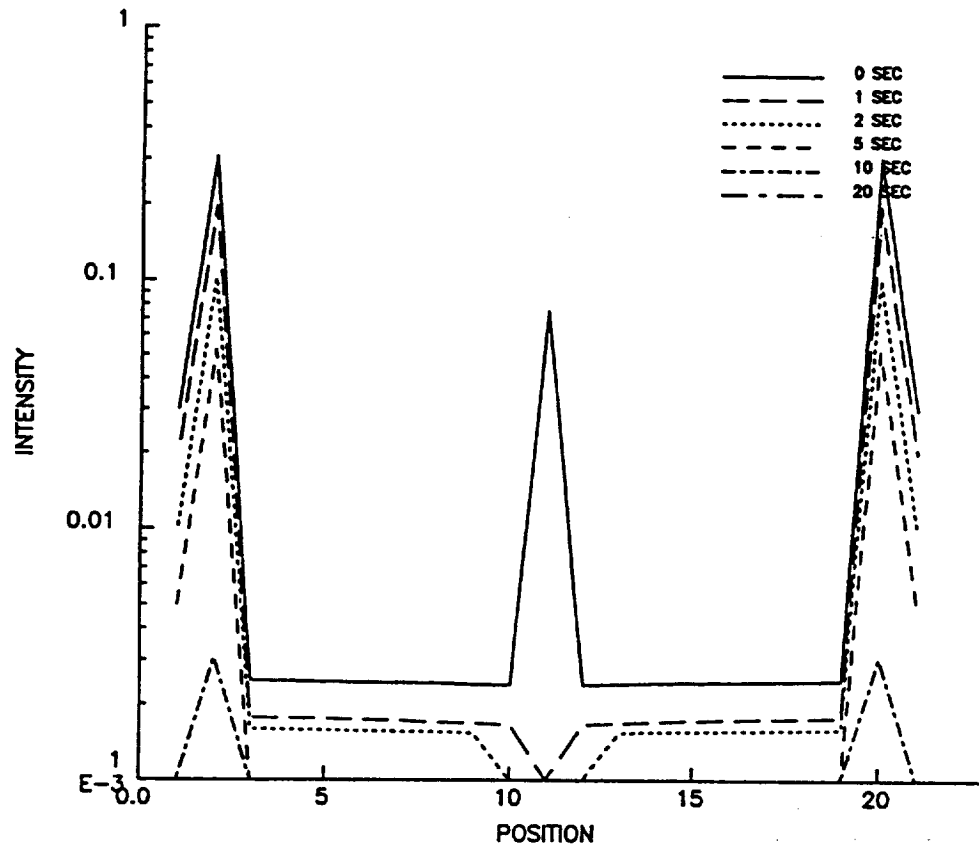


**Figure 3.12: Model T Emission Profile At 70 keV**

This shows the emission for 21 pixels composing the loop. In this profile early in time, the central pixel is almost as bright as the footpoint pixels. This is expected as the highest energy electrons escape from the kernel to produce emission in the footpoints. Except for the short burst of emission from the apex at  $t = 0$ , this signature, in general, resembles that of the Model N-T at the same energy.

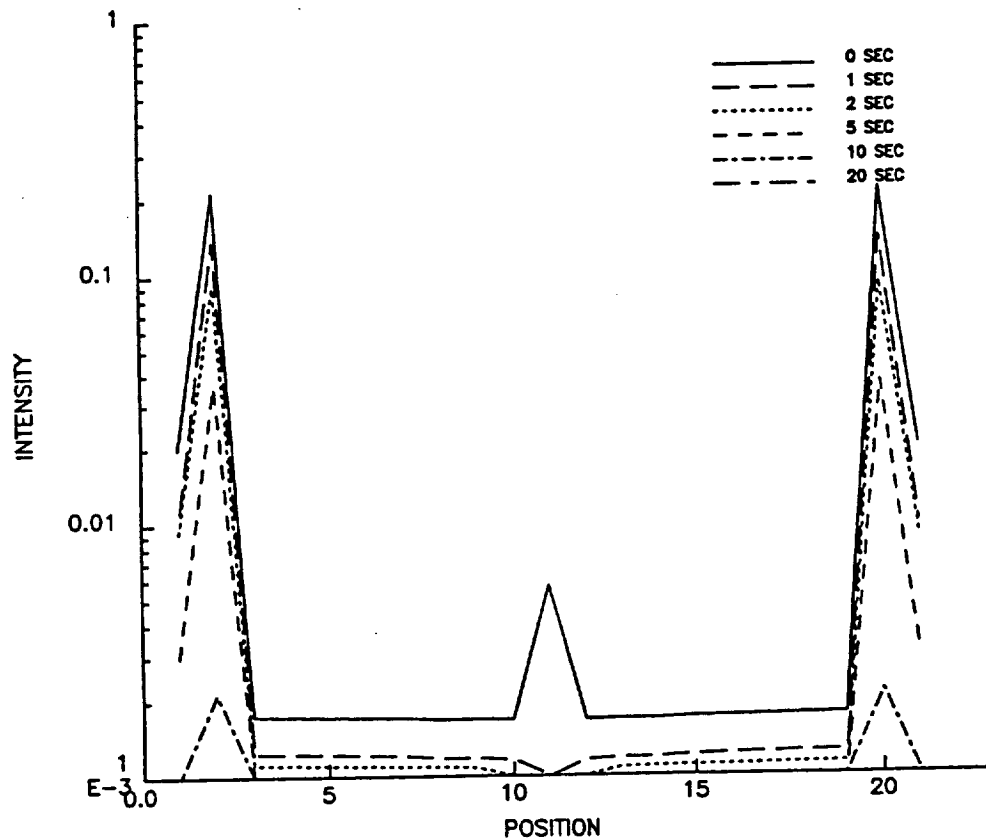


**Figure 3.13: Model T Emission Profile At 100 keV**

This shows the emission for 21 pixels composing the loop. Very early in time, the a three-point signature is present; however, in a short time a situation is reached where relatively few high-energy electrons are available in the kernel for producing high-energy photons since most have escaped to the footpoints. In general, after  $t = 0$ , this signature will resemble that of the Model N-T at the same energy.

Chapters IV, V, and VI will discuss the two telescopes which we shall use to view these profiles and examine the capabilities of these instruments. Chapter VII will meld together these chapters and the results from Chapter II and III to determine if these profiles can indeed be imaged with a Fourier telescope to distinguish between the two models.

## IV. THE FOURIER TELESCOPE

### A. INTRODUCTION

Chapters II and III discussed the emission from Model N-T and Model T as functions of time, energy, and position. A detailed comparison will be discussed in Chapter VII; however, it is sufficient here to point out that discernable signatures *were* discovered to exist between the two models.

Model N-T was characterized by a *footpoint* structure which subsequently evolved into a filled loop. By contrast, from Chapter III, Model T initially exhibited a bright central region in addition to the footpoint emission from the escaping high-energy electrons. This central region spread downward along the loop as a consequence of the diffusion of heat into the surrounding plasma. These spatial emission signatures are in principle sufficient to allow a discriminating test between the two models through imaging.

Now, the question becomes whether a Fourier telescope can view those profiles to provide the observer with a discriminating set of images. This chapter will discuss the history and introduce the basic concepts which form the foundation for Fourier telescopes while Chapters V and VI will discuss the spatial modulation collimator and the rotating modulation collimator, respectively, in greater detail. Chapter VII will then discuss the capabilities of the Fourier telescope to image the signatures derived in Chapters II and III.

Hard x-rays (10-100 keV) cannot be imaged by conventional optics such as lenses or grazing incidence mirrors. Only recently has the technology been developed to allow these types of sources to be imaged with reasonable resolution. Surprisingly, this technology is an extension of the techniques used in radio astronomy.

Essentially, the Fourier telescope concept involves sampling selected Fourier

components from a wavefront emitted by an extended source on the Sun's surface. Each component may be visualized as a single point on a common complex surface. By measuring a number of discrete components over a sufficiently large spatial frequency spectrum, this Fourier surface may be approximated. A Fourier transform of this surface function yields an approximate or a *dirty* image. The heritage of radio astronomy comes to the rescue in that several algorithms, which have been proven over the years, have been developed to *clean* the dirty image to produce a more meaningful result.

Since obtaining final images requires a tremendous amount of numerical processing, end-to-end numerical simulations are vital to both the design and the data analysis phases of a mission. In the design stage, the simulations can help keep track of performance gains or losses versus engineering trade-offs, and, in the data analysis stage, the observer needs to know whether the image he has obtained was created with enough photons to insure good imaging.

In principle, Fourier telescopes can be divided in two general classes: those that rotate (rotation modulation collimators) and those that do not, spatial modulation collimators (Campbell et al., 1991a; Hurford, 1977).

Figure 4.1 illustrates a basic telescope geometry with two grid planes followed by a detector assembly. Grid pairs can be constructed to modulate the incoming wavefront over the detector allowing a particular component to be measured (Figure 4.2). Typical geometries from proposed telescopes were used to develop the telescope models described in Chapters V and VI. Instrument imperfections such as twist, bending, uneven thermal expansion, etc. can also be addressed individually and in combination using simulations.

As mentioned earlier, conventional imaging techniques use reflection or refraction of the incident radiation (e.g., Hecht and Zajac, 1976). Since these processes do not work well at wavelengths  $\leq 2 \text{ \AA}$ , non-focusing Fourier colli-



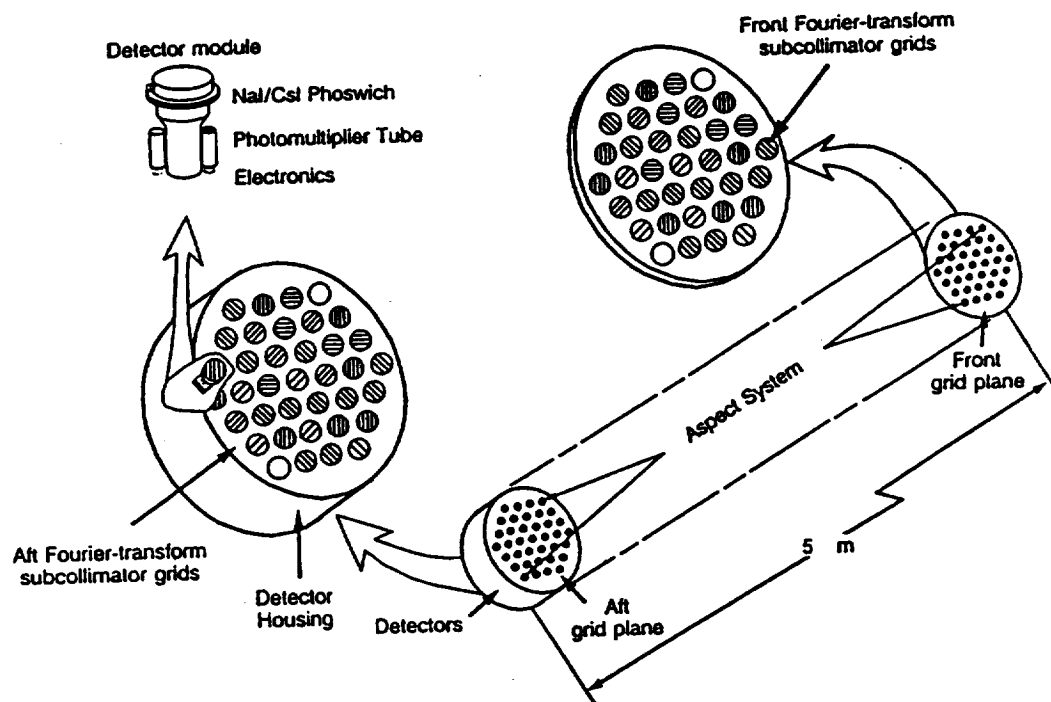


**Figure 4.1: Basic Fourier Telescope Geometry**

This shows a conceptual Fourier telescope. Each plane is composed of several grids with slit spacings corresponding to the spatial frequencies to be measured. The bottom plane's grids are directly related and aligned to those in the top plane so that each Fourier component is provided by a grid pair illuminating a detector.

## Spatial Modulation Collimator

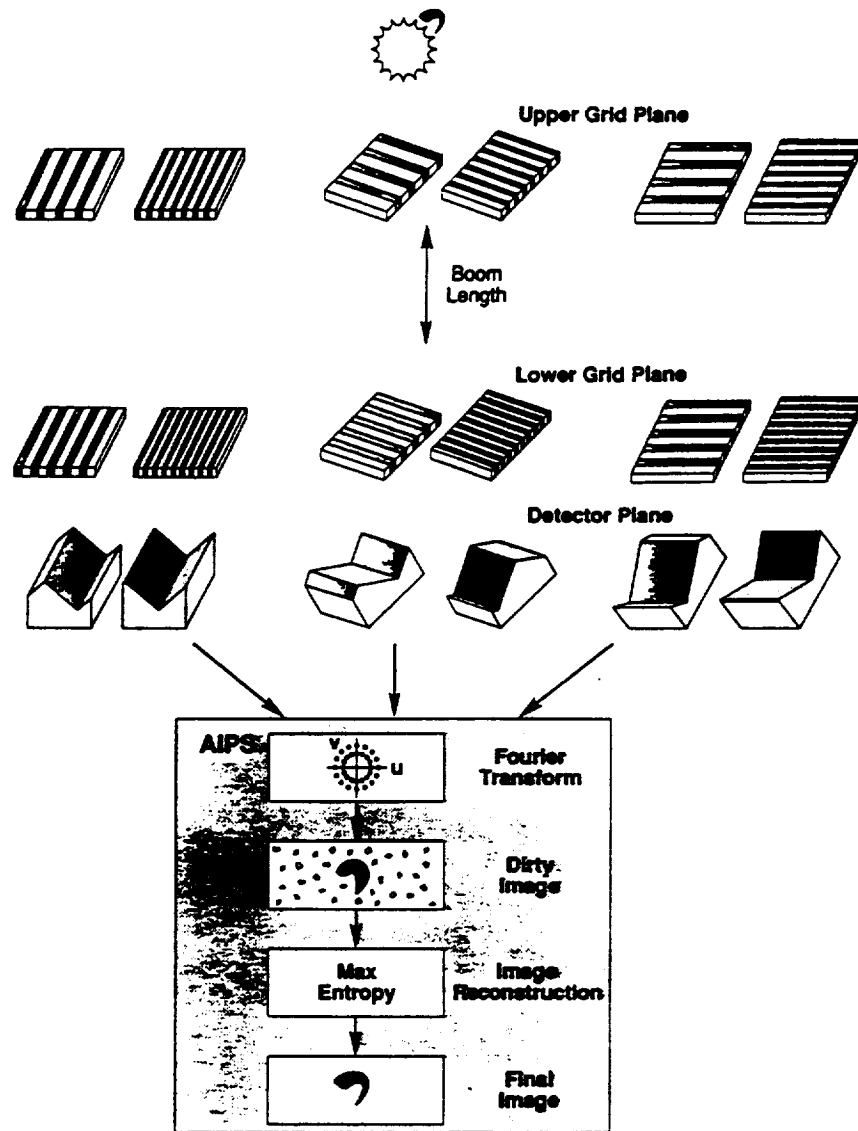


Figure 4.2: Basic Fourier Telescope Imaging Concept

mation techniques must be used for image formation. The two-grid modulation collimator first introduced by Oda (1965) provided a single Fourier component. It had the advantage of simultaneous measurements of signal and background; and, it also had the ability to locate a source.

Extending the concept (Bradt et al., 1968) to multiple grids or rotational scanning permitted the formation of true images, either continuously spread across the image plane or subdivided into discrete picture elements by subcollimators that feed independent detector elements (van Beek, 1975). A practical limit on the angular resolution of these multiple-grid collimators was the need for mechanical rigidity of the support structure. The structure had to maintain the relative positions of the grids to a fraction of the individual slit width which in practical systems (van Beek, 1975) may be as small as  $50\ \mu$ .

Makishima et al. (1978) developed a two-grid modulation collimator that measured the corresponding Fourier component of the angular distribution of the source. Thus, a single subcollimator determined the identical parameter measured by a two-element interferometer as used in radio astronomy. As in aperture synthesis (Fomalant and Wright, 1974), a number of such measurements can be combined to produce an image.

## B. Theory

Consider a point source located some distance from the observer. The emitted radiation may be envisioned as an electromagnetic spherical wave emanating from the source into space. When this wave reaches the instrument in low-Earth orbit it is essentially planar over the extent of the telescope (typical diameter of 1 meter). Mathematically, this wave could be described by taking the Fourier transform of the brightness distribution of the point source (Steward, 1987). In

two dimensions, the Fourier transform for the brightness distribution  $B(x, y)$  may be written generally as

$$f(u, v) = \int_{-\infty}^{\infty} B(x, y) e^{2\pi i(ux+vy)} dx dy \quad (4.1)$$

where  $u$  and  $v$  are spatial frequencies. Taking the inverse transform,

$$B(x', y') = \int_{-\infty}^{\infty} f(u, v) e^{-2\pi i(ux'+vy')} du dv \quad (4.2)$$

provides an image.

Most optics texts discuss extensively the use of the Fourier transform in a related operation in which the  $\vec{E}$  field vector associated with an electromagnetic wave emanating from the point source and measured a great distance from that source will be transformed. This transformation may be described mathematically by a Fourier transform and the intensity in the image plane may be obtained by taking the modulus squared of the complex vector. This particular approach is especially useful in treating diffraction and many other wave-related effects. There is an associated approach in which the brightness distribution from the source as measured a great distance away may also be represented by a Fourier transform. Taking the inverse transform in principle provides an image directly.

In the laboratory an analogous experiment could be performed in which a source was placed at the left focal point of a lens. Another lens would be placed behind the first and at the right focal point of this lens an image could be observed. However, if the intensity distribution is measured between the lenses, one finds that the radiation has structure in this region as well from which a legitimate image may be obtained.

As mentioned above, there is an interesting but not altogether unexpected parallel with radio astronomy which also constructs its images from measured

Fourier components. The two-element interferometer provides high resolution by correlating the signals of the two antennas (Figure 4.3). The correlation is normally achieved by the multiplication or addition of the signals, which produces a spatial modulation of the primary beam of the antennas with interference fringes (Figure 4.4). In this way fine structure is introduced into the primary beam to increase the resolution.

The response of the system to a point source of monochromatic radiation of frequency  $\omega$  or wavelength  $\lambda$  can be described by a voltage  $E$  proportional to the sum of the electric fields generated at the feed of each telescope at slightly different times. The time difference is called the geometric delay and is denoted by  $\tau$ . The voltages at the multiplier input are

$$V_1 \propto E \cos(\omega t) \quad (4.3)$$

$$V_2 \propto E \cos[\omega(t - \tau)] \quad (4.4)$$

and

$$V_2 = E \cos\left(\omega t - \frac{2\pi B}{\lambda} \cos\theta\right) \quad (4.5)$$

where  $B$  is the separation of the two antennas,  $\lambda$  is the wavelength of the radiation, and  $\theta$  is the angle between the point source and the line joining the two antennas. The expression  $(E/\lambda) \cos\theta$ , the interference term, gives the phase path-length difference of the radiation travel along the two possible paths. The diurnal motion of the Earth causes  $\theta$  to vary with time. The output,  $R(t)$ , of the multiplier, after a high-frequency term is rejected by a low pass filter, is

$$R(t) \propto S \cos\left[\frac{2\pi B}{\lambda} \cos\theta(t)\right] \quad (4.6)$$

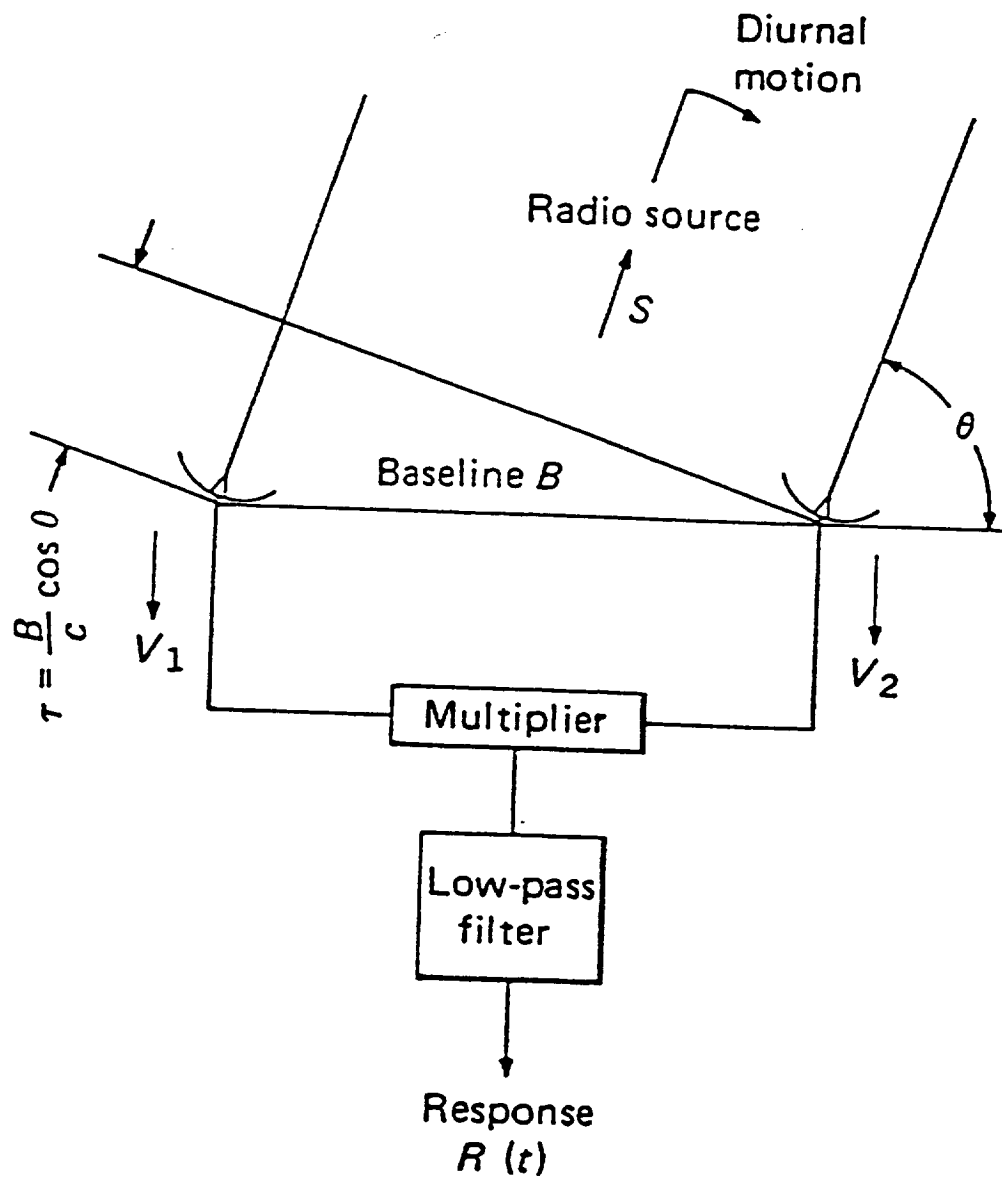


**Figure 4.3: A Basic Radiotelescope**

The illustrates the concept of a radiotelescope. The principle here is that the time difference in the arrival of the wavefront leads to an interference pattern which is directly related to a Fourier component.

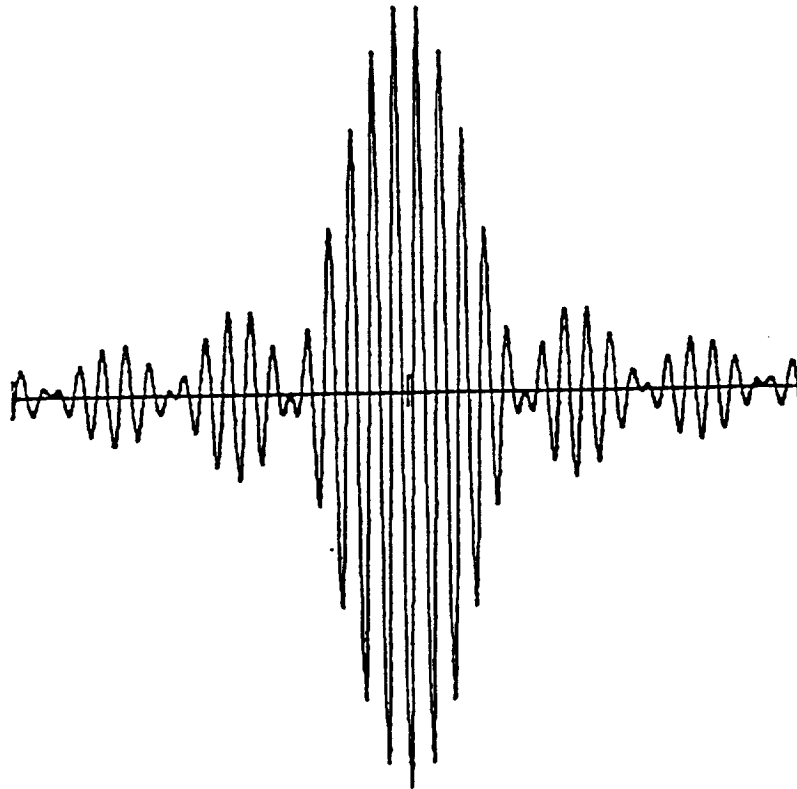


**Figure 4.4: A Typical Interferometer Response**

The envelope of the response is sinusoidal in nature and directly related to a Fourier component in that one may obtain a phase shift and an amplitude which are sufficient to define a phasor in the complex plane. The real and imaginary components of the visibility function are then easily obtained as components of the phasor.

This is the basic equation of interferometry. The flux density, or power  $S$ , of the source has replaced  $E^2$ . The fringe spacing is given by the angle which produces a change of one wavelength in the path-length difference.

The phase path-length difference  $(\frac{B}{\lambda}) \cos\theta$  can be more generally written as  $\vec{B} \cdot \vec{s}$  where  $\vec{B}$ , the physical spacing, is equal to the element separation in wavelengths and its direction is that of the line joining the elements. The baseline direction will be defined as a vector from telescope 2 toward telescope 1. The preceding equation then becomes

$$R(t) \propto S \cos[2\pi \vec{B} \cdot \vec{s}(t)] \quad (4.7)$$

The response of a two-element interferometer to an extended source can be obtained by considering the source to be a collection of point images and summing their individual responses. Let  $\vec{s}$  be the vector to a convenient position near the source. This point is denoted as the phase center. Any other point can be denoted by  $\vec{s} + \vec{\sigma}$ . If  $I(\vec{\sigma})$  describes the brightness distribution (angular distribution of power), then the response to the extended source is

$$R(t) = \int I(\vec{\sigma}) \cos[2\pi \vec{B} \cdot (\vec{s}(t) + \vec{\sigma})] d\vec{\sigma}. \quad (4.8)$$

A useful quantity in interferometry is the projected spacing  $\vec{b}$  of the physical baseline  $\vec{B}$  as viewed from a radio source. The projected spacing  $\vec{b}$  is given by

$$\vec{b} = \vec{s} \times (\vec{B} \times \vec{s}) \quad (4.9)$$

$$= \vec{B} - (\vec{s} \cdot \vec{B}) \vec{s}. \quad (4.10)$$

Generally, the projected spacing is resolved into components along directions to the east and north, which are commonly denoted  $u$  and  $v$ , respectively.



Since the angular size of the region observed is limited by the extent of the antenna response (typically less than  $1^\circ$ ), the phase term can be expanded to first order for sufficient accuracy,

$$\vec{B} \cdot (\vec{s} + \vec{\sigma}) = \vec{B} \cdot \vec{s} + \vec{B} \cdot \vec{\sigma} \quad (4.11)$$

$$\approx \vec{B} \cdot \vec{s} + \vec{b} \cdot \vec{\sigma} \quad (4.12)$$

Since  $\vec{\sigma}$  is nearly perpendicular to  $\vec{s}$ , only the projected spacing  $\vec{b}$  is retained in the second term of the cosine. The response becomes

$$R(t) = \int_{-\infty}^{+\infty} I(\vec{\sigma}) \cos[2\pi \vec{B} \cdot \vec{s} + 2\pi \vec{b} \cdot \vec{\sigma}] d\vec{\sigma} \quad (4.13)$$

This may be expanded into

$$R(t) = \cos(2\pi \vec{B} \cdot \vec{s}) \int_{-\infty}^{\infty} I(\vec{\sigma}) \cos(2\pi \vec{b} \cdot \vec{\sigma}) d\vec{\sigma} \quad (4.14)$$

$$- \sin(2\pi \vec{B} \cdot \vec{s}) \int_{-\infty}^{\infty} I(\vec{\sigma}) \sin(2\pi \vec{b} \cdot \vec{\sigma}) d\vec{\sigma} \quad (4.15)$$

However, it is much easier to work with the more compact complex form

$$R(t) = \text{Re} \{ e^{2\pi i \vec{B} \cdot \vec{s}(t)} \int_{-\infty}^{+\infty} I(\vec{\sigma}) e^{2\pi i \vec{b}(t) \cdot \vec{\sigma}} d\vec{\sigma} \}. \quad (4.16)$$

Now, define the visibility function by the following expression,

$$V = \int_{-\infty}^{\infty} I(\vec{\sigma}) e^{2\pi i \vec{b} \cdot \vec{\sigma}} d\vec{\sigma}. \quad (4.17)$$

This integral is a complex number. The amplitude of  $V$  is proportional to the amplitude of the fringe pattern and the argument of  $V$  equals the phase shift in the fringe pattern from that of the response to a point source at the

phase center. Clearly, the visibility function is the Fourier transform of the brightness distribution. Since, in radio astronomy, the time variability of the source is normally less than that due to the diurnal motion of the source, the instantaneous response can be rewritten as (Hurford and Hudson, 1980)

$$R = \text{Re} \left\{ K \int_{-\infty}^{+\infty} \int_{-\infty}^{+\infty} I(x, y) e^{2\pi i(ux+vy)} dx dy \right\} \quad (4.18)$$

where  $K$  is independent of the source. The integral has been explicitly written in terms of eastward and northward displacements  $(x, y)$  on the sky, and  $(u, v)$  are the corresponding components of  $\vec{b}(t)$ . Note that the response depends only on the spatial frequency content in the source that corresponds to  $u$  and  $v$ .

This can be further simplified by rewriting the integral in terms of  $(\theta, \phi)$ , orthogonal coordinates in the sky parallel and perpendicular to  $\vec{b}$ ,

$$R = \text{Re} \left\{ K \int_{-\theta_{\min}}^{+\theta_{\max}} F(\theta) e^{2\pi i b \theta} d\theta \right\} \quad (4.19)$$

where

$$F(\theta) = \int_{-\phi_{\min}}^{+\phi_{\max}} I(\theta, \phi) d\phi \quad (4.20)$$

is the projection of the source brightness distribution perpendicular to  $\vec{b}$ .

To characterize the modulation collimator response (i.e. Moire fringes) in x-ray astronomy, the transmission pattern may be represented by a triangular wave  $\Lambda(\theta)$  that repeats with angular period  $P$ :

$$\Lambda(\theta) = 1 - \frac{2|\theta|}{P}, \quad (4.21)$$

for

$$\frac{-P}{2} \leq \theta \leq \frac{P}{2} \quad (4.22)$$

and

$$\Lambda(\theta \pm P) = \Lambda(\theta). \quad (4.23)$$

A scanning modulation collimator sweeps out the angular range  $P$  in a finite time, and the counting rate as a function of time must be converted to the angular profile from an aspect solution that describes the collimator motion. The angular response can be modeled with a function  $N(\theta)$  noting that  $N(\theta)\Delta\theta$  is the probability of  $\Delta N$  counts in the angular range  $\Delta\theta$ :

$$N(\theta) = A \int_{-\psi_{min}}^{+\psi_{max}} [0.5 F(\psi) \Lambda(\theta - \psi) + B] \Delta t d\psi, \quad (4.24)$$

where  $F(\psi)$  is the source brightness contribution (photons  $\text{cm}^{-2} \text{s}^{-1} \text{radian}^{-1}$ ) integrated parallel to the collimator aperture (a 50% maximum response is assumed for slit widths and boundary material of equal spacing);  $B$  is the background rate in counts  $\text{cm}^{-2} \text{s}^{-1}$ ,  $A$  the detector area ( $\text{cm}^2$ ) and  $\Delta t$  the integration time (s).  $\psi$  is the brightness distribution parameter across the grid.

The complex visibility function as measured by a given collimator may be written as

$$V = \frac{2}{P} \int_{-\frac{P}{2}}^{\frac{P}{2}} N(\theta) e^{i\frac{2\pi}{P}\theta} d\theta. \quad (4.25)$$

Substituting, the following is obtained

$$V = \frac{A}{P} \int_{-\psi_{min}}^{+\psi_{max}} \int_{-\frac{P}{2}}^{\frac{P}{2}} [F(\psi) \Lambda(\theta - \psi) + 2B] \Delta t e^{i\frac{2\pi}{P}\theta} d\theta d\psi. \quad (4.26)$$

Since  $\Lambda(\theta - \psi)$  is periodic, this becomes

$$V = \frac{A\Delta t}{P} \int_{-\psi_{min}}^{+\psi_{max}} F(\psi) e^{i\frac{2\pi}{P}\psi} d\psi \int_{-\frac{P}{2}}^{\frac{P}{2}} \Lambda(\theta') e^{i\frac{2\pi}{P}(\theta')} d\theta'. \quad (4.27)$$

If we now approximate the periodic function with a sinusoid with the same amplitude and frequency and substitute for  $\Lambda(\theta')$  we obtain

$$V = c_1 \int_{-\psi_{min}}^{+\psi_{max}} F(\psi) e^{i \frac{2\pi}{P} \psi} d\psi, \quad (4.28)$$

where  $c_1$  is a constant.

This has the same general form as the response for the radio interferometer examined previously (equation 4.17). However, we note that the triangular response used in this analysis offers in principle higher Fourier harmonics which may potentially be used to provide higher resolution information about the source (Hurford and Hudson, 1980).

The implication of this correspondence for x-ray astronomy is that it may take advantage of many of the techniques and methods which have been rigorously developed over the years for radio astronomy. This identity is also interesting in that for radio waves the characteristic periodic variation of response with angle comes from wave interference, while for x-rays it comes from geometrical shadowing.

Along these lines, a Fourier transform telescope consists of a set of individual modulation collimators (subcollimators) that feed discrete detectors. A subcollimator is equivalent to one baseline or a simple two-element interferometer in radio astronomy. A measurement of the amplitude

$$V = \sqrt{[Re(V)]^2 + [Im(V)]^2} \quad (4.29)$$

and phase

$$\alpha = \tan^{-1} \left[ \frac{Im(V)}{Re(V)} \right] \quad (4.30)$$

determines all of the necessary information regarding the Fourier component measured by a given subcollimator.

$Re$  and  $Im$  are the real and imaginary representation of the components of the complex visibility function in the complex plane at a single point in the  $(u, v)$  plane. Since the visibility function  $V(u, v)$  in the *observational plane* is directly related to the brightness function in the *object plane* via a Fourier transform, an image is obtained from the inverse Fourier transformation of the visibility  $V(u, v)$ .

The corresponding  $(u, v)$  coordinates are just

$$u = \frac{1}{P} \cos \theta \quad (4.31)$$

and

$$v = \frac{1}{P} \sin \theta. \quad (4.32)$$

where  $P$  is the angular period of the grids. For slits and solid slats of the same width,  $P = (2s/d)$ , where  $s$  is the slit/slat width and  $d$  is the grid separation. The collimator period may be related to  $(u, v)$  by

$$P = \frac{1}{\sqrt{u^2 + v^2}}. \quad (4.33)$$

Finally, it should be noted that Fourier telescopes are *photon counting* instruments. In other words, the telescope takes a number of photons and through numerical reconstruction provides an integrated image. It leaves to the observer the task of organizing the photons into energy and time bins. Usually, the observer accomplishes this with an innovative detector design. This is a powerful feature of this type of instrument since, in the case of insufficient flux, it allows

one simply to combine bins, both in energy and/or in time, to provide enough photons for an image.

### C. THE ASTRONOMICAL IMAGING PROCESSING SYSTEM (AIPS)

AIPS, developed and maintained by the National Radio Astronomy Observatory (NRAO), is widely accepted today in the radio astronomy community (Greisen, 1986). It is a highly sophisticated software system requiring over 180,000 blocks of VAX disk space to run. At the core of the multitude of software routines are those which allow the user to bring Flexible Image Transport System (FITS) formatted  $(u, v)$  data into AIPS (Greisen and Harten, 1981; Wells, Greisen, and Harten, 1981); fast Fourier transform the data to form a dirty map; clean the dirty map in a number of independent ways to form an image; and display the image in a number of different ways. Peripheral software allows the user to enhance an image by rotating it, zooming in or out, or suppressing background noise. Figure 4.5 shows the AIPS user manual cover. It actually does contain recipes such as banana nut bread in addition to being an excellent reference.

AIPS uses the equatorial system of coordinates. In this system, the Earth's equator is the plane of reference. The poles are at the intersection of the Earth's axis with the celestial sphere, an imaginary surface at a large distance with the Earth at its center. Thus, the ordinate of AIPS output images will be given as the *declination* in units of degrees, arc minutes, and arc seconds while the abscissa will be given as the *right ascension* in units of hours, minutes, and seconds.

One major advantage in using AIPS is that it allows a dirty image to be cleaned in several different independent ways. Two of the most widely used are the CLEAN algorithm and the Maximum Entropy Method (MEM). In the CLEAN method the respective phases and amplitudes are combined with the

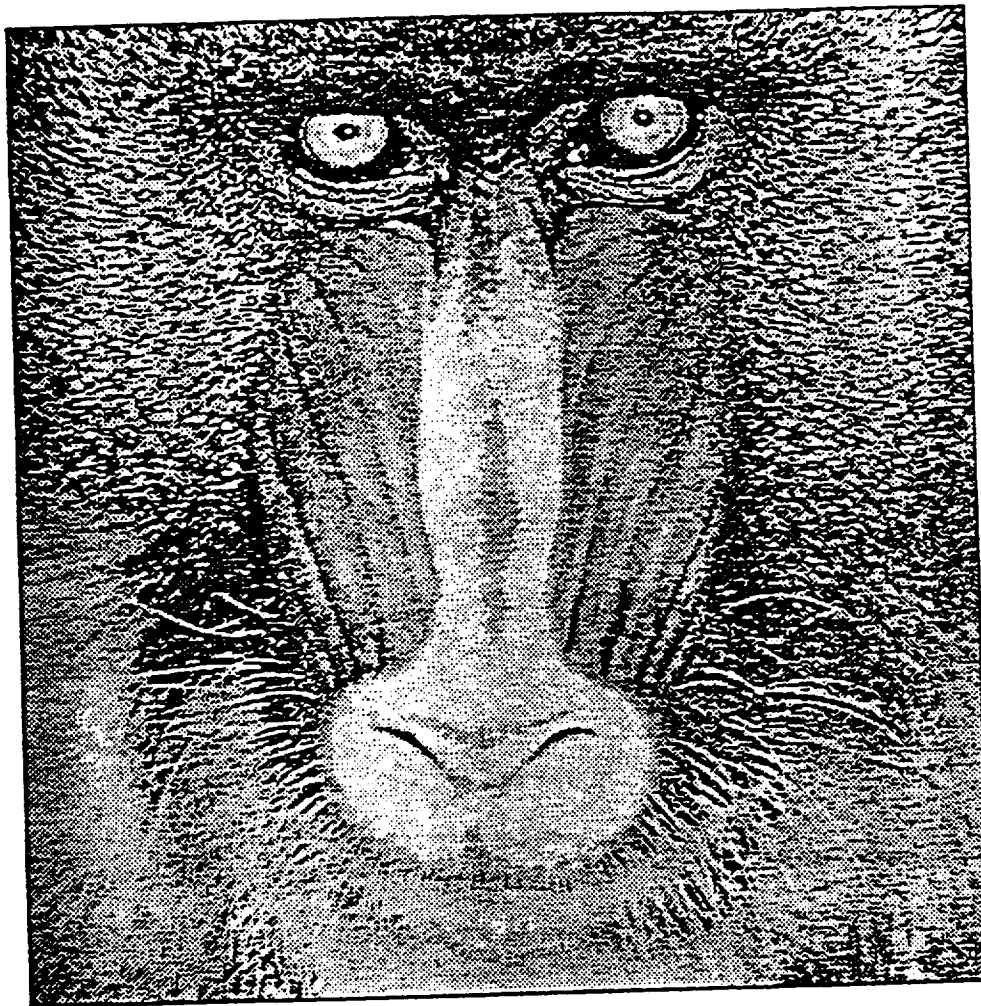


**Figure 4.5: AIPS Cookbook Cover**

(NRAO, Virginia, 1986)

measured Fourier components to produce an *uncleaned* image. This preliminary image generally has large sidelobes, particularly if there are one or more dominant point sources of emission in the field of view.

The CLEAN algorithm attempts to reduce these sidelobes by iteratively deconvolving the image with the expected response of an ideal point source including sidelobes. This method has been shown to be effective for a wide variety of source configurations, although the method works better for collections of point sources than for diffuse emission regions. The advantages of the CLEAN method are that it is relatively fast and theoretically simple to apply. Some disadvantages are that the method can produce images with areas of negative pixel brightness, that statistical errors are somewhat difficult to incorporate, particularly when the errors vary from component-to-component, and that significant sidelobes can still be present in the image, particularly if the statistical errors are large.

The Maximum Entropy Method attempts to produce the *smoothest* (highest entropy) image compatible with the data. Advantages of the method are that all image pixels have positive brightness and the statistical errors of individual Fourier components are easily incorporated into the analysis. While MEM has a bias toward diffuse sources of emission, in practice the method works well even for point sources, producing images with lower sidelobes and reduced artifacts than the CLEAN algorithm.

One of the strengths of the numerical model is that a dirty image set can be cleaned conveniently using both techniques and then the images compared. By using known inputs, the techniques can be compared in different scenarios and the best one chosen. In addition, artifacts which might be introduced by assumptions in the techniques will become apparent and will be useful information when real data are obtained and processed through the model. AIPS, obtained from NRAO,



has been adapted to process x-ray data.

As part of the verification process,  $(u, v)$  data were obtained from Palmer and Prince (1987). In this experiment, a Fourier telescope was developed in the laboratory as a pathfinder for future development. Grids were fabricated from soldering wire, and small bits of radioactive cobalt were used as hard x-ray sources. Since a steady state source was used, the telescope could view as long as was necessary to obtain enough photons for an image. Also, the source distribution could be rotating rather than the telescope. The experiment was a success and paved the way for more advanced developments.

Figure 4.6 shows the Palmer and Prince (1987) results using three dimensional contour plotting, gray scale graphics, and contour plot images using both CLEAN and MEM. While the author noted that maximum entropy seemed to produce a higher quality image, no such difference was found here in his data using AIPS. This may be attributed to the fact that the AIPS algorithms are highly sophisticated and under scrutiny from many users and are constantly being improved. However, for more complicated images such as the filled loop (Chapters V and VI), MEM did provide better images than CLEAN. Figures 4.7, 4.8, and 4.9 show the AIPS output using the Palmer data in contour, three dimensional, and grey scale. The results are reproduced exactly with the AIPS CLEAN algorithm.

In order to work with these data, a complicated linking program was required to convert the FORTRAN data into a FITS file acceptable to AIPS. The data were then brought into AIPS and fast Fourier transformed to obtain a dirty map. This map was then cleaned using several different algorithms and displayed in several different graphic formats. AIPS duplicated the results found in the literature exactly, thus greatly increasing our confidence that the software had been successfully implemented.

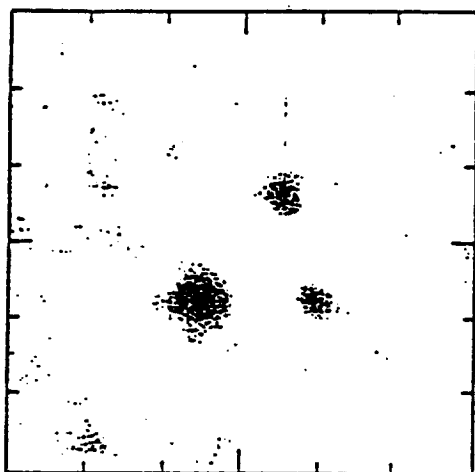


FIGURE 5. GRAY SCALE PLOT OF MAXIMUM ENTROPY IMAGE SHOWN IN FIGURE 4B.



FIGURE 6. THREE-DIMENSIONAL CONTOUR PLOT OF THE MAXIMUM ENTROPY IMAGE SHOWN IN FIGURE 4B AND FIGURE 5.

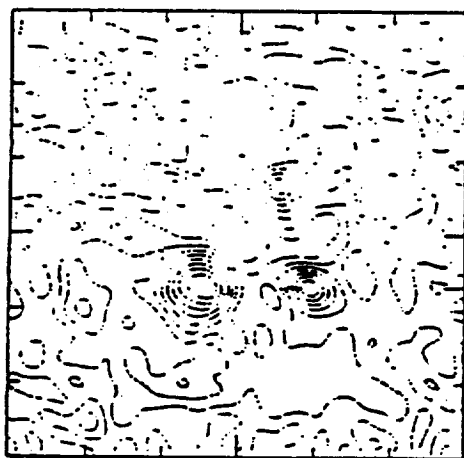


FIGURE 4A. CONTOUR PLOT OF THE IMAGE OF THREE  $^{57}\text{Co}$  SOURCES PRODUCED USING THE CLEAN ALGORITHM. CONTOURS AND SIZE OF FIELD OF VIEW ARE THE SAME AS IN FIGURE 3A.

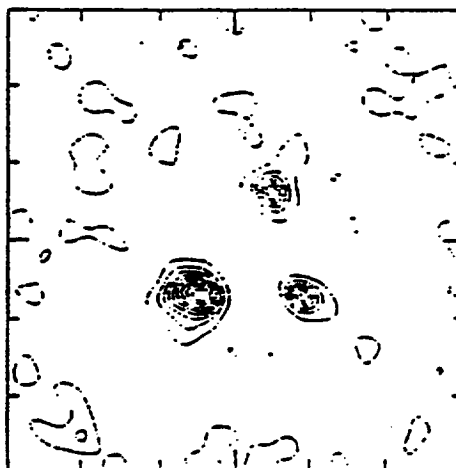
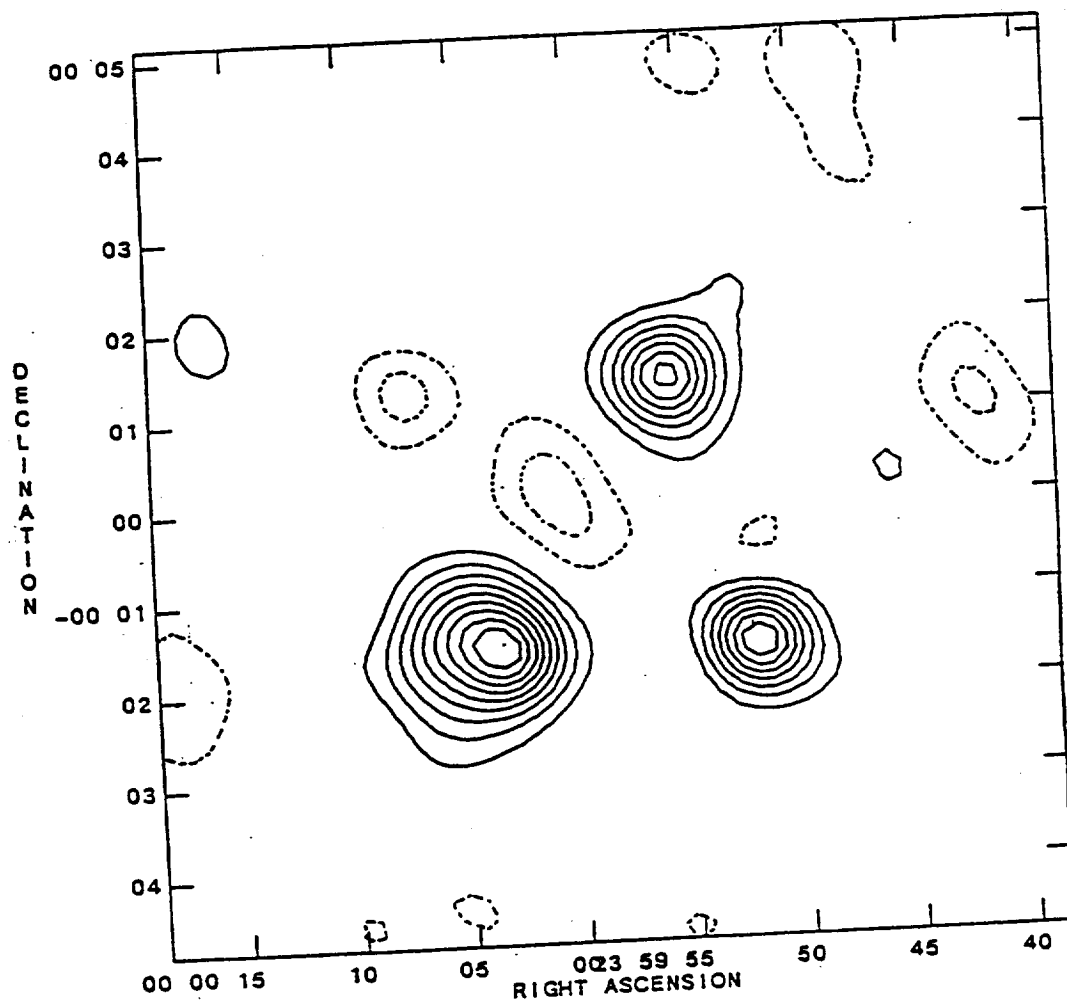


FIGURE 4B. CONTOUR PLOT OF THE IMAGE OF THREE  $^{57}\text{Co}$  SOURCES PRODUCED USING THE MAXIMUM ENTROPY METHOD. THE DATA SET FOR THE IMAGE WAS IDENTICAL TO THAT USED TO PRODUCE FIGURE 4A.

### Figure 4.6: Palmer Results

Palmer built a laboratory version of a spatial modulation collimator using soldering wire for grids and three cobalt sources. His telescope was successful in producing in the laboratory hard x-ray images of the sources.



**Figure 4.7: AIPS Contour Of Palmer Results**

Using data from an actual laboratory spatial modulation collimator, AIPS duplicated the Palmer's results. The contours in this image representation are percentages (10 % increments) of the peak value in the field of view.

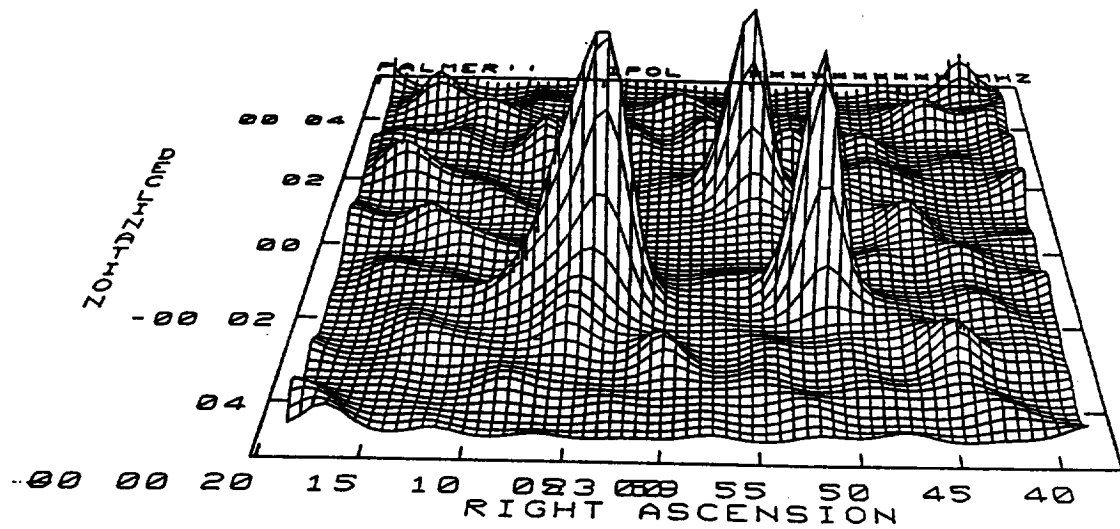


**Figure 4.8: AIPS 3-D Of Palmer Results**

It is useful to have both three-dimensional displays and contour displays with which to analyze data. AIPS provides both. Here, AIPS has processed data from a laboratory telescope to duplicate those results.

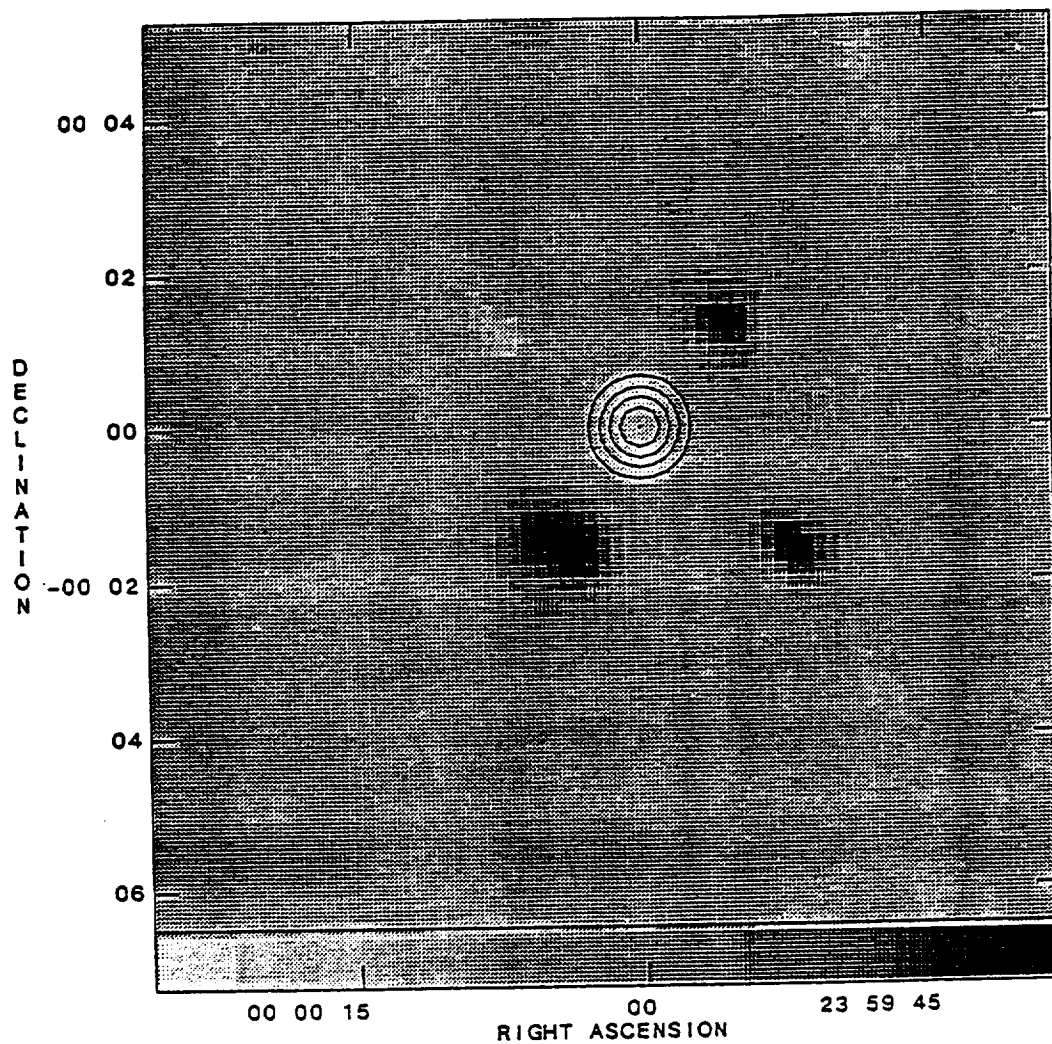


**Figure 4.9: AIPS Grey Of Palmer Results**

This is another example of the versatility found in AIPS. Here, using data taken from a basic laboratory telescope, a duplicate grey scale image was obtained. The contour in the center is a representation of the point spread function of the telescope.

## D. POTENTIAL ENGINEERING CONSTRAINTS

Numerical models typically precede the actual hardware development of a complex system and generally if the system does not perform well numerically then its development is terminated at that point. Hence, numerical models provide relatively inexpensive proof of principles tested in the systems development process.

In building the actual system the designer may be forced to accept compromises to the ideal due to cost and/or schedule constraints. Reducing the grid thickness is one example in which weight, cost, and manufacturing time might be reduced. The technical implications of such a change would be to allow high energy photons to penetrate one or both grids. These photons would essentially then constitute a source of random noise on the detector. Other sources of random noise would be the cosmic background and the detector itself (internal noise). Fortunately, all of this results in a relatively uniform background of counts while the modulation provided by the telescope rides upon this uniform background level. **This feature makes the Fourier telescope tolerant to random noise.**

Real detectors will offer other design challenges such as decreasing efficiency at higher energies, variable sensitivity as a function of time, and manufacturing difficulties for large sensitive areas. For our particular systems operating from 10 to 100 keV, efficiencies available from off-the-shelf detectors are close to 100%.

The hardware development of the Fourier telescopes described in Chapters V and VI will have some risks associated with it and these risks will grow as one attempts to extend the technology to energies above 100 keV. For example, grid manufacturing still remains a high risk issue, especially for the finer ones providing 1-4 arc second spatial resolution. Figure 4.10 shows the throughput of

tungsten for different thicknesses. Clearly for 10-100 keV the grids can easily be made opaque using a modest thickness; however, as one moves to higher energies increasing grid thickness may be necessary. For the finer grids, this may present a formidable manufacturing challenge.

Given that these grids can be successfully built, they must then be mounted into a structure 5 meters long in such a way as to provide high precision alignment between grid pairs. The alignment error must be on the order of a few microns. The telescope must then be accurately pointed.

Detector saturation is another high risk area. Around  $10\ \mu$ , there is a danger of saturating the detector with too much flux and at energies above 100 keV detector efficiency may change drastically with energy. The Burst and Transient Source Experiment (BATSE) is presently in orbit using large, NaI(Tl) detectors ( $127\ \text{cm}^2$ ) in the 15 keV-110 MeV range for sensing hard x-rays and gamma rays. These compare very well with our  $100\ \text{cm}^2$  detectors used in our two telescopes. From 10-100 keV, the BATSE detector efficiency is uniformly 90-100%.

In addressing the saturation problem, Figure 4.11 illustrates the throughput characteristics of aluminum. Clearly, an aluminum shield of modest thickness covering the end of the telescope could be constructed to eliminate low-energy saturation problems. Indeed, by simply varying the thickness one could *tune* the shield to provide practically any desired response.

Figure 4.12 illustrates for an actual bright flare the BATSE detector saturation and the SMC imaging thresholds. Clearly, for a thin aluminum shield 0.04 centimeters thick we can image the flare from 10-100 keV without fear of saturation.

Therefore, while our simulations will represent a best case for Fourier telescope performance, it will be a meaningful best case in that both grids and detectors can be reasonably constructed to provide

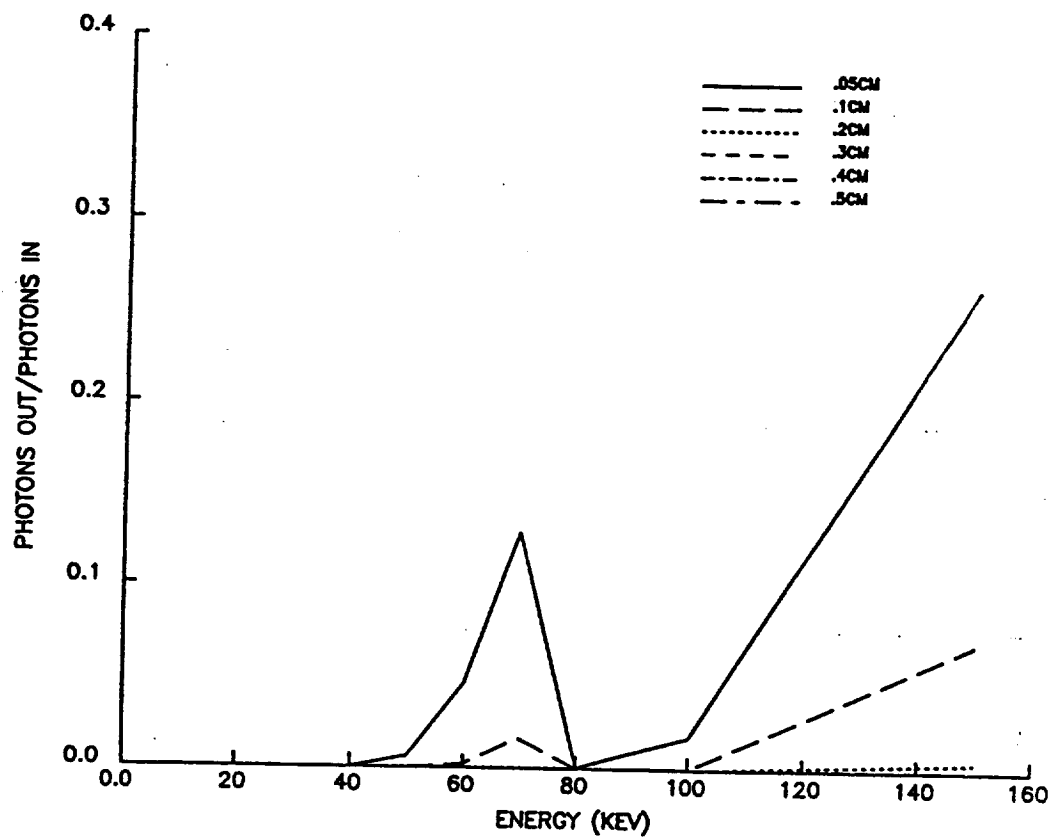


**Figure 4.10: Tungsten Throughput**

For a very reasonable tungsten thickness of only 0.3 centimeters, the grids can be made opaque to x-rays from 10-100 keV.



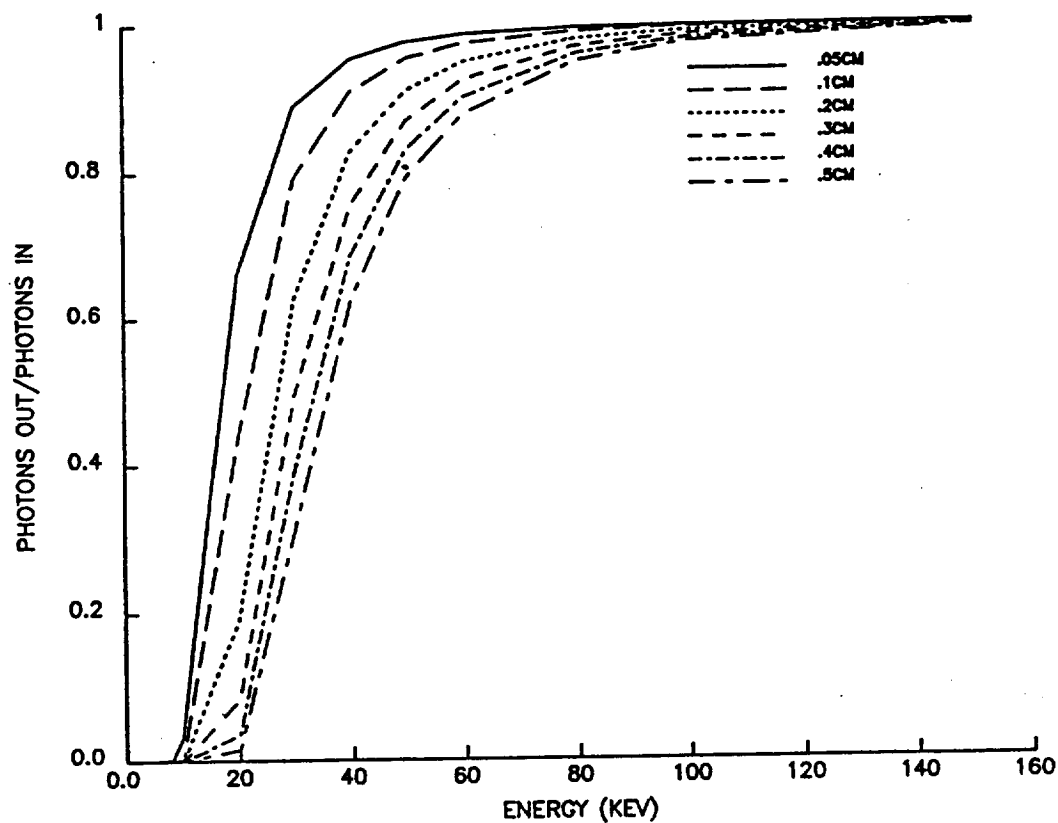


**Figure 4.11: Aluminum Throughput**

This shows the throughput for different thicknesses of aluminum as a function of energy. Clearly, an aluminum shield of reasonable thickness can be constructed to eliminate flux below 10 keV and avoid detector saturation problems.

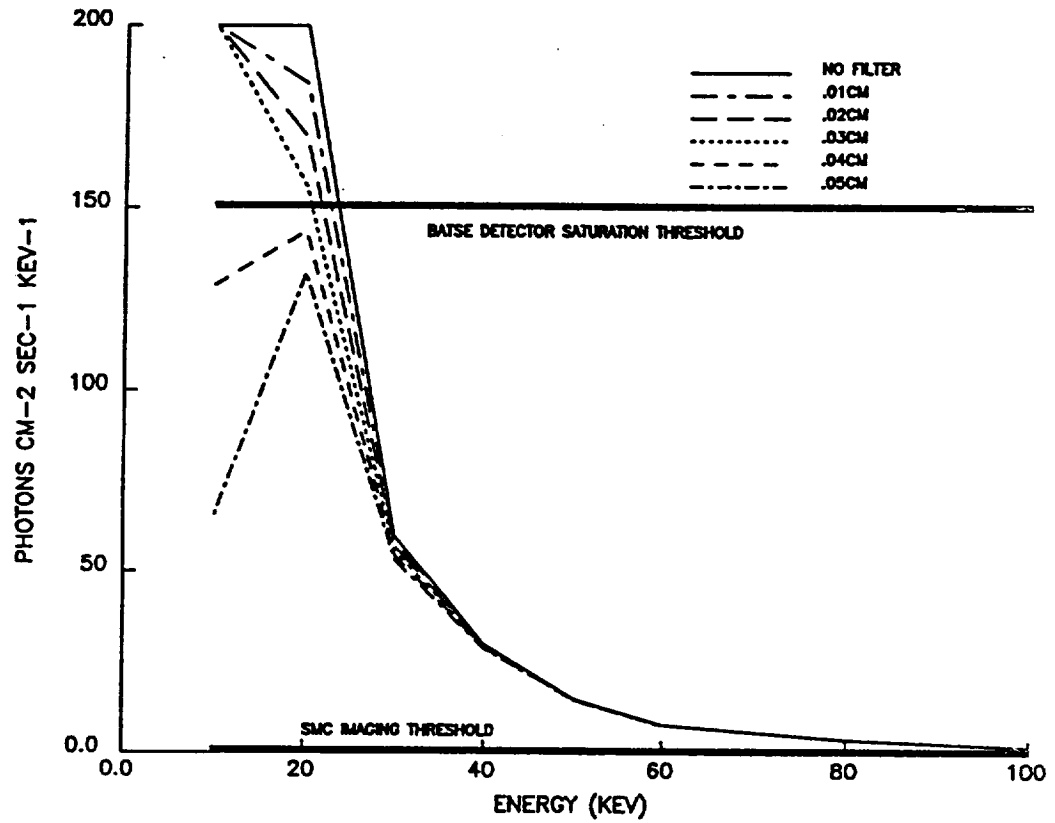


**Figure 4.12: BATSE Detector And SMC Imaging Thresholds**

Using the Burst and Transient Source Experiment (BATSE) detector (currently operating in orbit) as a reference, and choosing a bright flare, clearly for a very reasonable thickness aluminum shield of 0.04 cm, detector saturation could be avoided completely while retaining a flux level well above the Fourier telescope imaging threshold.

close to ideal performance between 10-100 keV.

## E. SUMMARY

Fourier telescopes can be designed in several different ways to optimize available resources. The rotation modulation collimator approach, which will be taken in Chapter VI, will essentially consist of modulating the x-ray wavefront in time with two different grid pairs (i.e., modulation periods) corresponding to angular resolutions  $\cong 4$  and 8 arc seconds. The temporal modulation will be accomplished by rotating the telescope, consisting in this case of 48 grid pairs representing the two spatial frequencies, about its line of sight axis. Each spatial frequency will be represented by 12 cosine and 12 sine grid pairs with a relative orientation between each of 15 degrees. This design will allow a relatively large number of Fourier components to be measured per grid pair and allow the use of a single detector rather than a spatially discriminating detector behind each. Furthermore, *snapshot* images of very bright sources may be obtained.

Since the RMC must integrate over the time of rotation of the telescope, rotating the telescope faster may improve the temporal resolution. On the other hand, this will decrease the number of effective counts or photons reaching the detector for a given Fourier component. For solar flare processes which evolve over time scales of several minutes, this does not present a problem; however, most impulsive flare processes evolve over time scales of seconds. Also, for some basic RMC designs, the observer must have a priori knowledge of the rough location of the source in order to remove all ambiguities from the final image. Image information may also be lost as the source moves into the near vicinity of rotational axis of the telescope. All of these concerns raise the question as to how well flares may be resolved at the edge of the RMC performance envelope.

The importance of numerical modeling for exploring the validity of low photon count images as well as an optimization tool is evident.

An alternative method which avoids the temporal resolution problem experienced with the rotating collimator is to use spatial collimation. If a grid geometry is selected so that the bottom grid slits are a little narrower than those in the top grid, a grid pair can be designed to distribute the incoming beam in one period of a triangular response across the detector area. This spatial triangular response is equivalent to the temporal triangular response produced by the rotating collimator. Thus, a simple imaging collimator with one grid pair with a **position-sensitive** detector may measure one Fourier component of the source angular distribution. Unfortunately, this Moire pattern now requires a spatially sensitive detector array to measure intensity across the pattern. Thus, the trade-off in going this way is more inherent engineering complexity as compared to the RMC.

Chapters V and VI will discuss the spatial modulation collimator and the rotating modulation collimator in greater detail and Chapter VII will discuss a comparison between images of synthetic flares constructed using Models N-T and T.

## V. THE SPATIAL MODULATION COLLIMATOR

### A. INTRODUCTION

In Chapters II and III, significant differences in emission profiles as a function of time, energy, and loop position were found to exist between Model T and Model N-T. This chapter will describe the construction of a spatial modulation collimator which will later be used to view these profiles to determine if the differences can be imaged. Chapter VII will discuss the differences between the images in greater detail. In addition, some basic Fourier telescope degradations and limitations will be discussed in this chapter and in Chapter VI.

A basic telescope design using 48 grids, but only two spatial frequencies, was employed for this design. Design parameters were chosen to be representative of instruments being flown at the current time and proposed to be flown in the near term. The Fortran code used to simulate the telescope may be found in Appendix C. Figure 5.1 illustrates the  $(u, v)$  plane coverage for the telescope. Note the limited coverage afforded by this design; yet, as we will see later in Chapter VII, the telescope shall perform reasonably well against the physical profiles from Chapters II and III.

This particular telescope uses a grid geometry in which the bottom grid slits are a little narrower than those in the top grid such that the incoming beam is distributed in one period of a triangular response across the detector area. If the grids are copied onto acetate and then superimposed, one obtains a single period Moire fringe pattern equivalent to the detector pattern produced by a single point source. Moving the grids apart in a direction perpendicular to the slits is equivalent to moving a point source away from the telescope line of sight. Figure 5.2 and Figure 5.3 illustrate the principle. By moving Figure 5.2 over Figure 5.3, one can generate Moire fringe patterns similar to those which would

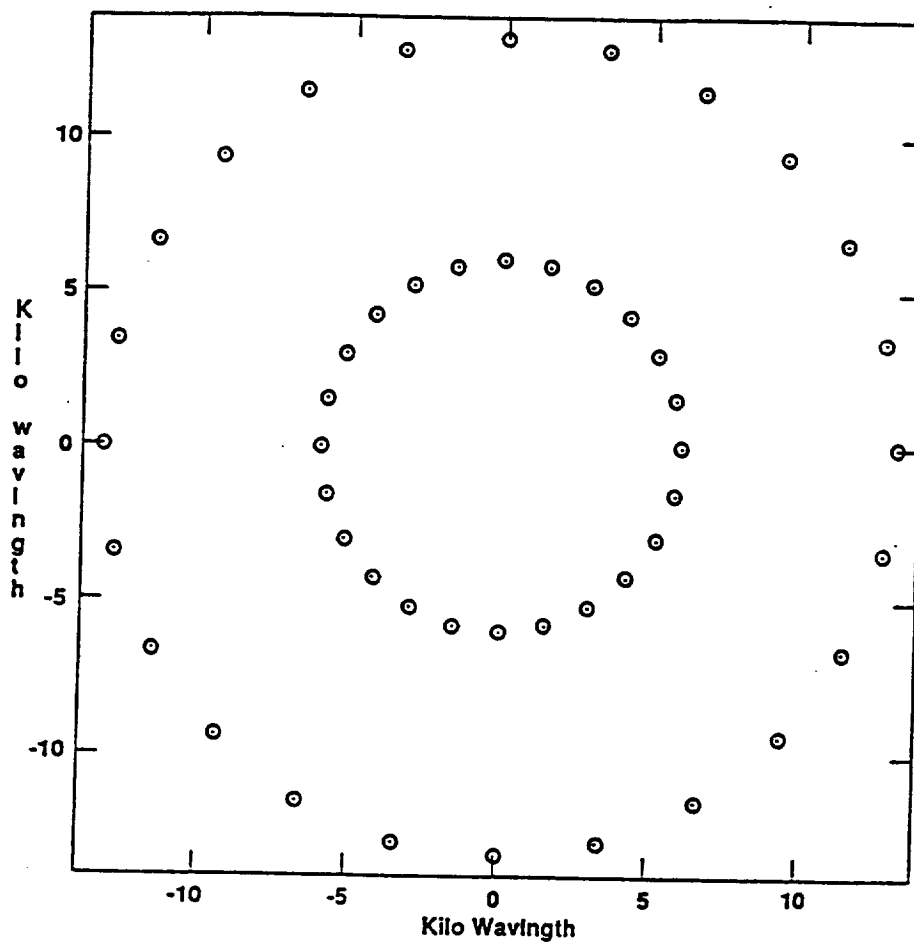


**Figure 5.1: SMC Fourier Plane Coverage**

The apparent limited coverage of the  $(u, v)$  plane is illustrated here. This gives rise to noise internal to the processing which manifests itself as artifacts in the final image. Fortunately, techniques such as the maximum entropy method can be used to reduce this noise.

be seen by an x-ray detector.

Since we are measuring broad fringes, only one-dimensional, low resolution detectors are necessary. Figure 5.4 shows the effect of a point source located 20 arc seconds from the telescope pointing axis.

Each photon as it strikes the detector along the local  $x$  axis may be viewed as a phasor in the complex visibility plane with amplitude one and a phase angle given by its  $x$  position. Since  $x$  varies from 0 to  $2\pi$ , the phase may be read directly from the data for that particular photon. A resultant may then be calculated and the real and imaginary parts of the Fourier component may then be found from

$$Re = \sum_{i=1}^n \cos\theta_i \quad (5.1)$$

and

$$Im = \sum_{i=1}^n \sin\theta_i \quad (5.2)$$

where  $n$  is the number of photons reaching the detector. The associated  $(u, v)$  coordinates may then be found as described earlier in Chapter IV.

The generation of this Moire pattern now requires a one-dimensional, spatially sensitive detector array measuring intensity across the pattern. Palmer and Prince (1987) determined that the pixel size of the detectors need only to be of modest size. This is because we are taking advantage of the fringes produced by the interference of the grid pair with the incoming wavefront. As found elsewhere in optics and radio astronomy, these fringes are extremely sensitive to the location of the source. A point source at any angle will produce a peak counting rate somewhere on the detector; the location and height of this peak corresponds to the phase,  $\Phi$ , and the amplitude,  $A$ . Thus, one grid pair with





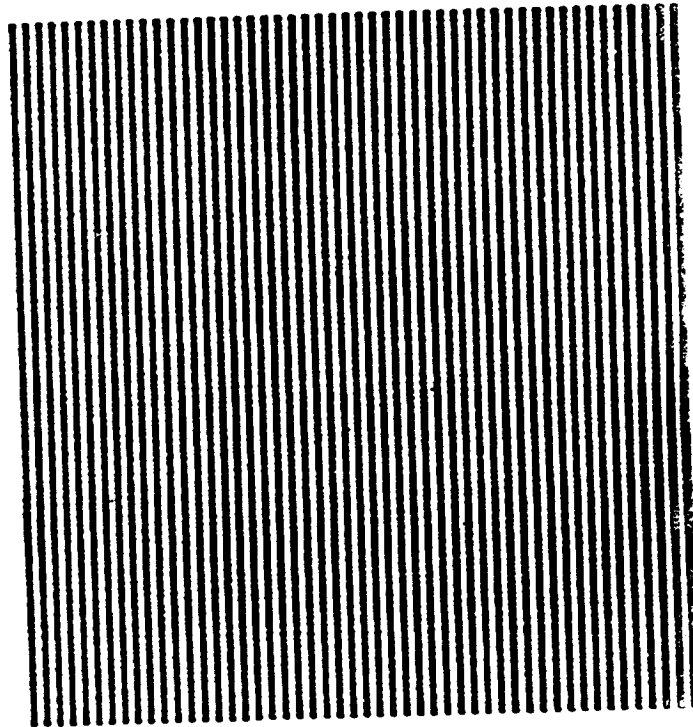


**Figure 5.3: SMC Lower Grid**

This grid contains  $(n + 1)$  slits and slats which in conjunction with the  $(n)$  top grid produces a 1 cycle beat pattern on the detector (Crannell, 1988).

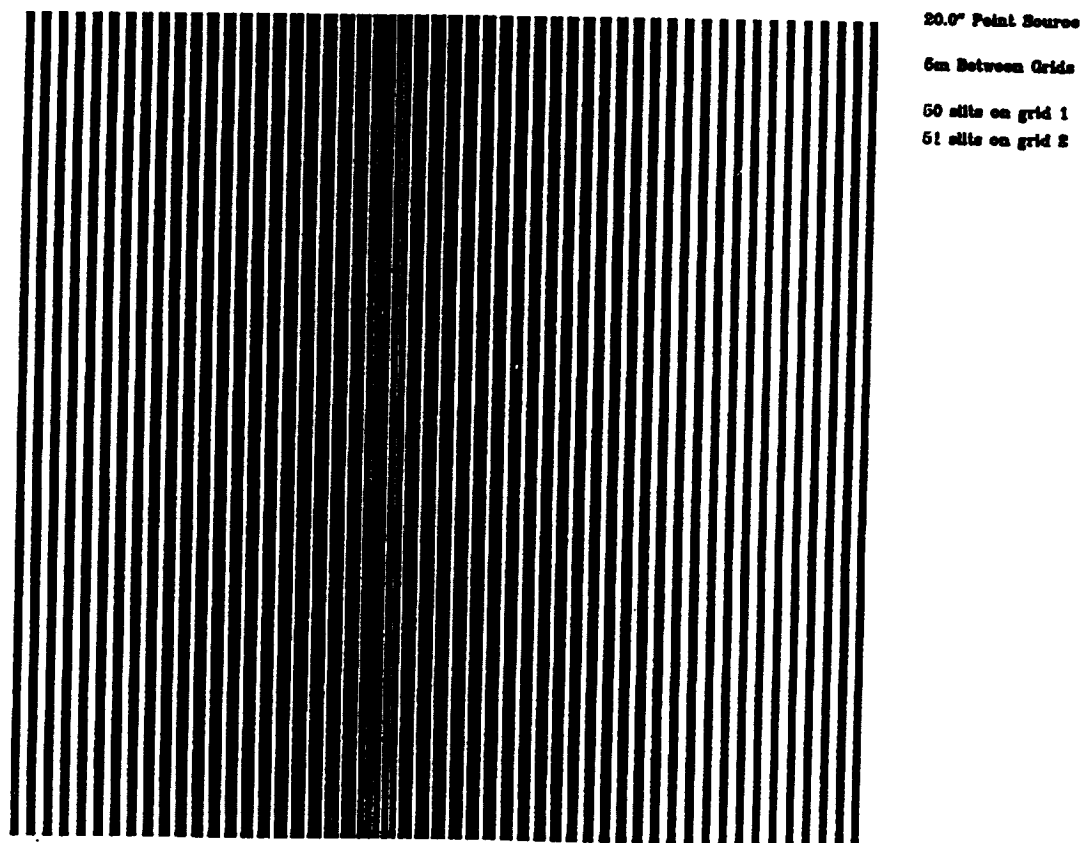


**Figure 5.4: SMC Moire Fringes For Point Source At 20"**

Note the fringe pattern is somewhat similar to a radio telescope response with a fine modulation pattern overlying a more coarse pattern. The coarse pattern contains the information about the source. The location of the peak of the pattern from the center of the grid and the amplitude of the pattern are sufficient to provide both the real and imaginary components of the visibility function. The slit width, grid pair separation, and grid orientation provide the  $(u, v)$  coordinates for these components.

a position-sensitive detector can measure one Fourier component of the source brightness distribution (Campbell et al., 1991b).

The combination of data from many such subcollimators, each with its position-sensitive readout, permits the synthesis of an image (Crannell, 1988). Different slit orientations and spacings generate the different Fourier components needed. In essence the Fourier-component measurement consists of a three-parameter fit  $(A, \Phi, n)$  to each subcollimator output, where  $n$  is the mean count level.

The geometry used for our SMC includes two slit widths of 0.0275 and 0.0125 cm with a 500 cm separation between grids. This allows the measurement of two spatial frequencies over a set of equally spaced orientations in the  $(u, v)$  plane. Using this telescope geometry, an end-to-end Monte Carlo model (Appendix C) was developed using the spatial modulation collimator approach to investigate telescope performance under various flux conditions. Individual detector size was selected to be 100 cm<sup>2</sup> for a total sensitive area of 4800 cm<sup>2</sup>. Table 5.1 compares our SMC to the Solar-A (YOHKOH) and HESP instruments.

## B. THEORY

In principle a single high intensity burst of photons from an extended source will provide exactly the same image as the same source emitting a single photon sequentially from random points within the source provided the population of photons in both cases is large enough for imaging. This principle is the key to allowing one to simulate optical systems numerically. Of course, in practice, one is limited by the performance characteristics of real detectors (e.g., detector saturation). However, as discussed in Chapter IV for the energy range 10-100 keV, we may be confident that our results are representative of the best case performance for the telescope.

	SMC	YOHKOH	HESP
grid material	tungsten	tungsten	tungsten
grid pairs	48	64	12
grid thickness	.3 cm	.5 mm	.3 - 4 cm
pairs/Fourier comp.	1	2	1 or 2
image ambiguity	no	no	yes (w/ 1 pair)
centerline image cap.	yes	yes	no (w/ 1 pair)
rotation required	no	no	yes
time resolution	1 s	1 s	TBD
grid separation	5 m	1.4 m	5 m
spatial frequencies	2	6	12
spatial resolution	4 arcsec	5 arcsec	2 arcsec
finest slit width	.0125 cm	.0060 cm	.0050 cm
detector material	NaI	NaI	Germanium
detector area/pair	100 cm <sup>2</sup>	4 cm <sup>2</sup>	TBD
det. elements/pair	8	1	1
total sensitive area	4800 cm <sup>2</sup>	256 cm <sup>2</sup>	TBD
energy range	10-100 keV	15-100 keV	10 keV -20 MeV
field of view	full sun	full sun	full sun

Table 5.1: Our SMC Compared To YOHKOH And HESP

Recalling that at large distances photon trajectories from the same point are essentially parallel, a photon may fall anywhere randomly on the surface of the telescope. Thus, each photon arriving at the face of the telescope has associated with it two angles representing the source location in the sky. Each photon arrived at a randomly selected grid (48 total) in the top grid plane with a randomly selected subset of angles (relating it back to the set of angles describing the extended source) at a randomly selected local  $(x, y)$  coordinate on the grid. The model was then tested to see if the photon survived passage through the first grid, calculated its  $(x, y)$  position on the second one, and tested to see if it survived passage through the second grid. This produced a detector response which can be reduced to Fourier components and converted to an image as described previously (Figure 5.6).

### C. RESULTS

Figure 5.6 illustrates the solar flare input model and gives a close-up view of the synthetic flare configuration chosen for simulation. The flare is made up of 21 pixels of equal size. An odd number was chosen so as to provide a point at the apex of the loop and one at the footpoints.

Figure 5.7 illustrates the *dirty* image of a full flare created from the synthetic flare by allowing each of the 21 pixels to have an equal probability of producing a photon. Figure 5.8 shows a cleaned version of the flare. Due to the fact that only two spatial frequencies were being measured, the telescope seemed to have greater difficulty with the extended, more complicated, image than it did with the simpler two footpoint test image. As one can see the spatial resolution of the instrument is about 4 arc seconds, consistent with the selected spatial frequency. Approximately  $10^4$  photons per 4 by 4 arc second telescope resolution cell are required by the telescope to form a meaningful extended image (at the Earth).

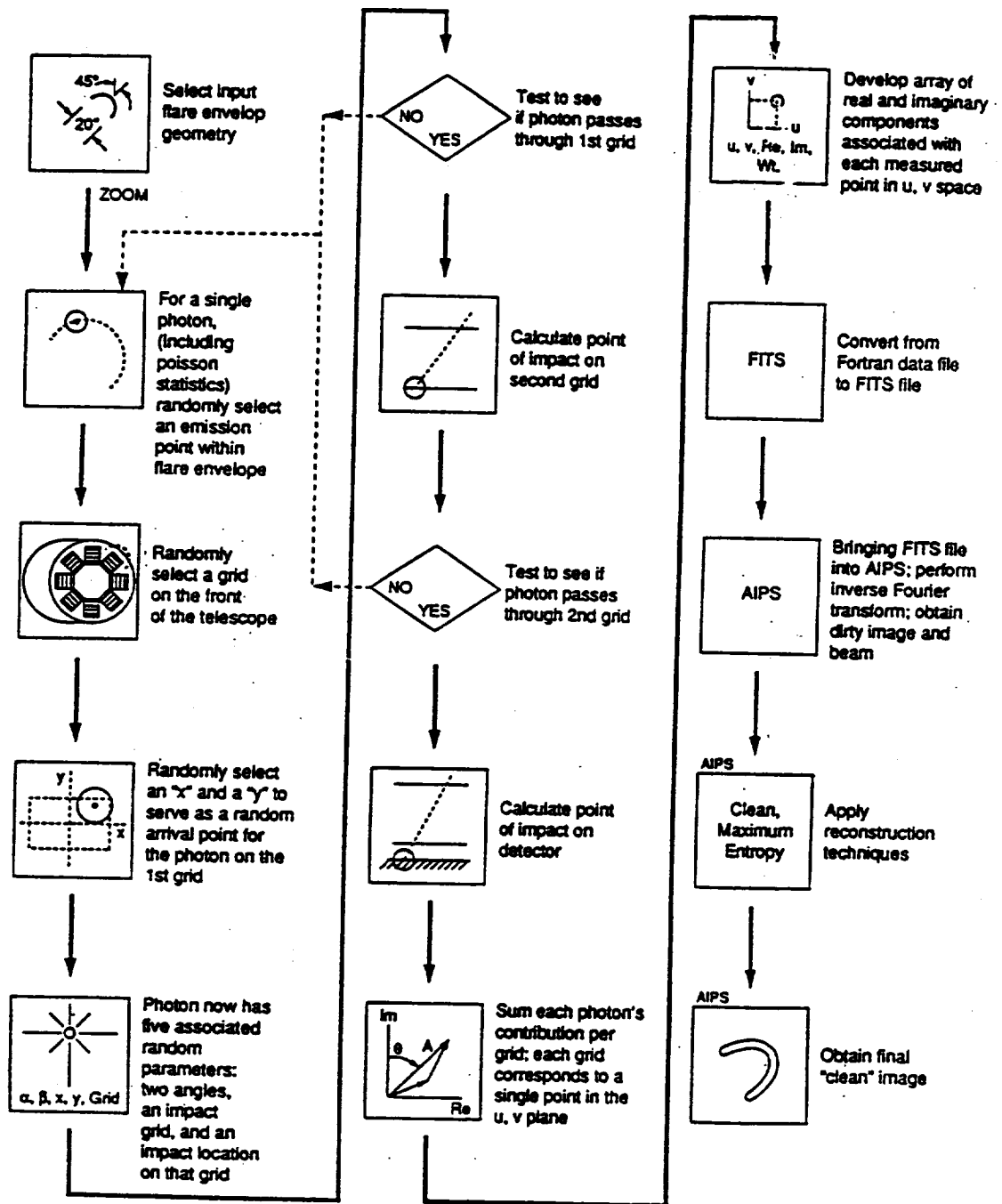
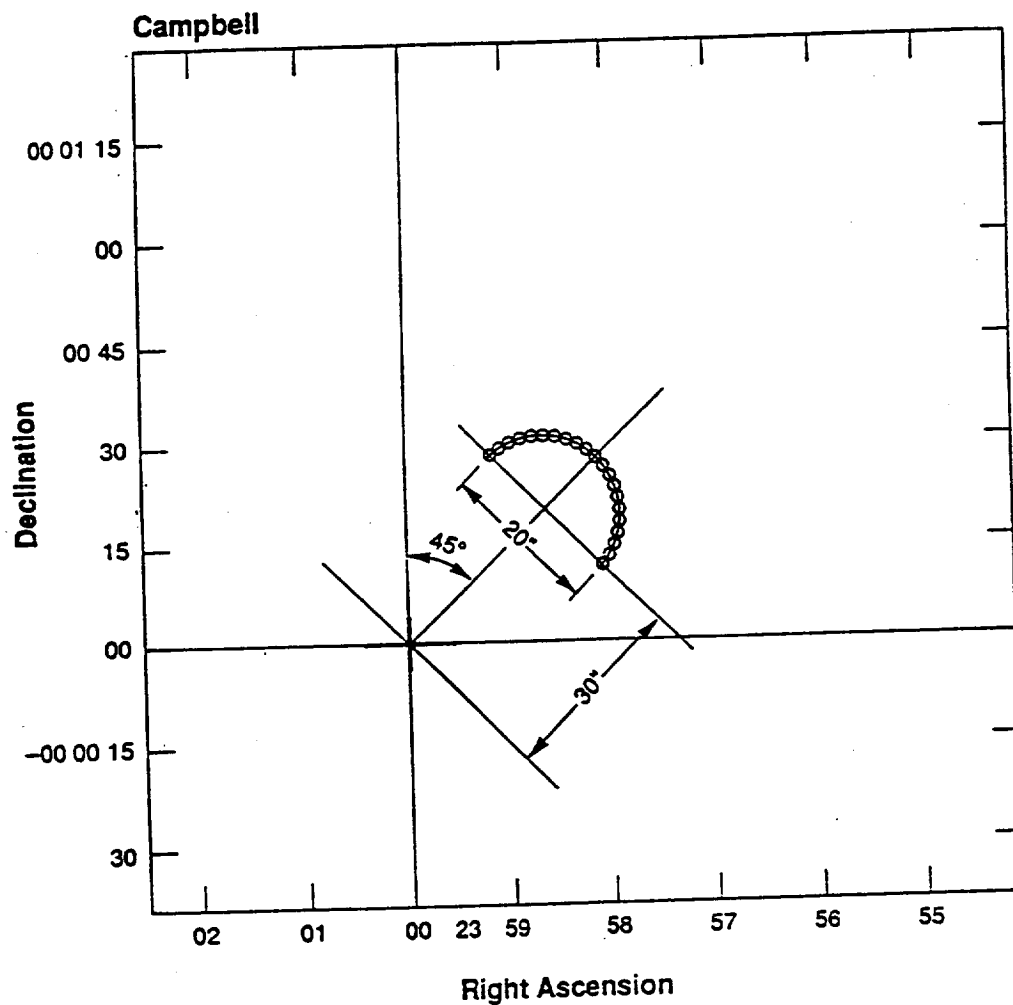


Figure 5.5: SMC Numerical Model



**Figure 5.6: SMC And RMC Flare Model**

This model consists of 21 pixels equally spaced to form a half circle. (An odd number was chosen so as to provide a pixel at the top of the loop and one at the footpoint.) If most or all of the pixels have an equal probability of emitting a photon the telescope with 4 arc second resolution will *see* the loop as an extended source.

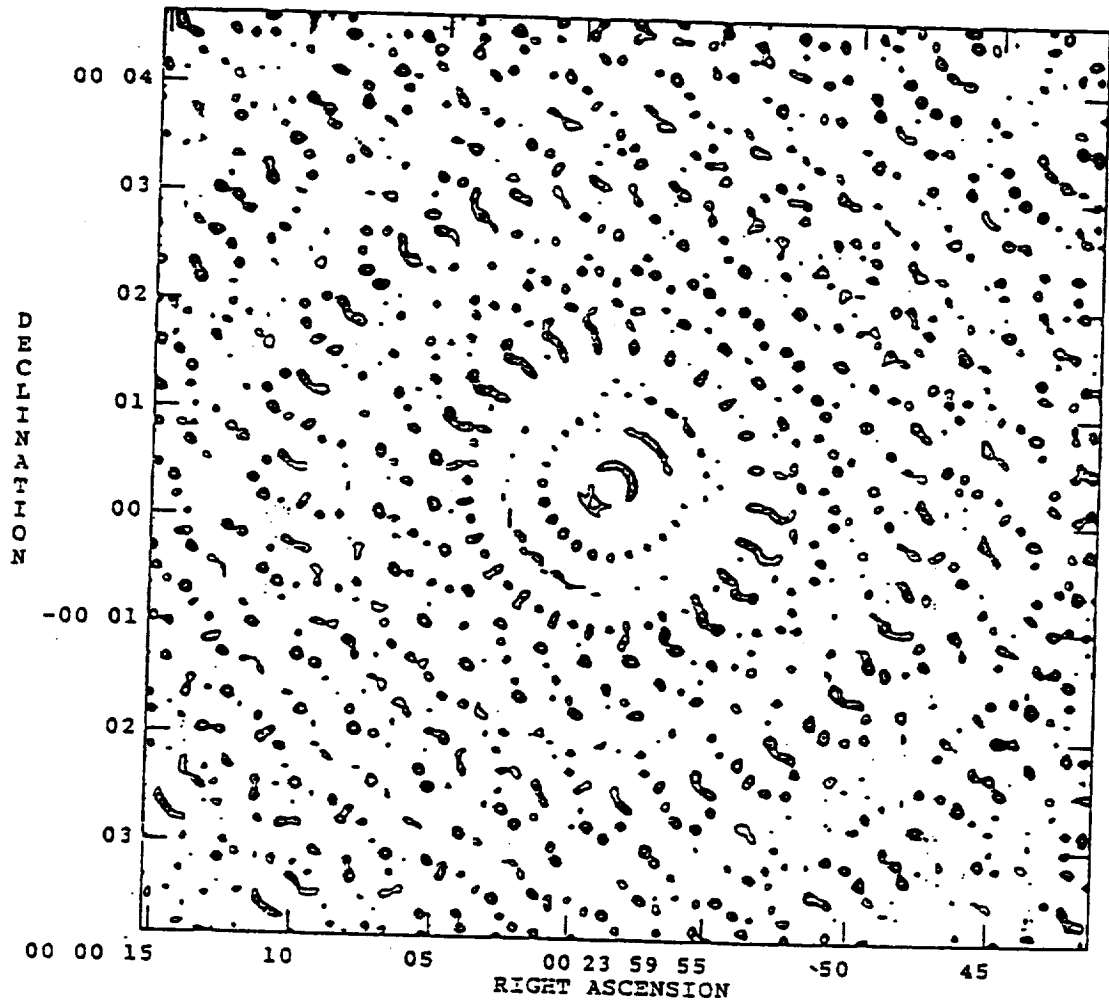
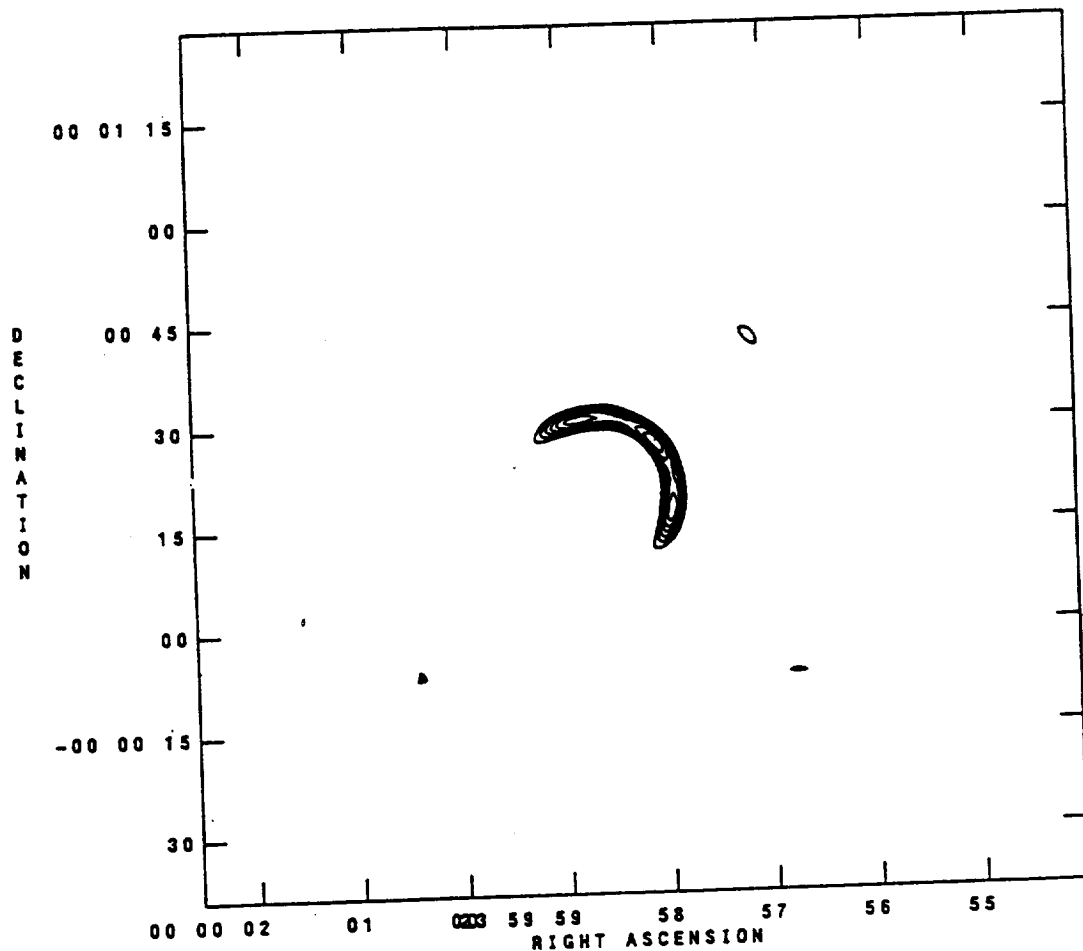


Figure 5.7: SMC Dirty Image Of Loop

The y-axis is in arc minutes and the x-axis is in hours, minute, seconds from Sun center. In this dirty image, there was an equal probability that all parts of the loop would emit a photon. An observer seeing this image for the first time would note the symmetrical pattern and suspect that cleaning would reveal a significant image at the center of the pattern.





**Figure 5.8: SMC Clean Image Of Loop**

This shows the effects of the cleaning and zooming features in AIPS to better display the resultant image. This is the final output of our basic spatial modulation collimator and indicates the promising potential of this instrument for viewing complicated shapes. The y-axis is in arc seconds and the x-axis is in hours, minutes and seconds from Sun center. The imaging threshold for extended sources such as these was found to be  $\cong 10^4$  photons per 4 by 4 arc second telescope resolution cell (at the Earth).

These instruments have an associated point spread function similar to that for any optical telescope (or a *beam* in radio astronomy). Even for the basic telescope configuration selected, the point spread function exhibits the sharp central peak necessary for high resolution imaging (Figure 5.9 ).

Next choosing a two footpoint object for use as a standard test configuration, the footpoints were displaced from Sun center in ever increasing increments until the test image was seriously degraded. In the example shown in Figure 5.10, the footpoints show little change at 15 arc minutes as compared to those at 30 arc seconds. Beyond 17 arc minutes the image began to seriously degrade; however, 17 arc minutes (34 arcminute diameter) should be sufficient to provide full Sun coverage.

During the development of the SMC, one systems-related question frequently arises when applying the conceptual technology to real structures and pointing systems. One of the most pressing issues has been the subject of *twist* defined as the rotation of one grid with respect to the other due to elastic deformation of the structure supporting, separating, and serving to keep the grids aligned. Private conversations with the designers of HEIDI have indicated that they expect to control twist to the sub arc second level.

Twist was found to become increasingly significant above 2 arc minutes (Figure 5.11). For twist less than this, the images were stable. Current applications are expected to limit twist to a several arc seconds.

Fourier telescopes are also limited in dynamic range. In other words, the telescope takes the the brightest source in the field of view as a reference baseline and images only those other sources within approximately a factor of 10. If a source is weaker than a factor of 10 from the brightest source, then it will most likely be lost in the artifacts produced by the telescope. Figure 5.12 illustrates

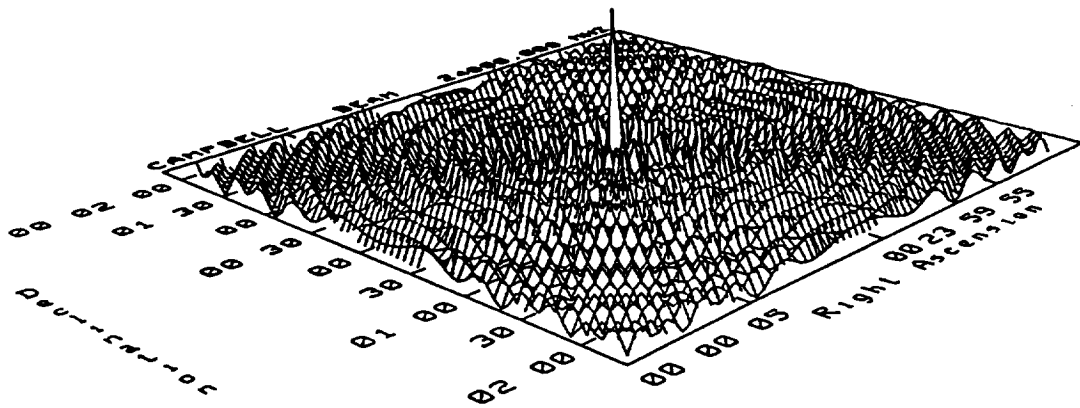


**Figure 5.9: SMC Point Spread Function (Beam)**

This basically shows how the telescope would image a single point source. Clearly, having a bright central peak which stands out above the noise is crucial to successful imaging. In radio astronomy terminology, this would be described as a *beam*.

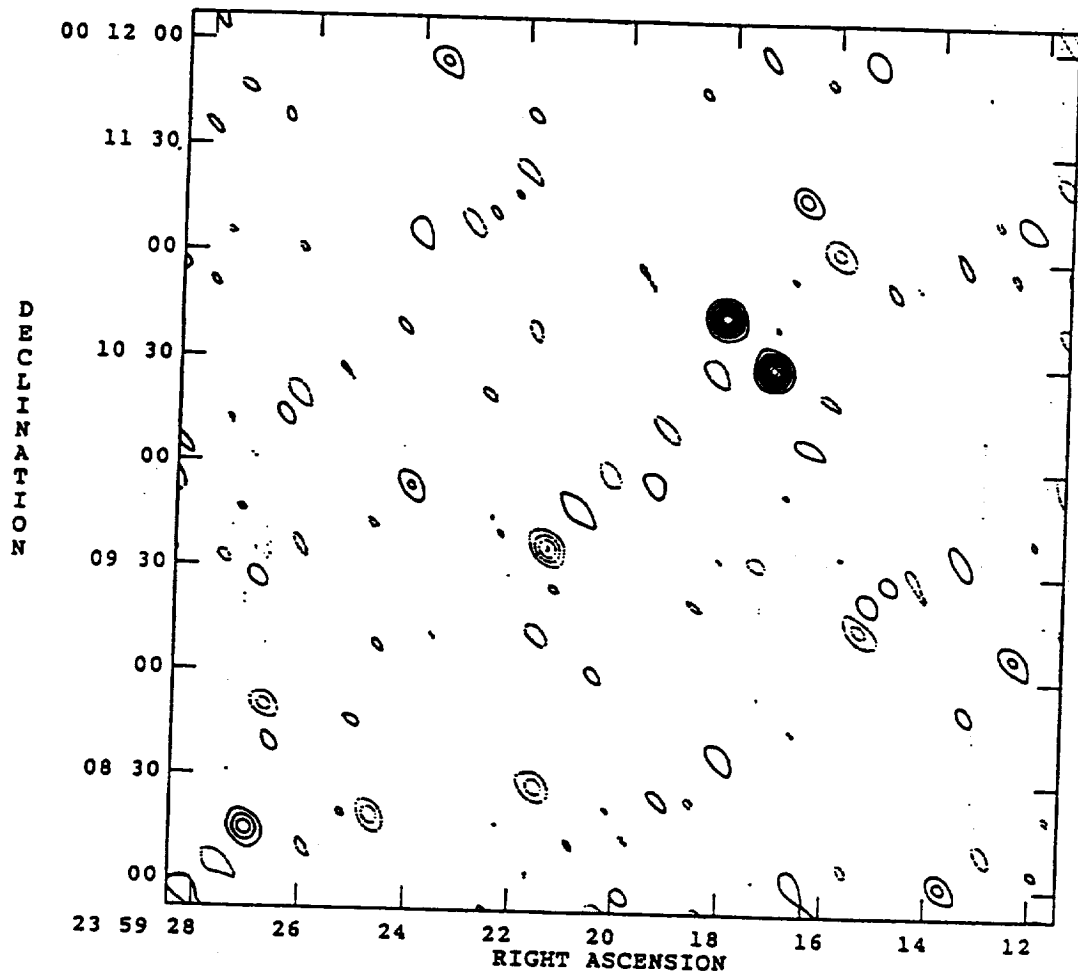


**Figure 5.10: SMC Full Sun Field Of View Demonstrated**

This shows two footpoints near the limb of the Sun and verifies that the spatial modulation collimator can accomplish full Sun field of view imaging for the geometry used. It also illustrates the point that the effective field of view of the telescope is much less than the geometrical field of view. The y-axis is in arc minutes and the x-axis is in hour, minutes, and seconds from Sun center.

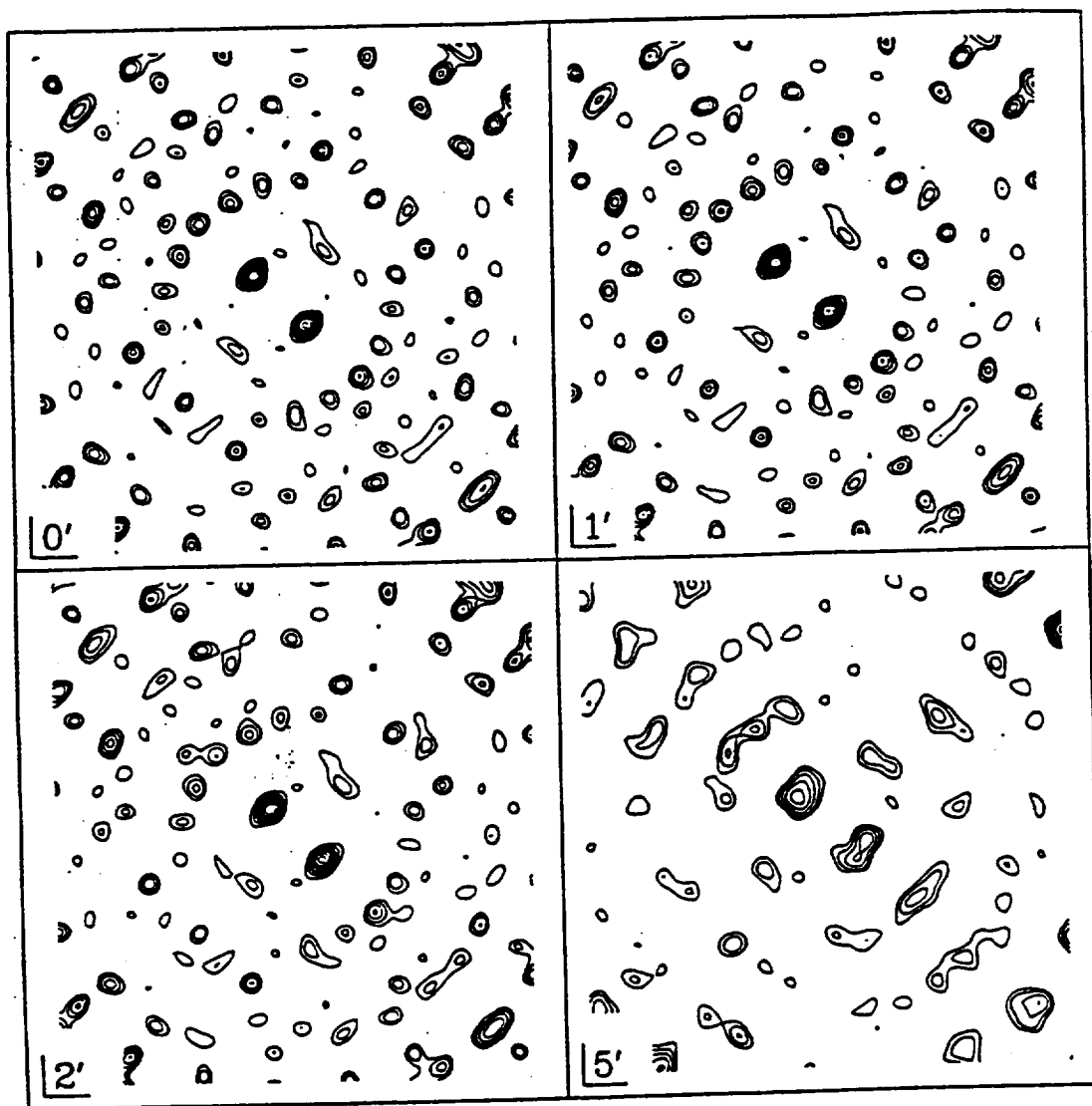


**Figure 5.11: SMC Twist**

This shows the spatial modulation collimator operating with twist between the two grids. The four dirty images show that little degradation occurs below 2 arc minutes. Current designs expect to hold twist to a few arc seconds.

this aspect with a two footpoint minimum flux input model. The brightest footpoint's probability of emitting a photon is 10 times that of the weakest.

#### D. SUMMARY AND CONCLUSIONS

This chapter has described the construction and verification of a simulated Fourier telescope for viewing the Sun. No rotation is required for this instrument; hence, we call it a spatial modulation collimator. A very basic telescope was constructed measuring only two spatial frequencies, yet it did surprisingly well. Test highlights are discussed below.

The emission profiles from Chapters II and III were also viewed by the telescope to determine in general if Fourier telescopes could resolve the differences in the two sufficiently. **Indeed, the profiles when viewed by the spatial modulation collimator did result in significantly different images.** This will be discussed further in Chapter VII.

One of the answers that the numerical model provides is the number of random photons from a synthesized object required to make an image. The telescope simply counts photons (i.e., builds Fourier components statistically) to create an image. It leaves to the observer the task of managing bin sizes and energies. Once the telescope imaging threshold requirement is known, one can compare the threshold to real observations. Generally, for the SMC,  $\cong 10^4$  photons per 4 arc second by 4 arc second telescope resolution cell were sufficient to adequately image Model T and Model N-T signatures, respectively. Imaging above this threshold guaranteed that image location, shape, and orientation were reproduced correctly constrained only by the spatial resolution capability of the telescope. As the photon level was decreased, shape degraded first, followed by orientation, and then finally position. Generally, the threshold marked the beginning of a gradual deterioration rather than a sharp break.

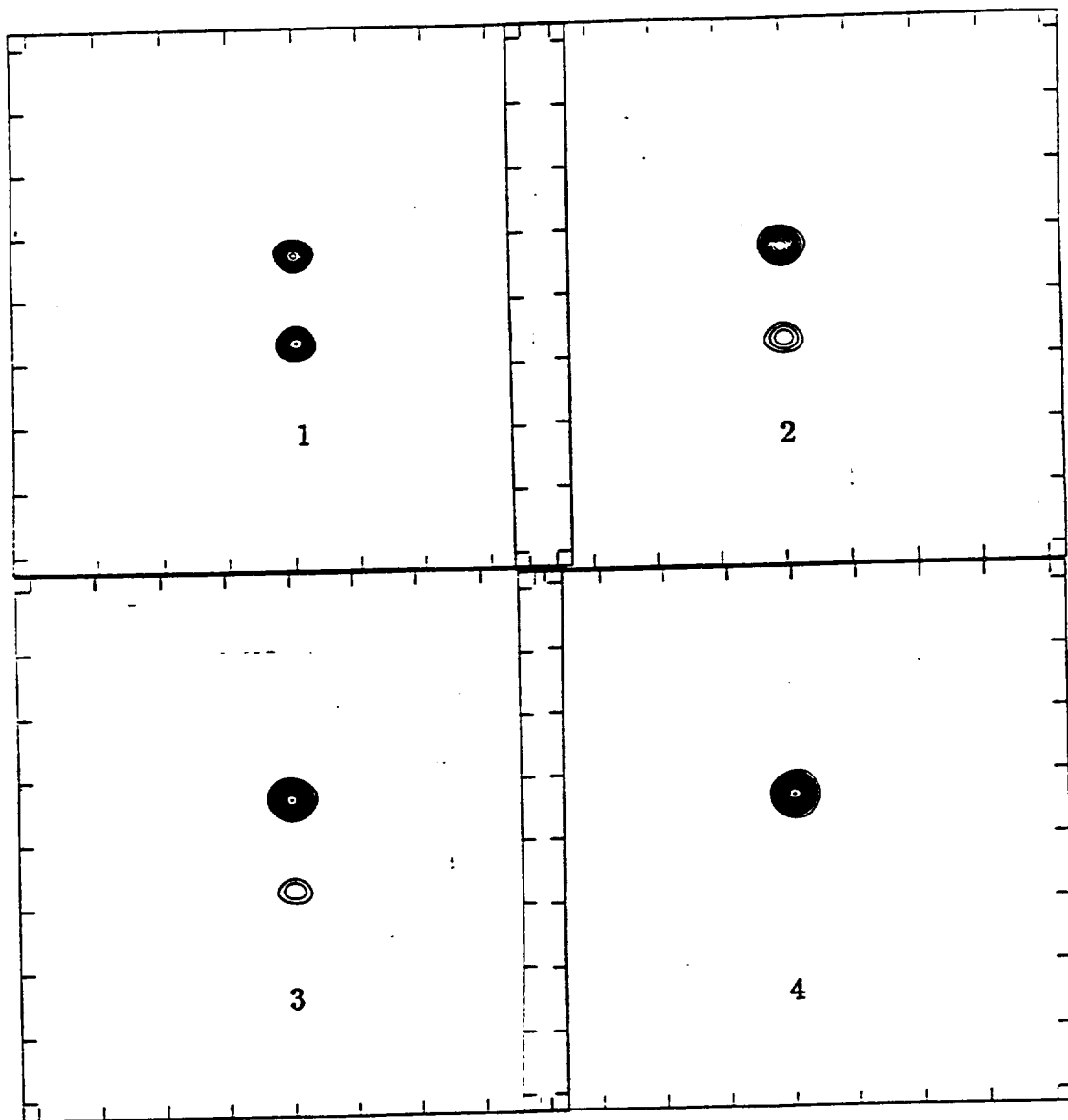


**Figure 5.12: Dynamic Range Illustrated**

Only two footpoints are emitting in this test. In the first three images, the probability of the upper footpoint emitting a photon was 1, 5, and 10 times greater than that of the lower point, respectively. In the fourth image, the probability of the upper point emitting a photon is 20 times greater than that of the lower point. Clearly, the Fourier telescope is limited in imaging contrasts greater than 10:1.

The field of view of the telescope was checked. In general, one would prefer to have full Sun coverage with the telescope to simplify pointing problems; however, this may be categorized as a highly desirable requirement rather than an absolute one. In the case of the spatial modulation collimator, full Sun coverage was achieved for the  $10 \times 10$  cm grid pairs with 5 meter separations; however, this *effective* field of view was only 25% the geometrical field of view as normally calculated for optical instruments.

The telescope was found to be very tolerant to random noise on the detector. This was to be expected since the information necessary for imaging is taken from the **relative** modulated signal rather than the total, absolute one. In other words, the information for imaging is found in the modulation which rides on top of the somewhat uniform random noise curve. Naturally, systematic noise will defeat this instrument as it will most others. The tolerance to noise is also necessary to the successful performance of the instrument in that one would expect a higher level of random noise to be present due to the large detector area required.

One note of caution is that the telescope generally will try to provide a solution even in the absence of sufficient flux. An observer attempting to image a flare in low flux conditions may get a low quality image that may be misleading. Care should be taken in drawing major conclusions from limited flux images.



## VI. THE ROTATION MODULATION COLLIMATOR

### A. INTRODUCTION

In the last chapter we constructed a simulation of a spatial modulation collimator to view the emission profiles from the Model N-T (Chapter II) and the Model T (Chapter III). In this chapter, we shall construct a simulation of a rotating modulation collimator simulation for viewing the same profiles (Appendix D). In addition, we shall discuss various telescope limitations and degradations.

Rotating the telescope allows the design of the SMC discussed in the previous chapter to be simplified. First, the grid pairs required now are  $(n, n)$  grids to modulate the incoming photons as opposed to the SMC  $(n, n + 1)$  scheme. Second, while we retained the 48 grid pairs ( $4800 \text{ cm}^2$ ), the slit spacings (0.0125 and 0.0275 cm), and the grid separation (5 m), the detector for each grid pair now only needs to be composed of a single element. By rotating this design at 10 rpm the  $(u, v)$  plane could be mapped every 0.25 seconds. Clearly, this approach results in a much simpler engineering design with the trade-off that rotation is now required. In other words, the resulting image will be integrated over the time required by the telescope to sequentially map the  $(u, v)$  plane.

### B. THEORY

Figure 6.1 illustrates a ray trace model for the RMC as well as its basic operation. The rays will penetrate all the way through both grids to the detector or they will be stopped by one of the grids. Moving the point source with respect to the grids will produce a regular sawtooth pattern as shown in Figure 2.

Now, if one rotates the grids, the detector response may be found by examining the vector  $\vec{A}$  which denotes a ray of light passing through a grid at an

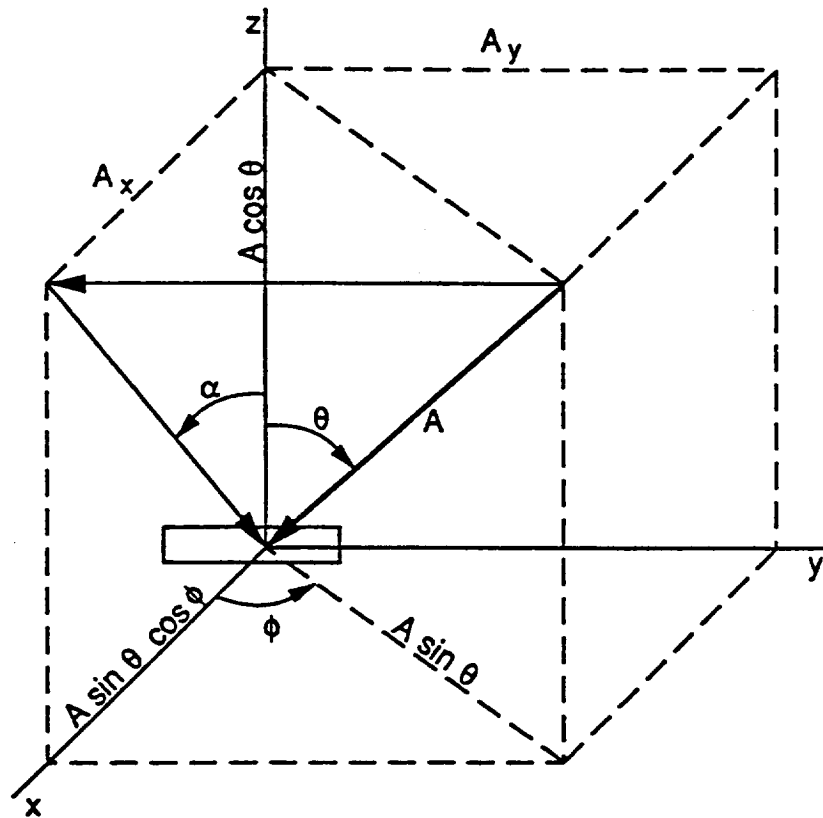


**Figure 6.1: RMC Ray Trace Model**

This illustrates the idea that a ray coming from any direction (rotating telescope) may be divided into a contributing component across the slits and a noncontributing one along the slits. The strength of the signal on the detector at angles  $(\theta, \phi)$  will correspond to the value of the regular sawtooth at the angle  $(\alpha)$ .

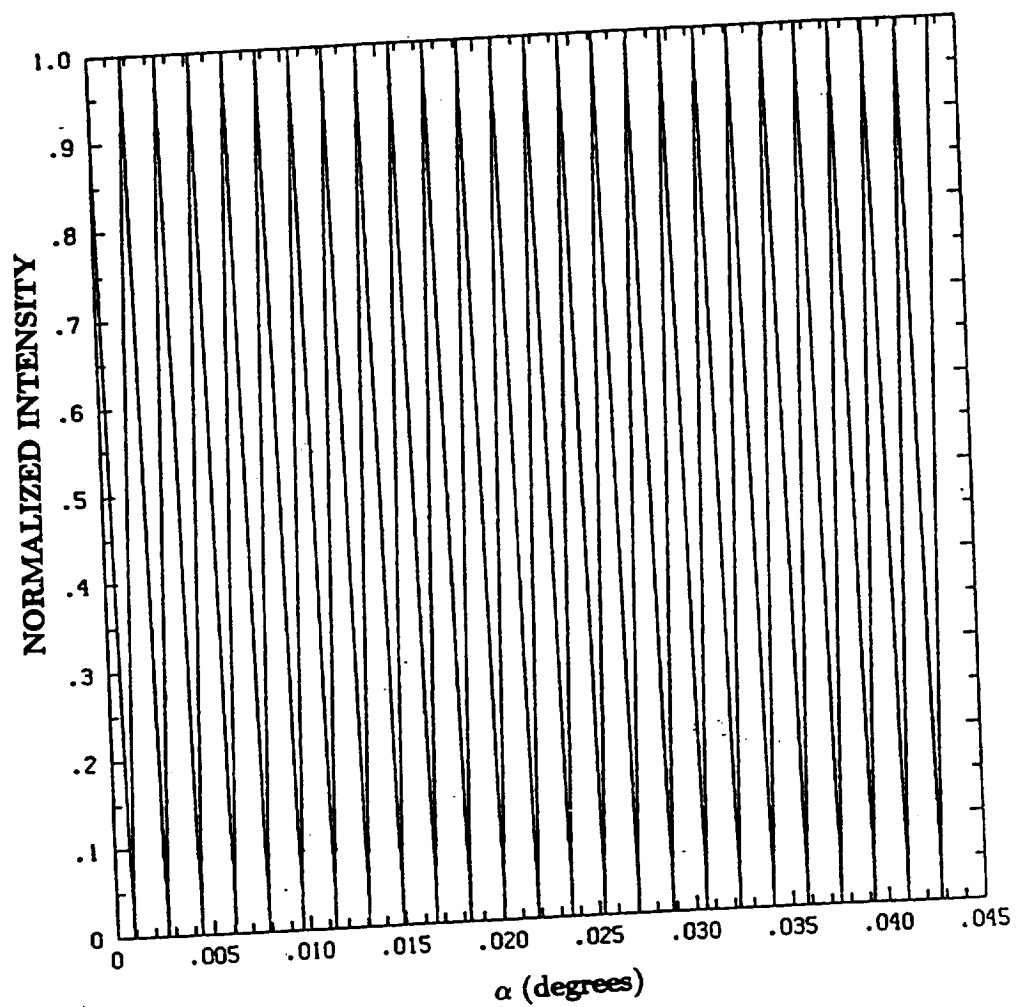


**Figure 6.2: RMC Sawtooth**

This is a regular sawtooth produced by typical grid geometries. Note the maxima and minima are separated by very small angles; hence, only a small movement of the source across the sky will produce a sawtooth pattern.

arbitrary angle.  $\vec{A}$  may be reduced to two components parallel and perpendicular to the slit direction. The amplitude of the component parallel to the slit does not contribute to the detector pattern while the value of the perpendicular component is taken from the regular sawtooth curve (Figure 6.2) corresponding to an offset angle  $\alpha$  from the pointing axis.

Given the angle of rotation of the telescope about its line of sight  $\phi$  and given the angle of the source  $\theta$  from the pointing axis, the angle  $\alpha$  may be calculated. From Figure 6.1, we may write the following expression,

$$\tan \alpha = \tan \theta \cos \phi \quad (6.1)$$

giving

$$\alpha = \tan^{-1}[\tan \theta \cos \phi]. \quad (6.2)$$

For small  $\theta$  this reduces to

$$\alpha = \theta \cos \phi. \quad (6.3).$$

From Figure 6.3, one observes that for a regular sawtooth the zeroes of the intensity are located at

$$(\alpha_{min})_n = \tan^{-1} \left[ \frac{(2n+1)s}{d} \right] \quad (6.4)$$

for

$$n = 0, 1, 2, 3, \dots$$

where  $d$  is the distant between grid planes and  $s$  is the slit width. Similarly, the maxima are located at

$$(\alpha_{max})_n = \tan^{-1} \left( \frac{2ns}{d} \right) \quad (6.5)$$

for

$$n = 0, 1, 2, 3, \dots$$

Equating these two expressions with equation (6.1) gives the maxima and minima of the amplitudes for the corresponding rotational angle of the telescope,

$$(\phi_{max})_n = \cos^{-1} \left[ \frac{(2n)s}{d \tan \theta} \right] \quad (6.6)$$

$$(\phi_{min})_n = \cos^{-1} \left[ \frac{(2n+1)s}{d \tan \theta} \right] \quad (6.7)$$

where

$$n = 0, 1, 2, 3, \dots$$

These expressions allow the computation of the RMC ray trace detector response. Figure 6.4 illustrates the compressed sawtooth found from this ray trace model. These ray traces, while not used directly for imaging, provide useful information regarding the rotating collimator. For the ray trace variable sawtooth, as the point source angle from the pointing axis,  $\theta$ , increases, the sawtooth frequency will increase. For a specific  $\theta_i$ , as the angle,  $\phi$ , (Figure 6.1) is varied from 0 to  $2\pi$ , the location of the frequency minima of the curve in Figure 6.3 will also vary between 0 and  $2\pi$  in a corresponding manner. In addition, the sawtooth repeats itself for the second  $180^\circ$  of rotation.

At this point we leave the ray trace model and (similar to the SMC) use a more realistic random, photon counting model to obtain images. As will be

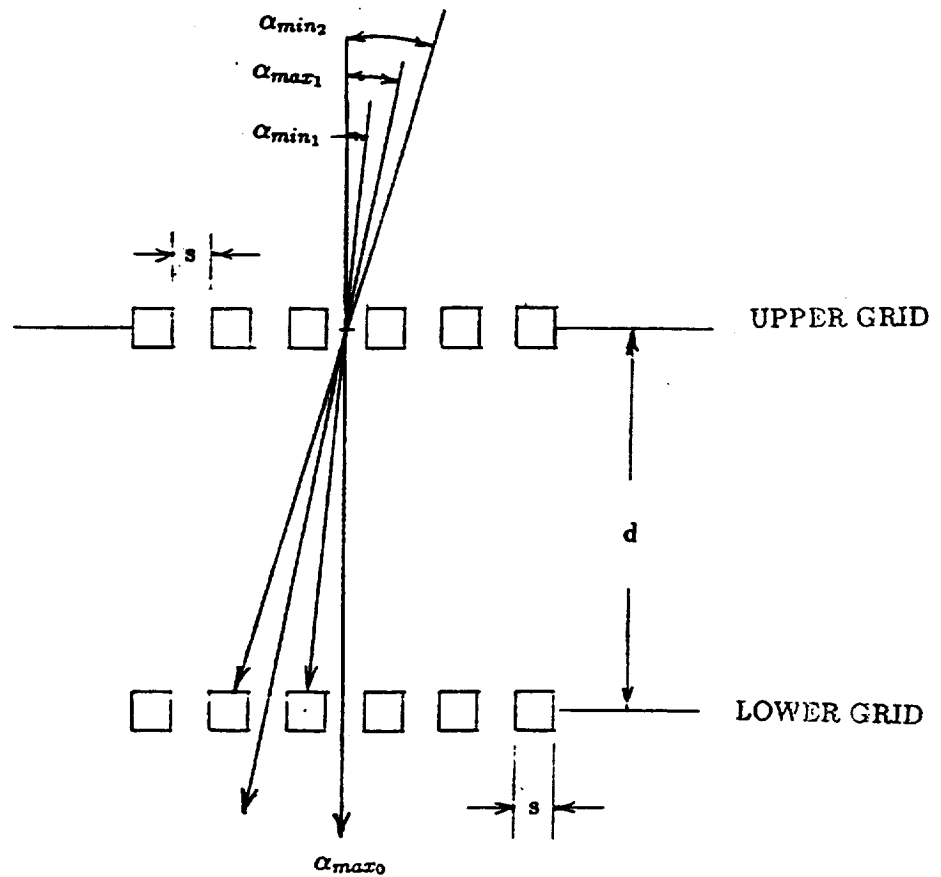


**Figure 6.3: Grid Pair Maxima and Minima**

For a given geometry, this illustrates that for a point source moved across the sky perpendicular to the slits of a grid pair, sets of associated angles exist corresponding to intensity maxima and minima. Note, changes in the slit width,  $s$ , and/or the grid separation,  $d$ , will cause significant changes in the repetitive pattern of maxima and minima seen by the detector.

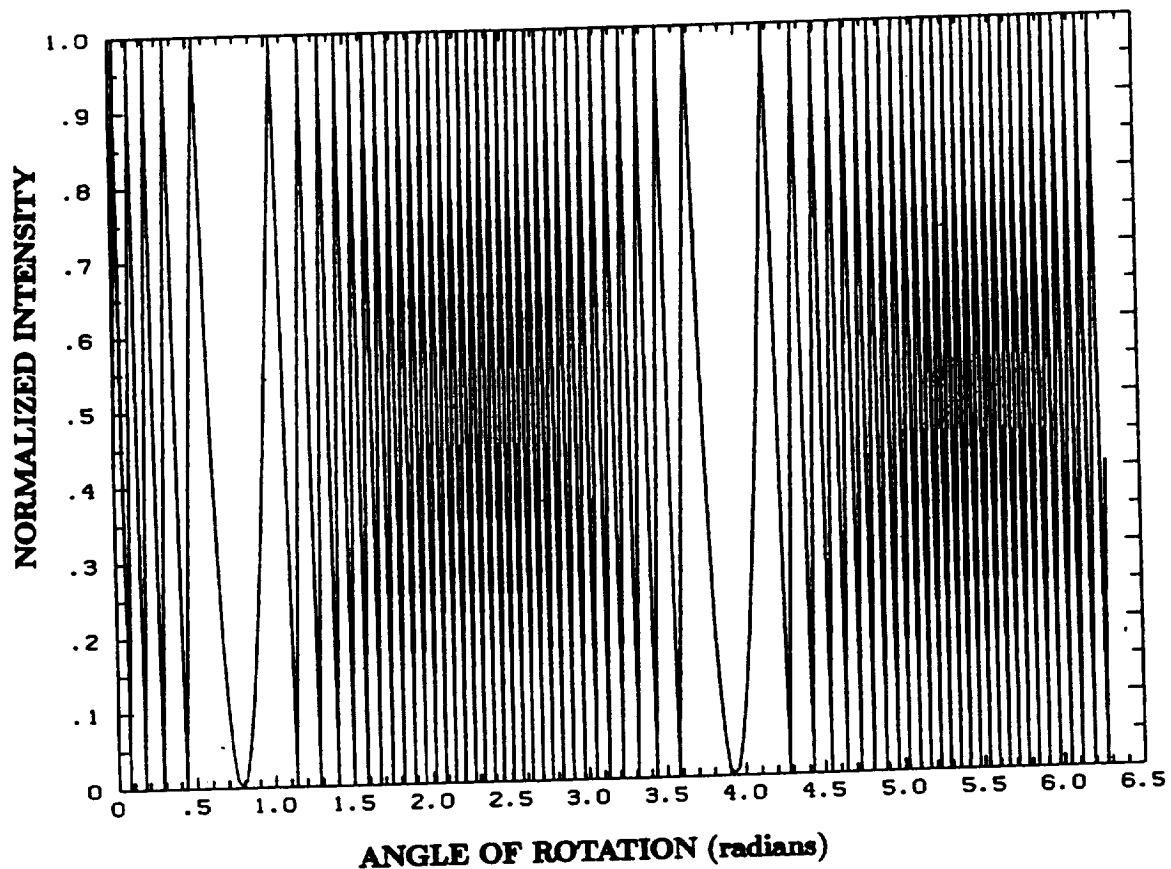


**Figure 6.4: RMC Ray Trace Compressed Sawtooth**

This variable sawtooth trace obtained from rotating the telescope through one full rotation while observing a point source located at an angle  $\theta$  off the line of sight axis rotated by a second angle  $\phi_0$  in a plane perpendicular to the line of sight axis. Although somewhat subtle, one can readily see that  $\phi_0$  is  $45^\circ$ . The angle  $\theta$  can only be determined by the level of compression of the sawteeth. As the point source is moved further away from the line of sight the compression of the sawteeth rapidly exceeds the line width of the printer giving a solid black square.

seen later, the ray trace model was valuable in the development of the RMC simulation code in verifying that the form of the detector response was correct. Figure 6.5 illustrates the numerical model used for the RMC and while it is similar to the SMC model, there are distinct differences. For example, the photon is now associated with a random rotation angle of the telescope, and two grid pairs are used to provide the real and imaginary components for one point in the  $(u, v)$  plane. Table 6.1 compares this RMC to Solar-A (YOHKOH) and to the proposed HESP instrument.

The detector output for our random, photon counting RMC model is illustrated in Figure 6.6 for both the real (cosine) and imaginary (sine) components of a single point source. Each spatial frequency is represented by two curves. Each curve represents essentially all Fourier components for that particular spatial frequency. These curves approximate sinusoids and thus, for a specific time of rotation, the real and imaginary values of the respective Fourier components can be read directly. In other words, these four curves contain all the information necessary to create an unambiguous image of the associated point source. In the same manner as the SMC, the RMC via AIPS first provides a *dirty image* which must be processed to obtain a *clean*, final image (Figure 6.7).

The telescope point spread function is illustrated in contour in Figure 6.8 and in a three-dimensional plot in Figure 6.9. The dominant central tendency indicates that the telescope will image well. The surrounding higher order maxima are a source of noise in the resultant image. AIPS provides software to allow these images to be deconvolved allowing the observer to remove this noise numerically.

## C. RESULTS

Figure 6.10 shows a clean image of a full 21 pixel loop. Note, the image



	RMC	YOHKOH	HESP
grid material	tungsten	tungsten	tungsten
grid pairs	48	64	12
grid thickness	.3 cm	.5 mm	.3 - 4 cm
pairs/Four. comp.	2	2	1 or 2
image ambiguity	no	no	TBD
centerline image cap.	yes	yes	TBD
rotation required	yes	no	yes
time resolution	1 s(10 rpm)	1 s	TBD
grid separation	5 m	1.4 m	5 m
spatial frequencies	2	6	12
spatial resolution	4 arcsec	5 arcsec	2 arcsec
finest slit width	.0125 cm	.0060 cm	.0050 cm
detector material	NaI	NaI	Germanium
detector area/pair	100 cm <sup>2</sup>	4 cm <sup>2</sup>	TBD
det. elements/pair	1	1	1
total sensitive area	4800 cm <sup>2</sup>	256 cm <sup>2</sup>	TBD
energy range	10-100 keV	15-100 keV	10 keV -20 MeV
field of view	full sun	full sun	full sun

Table 6.1: Our RMC Compared To YOHKOH And HESP

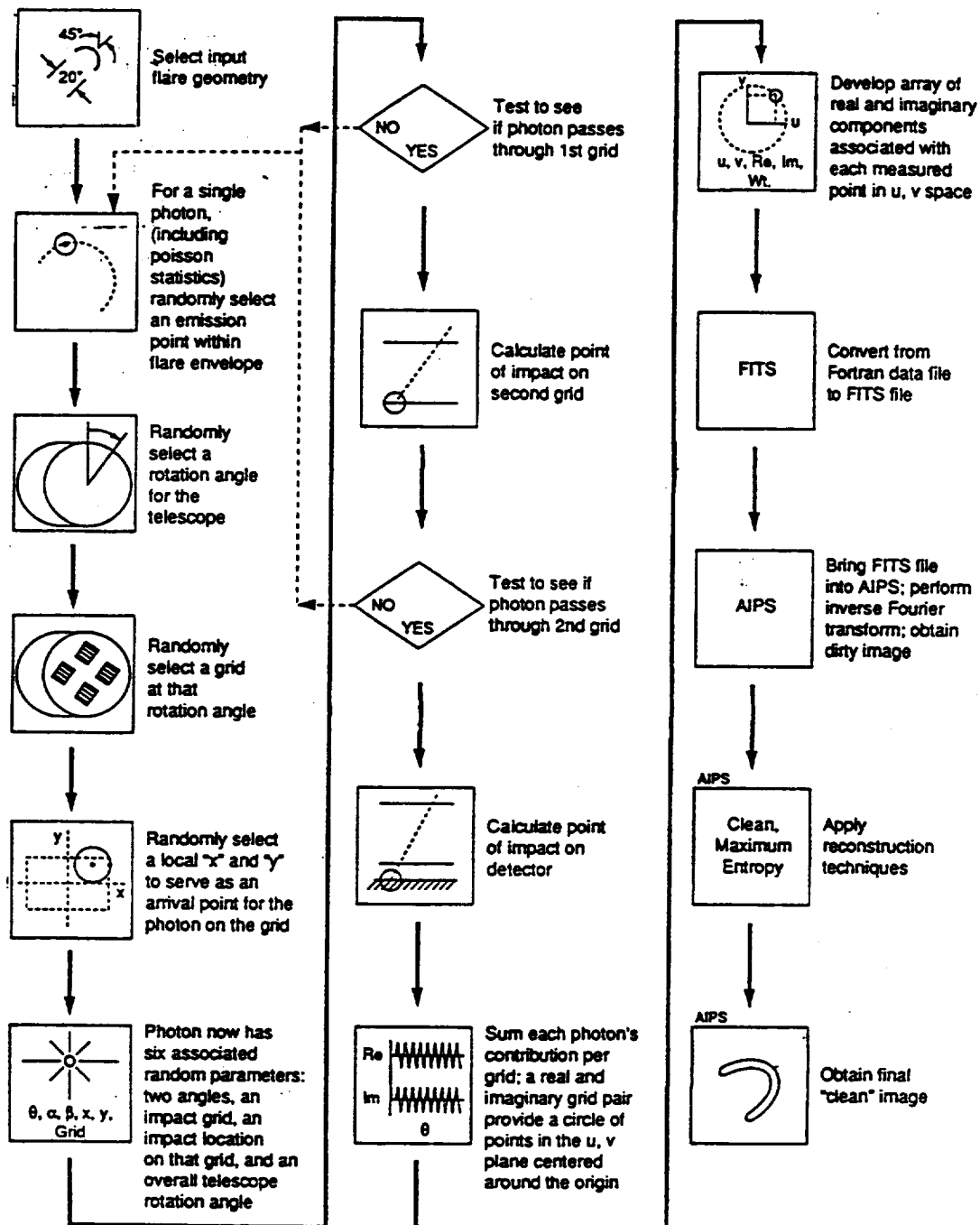
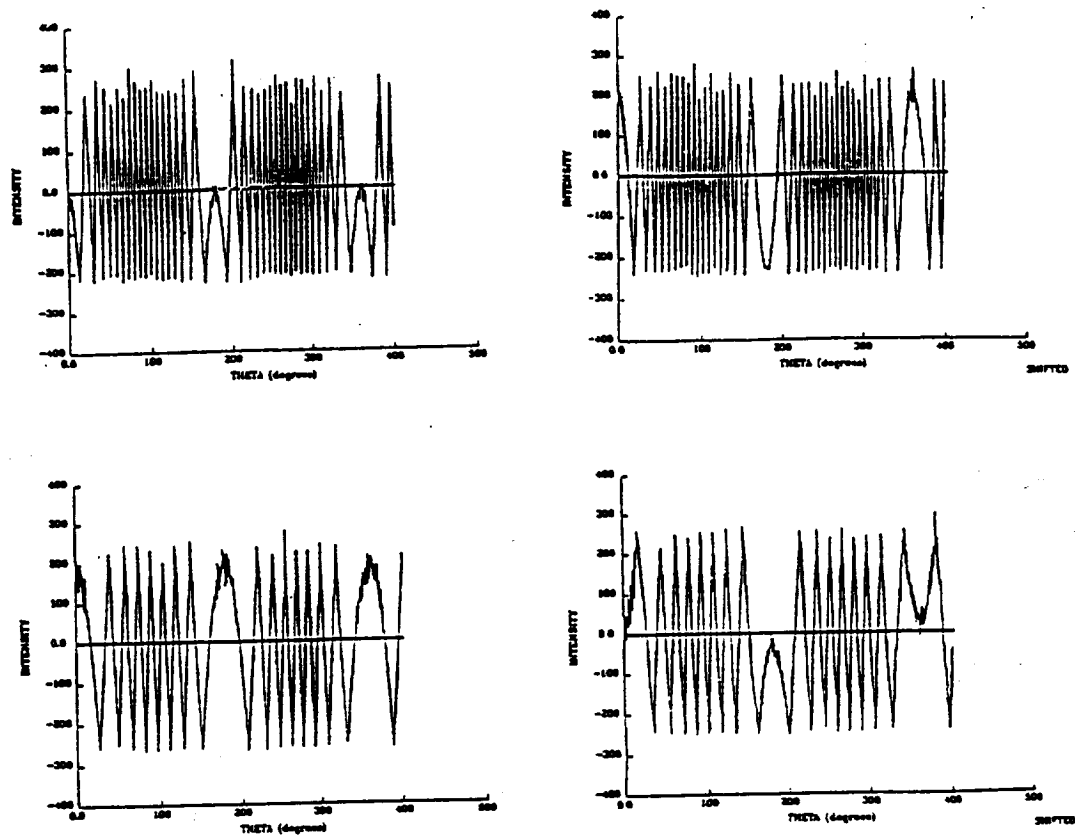
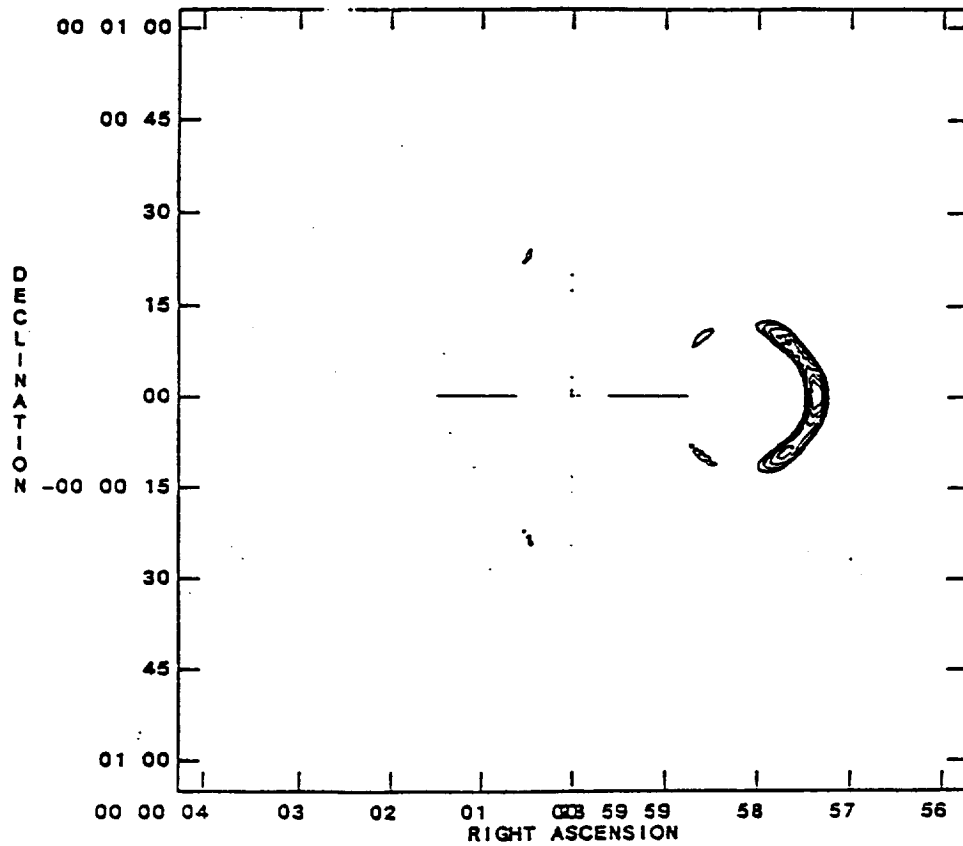


Figure 6.5: RMC Simulation Model



**Figure 6.6: RMC Real And Imaginary Photon Sawtooths**

This shows the real and imaginary traces for a rotating modulation collimator. All Fourier components may be obtained from these four curves. These four curves in fact constitute the image of a point source located 90 arc seconds from the line of sight axis.



**Figure 6.7: RMC Cleaned Loop**

An example of a clean image of a loop. In this case, 21 pixels constitute the loop each having an equal probability of emitting a photon. Clearly, a basic rotating modulation collimator having only two spatial frequencies shows promise for imaging complex shapes. The imaging threshold for complex images such as this was found to be  $\cong 10^4$  photons per 4" by 4" telescope resolution cell (at the Earth). This performance is similar to that of the SMC discussed in Chapter V.

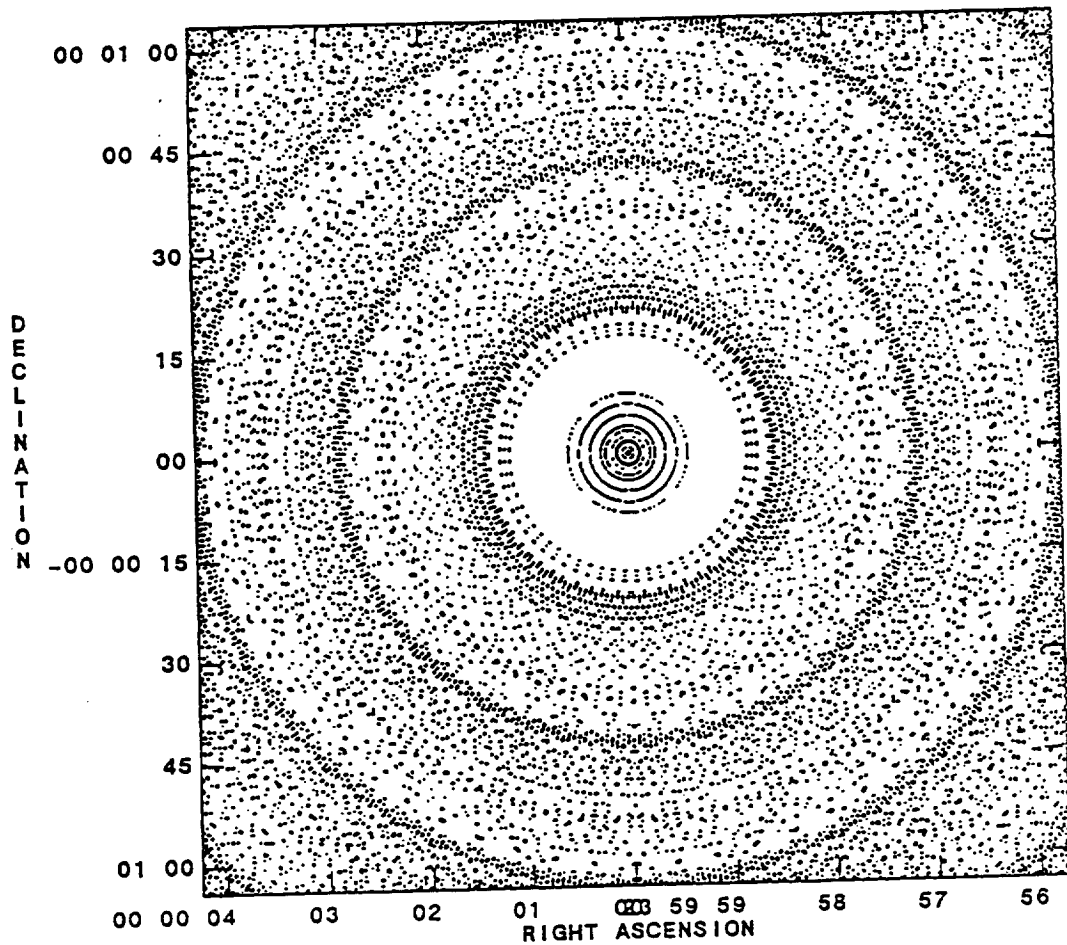


**Figure 6.8: RMC Point Spread Function (Beam)**

This image of the rotating modulation collimator's point spread function was included to illustrate the need for other graphical approaches and to point out the symmetry provided by the telescope. This symmetry is important to the construction of an image.

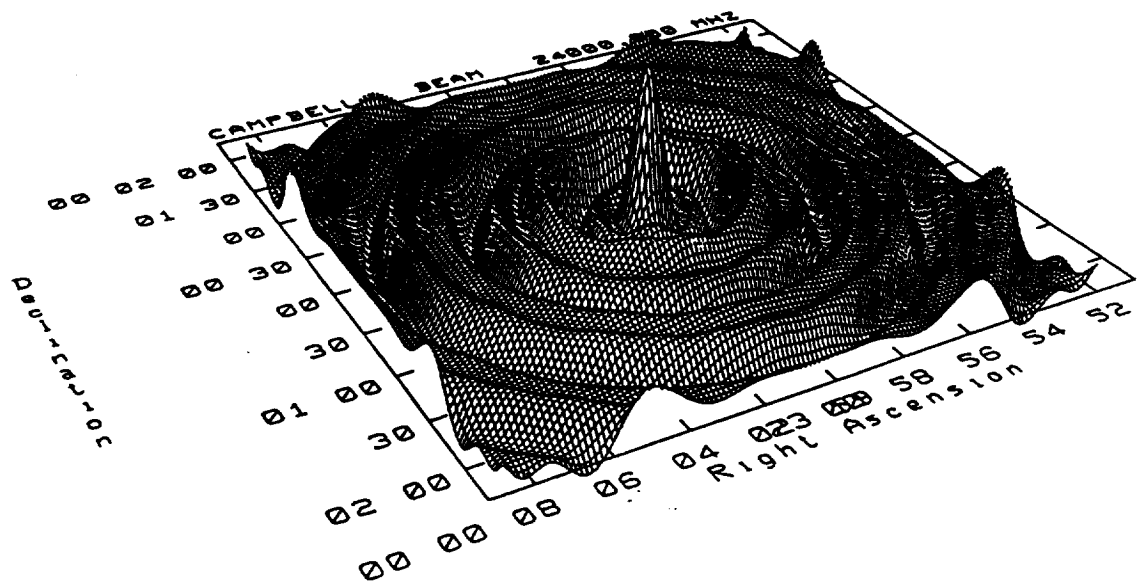


**Figure 6.9: RMC Beam 3-D Representation**

The bright central peak is necessary for successful imaging in that the point spread function illustrates the ability of the telescope to recreate a point source.

is rotated  $90^\circ$  from Figure 6.7, illustrating the telescope's ability to image the loop rotated at any angle. As for the SMC, a stable RMC image requires  $\cong 10^4$  photons per 4 arc second by 4 arc second telescope resolution cell (at the Earth). Again, only about 25% of the available photons are reaching the detector. In addition, the telescope successfully accomplished full Sun imaging achieving about 4 arc seconds spatial resolution. And, as with the SMC, the RMC is highly tolerant of random noise on the detector since the modulation contains all the necessary information.

Figure 6.11 illustrates the twin point source dirty image of the RMC. Note the distinct differences between the patterns of the noise around the point sources as compared to those in Chapter V. Figure 6.12 illustrates the effects of twist on the RMC. Note, image integrity is maintained up to 2 arc minutes of twist. Above this limit the image begins to degrade in shape. At 10 arc minutes, the image is lost completely. Private conversations with the designers of HEIDI have indicated that they expect to control twist to the arc second level. Clearly, given this type of alignment control, twist will not be a factor in the imaging quality of the telescope.

## D. SUMMARY

In this chapter, we have constructed and verified an RMC photon counting simulation. The design parameters chosen were essentially the same as those of the SMC. This RMC employed 48 grid pairs and required only  $15^\circ$  rotation to completely map the  $(u, v)$  plane (2.5 rpm for 1 second temporal integration). A single fourier component required the output from two grid pairs (i.e., a real and an imaginary). Low flux imaging performance was found to be approximately the same as the SMC. In addition, for high flux levels *snapshot* images could be attained for time intervals on the order of a fraction of a second.

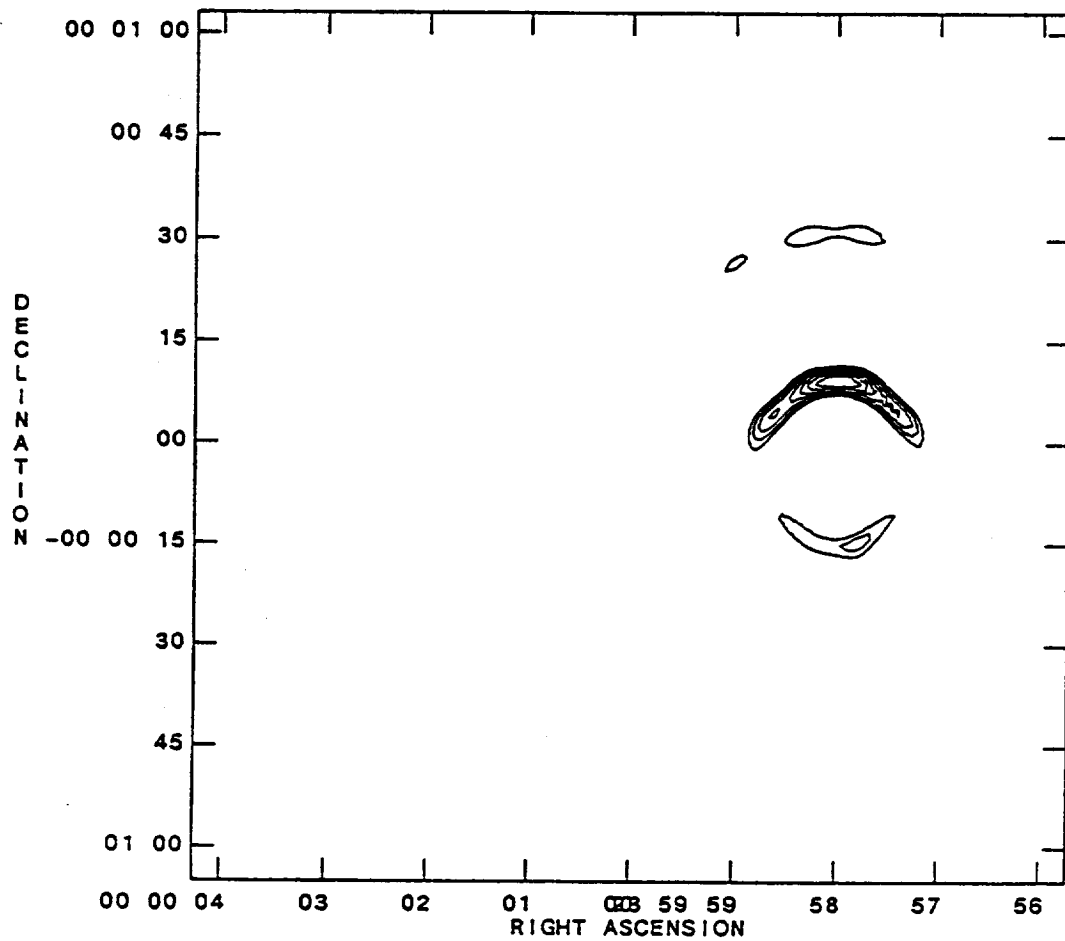


**Figure 6.10: RMC Rotated Loop**

In this case, a uniformly emitting loop was rotated to test the telescopes ability to image it at an different angle. Clearly, even a basic rotating modulation collimator shows promise for imaging complex shapes.



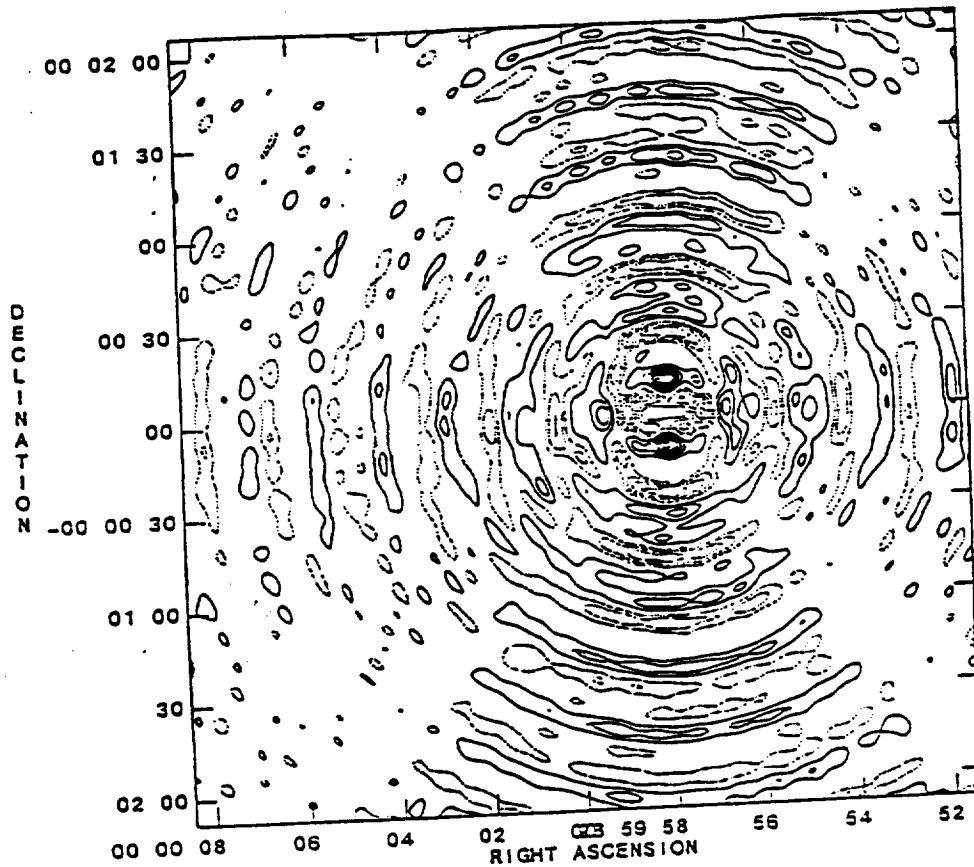


**Figure 6.11: RMC Footpoint Image**

A dirty image of two footpoints is provided here to illustrate the difference in noise patterns between the RMC and the SMC. However, both patterns while different are symmetrical in nature consistent with their point spread functions. The observer would expect to find a real image at the center of such a pattern.

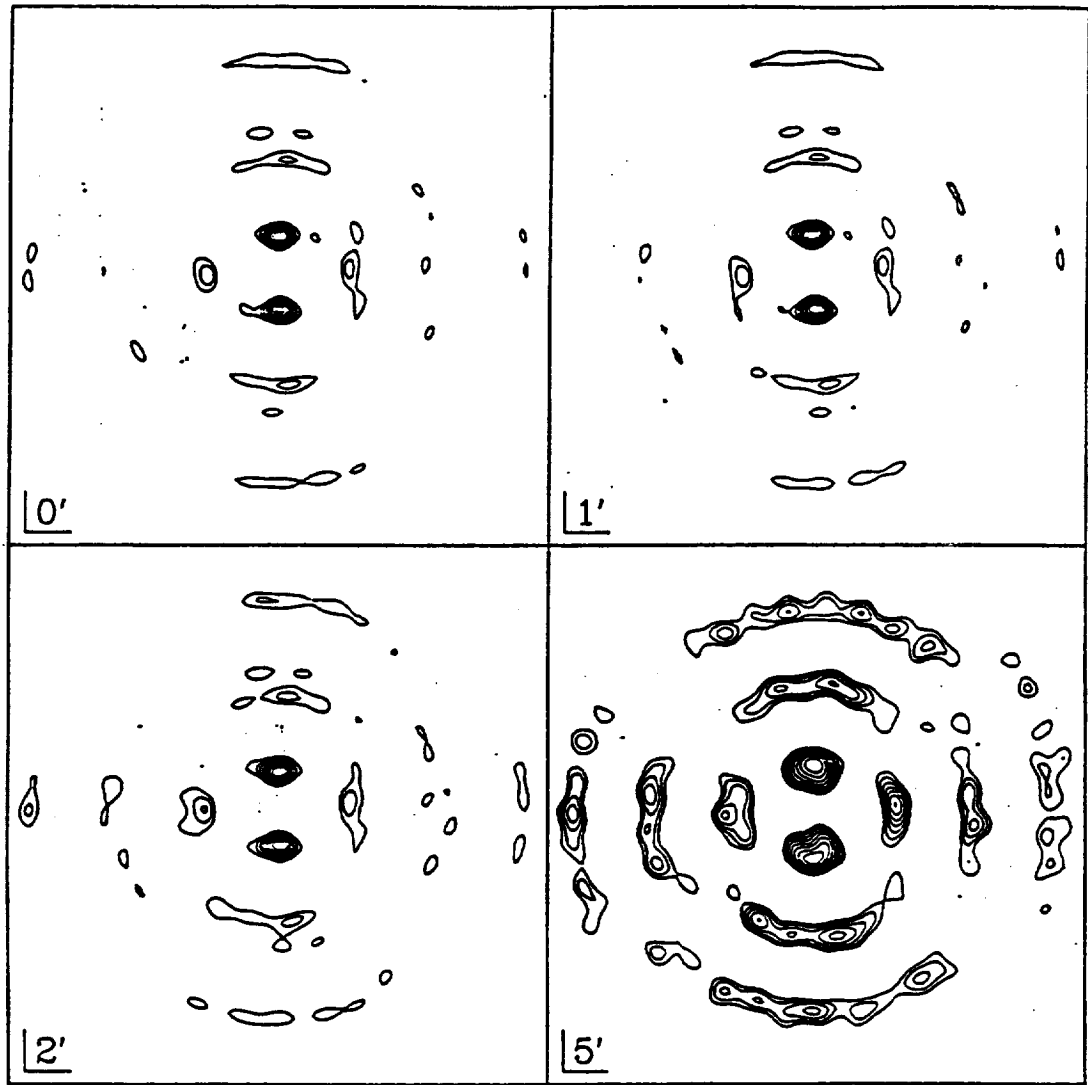


**Figure 6.12: RMC Twist**

These four dirty images of two footpoints clearly show little or no significant change below 2 arc minutes. Designers believe that twist may be reasonably restricted to a few arc seconds in actual designs.

It should be noted that another advantage of the RMC approach is to allow the use of fewer grids at the expense of reduced sensitive area. For example, four grid pairs is the minimum number which could be used to accomplish imaging similar to what we have done with the SMC and the RMC (i.e., two spatial frequencies), all other design parameters remaining the same. A 1 second temporal integration requirement would mean that this design would have to be rotated at 30 rpm, and the threshold for imaging extended sources would increase by an order of magnitude.

In conclusion, the 48 grid pair RMC was found to be virtually equivalent to the SMC in performance. Both telescopes offer advantages and disadvantages which can translate to flexibility for the designer. Chapter VII will discuss the performance of a Fourier telescope viewing the flare profiles derived in Chapter II and III.

## VII. FOURIER IMAGES OF SYNTHETIC FLARE PROFILES

The primary objective of this work is to address how well Fourier telescopes can image hard x-ray sources on the Sun. In answering this question, two elemental loop models, the Model T (Chapter II) and the Model N-T (Chapter III), both employing typical geometries and x-ray flare characteristics, were investigated quantitatively. The dependence of the x-ray emission intensity upon time, energy, and loop position was determined (Chapters II and III).

Given the fact that significant spatial differences were found at particular energies and times in the two hard x-ray models, the question now becomes how well can a Fourier telescope resolve these. A basic SMC (Chapter IV) and a basic RMC (Chapter V) employing typical geometries (e.g., grid separations, slit widths, detector areas) and individual, random photon counting were constructed numerically. AIPS was modified to process the output from these simulations and to reconstruct clean images (Chapter III). Both Fourier telescopes with similar designs (e.g., sensitive areas, spatial frequencies, etc.) were found to perform equally well against test cases. In this chapter, we investigate the performance of the Fourier telescope against the Model T and the Model N-T profiles to determine if the differences found in those profiles may be imaged.

Figure 7.1 qualitatively summarizes the hard x-ray emission from the Model N-T as a function of time, energy, and loop position. At low photon energies and early in time, the predominant emission originates in the footpoints of the loop. Later in the event, thermal effects dominate to produce a bright central peak. At higher energies, the twin footpoint emission dominates throughout the event. At the end of the event at low energies, after beam shutoff, a filled loop remains while no significant emission is observed at higher energies.

Similarly, Figure 7.2 qualitatively summarizes the hard x-ray emission from

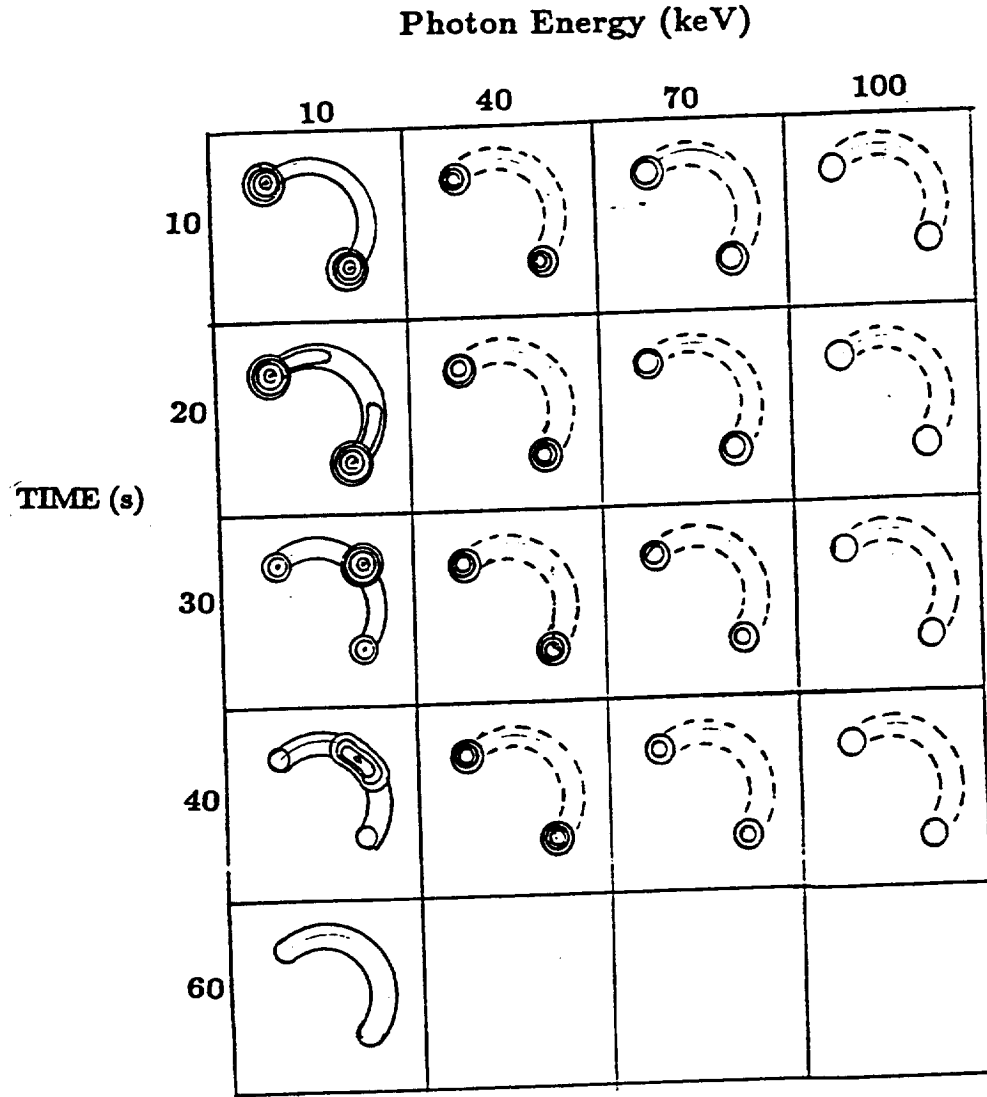


**Figure 7.1: Model N-T Intensity Profiles**

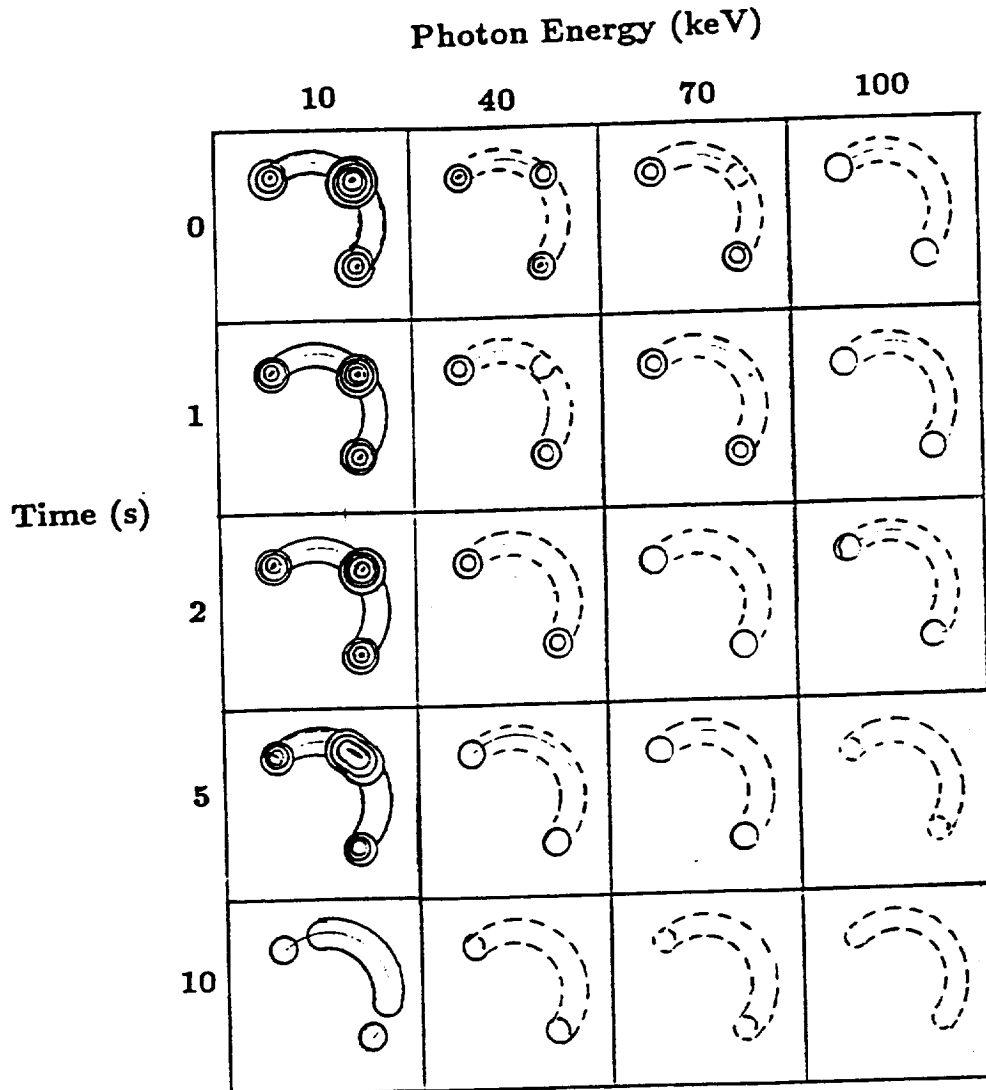
This illustrates qualitatively the intensity as a function of flare position at several energies for several different times (Chapter II). The broken lines indicate that emission is occurring at that location but that its intensity is below the Fourier telescope imaging threshold.

the Model T as a function of time, energy, and loop position. At low photon energies and early in time, the predominate hard x-ray emission originates in the apex of the loop and spreads to adjoining pixels as the hot kernel grows. The intensity decreases in time reflecting the rapid cooling of the emitting plasma within the kernel. Nonthermal emission is predominant in the footpoints but is overshadowed by the thermal emission from the kernel. The triple emission point signature is prevalent from 10-40 keV. At higher energies and very early in time, a brief pulse of thermal emission is noted at the beginning of the event, but it disappears quickly leaving only emission from the footpoints. At higher energies and later in time, the Model T mimics the Model N-T to a degree in that weak emission from the footpoints is all that is visible.

Thus, we see that while ambiguities exist between the two models, especially at higher energies, there is sufficient information at lower energies (i.e., 10-40 keV) to distinguish between the two x-ray models. This information must be in the form of sequential observations with approximately 1 second integration times and 4 arc second spatial resolution starting preferably just prior to the start of and continuing throughout the impulsive phase.

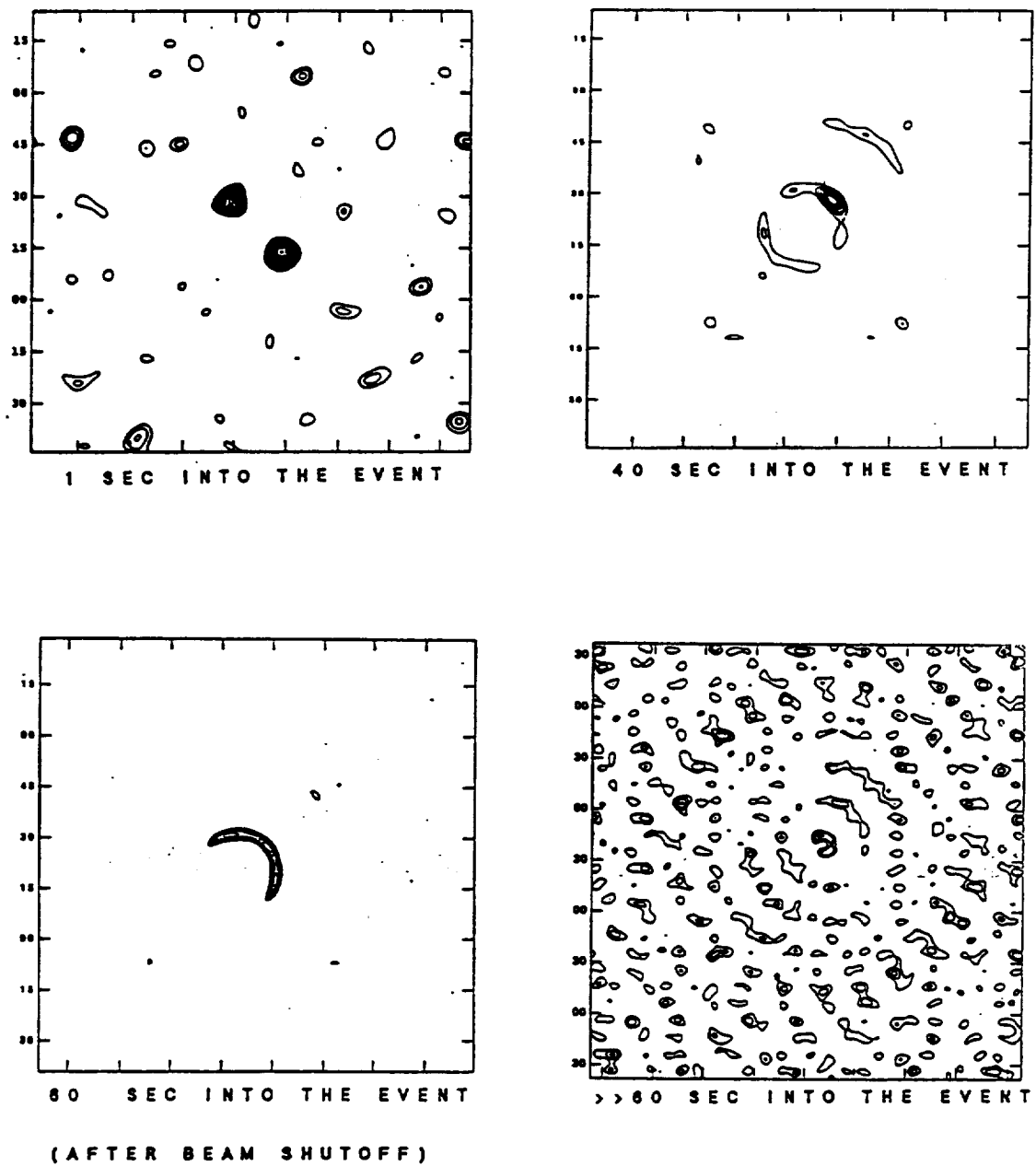
Figure 7.3 illustrates the Fourier telescope's view of the Model N-T x-ray flare at four different times at 10 keV based upon a 1 second integration time and 10 keV bins.

Figure 7.4 shows the telescope's view of the Model T at selected times at 10 keV. Early in time, the telescope will view this model as a single bright source. Due to dynamic range limitations, this single source will dominate the image. As the event proceeds the bright central source spreads and begins to diminish in intensity. Since there was only one energy release in this model, the loop rapidly cools and imaging is lost after 10 seconds into the event. The four sequential images shown in Figure 7.4 are based upon a 1 second integration time, 10 keV



**Figure 7.2: Model T Intensity Profiles**

This illustrates qualitatively the intensity as a function of flare position at several energies for several different times (Chapter III). The broken lines indicate that emission is occurring at that location but that its intensity is below the Fourier telescope imaging threshold.



**Figure 7.3: Model N-T Hard X-ray Images At 10 keV**

These four images were formed from the quantitative profiles for this x-ray model and are based on a 1 second integration time, 10 keV bins, and a 4800 cm<sup>2</sup> sensitive area.



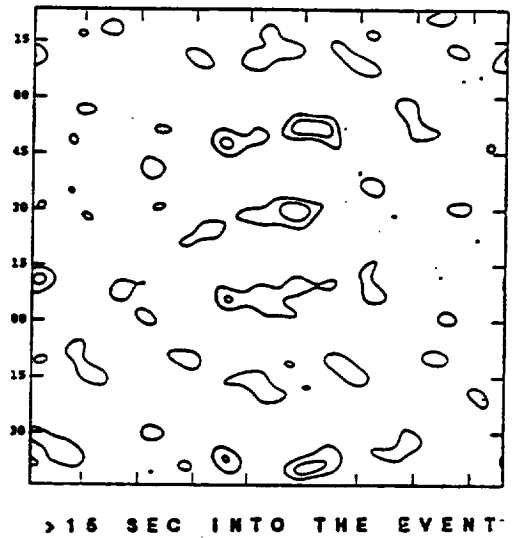
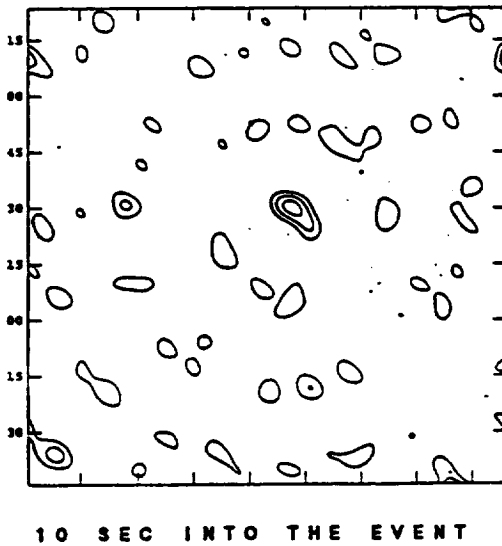
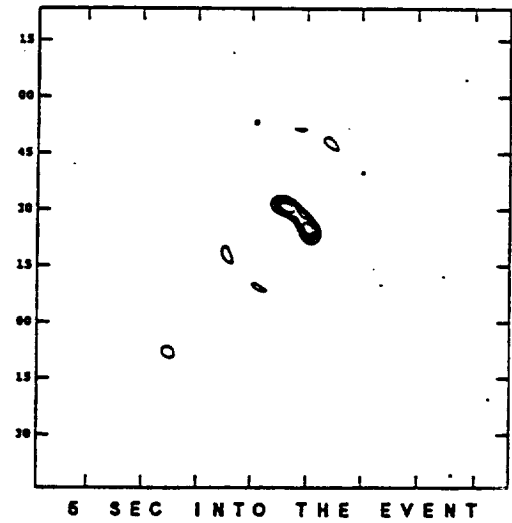
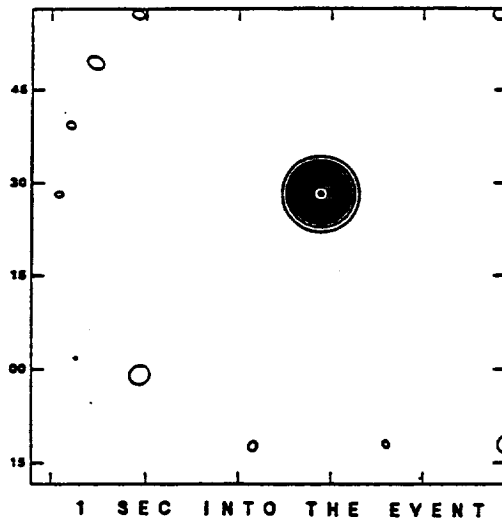
bins, and a  $4800 \text{ cm}^2$  sensitive area.

Figure 7.5 shows a comparison of how a Fourier telescope would image the Model N-T and the Model T profiles at selected times at 40 keV. At 1 second into the event, distinctive images are observed. However, the Model T rapidly fades from view. This implies a requirement that imaging take place early in the impulsive phase. Again, images are based upon 1 second integration times, 10 keV bins, and a  $4800 \text{ cm}^2$  sensitive area. **Clearly, the Fourier telescope can potentially observe differences in the signatures from 10 to 40 keV early in the event.**

Figure 7.6 shows a comparison of the two models at 100 keV. Only Model N-T will be clearly imageable 1 second into the event at this energy, although Model T may faintly mimic its signature.

Clearly, from Figures 7.1 and 7.2 for photon energies at and below 40 keV, differences are present in the hard x-ray model profiles. Figures 7.3 and 7.4 illustrate that these differences also are also present to some degree in the images at 10 keV. Early in the event, the Model T is imaged as an expanding bright point at the apex of the loop (dynamic range suppresses the footpoints) while the Model N-T gives the distinctive twin footpoint signature.

Briefly at the beginning of the event at 40 keV (Figure 7.4), the Model T provides a triple point signature but soon evolves to a state which is nonimageable while the Model N-T provides a twin footpoint signature throughout the period in which a beam is present. Above 50 keV at all times during the event the Model T profile generally begins to look like that of the Model N-T in that emission from the footpoints is dominant. Any small differences in these profiles will be further suppressed in the associated Fourier telescope image. **Thus, the optimum energies for viewing flares as indicated by the images of hard x-ray model profiles will be from 10 to 40 keV.** Primarily, this is because



**Figure 7.4: Model T Hard X-ray Images At 10 keV**

These four images are from the quantitative hard x-ray profiles and are based upon a 1 second integration time, 10 keV bins, and a  $4800 \text{ cm}^2$  sensitive area.

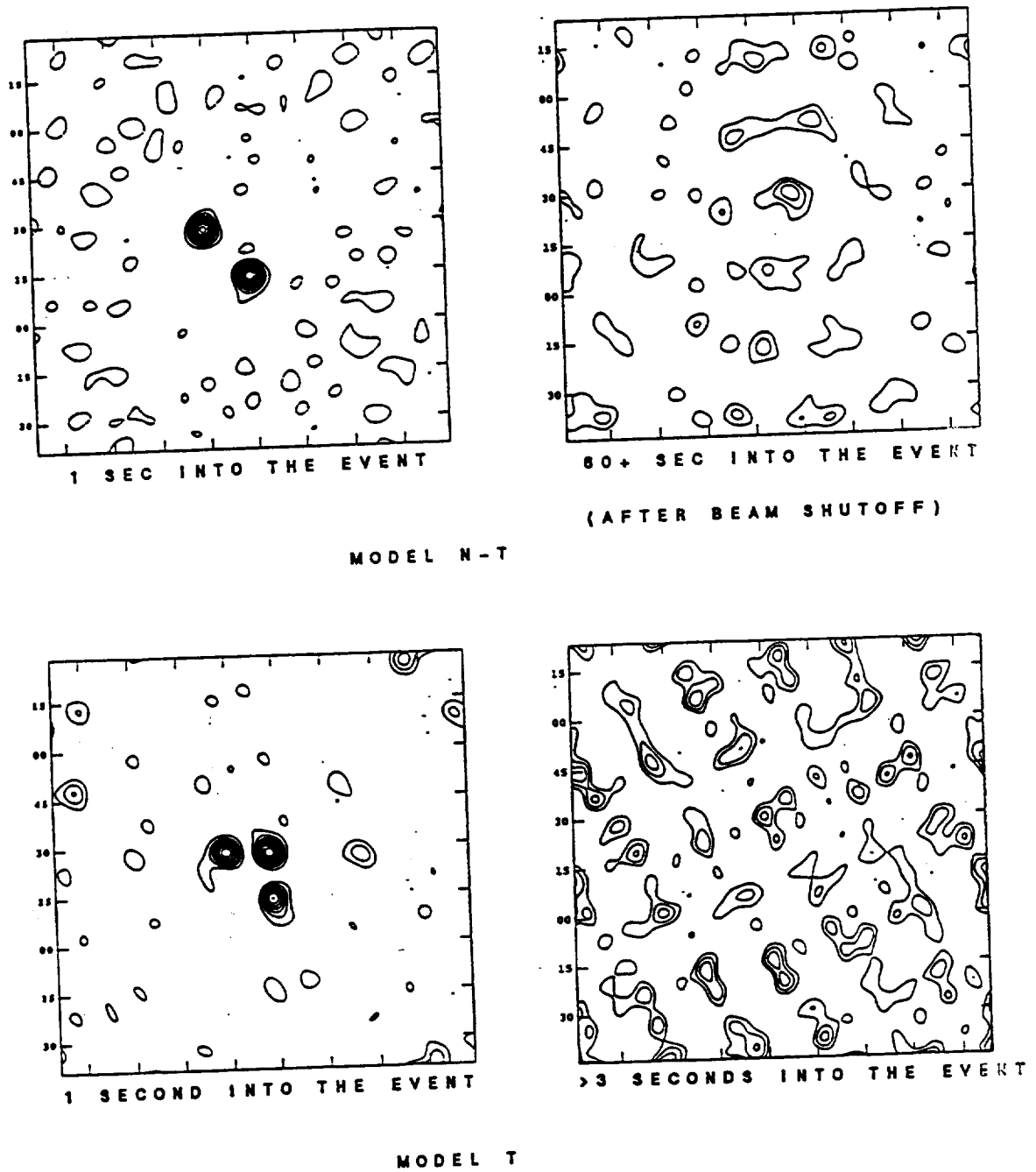
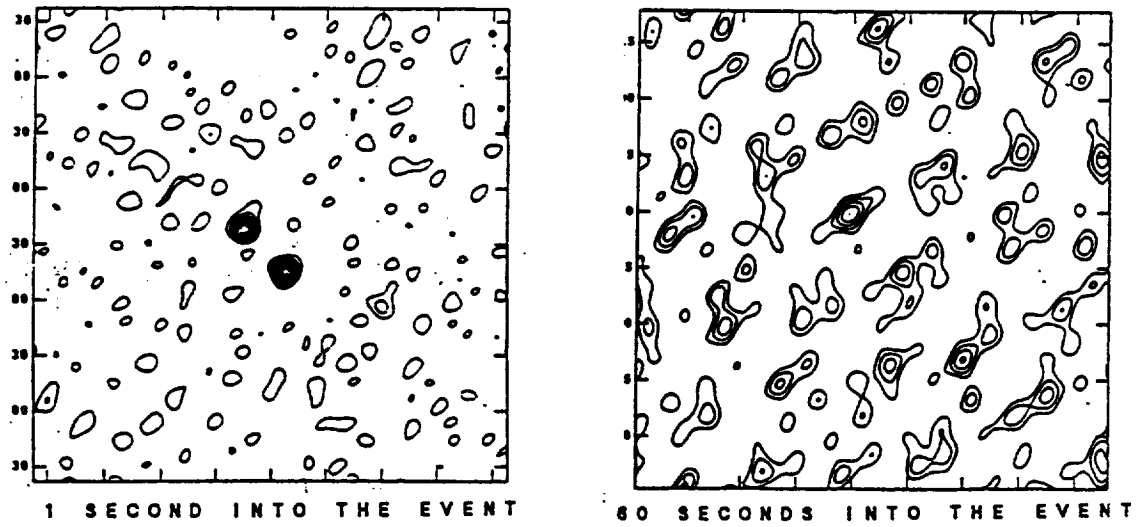
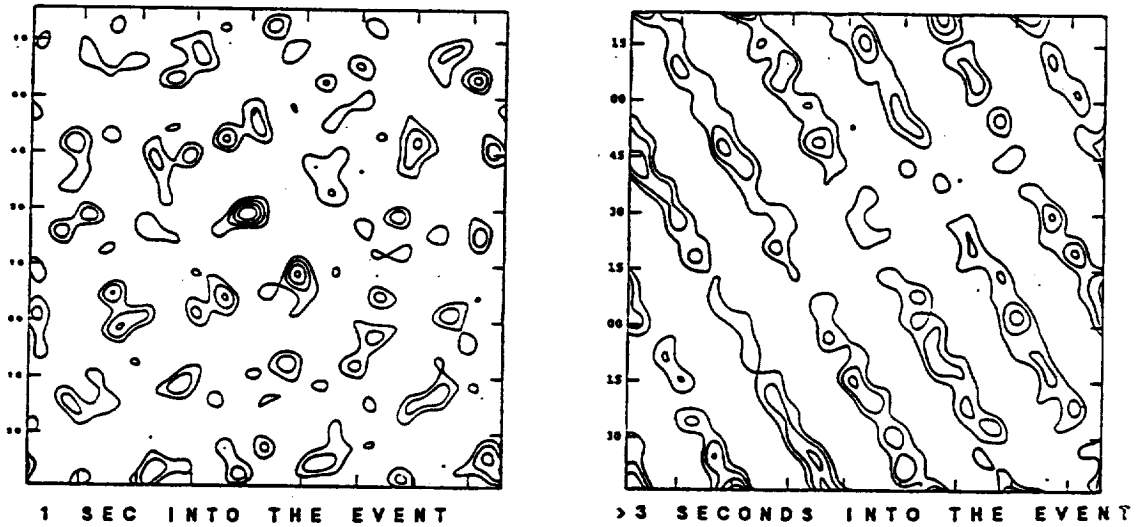


**Figure 7.5: Model N-T And Model T Hard X-ray Images At 40 keV**

The upper two images are the Model N-T and the lower two are the Model T. Images are from the quantitative hard x-ray profiles derived in Chapters II and III and are based on 1 second integration time, 10 keV bins, and a  $4800 \text{ cm}^2$  sensitive area.



MODEL N-T



MODEL T

**Figure 7.6: Model N-T And Model T Hard X-ray Images At 100 keV**

The Model N-T images show a clear footpoint signature while the Model T images seem to weakly mimic the Model N-T. Images are based on 1 second integration time, 10 keV bins, and a 4800 cm<sup>2</sup> sensitive area.

the thermal component of the hard x-ray emission in each model, in general, is crucial to providing discriminating differences in the images.

Temporal resolution is also seen to be important in comparing the Model N-T and Model T profiles. For higher energies 40 keV and above, a few seconds should suffice to provide a reasonable image. However, for energies less than 40 keV especially in the Model T, significant changes in emission signatures are occurring on temporal scales of a second or less. Therefore, our choice of a one second integration time for our telescopes was a good one. In addition, the capability to provide shorter integration times is indicated as a desirable requirement.

**In conclusion, Model N-T and Model T each exhibit emission profiles which, given a favorable viewing angle, can generally be imaged by a Fourier telescope with reasonable design parameters.**

## VIII. SUMMARY AND CONCLUSIONS

The primary objective of this work was to address how well Fourier telescopes can image hard x-ray sources on the Sun. In answering this question, two elemental loop models, the Model T (Chapter II) and the Model N-T (Chapter III), both employing typical geometries and x-ray flare characteristics, were investigated quantitatively. The dependence of the x-ray emission intensity upon time, energy, and position was determined (Chapters II and III). The spectra of the Model N-T and the Model T were consistent with observations. However, no significant differences were found between the two spectra further illustrating the need for an imaging approach.

Given the fact that significant spatial differences were found at particular energies and times in the two models (Chapters II, III, and VII), the question then became how well a Fourier telescope could resolve these. A basic SMC (Chapter IV) and a basic RMC (Chapter V) employing typical geometries (e.g., grid separations, slit widths, detector areas) and individual, random photon counting were constructed numerically. AIPS was modified to process the output from these simulations and to reconstruct clean images (Chapter III). Both Fourier telescopes with similar designs (e.g., sensitive areas, spatial frequencies, etc.) were found to perform equally well. The profile differences discussed previously were then provided as input for the Fourier telescope and imaged using AIPS. The results of this work were discussed in Chapter VII. In short, the Fourier telescope was found to be able to resolve these differences early in the event and from 10 to 40 keV.

### A. CONCLUSIONS

Both basic telescopes measuring only two spatial frequencies required approximately  $10^4$  photons per  $4 \times 4$  arc second telescope resolution cell (at the

Earth) to image clearly an extended source. While both types of telescope provided different trade-offs, both were viewed as equally promising for viewing the Sun at 1 arc second spatially and at 1 second temporally.

Image degradation due to low flux levels was found to occur in stages. As the flux level gradually decreased, image sharpness destabilized first followed by image orientation and last by image position. Thresholds were chosen as that flux level at which image sharpness first showed significant loss of sharpness or resolution in the extended source case. Hence, even for flux levels below the threshold some information may be obtainable from the source.

**Rotation is not an absolute requirement in constructing Fourier telescopes.** The spatial modulation collimator could easily be integrated into a three-axis pointing system, thus allowing complementary instrumentation to be accommodated.

Numerical simulations incorporating AIPS are very useful in understanding the performance of Fourier telescopes. For example, we discovered that effective fields of view for both the SMC and RMC are significantly smaller (i.e., 1:4) than the geometrical ones. This means that overall grid areas and hence detector areas are strongly coupled for full Sun viewing to boom/cannister lengths. The individual detector sizes for both the SMC and the RMC were  $10 \text{ cm}^2$  and provided a 34 arc minute field of view with 4 arc seconds of spatial resolution. The grid separation used was 5 meters.

The Fourier telescope offers the observer in principle a large bandpass. Indeed, HESP is planned to operate from 10 keV out to 4 MeV. In practice, the Fourier telescope's applicability is limited in both the long and short wavelength regimes. In the former case, it is diffraction limited and in the latter by detector and grid limitations.

The trade-off to the wide bandpass using these types of telescope is that

the dynamic range is inherently limited (Chapter V). In other words, in the relative manner in which the telescope ignores random noise, it also sees only the brightest points within its field of view to within about an order of magnitude in brightness. For an extremely bright central peak with bright footpoints against a background almost as bright, the telescope will image the bright central peak and the footpoints will be lost in the artificial noise generated due to the limited coverage of the  $(u, v)$  plane. There are some techniques which may be developed in future work which may improve upon this basic limitation.

**Detailed numerical modeling is a necessary step toward successfully optimizing the design of these instruments.** No purely analytical approach is going to be able to determine the number of photons which provide a good image simply because a good image is determined by the observer comparing the image to the original synthetic object. Also, through modeling the  $(u, v)$  plane coverage can be tested and an optimum verified. Another good example is twist. Only an observer looking at images illustrating the effects of different levels of twist can decide at which point twist becomes unacceptable, and only a numerical simulation allows one to look at twist independent of the other degrading effects.

Hence, both numerical and analytical approaches are useful in understanding these instruments. However, the numerical approach provides the *proof of the pudding*.

Finally, additional considerations for high time and spatial resolution is the fact that there may be other hard x-ray models yet to be developed which may also be consistent with observations and many loops may be involved in a single flare. These loops may be triggered in a somewhat sequential manner; thus, the telescope must be able to have sufficient resolution to resolve these overlapping sequences. The proposed HESP mission offers the technology to do just that.



## B. OPTIMIZATION RECOMMENDATIONS FOR THE FUTURE

Different approaches may be taken to optimizing a design of a future mission depending upon the cost and schedule constraints involved. For an orbital platform, one would prefer to be able to look not only at hard x-rays but also at many other wavelengths and spectral lines and perhaps have a colocated magnetograph all operating simultaneously. Generally, one would want three-axis pointing since that would simplify the design of most of the instruments. This is a high cost approach similar to the Hubble Space Telescope requiring a decade or more of development time.

For this case, a spatial modulation collimator would be the optimum choice for the hard x-ray imager. Within reasonable geometries, six spatial frequencies representing 1, 3, 6, 13, 27, and 56 arc second resolution would be measured using 72 grid pairs each measuring  $10 \times 10 \text{ cm}^2$  for a total collecting area of  $7200 \text{ cm}^2$  (less than a 1 meter diameter aperture). Each spatial frequency would be measured by 12 grid pairs oriented from  $0^\circ$  to  $180^\circ$  in  $15^\circ$  steps.

The grid separation would be 5 meters. The grid material would be tungsten and an aluminum filter would shield the aperture to prevent detector saturation from low energy flux. High purity germanium would be the best choice for the detector which would be composed of an array of seven elements. Telemetry requirements would be significantly reduced as each transmitted image would simply be an array of  $2 \times 72$  numbers, the real and imaginary components of the brightness distribution. The hard x-ray telescope would image the Sun from 10 keV to as high an energy as cost and schedule constraints would allow.

For the moderate cost case, a dedicated Fourier Telescope is recommended. This would be an RMC to minimize the cost involved in providing the detector arrays as required by the SMC. In this case, 48 grid pairs would provide imaging

at spatial frequencies represented by 1, 3, 6, 13, 27, and 56 arc seconds. Each spatial frequency would be measured by 10 grid pairs, 5 real and 5 imaginary, oriented from  $0^\circ$  to  $180^\circ$  in  $45^\circ$  steps. The grid sizes would again be  $100 \text{ cm}^2$  separated by a spacing of 5 meters. However, in this approach, only single detectors would be required but telemetry requirements would be increased as each time tagged photon event would need to be transmitted. The hard x-ray telescope would image the Sun from 10 to 100 keV.

The large detector area per grid pair would ensure full Sun coverage while the 5 meter separation between grid planes would allow us to use grids with broader slit widths, thus reducing the manufacturing risk somewhat. The telescope would be rotated at 15 rpm to ensure a 1 second integration time with a snapshot every 0.5 seconds.

### C. RECOMMENDATIONS FOR FUTURE RESEARCH

The limited dynamic range of these telescopes may possibly be improved by masking the brightest sources and reconstructing the map. In effect, one could strip away one layer at a time in an attempt to reveal more diffuse emission regions. This would be an important investigation with implications for Solar-A and HESP data analysis.

HEIDI and especially Solar-A should be useful experiments for determining the practical applicability of Fourier telescopes to viewing solar flares. In addition, other approaches to the hard x-ray imaging problem are being pursued. These include the Fresnel zone plate, the Fresnel spiral, the grazing incident multilayer telescope (Walker et al., 1988), and a multi-crystal Bragg diffraction lens (Smithers, 1991).

The Fresnel zone plate and the Fresnel spiral are also variations of a Fourier telescope and investigations have begun and will continue in the future to determine the effectiveness of these instruments. An example of the Fourier spiral is shown in Figures 8.1 and 8.2. Figure 8.1 is transparent and by superimposing it on Figure 8.2, a Moire fringe pattern is produced. Offsetting one spiral with respect to the other is equivalent to a single point source illuminating a spiral pair at the same angle from the telescope pointing center.

Initial results indicate that both instruments provide an annular field of view. If the designer attempts to enlarge the outer boundary of the field of the view, the inner boundary also expands and vice versa. As the point source moves further away from the pointing center of the telescope, the fringes become very fine and at a small angle from the center the fringes disappear altogether, thus defining the annular field of view. Also, the outer boundary falls far short of full sun coverage for acceptable inner boundary geometries.

Figure 8.3 illustrates the Fourier transform of four point sources and Figure 8.4 illustrates the spiral pair detector pattern when illuminated by four point sources. The two dimensional Fourier transform of four point sources produces a checkerboard pattern in the  $(u, v)$  plane. Clearly, the basic Moire pattern in Figure 8.4 suggests the correspondence of the Moire fringes to a Fourier transform.

The basic spiral pair response is a Fourier transform superimposed upon a Fresnel kernel. Future work should continue to look at this device to see if actual images can be reconstructed. The Fourier spiral telescope would probably require a minimum of four spiral pairs each requiring a two dimensional array detector.

Hard x-ray detector research for application in Fourier telescope should be initiated. The Marshall Space Flight Center (MSFC) offers exceptional facilities





**Figure 8.2: The Fourier Spiral (Opaque)**

Follow the instructions given for the preceding figure to form the detector pattern for a single point source.

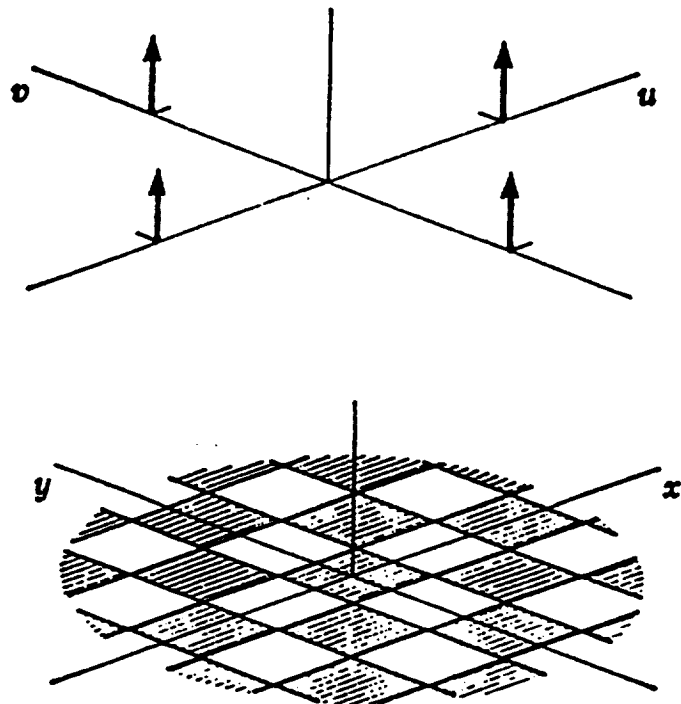


**Figure 8.3: The Fourier Transform Of Four Point Sources**

The two dimensional Fourier transform of four point sources produces a checkerboard pattern (Bracewell, 1965).

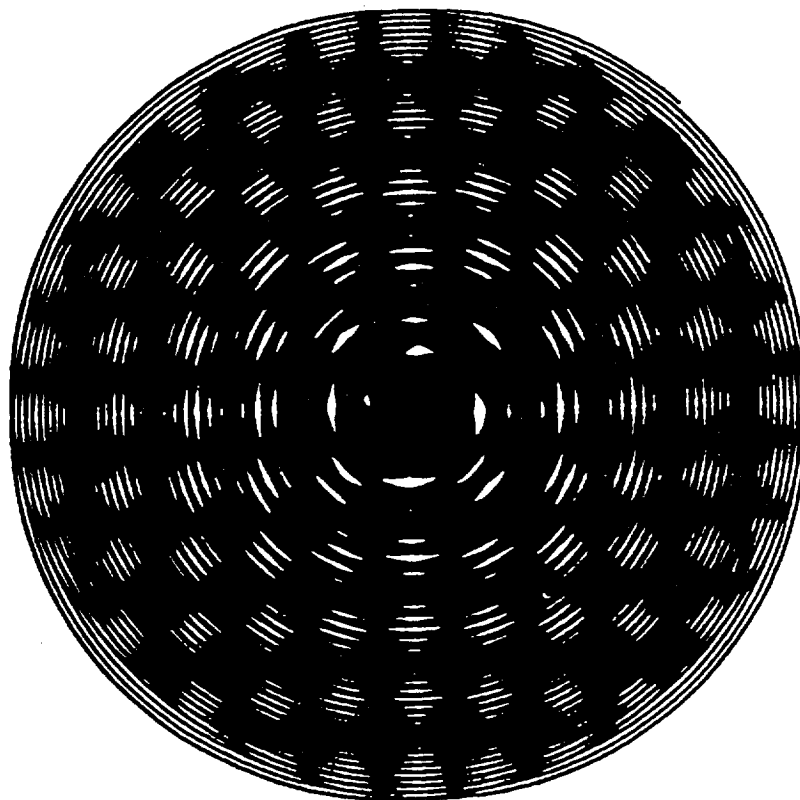


**Figure 8.4: Four Fresnel Spiral Equivalent Point Sources**

This basic Moiré pattern corresponds to a Fourier transform of the four point sources shown in Figure 8.3.

for this type of research including the AXAF test facility. Innovative means of manufacturing and aligning Fourier grids should be investigated. Integrating numerical modeling with the flexible boom technology found at MSFC would be an interesting and significant experiment. Developing a numerical model of Solar-A would allow insight into the possible pitfalls of analyzing the real data.

Finally, the lunar P/OF Observatory concept with NASA offers the chance to place an observatory on the Moon, thus taking advantage of being ground-based without an intervening atmosphere degrading or, in the case of x-rays, completely absorbing the radiation. This observatory would provide sub arc second spatial resolution and tremendously improved sensitivity for Fourier telescopes and other instruments. This would allow, for example, weak, small flares to be fully resolved both spatially and temporally. Designing the telescope for such an observatory should begin with numerical modeling. Other parallel planning should be done in the engineering areas such as pointing and control, structures, and foundations in the lunar ground.

Hard x-ray imaging of the Sun is needed and is doable now and should provide a plethora of new questions for astrophysicists for generations to come.



## APPENDIX A

### Model N-T Code

This appendix contains an example of the code used in Chapter II for calculating the hard x-ray emission as a function of time, energy, and loop position and is based on one developed by Peng Li at the University of Alabama in Huntsville.

```

C  HARD X-RAY SPATIAL STRUCTURE
C  This program is used to calculate the hard X-RAY spatial structure
c  of the non-thermal electron heated solar atmosphere. This part is the
c  main program
C
C23456789112345678921234567893123456789412345678951234567896123456789712

*****
      program main

C  Declaration

      INTEGER I,J,M,SMO
      REAL XA(101),Y(101),Zcc(1E3),X(101,1E3),L(1E3),Nm(1E3),T(1E3)
      REAL Jn(101,1E3),Jn(101,1E3),Ep(101),XS1,B,Ec,FLUX,Inmin
      REAL Un,Uth,Uo,JIN(500),JT(500),N1(1E3),N(1E3),k,r,c,e,p
      REAL ITH(101,1E3),EX(101,1E3),Ithto(101),Into(101),TIMENO,g
      REAL JND(101,1E3),Ithb(500),Inb(500),Itha(500),Ina(500)
      REAL SLOP,L1(500),JN1(101,25),ITH1(101,25),TOT(101,25)
      REAL POS(20),XLEN(20)

      DATA R/8.52E8/,C/1.38E-23/,e/1.6E-16/,p/1.E38/
      DATA B/4./,XS1/.05/

C  FIRST DEFINE THE PARAMETERS FOR CALCULATION OF NON-THERMAL CAS

C  TYPE*, 'ENTER THE UN,M,Uo,Flux,Ec'
C  Accept*,Un,M,Uo,Flux,Ec
C
      TYPE *, 'REMEMBER TO DELETE ALL NT*.DAT;* FIRST'
      TYPE *, 'ENTER THE UNIT NUMBER:11,12,13,14,OR 15'
      ACCEPT *,UNUM

      OPEN(UNIT=11,FILE='T10.DAT',STATUS='OLD')
      OPEN(UNIT=12,FILE='T20.DAT',STATUS='OLD')
      OPEN(UNIT=13,FILE='T30.DAT',STATUS='OLD')
      OPEN(UNIT=14,FILE='T40.DAT',STATUS='OLD')
      OPEN(UNIT=15,FILE='T60.DAT',STATUS='OLD')

C
      OPEN(UNIT=16,FILE='MODNT1.DAT',STATUS='NEW')
      OPEN(UNIT=17,FILE='MODNT2.DAT',STATUS='NEW')
      OPEN(UNIT=18,FILE='MODNT3.DAT',STATUS='NEW')
      OPEN(UNIT=19,FILE='MODNT4.DAT',STATUS='NEW')

C
      OPEN(UNIT=20,FILE='NT1.DAT',STATUS='NEW')
      OPEN(UNIT=21,FILE='NT2.DAT',STATUS='NEW')
      OPEN(UNIT=22,FILE='NT3.DAT',STATUS='NEW')
      OPEN(UNIT=23,FILE='NT4.DAT',STATUS='NEW')
      OPEN(UNIT=24,FILE='NT5.DAT',STATUS='NEW')
      OPEN(UNIT=25,FILE='NT6.DAT',STATUS='NEW')

C

```

```

M=1
EC=15.0
FLUX=1.0E11
C  UO=11
C
C
C
C
DO 5 J=1,100
  Ep(J)=J
  Y(J)=Ep(J)/Ec
  IF(Y(J).GE.1) THEN
    Y(J)=1
  END IF
5  CONTINUE

C  READ IN THE DATA FOR NONTHERMAL CASE

DO 10 I=1,450
  READ(UNUM,*)Zcc(I),Nm(I),L(I),T(I)
C  TYPE *ZCC(I),NM(I),L(I),T(I)
10  continue
C
C
C
C  NOW, GET THE COLUMN DENSITY
C
DO 30 I=1,449
  N1(I)=0.000000
  N1(I+1)=N1(I)+Nm(450-I)*L(450-I)
30  continue

C  NOW, CHANGE THE ARRAY ORDER

DO 35 I=1,449
  N(I)=N1(451-I)
C  IF (ILT.50) THEN
  WRITE(18,*)'POS=',I,'COLUMN DENSITY =' ,N(I)
C  ENDIF
35  CONTINUE

k=2.6e-18
C
DO 38 J=1,100
DO 40 I=1,449
  X(J,I)=(2.*K*N(I))/Ep(J)**2
C  IF(J.EQ.10.AND.I.LE.50) THEN
C  WRITE(17,*)'X=',X(J,I)
C  ENDIF
40  CONTINUE
38  CONTINUE
C  TYPE *,X(J,I)
C
C  WE KNOW X(J,I) AND "Ep(J)/Ec",B, WE ARE READ TO USE THE SUBROUTINE
C

```

C23456789112345678921234567893123456789412345678951234567896123456789712

```

CALL INS(X,Y,XS1,B,JN,JN)
C
C
IF (UNUM.EQ.11) THEN
  TIMENO=10.
ENDIF
IF (UNUM.EQ.12) THEN
  TIMENO=20.
ENDIF
IF (UNUM.EQ.13) THEN
  TIMENO=30.
ENDIF
IF (UNUM.EQ.14) THEN
  TIMENO=40.
ENDIF
IF (UNUM.EQ.15) THEN
  TIMENO=60.
ENDIF
C
IF(TIMENO.LE.30) THEN
  G=TIMENO/30
ELSE
  G=2-TIMENO/30
END IF
C*****
C FOR UNIFORM RESPONSE CASE ONLY
C  G=1.0
C*****
C
DO J=1,100
C
C
DO 50 I=1,449
  JT(J)=285*4/(B+2)/(B-1)*Flux*G*(Ec**(B-2))*(Ep(J)**(1-B))
  JND(J,I)=ABS(JN(J,I)-JN(J,I+1))
  ln(J,I)=JND(J,I)*JT(J)
C  TYPE *,JN(J,I)
C  IF(J.EQ.10.AND.I.LE.50)THEN
C    WRITE(18,*)'KEV='J,'POS='I,'JDIFF='JND(J,I)
C  ENDIF
50  continue
C
C
C  NOW IS THE TIME TO CALCULATE THE THERMAL CASE
C
C
DO 70 I=1,449
  EX(J,I)=(Ep(J)*e)/(C*T(I))
  IF(EX(J,I).GT.87) THEN
    lth(J,I)=(1.2e-11)*Nm(I)**2*L(I)/p/(Ep(J)*SQRT(T(I)))
  else
    lth(J,I)=(1.2e-11)*Nm(I)**2*L(I)/EXP(Ep(J)*e/(C*T(I)))/

```

```

1  (Ep(J)*SQRT(T(I)))
C
  END IF
C
70  continue
C
C NOW CALCULATE THE EMISSION AS A FUNCTION OF FOOTPOINT PIXEL POSITI
C FOR ELEVEN PIXELS
C
C
DO I=1,450
  L1(I)=ZCC(I)/1.4E9
C   TYPE *,I=',I,L(I)='L(I),L1(I)='L1(I)
  IF(L1(I).LE.(.096))THEN
    IN1(J,1)=IN1(J,1)+IN(J,I)
    ITH1(J,1)=ITH1(J,1)+ITH(J,I)
    TOT(J,1)=IN1(J,1)+ITH1(J,1)
    POS(1)=I*1.0
    XLEN(1)=ZCC(I)
C   TYPE *,I=',I,ZCC(I)='ZCC(I)
  ENDIF
  IF(L1(I).GT.(.096).AND.L1(I).LE.(.191))THEN
    IN1(J,2)=IN1(J,2)+IN(J,I)
C   TYPE *,IN1(J,2)
    ITH1(J,2)=ITH1(J,2)+ITH(J,I)
    TOT(J,2)=IN1(J,2)+ITH1(J,2)
    XLEN(2)=ZCC(I)
    POS(2)=I*1.0
  ENDIF
  IF(L1(I).GT.(.191).AND.L1(I).LE.(.286))THEN
    IN1(J,3)=IN1(J,3)+IN(J,I)
    ITH1(J,3)=ITH1(J,3)+ITH(J,I)
    TOT(J,3)=IN1(J,3)+ITH1(J,3)
    POS(3)=I*1.0
    XLEN(3)=ZCC(I)
  ENDIF
  IF(L1(I).GT.(.286).AND.L1(I).LE.(.381))THEN
    IN1(J,4)=IN1(J,4)+IN(J,I)
    ITH1(J,4)=ITH1(J,4)+ITH(J,I)
    TOT(J,4)=IN1(J,4)+ITH1(J,4)
    POS(4)=I*1.0
    XLEN(4)=ZCC(I)
  ENDIF
  IF(L1(I).GT.(.381).AND.L1(I).LE.(.476))THEN
    IN1(J,5)=IN1(J,5)+IN(J,I)
    ITH1(J,5)=ITH1(J,5)+ITH(J,I)
    TOT(J,5)=IN1(J,5)+ITH1(J,5)
    POS(5)=I*1.0
    XLEN(5)=ZCC(I)
  ENDIF
  IF(L1(I).GT.(.476).AND.L1(I).LE.(.571))THEN
    IN1(J,6)=IN1(J,6)+IN(J,I)
    ITH1(J,6)=ITH1(J,6)+ITH(J,I)
    TOT(J,6)=IN1(J,6)+ITH1(J,6)

```

```

    POS(6)=I*1.0
    XLEN(6)=ZCC(I)
ENDIF
IF(L1(I).GT(.571).AND.L1(I).LE(.666))THEN
    IN1(J,7)=IN1(J,7)+IN(J,I)
    ITH1(J,7)=ITH1(J,7)+ITH(J,I)
    TOT(J,7)=IN1(J,7)+ITH1(J,7)
    POS(7)=I*1.0
    XLEN(7)=ZCC(I)
ENDIF
IF(L1(I).GT(.666).AND.L1(I).LE(.761))THEN
    IN1(J,8)=IN1(J,8)+IN(J,I)
    ITH1(J,8)=ITH1(J,8)+ITH(J,I)
    TOT(J,8)=IN1(J,8)+ITH1(J,8)
    POS(8)=I*1.0
    XLEN(8)=ZCC(I)
ENDIF
IF(L1(I).GT(.761).AND.L1(I).LE(.856))THEN
    IN1(J,9)=IN1(J,9)+IN(J,I)
    ITH1(J,9)=ITH1(J,9)+ITH(J,I)
    TOT(J,9)=IN1(J,9)+ITH1(J,9)
    POS(9)=I*1.0
    XLEN(9)=ZCC(I)
ENDIF
IF(L1(I).GT(.856).AND.L1(I).LE(.951))THEN
    IN1(J,10)=IN1(J,10)+IN(J,I)
    ITH1(J,10)=ITH1(J,10)+ITH(J,I)
    TOT(J,10)=IN1(J,10)+ITH1(J,10)
    POS(10)=I*1.0
    XLEN(10)=ZCC(I)
ENDIF
IF(L1(I).GT(.951).AND.L1(I).LE(1.0))THEN
    IN1(J,11)=IN1(J,11)+2*IN(J,I)
    ITH1(J,11)=ITH1(J,11)+2*ITH(J,I)
    TOT(J,11)=IN1(J,11)+ITH1(J,11)
    POS(11)=I*1.0
    XLEN(11)=ZCC(I)
ENDIF
ENDDO

```

C

```

    IN1(J,12)=IN1(J,10)
    ITH1(J,12)=ITH1(J,10)
    TOT(J,12)=TOT(J,10)
    IN1(J,13)=IN1(J,9)
    ITH1(J,13)=ITH1(J,9)
    TOT(J,13)=TOT(J,9)
    IN1(J,14)=IN1(J,8)
    ITH1(J,14)=ITH1(J,8)
    TOT(J,14)=TOT(J,8)
    IN1(J,15)=IN1(J,7)
    ITH1(J,15)=ITH1(J,7)
    TOT(J,15)=TOT(J,7)
    IN1(J,16)=IN1(J,6)

```

```

      ITH1(J,16)=ITH1(J,6)
      TOT(J,16)=TOT(J,6)
      IN1(J,17)=IN1(J,5)
      ITH1(J,17)=ITH1(J,5)
      TOT(J,17)=TOT(J,5)
      IN1(J,18)=IN1(J,4)
      ITH1(J,18)=ITH1(J,4)
      TOT(J,18)=TOT(J,4)
      IN1(J,19)=IN1(J,3)
      ITH1(J,19)=ITH1(J,3)
      TOT(J,19)=TOT(J,3)
      IN1(J,20)=IN1(J,2)
      ITH1(J,20)=ITH1(J,2)
      TOT(J,20)=TOT(J,2)
      IN1(J,21)=IN1(J,1)
      ITH1(J,21)=ITH1(J,1)
      TOT(J,21)=TOT(J,1)
C
C
      DO I=1,21
C      TYPE *,XA(I),ITH(J,I),IN(J,I),'KEV='J','CM='J
C      RE=1.496E13
      ITH1(J,I)=ITH1(J,I)*(4.444E-11)
      IN1(J,I)=IN1(J,I)*(4.444E-11)
      TOT(J,I)=TOT(J,I)*(4.444E-11)
C      IF(J.EQ.10)THEN
C      WRITE(16,*)'KEV='J','
C      WRITE(16,*)'POSITION='J
C      WRITE(16,*)'XA='XA(I)
C      WRITE(16,*)'THER PHOT='ITH(J,I)
C      WRITE(16,*)'NONTHER PHOT='IN(J,I)
C      ENDIF
      ENDDO
      ENDDO
C
      DO KA=1,11
      WRITE(17,*)KA,'','POS='POS(KA),'','XLEN='XLEN(KA)
      ENDDO
C
C
      DO M=1,10
      IA=M*10
      XINTOT=0.0
      XITHTOT=0.0
      DO K1=1,21
      WRITE(16,*)IA,K1,IN1(IA,K1),ITH1(IA,K1),TOT(IA,K1)
      XINTOT=XINTOT+IN1(IA,K1)/(4.444E-11)
      XITHTOT=XITHTOT+ITH1(IA,K1)/(4.444E-11)
      ENDDO
      XTOT=XINTOT+XITHTOT
C      WRITE(17,*)'KEV='IA,'XINTOT='XINTOT
      WRITE(19,*)'KEV='IA,'XINTOT='XINTOT,
1      'XITHTOT='XITHTOT,'XTOT='XTOT
      ENDDO

```

```

C
  DO K1=1,21
    WRITE(20,*)K1
    DO M=1,10
      IA=M*10
      IF(IA.EQ.10)THEN
C        WRITE(21,*)TOT(IA,K1)
C        WRITE(21,*)ITH1(IA,K1)
        WRITE(21,*)IN1(IA,K1)
      ENDIF
      IF(IA.EQ.40)THEN
C        WRITE(22,*)TOT(IA,K1)
C        WRITE(22,*)ITH1(IA,K1)
        WRITE(22,*)IN1(IA,K1)
      ENDIF
      IF(IA.EQ.70)THEN
C        WRITE(23,*)TOT(IA,K1)
C        WRITE(23,*)ITH1(IA,K1)
        WRITE(23,*)IN1(IA,K1)
      ENDIF
      IF(IA.EQ.100)THEN
C        WRITE(24,*)TOT(IA,K1)
C        WRITE(24,*)ITH1(IA,K1)
        WRITE(24,*)IN1(IA,K1)
      ENDIF
    ENDDO
  ENDDO
C
C
C23456789112345678921234567893123456789412345678951234567896123456789712
C
  DO 45 J=1,100

    lthb(J)=0
    ln b(J)=0
    ltha(J)=0
    lna(J)=0
    lthto(J)=0
    into(J)=0

C   NOW TO CACULATE THE FOOTPOINT EMISSION OF ONE ARC SECOND

    DO 80 I=1,M
      lthb(J)=lthb(J)+lth(J,I)
      ln b(J)=ln b(J)+ln(J,I)
80    CONTINUE

C   NOW CACULATE THE TOTAL EMSSION OF T & N FROM THE WHOLE LOOP

    into(J)=JT(J)
    DO 90 I=1,449
      lthto(J)=lthto(J)+lth(J,I)
90    CONTINUE

```



C NOW THE TOP OF THE LOOP OF ONE ARC SECOND

DO 100 I=445,449

Itha(J)=Itha(J)+Ith(J,I)

C IF(J.LE.SMO) THEN

Ina(J)=Ina(J)+In(J,I)

C ELSE

C SLOP=ALOG(ALOG10(Ina(SMO))/ALOG10(Inmin))/ALOG(50./SMO)

C Ina(J)=10\*\*(alog10(Inmin)\*(50./J)\*\*SLOP)

C END IF

100 CONTINUE

C IF(Ina(J).GE.Ina(J-1)) THEN

C Ina(J)=Ina(SMO)-(Ina(SMO)-Inmin)/(50-SMO)\*(J-SMO)

C

C23456789112345678921234567893123456789412345678951234567896123456789712

C

C WRITE(Uo,102)Ep(J),Ithb(J),Inb(J),Itha(J),Ina(J),Ithto(J)

C WRITE(6,\*)Ep(J),Ithto(J),Into(J)

102 FORMAT(1X,F8.2,1X,6(E10.5,1X))

45 CONTINUE

CLOSE(UNIT=11)

CLOSE(UNIT=12)

CLOSE(UNIT=13)

CLOSE(UNIT=14)

CLOSE(UNIT=15)

CLOSE(UNIT=16)

CLOSE(UNIT=17)

CLOSE(UNIT=18)

CLOSE(UNIT=19)

CLOSE(UNIT=20)

CLOSE(UNIT=21)

CLOSE(UNIT=22)

CLOSE(UNIT=23)

CLOSE(UNIT=24)

CLOSE(UNIT=25)

STOP

END

\*\*\*\*\*

C

SUBROUTINE INS(X,Y,XS1,B,JN,JN)

```

*****
C  HARDX2.FOR; IS THE PROGRAM CONSIDER THE LOW PART OF X(J,I)
C  AND IN ORDER TO GET AWAY THE WIGGLES
C
*****
C
C23456789112345678921234567893123456789412345678951234567896123456789712

C  THIS PROGRAM IS USED TO CALCULATE THE HARD X-RAY SPATIAL STRUCT
C  WITH THE ENERGY SPECTRUM OF A POWER LAW WITHOUT CUT-OFF.

C  DECLARE
    INTEGER I,J,N
    REAL JIN(101),Y(101),A(101),B,XS(101),X(101,1E3),XS1
    REAL J5(101,1E3),J0(101,1E3),JN(101,1E3),J1(101,1E3),J2(101,1E3)
    REAL J1(101,1E3),J2(101,1E3),J3(101,1E3),J4(101,1E3)

C  DEFINE THE PARAMETER
C  TPYE*, 'ENTER Y,B,XMAX,XMIN,N,XS1'
C  ACCEPT*,B,XMAX,XMIN,N,XS1

C
DO 5 J=1,100
  A(J)=Y(J)**2
  XS(J)=1/A(J)-1
  JIN(J)=(4*Y(J)-A(J)**2-3)/12+1/(2-B)-Y(J)/(1-B)
5  CONTINUE

C  WE NOW READ TO CACULATE THE CUMULATED INTENSITY JN,WE WILL
C  HAVE ONE LOOP AND TWO BLOCKS WITH IF

DO 8 J=1,100
DO 10 I=1,449
C  TYPE *,J=',I=',I
C  X(J,I)=10**((XMIN+(XMAX(J)-XMIN)*(I-1)/N))
C  TYPE *,X=',X(J,I)
C  NOW WE BEGIN THE FIRST IF BLOCK
C
  IF(X(J,I) LE XS(J)) THEN
C
C23456789112345678921234567893123456789412345678951234567896123456789712
C
    J1(J,I)=A(J)**2/12*(-3*(1+X(J,I))**2+4*(X(J,I)+1)**1.5-1)
    J2(J,I)=.25*(((1-A(J)*X(J,I))**1.5-A(J)**2*(1+X(J,I))**.5)
1    +.5*A(J)*X(J,I)
1    *(SQRT(1-A(J)*X(J,I))-A(J)*SQRT(1+X(J,I)))
1    +.5*(A(J)*X(J,I))**2
1    *ALOG(Y(J)*(1+SQRT(1+X(J,I)))/(1+SQRT(1-A(J)*X(J,I))))
1    +A(J)**2*(1+X(J,I))**2-1)
C
C
  IF(X(J,I) LT XS1) THEN

```

```

C
J0(J,I)=J1(J,I)+J2(J,I)
JN(J,I)=J0(J,I)/JIN(J)

C
ELSE IF(X(J,I).GE.XS1.AND.X(J,I).LE.XS(J))THEN
C
C
C
IF(B.EQ.4)THEN
I1(J,I)=2*(1-(1-A(J)*X(J,I))**1.5)/3
ELSE IF(B.EQ.5)THEN
I1(J,I)=.25*(ASIN((A(J)*X(J,I))**.5)-SQRT(A(J)*X(J,I)
1 *(1-A(J)*X(J,I)))*(1-2*A(J)*X(J,I)))
ELSE IF(B.EQ.6)THEN
I1(J,I)=2*(2-(3*A(J)*X(J,I)+2)*(1-A(J)*X(J,I))**1.5)/15
END IF
C
C
J3(J,I)=.5*((A(J)*X(J,I))**(1-.5*B)*I1(J,I)-2/(B-2))
J0(J,I)=J1(J,I)+J2(J,I)+J3(J,I)
JN(J,I)=J0(J,I)/JIN(J)
END IF

C NOW WE WILL BEGIN THE SECOND BLOCK WITH THE FIRST IF
C
C
ELSE
C
C
IF(B.EQ.4)THEN
I2(J,I)=2*(1-1/(1+X(J,I))**1.5)/3
ELSE IF(B.EQ.5)THEN
I2(J,I)=.25*(ASIN(SQRT(X(J,I)/(1+X(J,I))))
1 -SQRT(X(J,I))*(1-X(J,I))/(1+X(J,I))**2)
ELSE IF(B.EQ.6)THEN
I2(J,I)=2*(2-(5*X(J,I)+2)/(1+X(J,I))**2.5)/15
END IF
C
C
C23456789112345678921234567893123456789412345678951234567896123456789712
C
J4(J,I)=JIN(J)+Y(J)/(1-B)*(A(J)*(1+X(J,I)))**(.5*(1-B))
1 -(A(J)*(1+X(J,I)))**((1-.5*B)/(2-B))
J5(J,I)=.5*(A(J)*X(J,I))**(1-.5*B)*I2(J,I)-(A(J)*(1+X(J,I)))
1 **((1-.5*B)/(B-2))
J0(J,I)=J4(J,I)+J5(J,I)
JN(J,I)=J0(J,I)/JIN(J)
C
C TYPE *,J4=',J4(J,I),J5=',J5(J,I)
C TYPE *,J0=',J0(J,I),JN=',JN(J,I)
C
C
END IF

```

```

C
  IF(JEQ.10.AND.ILE.50)THEN
C   WRITE(18,*)'X=',X(J,I),'JN=',JN(J,I),'JO=',JO(J,I),
C 1   'JIN=',JIN(J),'J=',J,'I=',I,'J4=',J4(J,I),
C 1   'J5=',J5(J,I)
    ENDIF
C 101 FORMAT(2X,F12.6,2X,F12.6)
10  CONTINUE
8   CONTINUE
C
C
  RETURN
  END

```

## APPENDIX B

### Model T Code

This appendix contains an example of the codes used in Chapter III for calculating the hard x-ray emission as a function of time, energy, and loop position. In addition, it contains the code used to calculate the evolution of  $L(t)$ ,  $T(t)$ ,  $v_1$ , and  $v_{lco}$  as functions of time.

```

PROGRAM MODT2
C
C*****
C THIS PROGRAM CALCULATES THE KERNAL THERMAL EMISSION AND
C THE FOOTPOINT NONTHERMAL EMISSION FOR THE MODEL T FLARE
C*****
C
C*****
C INITIALIZATION
C*****
C
  REAL*4 XI(100),ZI(100),SIX(100)
  REAL*4 WI(100),RI(100),WIT(100)
  REAL*4 TI(100),YI(100),XXPOS(20)
  REAL*4 XIT(100),SI(100),XXLEN(50)
  REAL*4 VI(100,100),UI(100,100)
  REAL*4 BI(100,100),AIT(100,100)
  REAL*4 XNLEN(25),XNCT(25),XXTE(25)
  REAL*4 XNCP(25,15),XJ(25,15),XXEC(15)
  REAL*4 XXN(25,15),XXI(25,25),XJEL(1001,501)
  REAL*4 XXEP(15),XXIN(25,25),XXJ(25,15)
  REAL*4 XJMX(15)
C
  OPEN(UNIT=11,FILE='MODT21.DAT',STATUS='NEW')
  OPEN(UNIT=12,FILE='MODT22.DAT',STATUS='NEW')
  OPEN(UNIT=13,FILE='MODT23.DAT',STATUS='NEW')
  OPEN(UNIT=14,FILE='MODT24.DAT',STATUS='NEW')
  OPEN(UNIT=15,FILE='T1.DAT',STATUS='NEW')
  OPEN(UNIT=16,FILE='T2.DAT',STATUS='NEW')
  OPEN(UNIT=17,FILE='T3.DAT',STATUS='NEW')
  OPEN(UNIT=18,FILE='T4.DAT',STATUS='NEW')
  OPEN(UNIT=19,FILE='T5.DAT',STATUS='NEW')
  OPEN(UNIT=20,FILE='T6.DAT',STATUS='NEW')
  OPEN(UNIT=21,FILE='N1.DAT',STATUS='NEW')
  OPEN(UNIT=22,FILE='N2.DAT',STATUS='NEW')
  OPEN(UNIT=23,FILE='N3.DAT',STATUS='NEW')
  OPEN(UNIT=24,FILE='N4.DAT',STATUS='NEW')
  OPEN(UNIT=25,FILE='N5.DAT',STATUS='NEW')
  OPEN(UNIT=26,FILE='N6.DAT',STATUS='NEW')
C
C
C PI=3.1416
C
C WRITE(13,*)'EMISSION FOR FOOTPOINTS AND APEX'
C
C*****
C CALCULATE AND WRITE THE KERNAL THERMAL EMISSION AT TIME=0
C*****

```

```

C
XALPHA=3.38
R=1.496E13
XKAPPA=1.106E-24
XK=8.617E-8
XME=9.1E-28
XMP=1.67E-24

XN=1.0E11
T0=2.0E8
XLO=1.0E8
AREA=4.132E15

C
C XI IS THE INTENSITY AT THE EARTH IN PHOTONS PER CM^2 PER KEV
C
C XEP IS THE ENERGY IN KEV
C
C CALCULATE XI IN XEP STEPS OF 10 FROM 10 - 100 KEV
C
  XEP=0.0
  DO N=1,21
    XEP=XEP+5.0
    XI1=3.0/((2*PI)**(1.5))
C    TYPE *,XI1=',XI1
    XI2=XKAPPA
C    TYPE *,XI2=',XI2
    XI3=((XMP/XME)**(.5))
C    TYPE *,XI3=',XI3
    XI4=(XN**2)*(AREA/R**2)*(XLO**2)/((XK*T0)**2)
C    TYPE *,XI4=',XI4
    XI5=((XK*T0/XEP)**4)
C    TYPE *,XI5=',XI5
    XI6=EXP(-XEP/(XK*T0))
C    TYPE *,XI6=',XI6
    XI7=2.0+(2*XEP/(XK*T0))+(XEP**2)/((XK*T0)**2)
C    TYPE *,XI7=',XI7
    XI8=XI1*XI2*XI3*XI4*XI5*XI6*XI7
C    TYPE *,XI8=',XI8
    XI9=XI1*XI2*XI3*XI4*XI5
C    TYPE *,XI9=',XI9
    XI10=XI9*((.333)*EXP(-XALPHA)*(XEP/(XK*T0))**3)
C    TYPE *,XI10=',XI10
    XI11=XI9*(EXP(-XALPHA))*XI7
C    TYPE *,XI11=',XI11
    XI12=XI9*((.333)*EXP(-XALPHA)*(XALPHA**3))
C    TYPE *,XI12=',XI12
    XI(N)=XI8+XI10-XI11-XI12
C    TYPE *,XI=',XI(N)
    X1=XALPHA*XK*T0
    IF(XEP.GT.X1)THEN
      XI(N)=0.0

```

```

      ENDIF
C   WRITE(11,*)'XI=',XI(N),'KEV=',XEP
      ENDDO
C
C THIS GIVES THE EMISSION FOR A UNIFORMLY TRUNCATED
C MAXWELLIAN ONLY. TO BE MORE ACCURATE LET'S
C MULTIPLY THIS BY 1/3 AND CALCULATE THE EMISSION
C ASSOCIATED WITH THE DISTRIBUTION PERPENDICULAR TO
C THIS ONE. WE WILL WEIGHT IT 2/3.
C
      XEP=0.0
      DO N1=1,21
        XEP=XEP+5.0
        ZI1=3.0/((2*PI)**(1.5))
C      TYPE *,ZI1=',ZI1
        ZI2=XKAPPA
C      TYPE *,ZI2=',ZI2
        ZI3=((XMP/XME)**(.5))
C      TYPE *,ZI3=',ZI3
        ZI4=(XN**2)*(AREA/R**2)*(XLO**2)/((XK*T0)**2)
C      TYPE *,ZI4=',ZI4
        ZI5=((XK*T0/XEP)**4)
C      TYPE *,ZI5=',ZI5
        ZI6=EXP(-XEP/(XK*T0))
C      TYPE *,ZI6=',ZI6
        ZI7=2.0+(2*XEP/(XK*T0))+(XEP**2)/((XK*T0)**2)
C      TYPE *,ZI7=',ZI7
        ZI(N1)=ZI1*ZI2*ZI3*ZI4*ZI5*ZI6*ZI7
C      TYPE *,ZI=',ZI(N1),'KEV=',XEP
      ENDDO
C
C LET XIT BE TOTAL THERMAL EMISSION IN PH/CM^2/KEV/SEC
C
      XEP=0.0
C   WRITE(13,*)'TOTAL THERMAL EMISSION AT TIME=0'
C   WRITE(13,*)'PHOTONS/CM^2/KEV/SEC'
      DO K=1,21
        XEP=XEP+5.0
        XIT(K)=(.333)*XI(K)+(.667)*ZI(K)
C      TYPE *,XIT=',XIT(K),'XI=',XI(K),'ZI=',ZI(K)
C      WRITE(13,*)'XI=',XI(K),'ZI=',ZI(K)
        XIT(K)=XIT(K)*1.2
C      WRITE(13,*)'KEV=',XEP,'XIT=',XIT(K)
      ENDDO
C
C*****
C*****
C CALCULATE EMISSION FROM FOOTPOINTS AT TIME=0
C*****
C*****
C

```



```

C CALCULATE GAMMA FUNCTION IN SEPARATE ROUTINE
C REMEMBER TO LINK BOTH MODT2 AND GAMMCP2 TOGETHER
C
YK=2.6E-18!SOME QUESTION HERE
C
C WRITE(13,*)'NONTHERMAL EMISSION AT TIME=0'
XEP=0.0
DO M=1,21
XEP=XEP+5.0
IF(XEP.LE.X1)THEN
YI1=(.5)*(PI**(-1.5))
C TYPE *,YI1=',YI1
YI2=XKAPPA/YK
C TYPE *,YI2=',YI2
YI3=XN*(AREA/(R**2))*XLO
C TYPE *,YI3=',YI3
C TYPE *,XN=',XN
C TYPE *,AREA=',AREA
C TYPE *,XLO=',XLO
YI4=XK*T0/XEP
C TYPE *,YI4=',YI4
YI5=(XALPHA**(1.5))*EXP(-XALPHA)
C TYPE *,YI5=',YI5
YI6=((1.5*XK*T0/XEP)+1)*GAMMP(XALPHA,1.5)
C TYPE *,YI6=',YI6
YI7=YI1*YI2*YI3
C TYPE *,YI7=',YI7
YI8=YI7*YI4*YI5
C TYPE *,YI8=',YI8
YI9=YI7*YI6
C TYPE *,YI9=',YI9
YI(M)=YI8+YI9
C TYPE *,XEP=',XEP,YI=',YI(M)
ENDIF
IF(XEP.GT.X1)THEN
YI1=(.5)*(PI**(-1.5))
C TYPE *,YI1=',YI1
YI2=XKAPPA/YK
C TYPE *,YI2=',YI2
YI3=XN*AREA*XLO/R**2
C TYPE *,YI3=',YI3
YI4=((XEP/(XK*T0))**.5)*EXP(-XEP/(XK*T0))
C TYPE *,YI4=',YI4
YI5=((1.5*XK*T0/XEP)+1.0)*GAMMP(XALPHA,1.5)
C TYPE *,YI5=',YI5
YI6=YI1*YI2*YI3
C TYPE *,YI6=',YI6
YI7=YI6*YI4
C TYPE *,YI7=',YI7
YI8=YI6*YI5
C TYPE *,YI8=',YI8

```

```

      YI(M)=YI7+YI8
C      TYPE *,XEP=',XEP,YI=',YI(M)
      ENDIF
      YI(M)=YI(M)*.333 !1/3 OF TOTAL FLUX COMES THIS WAY
      YI(M)=YI(M)-.3
C      WRITE(13,*)'KEV=',XEP,YI=',YI(M)
C      TYPE *,XEP=',XEP,YI=',YI(M)
      ENDDO
C
C CALCULATE TOTAL EMISSION FROM FLARE AT TIME=0
C
      XEP=0.0
C      WRITE(13,*)'TOTAL EMISSION AT TIME=0'
      DO J=1,21
        XEP=XEP+5.0
        TOTI=XIT(J)+YI(J)
C      WRITE(13,*)'KEV=',XEP,TOTI=',TOTI
      ENDDO
C
C
C
C*****
C CALCULATE EMISSION FROM THERMAL KERNAL AT 1 SEC
C*****
C
C
C TRUNCATED MAXWELLIAN IN ALONG PARALLEL AXIS
C WI IS PH/CM^2/KEV/SEC TRUNCATED
C RI IS PH/CM^2/KEV/SEC NONTRUNCATED
C
      XEP=0.0
      XALPHA=2.37 !REDEFINED HERE
      T0=6.906E7 !TEMP AT 1 SEC
      DO J=1,21
        XEP=XEP+5.0
        W11=3.0/((2*PI)**(1.5))
C      TYPE *,W11=',W11
        W12=XKAPPA
C      TYPE *,W12=',W12
        W13=((XMP/XME)**(.5))
C      TYPE *,W13=',W13
        W14=(XN**2)*(AREA/R**2)*(XLO**2)/((XK*T0)**2)
C      TYPE *,W14=',W14
        W15=((XK*T0/XEP)**4)
C      TYPE *,W15=',W15
        W16=EXP(-XEP/(XK*T0))
C      TYPE *,W16=',W16
        W17=2.0+(2*XEP/(XK*T0))+(XEP**2)/((XK*T0)**2)
C      TYPE *,W17=',W17
        W18=W11*W12*W13*W14*W15*W16*W17
C      TYPE *,W18=',W18

```

```

      WI9=WI1*WI2*WI3*WI4*WI5
C      TYPE *, 'WI9=', WI9
      WI10=WI9*((.333)*EXP(-XALPHA)*(XEP/(XK*T0))**3)
C      TYPE *, 'WI10=', WI10
      WI11=WI9*(EXP(-XALPHA))*WI7
C      TYPE *, 'WI11=', WI11
      WI12=WI9*((.333)*EXP(-XALPHA)*(XALPHA**3))
C      TYPE *, 'WI12=', WI12
      WI(J)=WI8+WI10-WI11-WI12
      E1P=14.1
      IF(XEP.GT.E1P)THEN
        WI(J)=0.0
      ENDIF
C      TYPE *, 'WI=', WI(J)
      ENDDO
C
C REGION TWO CONTRIBUTION
C
      XEP=0.0
      FCHAR=2.261E9
      F1P=2.73E9
      ECHAR=19.3
      E1P=14.1
      SLOP=(FCHAR-F1P)/(ECHAR-E1P)
      YINT=.5*(F1P+FCHAR)-.5*SLOP*(ECHAR+E1P)
      DO I=1,21
        XEP=XEP+5.0
        TI1=(.667)*((2/XME)**(.5))
C        TYPE *, 'TI1=', TI1
        TI2=XN*XKAPPA*(AREA/(4*PI*(R**2)))*XLO/XEP
C        TYPE *, 'TI2=', TI2
        TI3=(SLOP*(ECHAR**(1.5)))+(2*YINT*(ECHAR**(1.5)))
C        TYPE *, 'TI3=', TI3
        IF(XEP.LE.E1P)THEN
          TI4=(SLOP*(E1P**(1.5)))+(2*YINT*(E1P**(1.5)))
C        TYPE *, 'TI4=', TI4
        ENDIF
        IF(XEP.GT.E1P.AND.XEP.LT.ECHAR)THEN
          TI4=(SLOP*(XEP**(1.5)))+(YINT*(XEP**(1.5)))
C        TYPE *, 'TI4=', TI4
        ENDIF
        IF(XEP.GT.ECHAR)THEN
          TI4=0
        ENDIF
        TI5=-(2*SLOP)/(YINT**2)
        TI(I)=TI1*TI2*TI5*(TI3-TI4)
C        TYPE *, 'TI=', TI(I)
      ENDDO
C
C FULL MAXWELLIAN ALONG PERPENDICULAR AXIS
C AT TIME=1SEC

```

```

C
  XEP=0.0
  DO N1=1,21
    XEP=XEP+5.0
    RI1=3.0/((2*PI)**(1.5))
C    TYPE *,RI1=',RI1
    RI2=XKAPPA
C    TYPE *,RI2=',RI2
    RI3=((XMP/XME)**(.5))
C    TYPE *,RI3=',RI3
    RI4=(XN**2)*(AREA/R**2)*(XLO**2)/((XK*T0)**2)
C    TYPE *,RI4=',RI4
    RI5=((XK*T0/XEP)**4)
C    TYPE *,RI5=',RI5
    RI6=EXP(-XEP/(XK*T0))
C    TYPE *,RI6=',RI6
    RI7=2.0+(2*XEP/(XK*T0))+(XEP**2)/((XK*T0)**2)
C    TYPE *,RI7=',RI7
    RI(N1)=RI1*RI2*RI3*RI4*RI5*RI6*RI7
C    TYPE *,RI=',RI(N1),KEV=',XEP
  ENDDO
C
C LET WIT BE TOTAL THERMAL EMISSION IN PH/CM^2/KEV/SEC
C AT TIME=1SEC
C
  XEP=0.0
C  WRITE(13,*)'TOTAL THERMAL INTENSITY AT TIME=1'
C  WRITE(13,*)'PHOTONS/CM^2/KEV/SEC'
  DO K=1,21
    XEP=XEP+5.0
    IF(XEP.LE.E1P)THEN
      WIT(K)=(.333)*(WI(K)+TI(K))+(.667)*RI(K)
    ENDIF
    IF(XEP.GT.E1P.AND.XEP.LT.ECHAR)THEN
      WIT(K)=(.333)*TI(K)+(.667)*RI(K)
    ENDIF
    IF(XEP.GT.ECHAR)THEN
      WIT(K)=.667*RI(K)
    ENDIF
C    TYPE *,WIT=',WIT(K),WI=',WI(K),RI=',RI(K)
C    WRITE(13,*)'WI=',WI(K),RI=',RI(K)
    WIT(K)=WIT(K)*1.2
C    WRITE(13,*)'KEV=',XEP,'WIT=',WIT(K)
  ENDDO
C
C*****
C CALCULATE NONTHERMAL EMISSION AT TIME=1 SEC
C*****
C
  XALPHA=1.12 !REDEFINED HERE
  T0=2.0E8 !REDEFINED HERE AGAIN

```

```

      X1=XALPHA*XK*T0! REDEFINED HERE AGAIN
C   WRITE(13,*)'NONTHERMAL EMISSION AT TIME=1'
      XEP=0.0
      DO M=1,21
        XEP=XEP+5.0
        IF(XEP.LE.X1) THEN
          SI1=(.5)*(PI**(-1.5))
C         TYPE *,SI1=',SI1
          SI2=XKAPPA/YK
C         TYPE *,SI2=',SI2
          SI3=XN*(AREA/(R**2))*XLO
C         TYPE *,SI3=',SI3
C         TYPE *,XN=',XN
C         TYPE *,AREA=',AREA
C         TYPE *,XLO=',XLO
          SI4=XK*T0/XEP
C         TYPE *,SI4=',SI4
          SI5=(XALPHA**(1.5))*EXP(-XALPHA)
C         TYPE *,SI5=',SI5
          SI6=((1.5*XK*T0/XEP)+1)*GAMMP(XALPHA,1.5)
C         TYPE *,SI6=',SI6
          SI7=SI1*SI2*SI3
C         TYPE *,SI7=',SI7
          SI8=SI7*SI4*SI5
C         TYPE *,SI8=',SI8
          SI9=SI7*SI6
C         TYPE *,SI9=',SI9
          SI(M)=SI8+SI9
C         TYPE *,XEP=',XEP,SI=',SI(M)
        ENDIF
        IF(XEP.GT.X1) THEN
          SI1=(.5)*(PI**(-1.5))
C         TYPE *,SI1=',SI1
          SI2=XKAPPA/YK
C         TYPE *,SI2=',SI2
          SI3=XN*AREA*XLO/R**2
C         TYPE *,SI3=',SI3
          SI4=((XEP/(XK*T0))**.5)*EXP(-XEP/(XK*T0))
C         TYPE *,SI4=',SI4
          SI5=((1.5*XK*T0/XEP)+1.0)*GAMMP(XALPHA,1.5)
C         TYPE *,SI5=',SI5
          SI6=SI1*SI2*SI3
C         TYPE *,SI6=',SI6
          SI7=SI6*SI4
C         TYPE *,SI7=',SI7
          SI8=SI6*SI5
C         TYPE *,SI8=',SI8
          SI(M)=SI7+SI8
C         TYPE *,XEP=',XEP,SI=',SI(M)
        ENDIF
      SI(M)=SI(M)*.333!1/3 OF TOTAL FLUX COMES THIS WAY

```

```

        SIX(M)=SI(M)-YI(M)
        SIX(M)=SIX(M)-.3
C      TYPE *, 'SI=', SI(M), 'YI=', YI(M)
C      WRITE(13,*) 'KEV=', XEP, 'SIX=', SIX(M)
C      TYPE *, 'SIX=', SIX(M)
      ENDDO
C
C WRITE TOTAL EMISSION AT TIME=1SEC
C
C   WRITE(13,*) 'TOTAL EMISSION AT TIME=1SEC'
C
      XEP=0.0
      DO N=1,21
        XEP=XEP+5.0
        TOTI1=SIX(N)+WIT(N)
C      WRITE(13,*) 'KEV=', XEP, 'TOTI1=', TOTI1
      ENDDO
C
C*****
C CALCULATE EMISSION FOR TIME=2 THRU 30
C*****
C
C OVERALL LOOP
C
      XALPHA=3.38 !REDEFINED AGAIN
      XLO=1.0E8
      TIME=1.0
      XKE=1.38E-16 !ERG/K
      TEI=2.0E8 !INITIAL TEMP
      DO KT=2,30
C      TYPE *, 'INSIDE LAST LOOP'
        TIME=TIME+1.0
C      TYPE *, 'TIME=', TIME
        TE1=XLO*TEI
        TE2=3*((XLO*XKE*TEI/XMP)**(.5))*TIME
        TE3=(XLO)**(1.5)
        TE=TE1*((TE2+TE3)**(-.667))
        T0=TE
C      TYPE *, 'TEMP=', T0
C
C*****
C CALCULATE THERMAL EMISSION FOR TIME=2-30
C*****
C
C   WRITE(13,*) 'APEX THERMAL EMISSION FOR TIME=', TIME
      XEP=0.0
      DO N=1,21
        XEP=XEP+5.0
        VI1=3.0/((2*PI)**(1.5))
C      TYPE *, 'VI1=', VI1
        VI2=XKAPPA

```

```

C   TYPE *,VI2=',VI2
VI3=((XMP/XME)**(.5))
C   TYPE *,VI3=',VI3
VI4=(XN**2)*(AREA/R**2)*(XLO**2)/((XK*T0)**2)
C   TYPE *,VI4=',VI4
VI5=((XK*T0/XEP)**4)
C   TYPE *,VI5=',VI5
VI6=EXP(-XEP/(XK*T0))
C   TYPE *,VI6=',VI6
VI7=2.0+(2*XEP/(XK*T0))+(XEP**2)/((XK*T0)**2)
C   TYPE *,VI7=',VI7
VI8=VI1*VI2*VI3*VI4*VI5*VI6*VI7
C   TYPE *,VI8=',VI8
VI9=VI1*VI2*VI3*VI4*VI5
C   TYPE *,VI9=',VI9
VI10=VI9*((.333)*EXP(-XALPHA)*(XEP/(XK*T0))**3)
C   TYPE *,VI10=',VI10
VI11=VI9*(EXP(-XALPHA))*VI7
C   TYPE *,VI11=',VI11
VI12=VI9*((.333)*EXP(-XALPHA)*(XALPHA**3))
C   TYPE *,VI12=',VI12
VI(KT,N)=VI8+VI10-VI11-VI12
C   TYPE *,VI=',VI(KT,N)
X1=XALPHA*XK*T0
IF(XEP.GT.X1)THEN
  VI(KT,N)=0.0
ENDIF
C   TYPE *,VI=',VI(KT,N)
C   WRITE(11,*)'KEV=',XEP,'VI=',VI(KT,N)
ENDDO

C
C THIS GIVES THE EMISSION FOR A UNIFORMLY TRUNCATED
C MAXWELLIAN ONLY. TO BE MORE ACCURATE LET'S
C MULTIPLY THIS BY 1/3 AND CALCULATE THE EMISSION
C ASSOCIATED WITH THE DISTRIBUTION PERPENDICULAR TO
C THIS ONE. WE WILL WEIGHT IT 2/3.
C
  XEP=0.0
DO N1=1,21
  XEP=XEP+5.0
  UI1=3.0/((2*PI)**(1.5))
C   TYPE *,UI1=',UI1
  UI2=XKAPPA
C   TYPE *,UI2=',UI2
  UI3=((XMP/XME)**(.5))
C   TYPE *,UI3=',UI3
  UI4=(XN**2)*(AREA/R**2)*(XLO**2)/((XK*T0)**2)
C   TYPE *,UI4=',UI4
  UI5=((XK*T0/XEP)**4)
C   TYPE *,UI5=',UI5
  UI6=EXP(-XEP/(XK*T0))

```

```

C      TYPE *,UI6=,UI6
      UI7=2.0+(2*XEP/(XK*T0))+(XEP**2)/((XK*T0)**2)
C      TYPE *,UI7=,UI7
      UI(KT,N1)=UI1*UI2*UI3*UI4*UI5*UI6*UI7
C      TYPE *,UI=,UI(KT,N1),KEV=,XEP
      ENDDO
C
C LET XIT BE TOTAL THERMAL EMISSION IN PH/CM^2/KEV/SEC
C
      XEP=0.0
C      WRITE(13,*)'APEX THERMAL EMISSION AT TIME= ',TIME
C      WRITE(13,*)'PHOTONS/CM^2/KEV/SEC'
      DO K=1,21
        XEP=XEP+5.0
        AIT(KT,K)=(.333)*VI(KT,K)+(.667)*UI(KT,K)
C        TYPE *,AIT=,AIT(KT,K),VI=,VI(KT,K),UI=,UI(KT,K)
C        WRITE(13,*)'VI=,VI(KT,K),UI=,UI(KT,K)
        AIT(KT,K)=AIT(KT,K)*1.2
C        WRITE(13,*)'KEV=,XEP,AIT=,AIT(KT,K)
      ENDDO
C
C*****
C CALCULATE EMISSION FROM FOOTPOINTS FOR TIME=2-30 SEC
C*****
C
C      WRITE(13,*)'TOTAL NONTHERMAL EMISSION AT TIME= ',TIME
      XEP=0.0
      DO M=1,21
        XEP=XEP+5.0
        IF(XEP.LE.X1)THEN
          BI1=(.5)*(PI**(-1.5))
C          TYPE *,BI1=,BI1
          BI2=XKAPPA/YK
C          TYPE *,BI2=,BI2
          BI3=XN*(AREA/(R**2))*XLO
C          TYPE *,BI3=,BI3
C          TYPE *,XN=,XN
C          TYPE *,AREA=,AREA
C          TYPE *,XLO=,XLO
          BI4=XK*T0/XEP
C          TYPE *,BI4=,BI4
          BI5=(XALPHA**(1.5))*EXP(-XALPHA)
C          TYPE *,BI5=,BI5
          BI6=((1.5*XK*T0/XEP)+1)*GAMMP(XALPHA,1.5)
C          TYPE *,BI6=,BI6
          BI7=BI1*BI2*BI3
C          TYPE *,BI7=,BI7
          BI8=BI7*BI4*BI5
C          TYPE *,BI8=,BI8
          BI9=BI7*BI6
C          TYPE *,BI9=,BI9

```



```

      BI(KT,M)=BI8+BI9
C      TYPE *,'XEP=',XEP,'BI=',BI(KT,M)
      ENDIF
      IF(XEP.GT.X1)THEN
      BI1=(.5)*(PI**(-1.5))
C      TYPE *,'BI1=',BI1
      BI2=XKAPPA/YK
C      TYPE *,'BI2=',BI2
      BI3=XN*AREA*XLO/R**2
C      TYPE *,'BI3=',BI3
      BI4=((XEP/(XK*T0))**.5)*EXP(-XEP/(XK*T0))
C      TYPE *,'BI4=',BI4
      BI5=((1.5*XK*T0/XEP)+1.0)*GAMMP(XALPHA,1.5)
C      TYPE *,'BI5=',BI5
      BI6=BI1*BI2*BI3
C      TYPE *,'BI6=',BI6
      BI7=BI6*BI4
C      TYPE *,'BI7=',BI7
      BI8=BI6*BI5
C      TYPE *,'BI8=',BI8
      BI(KT,M)=BI7+BI8
C      TYPE *,'XEP=',XEP,'BI=',BI(KT,M)
      ENDIF
      BI(KT,M)=BI(KT,M)*.333 !1/3 OF TOTAL FLUX COMES THIS WAY
      BI(KT,M)=BI(KT,M)-.3
C      WRITE(13,*)'KEV=',XEP,'BI=',BI(KT,M)
C      TYPE *,'XEP=',XEP,'BI=',BI(KT,M)
      ENDDO
C
C CALCULATE TOTAL EMISSION FROM FLARE AT TIME=2-30
C
      XEP=0.0
C      WRITE(13,*)'TOTAL EMISSION AT TIME=',
C      DO J=1,21
C      XEP=XEP+5.0
C      TOTI=AIT(KT,J)+BI(KT,J)
C      WRITE(13,*)'KEV=',XEP,'TOTI=',TOTI
C      ENDDO
C
C BOTTOM OF OVERALL LOOP
C
      ENDDO
C
C*****
C*****
C CALCULATE NONTHERMAL COMPONENT USING THE COLUMN DENSITY
C*****
C*****
C
C CALCULATE THE PIXELS WHICH WILL SEE NONTHERMAL EMISSION
C

```

```

C  CALC LENGTH AND TEMPERATURE ARRAYS
C
  XKE=1.38E-16
  XLO=1.0E8
  T0=2.0E8
  XMP=1.67E-24
  DO I=1,21
    TIME=(I-1)*1.0
    XXLEN1=(3/XLO)
    XXLEN2=(XKE*T0/XMP)**(.5)
    XXLEN(I)=XLO*(1+(XXLEN1*XXLEN2*TIME))**(.667)
    XXLEN(I)=XXLEN(I)*.5 !LENGTH
C   TYPE *, 'LENGTH OF HALF KERNAL=' ,XXLEN(I)
  XXTE(I)=T0*(1+XXLEN1*XXLEN2*TIME)**(-.667) !TEMP
C   TYPE *, 'TEMP=' ,XXTE(I)
  ENDDO

C
C  CALC THE LOCATION OF FIRST NONTHERM PIXEL IN TIME
C
  XNLEN(1)=1.085E9
  XNLEN(2)=1.085E9
  XXPOS(1)=5.422E7
  TOTL=1.1393E9 !TOTAL HALF LOOP LENGTH IN CM
C
  DO JT=2,21 !JT IS TIME IN SECONDS
    DO I= 2,11
      XXPOS(I)=(I-1)*1.085E8
      IF(XXPOS(I).LT.XXLEN(JT)) THEN
        XNLEN(JT)=TOTL-XXPOS(I-1)
        TYPE *, 'XXPOS(I)=' ,XXPOS(I)
      C   ENDIF
    ENDDO
    TYPE *, 'JT=' ,JT
    TYPE *, 'XXLEN(JT)=' ,XXLEN(JT)
    TYPE *, 'XNLEN(JT)=' ,XNLEN(JT)
  ENDDO

C
C  CALCULATE THE COLUMN DENSITY FOR EACH PIXEL IN TIME
C
  DO KT=1,21
C
  XFLEN=1.0844E8 !ONE LOOP PIXEL LENGTH
  XNCT(KT)=(1.0E12+1.0E13)*XFLEN+
1  (1.0E11*(XNLEN(KT)-(2*XFLEN)))
  DO KU=1,10
    IF((KU*XFLEN).LE.(XNLEN(KT)-(2*XFLEN-1.0E7))) THEN
      XNCP(KT,KU)=KU*XFLEN*1.0E11 !INDIV PIX COL DENS
    ENDIF
    IF((KU*XFLEN).GE.(XNLEN(KT)-(XFLEN+1.0E7))) THEN
      XNCP(KT,KU)=XFLEN*1.0E13+(XNLEN(KT)-XFLEN)*1.0E11
    
```

```

      ENDIF
      IF((KU*XFLEN).GE.(XNLEN(KT)-1.0E7))THEN
        XNCP(KT,KU)=XFLEN*(1.0E12+1.0E13)+
1      (XNLEN(KT)-(2*XFLEN))*1.0E11
      ENDIF
      IF((KU*XFLEN).GE.(XNLEN(KT)+1.0E7))THEN
        XNCP(KT,KU)=0.0
      ENDIF
C      TYPE *, 'KT=',KT,'KU=',KU
C      TYPE *, 'PIXEL DENSITY=',XNCP(KT,KU)
C      TYPE *, 'XNLEN(KT)=' ,XNLEN(KT)
      ENDDO
    ENDDO
  C
  C
    TYPE*, 'ENTER PHOTON ENERGY (REAL)'
    ACCEPT 100,XEP
100  FORMAT(F8.3)
    TYPE*, 'ENTER TIME=1,2,3,4,5,6 (INTEGER)'
    ACCEPT 200,M
200  FORMAT(I5)
  C
  C PERFORM DOUBLE INTEGRATION
  C CALCULATE AT INFINITY
  C CARVE UP SURFACE FOR SIX TIMES, 0,1,2,5,10,20
  C
  C
  C DO M=1,6
    IF(M.EQ.1)THEN
      M7=1
    ENDIF
    IF(M.EQ.2)THEN
      M7=2
    ENDIF
    IF(M.EQ.3)THEN
      M7=3
    ENDIF
    IF(M.EQ.4)THEN
      M7=6
    ENDIF
    IF(M.EQ.5)THEN
      M7=11
    ENDIF
    IF(M.EQ.6)THEN
      M7=21
    ENDIF
    XNCOL=-.5E19 !COLUMN DENSITY INCREMENT
    TYPE *, 'XXTE(M7)=' ,XXTE(M7)
    DO I5=1,1000
      XNCOL=XNCOL+1.0E19
      XEO=9.0 !XEO IS THE ELECTRON ENERGY

```

```

DO I5=1,500
  XEO=XEO + 2.0
  IF((XEO**2).GT.(5.2E-18*XNCOL))THEN
    XJ1=1/(XEP*6*15.0*(6.242E8)**(.5))
  C   TYPE *,XJ1=',XJ1
  C   TYPE *,XEP=',XEP
    XJ2=(XKAPPA*2.0**(1.5))/((PI*XME)**(.5))
  C   TYPE *,XKAPPA=',XKAPPA
  C   TYPE *,XME=',XME
  C   TYPE *,XJ2=',XJ2
  C   TYPE *,XK=',XK,'XXTE(M7)='XXTE(M7)
    XJ3=(1.0E11)/((XK*XXTE(M7))**(1.5))
  C   TYPE *,XK=',XK
  C   TYPE *,XXTE(M7)='XXTE(M7)
  C   TYPE *,XJ3=',XJ3
    XJ4=XEO*EXP(-XEO/(XK*XXTE(M7)))
  C   TYPE *,XJ4=',XJ4,'XEO=',XEO
    XJ5=1/(((XEO**2)-(5.2E-18*XNCOL))**(1.5))
  C   TYPE *,XJ5=',XJ5
    XJ6=1.0E19*2.0 !INTEGRATION GRID SIZE
  C   TYPE *,XJ6=',XJ6
    XJ7=XJ1*XJ2*XJ3*XJ4*XJ5*XJ6
  C   TYPE *,XJ7=',XJ7
    XJMX(M7)=XJMX(M7)+XJ7 !J AT INFINITY, CLOSE ENOUGH
  C   TYPE *,XJMX(M7)='XJMX(M7)
    XJEL(I5,I5)=XJ7 !INTEGRAL DIFFERENTIAL ELEMENT
  ENDF
ENDDO
C   TYPE *,I5=',I5,'I5=',100
ENDDO
  TYPE *,M7=',M7
  TYPE *,XJEL=',XJEL(500,500)

C
C
C
C   XXEC IS CUTOFF ENERGY
C
C
C   XXEP IS PHOTON ENERGY PLUS COLUMN DEPTH ENERGY LOSS
C
  XXEC(M7)=3.38*(3*XK*XXTE(M7))
  C   TYPE *,XXEC(M7)='XXEC(M7)
DO I7=1,10
  XXEP(M7)=((XEP**2)+(5.2E-18*XNCP(M7,I7))**(1.5))
  C   TYPE *,XXEP(M7)='XXEP(M7)
  IF(XXEP(M7).GT.XXEC(M7))THEN
    XLLIM=XXEP(M7) !LOWER LIMIT OF INTEGRATION
  ELSE
    XLLIM=XXEC(M7) !LOWER LIMIT OF INTEGRATION
  ENDF
  C   TYPE *,XLLIM=',XLLIM

```

```

C   TYPE *,'XNCP(M7,I7)=' ,XNCP(M7,I7)
IF(XNCP(M7,I7).GT.0.0)THEN
  XNCOL=-.5E19 !COLUMN DENSITY INCREMENT
  DO I8=1,1000
    XNCOL=XNCOL+1.0E19
C   TYPE *,'XNCOL=' ,XNCOL
    IF(XNCOL.LE.XNCP(M7,I7))THEN
      XEO=9.0
      DO J8=1,500
        XEO=XEO+2.0
        IF(XEO.GE.XXLIM)THEN
          XJ(M7,I7)=XJ(M7,I7)+XJEL(I8,J8)
C       TYPE *,'M7=' ,M7,'I7=' ,I7
C       TYPE *,'I8=' ,I8,'J8=' ,J8
C       TYPE *,'XJ(M7,I7)=' ,XJ(M7,I7)
        ENDIF
      ENDDO
    ENDIF
  ENDDO
  ENDIF
  ENDDO
  ENDIF
  TYPE *,'M7=' ,M7,'I7=' ,I7
  TYPE *,'XJ(M7,I7)=' ,XJ(M7,I7)
ENDDO

C
C
C
C NORMALIZE J
C
  DO N3=1,10
    IF(XJMX(M7).GT.0.0)THEN
      XXJ(M7,N3)=XJ(M7,N3)/XJMX(M7) !NORM J
C   TYPE *,'XJ(M7,N3)=' ,XJ(M7,N3)
      XXN(M7,N3)=5.2E-18*XNCP(M7,N3)/(XEP**2) !DIMEN COL DENS
      IF(M7.EQ.1)THEN
        WRITE(21,*)XXN(M7,N3)
        WRITE(22,*)XXJ(M7,N3)
      ENDIF
      IF(M7.EQ.2)THEN
        WRITE(23,*)XXN(M7,N3)
        WRITE(24,*)XXJ(M7,N3)
      ENDIF
      IF(M7.EQ.3)THEN
        WRITE(25,*)XXN(M7,N3)
        WRITE(26,*)XXJ(M7,N3)
      ENDIF
    ENDIF
  ENDDO

C
CC CALCULATE I FROM J(I+1,J+1)-J(I,J)

```

```

C
DO J5=1,10
  IF(XNCP(M7,J5).GT.0.0)THEN
    XXI(M7,1)=XJ(M7,1)*4.128E15/(4*PI*(R**2))
    IF(J5.GT.1)THEN
      XXI(M7,J5)=ABS(XJ(M7,J5)-XJ(M7,J5-1))
C      TYPE *,M7=',M7,J5=',J5
C      TYPE *,XXI(M7,J5)=',XXI(M7,J5)
C      TYPE *,XJ(M7,J5)=',XJ(M7,J5)
C      TYPE *,XJ((M7,J5-1)='XJ(M7,J5-1)
C
C INTENSITY AT THE EARTH FOR A 1 ARC SECOND CROSS SECT AREA
C
      XXI(M7,J5)=XXI(M7,J5)*4.128E15/(4*PI*(R**2))
    ENDIF
C      TYPE *,M7=',M7,J5=',J5
C      TYPE *,XXI(M7,J5)=',XXI(M7,J5)
    ENDIF
  ENDDO
DO J5=1,10
  IF(M.EQ.1)THEN
    WRITE(16,*)XXI(M7,11-J5)
  ENDIF
  IF(M.EQ.2)THEN
    WRITE(15,*)XXI(M7,11-J5)
  ENDIF
  IF(M.EQ.3)THEN
    WRITE(17,*)XXI(M7,11-J5)
  ENDIF
  IF(M.EQ.4)THEN
    WRITE(18,*)XXI(M7,11-J5)
  ENDIF
  IF(M.EQ.5)THEN
    WRITE(19,*)XXI(M7,11-J5)
  ENDIF
  IF(M.EQ.6)THEN
    WRITE(20,*)XXI(M7,11-J5)
  ENDIF
ENDDO
C FOR T=0
C
  IF(M.EQ.1)THEN
    M8=XEP/5
C      TYPE *,M8=',M8
    WRITE(16,*)WIT(M8)
  ENDIF
C
C FOR T=1SEC
C
  IF(M.EQ.2)THEN !T=1SEC
    M8=XEP/5

```

```

        WRITE(15,*)XIT(M8)
    ENDIF
C
C FOR T=2 SECOND
C
    IF(M.EQ.3)THEN !T=2 SEC
        M8=XEP/5
        WRITE(17,*)AIT(M7,M8)
    ENDIF
C
C FOR T=5 SECOND
C
    IF(M.EQ.4)THEN !T=6 SEC
        M8=XEP/5
        WRITE(18,*)AIT(M7,M8)
    ENDIF
C
C FOR T=10SECOND
C
    IF(M.EQ.5)THEN !T=11 SEC
        M8=XEP/5
        WRITE(19,*)AIT(M7,M8)
    ENDIF
C
C
C FOR T=20SECOND
C
    IF(M.EQ.6)THEN !T=21 SEC
        M8=XEP/5
        WRITE(20,*)AIT(M7,M8)
    ENDIF
C
    DO J5=1,10
        IF(M.EQ.1)THEN
            WRITE(16,*)XXI(M7,J5)
        ENDIF
        IF(M.EQ.2)THEN
            WRITE(15,*)XXI(M7,J5)
        ENDIF
        IF(M.EQ.3)THEN
            WRITE(17,*)XXI(M7,J5)
        ENDIF
        IF(M.EQ.4)THEN
            WRITE(18,*)XXI(M7,J5)
        ENDIF
        IF(M.EQ.5)THEN
            WRITE(19,*)XXI(M7,J5)
        ENDIF
        IF(M.EQ.6)THEN
            WRITE(20,*)XXI(M7,J5)
        ENDIF
    
```

```

        ENDDO
C  ENDDO
C
C
C NOW FOOTPOINTS INTENSITY ARE AT THE TOP
C
C*****
C NOW THAT THE INTENSITIES ARE KNOWN WRITE INTO IDL FILES
C
C*****
C
C*****
C CLOSING
C*****
C
    TYPE *, 'PRAISE THE LORD, I AM FREE AT LAST'
    CLOSE(11)
    CLOSE(12)
    CLOSE(13)
    CLOSE(14)
    CLOSE(15)
    CLOSE(16)
    CLOSE(17)
    CLOSE(18)
    CLOSE(19)
    CLOSE(20)
    CLOSE(21)
    CLOSE(22)
    CLOSE(23)
    CLOSE(24)
    CLOSE(25)
    CLOSE(26)
C
    STOP
    END

```



```

PROGRAM MODT
C
C *****
C THIS PROGRAM CALCULATES THE LOWER CUTOFF VELOCITY OF THE
C MODEL T ESCAPING ELECTRONS AS A FUNCTION OF TIME
C *****
C
C *****
C INITIALIZATION
C *****
C
  VLCO=1.48E10
  T0=0.0
  TIME=0.0
  OPEN(UNIT=11,FILE='MODT1.DAT',STATUS='NEW')
  OPEN(UNIT=12,FILE='MODT2.DAT',STATUS='NEW')
  OPEN(UNIT=13,FILE='MODT3.DAT',STATUS='NEW')
  OPEN(UNIT=14,FILE='MODT4.DAT',STATUS='NEW')
  OPEN(UNIT=15,FILE='MODT5.DAT',STATUS='NEW')
  OPEN(UNIT=16,FILE='MODT6.DAT',STATUS='NEW')
C
C *****
C  LOOP
C *****
C
  DOWHILE (ILE.100)
    I=I+1
C
C *****
C CALCULATE THE LENGTH OF THE KERNAL AT WHICH TIME THE
C LAST PARTICLE IN THE VLCO FLUX STREAM REACHES THE FRONT
C *****
C
  A=(-3.857E12)/VLCO
  B=((-3.857E12)*T0)-1.0E12
  XL=-A/3.0
  YL1=(A**2)/9.0
  YL2=(-A)**3/27.0
  YL3=(-B/2.0)
  YL4=((A)**3)*(B/27.0)
  YL5=(B**2)/4.0
  YL6=(YL4+YL5)**.5
  YL7=(YL2+YL3+YL6)**(-1.0/3.0)
  YL=(YL1)*(YL7)
  ZL=(YL2+YL3+YL6)**(1.0/3.0)
  XLEN=(XL+YL+ZL)**2.0
  WRITE(11,*)'XLEN=',XLEN
C
C *****

```

```

C CALCULATE NEXT "T0" FROM XLEN/VLCO
C*****
C
  T0=T0+(XLEN/VLCO)
  WRITE(12,*)'T0=',T0
C
C*****
C CALCULATE AND SAVE TOTAL TIME ELAPSED
C*****
C
  TIME=TIME+T0
  WRITE(13,*)'TIME=',TIME
C
C*****
C CALCULATE TEMPERATURE AT THIS TIME
C*****
C
  TEMP=(2E16)*(((3.857E12)*TIME)+1.0E12)**(-2.0/3.0)
  WRITE(14,*)'TEMP=',TEMP
C
C*****
C SET VLCO AS VMAX, CALCULATE NEXT VLCO
C*****
C
  VMAX=VLCO
  FUN4=2.0E30
  FUN3=1.0E30
C
  DOWHILE (FUN3.LT.FUN4)
C    TYPE *,'VLCO=',VLCO
C    TYPE *,'VMAX=',VMAX
    VLCO=VLCO-1.0E6
C    TYPE *,'TEMP=',TEMP
    A2=(1.024E-6)*(TEMP**(-.5))
C    TYPE *,'A2=',A2
    B2=(3.297E-12)*(TEMP**(-1.0))
C    TYPE *,'B2=',B2
    F1=(2.067E15)*(TEMP**(3.0/2.0))
C    TYPE *,'F1=',F1
    F2=(A2/B2)*(1.0/B2)
C    TYPE *,'F2=',F2
    F3=(A2*VMAX**2.0)/(2.0*B2)
C    TYPE *,'F3=',F3
    F4=EXP(B2*(VMAX**2.0))
C    TYPE *,'F4=',F4
    F5=EXP(B2*(VLCO**2.0))
C    TYPE *,'F5=',F5
    F6=(A2*VLCO**2)/(2.0*B2)
C    TYPE *,'F6=',F6
    F7=(F2+F3)/F4
C    TYPE *,'F7=',F7

```

```

      FUN1=(F1+F7)*F5
C      TYPE *,FUN1=',FUN1
      FUN2=(F6+F2)
C      TYPE *,FUN2=',FUN2
      FUN4=FUN3
      FUN3=ABS(FUN1-FUN2)
C      TYPE *,FUN4=',FUN4
C      TYPE *,FUN3=',FUN3
      ENDDO
C
      FUN7=VLCO+1.0E6
      WRITE(15,*)'VLCO=',FUN7
      WRITE(16,*)'FUN3=',FUN3
C
      ENDDO
C
C*****
C CLOSING
C*****
C
      CLOSE(11)
      CLOSE(12)
      CLOSE(13)
      CLOSE(14)
      CLOSE(15)
      CLOSE(16)
C
      STOP
      END

```

## APPENDIX C

### SMC End-to-end, Photon Counting Design and Simulation

This appendix contains an example of the code defining the hard x-ray imaging telescope described in Chapter IV incorporated into the end-to-end simulation which gives as an output a data stream of Fourier components. This data stream is then processed in AIPS to produce a final image.

```

      PROGRAM XSTAR
C
C MODELS STARRING XRAY IMAGING TELESCOPE
C
C IN THIS MODEL WILL USE TWO SLIT WIDTHS AT 30 DEGREE SPACINGS
C
C SLIT WIDTHS AND SEPARATIONS WILL CORRESPOND TO THE NEW GRID
C
      INCLUDE 'XSTAR.INC/LIST'
C
C OVERALL LOOP FOR EACH INDIVIDUAL PHOTON
C
C SELECT NUMBER OF PHOTONS PER IMAGE (IPHOT)
C
      INTEGER*4 IPHOT
      TYPE *, 'ENTER NUMBER OF PHOTONS (INTEGER) PER IMAGE'
      ACCEPT 100, IPHOT
100  FORMAT(I)
      TYPE *, 'ENTER TWIST ANGLE (REAL, IN ARCSECONDS)'
      ACCEPT 200, TWIST
200  FORMAT(F8.3)
      TYPE *, 'TWIST(ARCSEC)=', TWIST
      TWIST=TWIST*(1.0/3600.0)*(PI/180.0)
      TYPE *, 'TWIST(RADIANS)=', TWIST
C
C  IPHOT=100000
C
      K1=0
      KK3=0
      IDUM=-3
C
      OPEN(UNIT=3, FILE='XSTAR.DAT', STATUS='NEW')
      OPEN(UNIT=12, FILE='XSTAR_POS.DAT', STATUS='NEW')
      OPEN(UNIT=10, FILE='XSTAR_POINT.DAT', STATUS='NEW')
C
C  PAINT EXTENDED FLARING ARC
C
      CALL XSTAR_FLARE
C
C PHOTON LOOP
C
      DO WHILE (IPHOT.GE.1)
C
      IPHOT=IPHOT-1
      PTEST=1
C
      TYPE *, '*****', IPHOT='IPHOT'
C  WRITE(3,*) IPHOT='IPHOT'
C

```

```

      K1=K1+1
C
      CALL XSTAR_GRID
C
C   TYPE *,MGRID=',MGRID,',',NGRID=',',NGRID
C   WRITE (3,*) 'MGRID=',MGRID,',',NGRID=',NGRID
C
C*****GRID ALIGNMENT CHECK*****
C
C      MGRID=1
C      NGRID=1
C
C*****
C NOW THAT A GRID HAS BEEN SELECTED, THE PHOTON ARRIVES AT A RANDOM L
C ON THE GRID WITH A RANDOM ANGLE ASSOCIATED WITH A POINT SOURCE
C
C RELATE POINT SOURCE TO TELESCOPE AXIS
C
      CALL XSTAR_POINT
C
C   TYPE *,MGRID=',MGRID',NGRID=',NGRID
C
C RELATE PHOTON ARRIVAL ANGLES TO LOCALIZED GRID COORDINATE SYSTEM
C
      CALL XSTAR_LOCAL
C
C   TYPE *,MGRID=',MGRID',NGRID=',NGRID
C   TYPE *,THETA3=',THETA3
C
C*****GRID ALIGNMENT TEST*****
C
C      PHI3=1.45444E-4
C      THETA3=0.0
C
C*****
C
C DETERMINE POINT OF ARRIVAL ON GRID
C PUT GRID COORD SYSTEM IN CORNER
C
      CALL XSTAR_COORD
C
C   TYPE *,MGRID=',MGRID',NGRID=',NGRID
C
C*****UNIFORM PHOTON DISTRIBUTION TEST*****
C
C      XPOS=(10.0/10000)*(IPHOT+1)
C      YPOS=0.0
C
C*****
C
C START SECOND LOOP TO TEST FOR PHOTON THROUGHPUT SURVIVAL

```

```

C
C TEST FOR PHOTON PENETRATION THROUGH THE FIRST GRID
C
C     CALL XSTAR_PEN
C
C     TYPE *, 'MGRID=', MGRID, 'NGRID=', NGRID
C     TYPE *, 'PTEST=', PTEST
C
C DETERMINE POINT OF IMPACT OF PHOTON ON SECOND GRID
C
C     IF (PTEST.EQ.1) THEN
C
C         CALL XSTAR_XY
C
C         TYPE *, 'MGRID=', MGRID, 'NGRID=', NGRID
C
C TEST FOR PHOTON PENETRATION OF SECOND GRID
C
C     CALL XSTAR_PEN2
C
C     TYPE *, 'MGRID=', MGRID, 'NGRID=', NGRID
C
C     ENDIF
C
C     TYPE *, 'PTEST=', PTEST
C
C DETERMINE PHOTON POINT OF IMPACT ON DETECTOR
C
C     IF (PTEST.EQ.1) THEN
C
C         CALL XSTAR_XY2
C
C         TYPE *, 'MGRID=', MGRID, 'NGRID=', NGRID
C
C DETERMINE FOURIER COMPONENT, BUILD MATRIX
C
C     CALL XSTAR_FOUR
C
C WRITE XPOS MATRIX
C
C     CALL XSTAR_MTX(KK3)
C
C     WRITE(12,*) XPOS, YPOS, XPOS2, YPOS2, XPOS3, YPOS3
C     ENDIF
C
C ENDDO
C
C WRITE FOURIER COMPONENT MATRIX TO AIPS FORMAT
C
C     TYPE *, 'NTOT=', NTOT
C     WRITE(3,*) 'NTOT=', NTOT

```

```

DO N1=1, TSLIT
DO N2=1, TGRID
WRITE(3,*) 'MGRID=', N1, 'NGRID=', N2, 'DTOT=', DTOT(N1,N2)
WRITE(3,*) BIN(N1,N2,1), BIN(N1,N2,2), BIN(N1,N2,3),
1 BIN(N1,N2,4), BIN(N1,N2,5), BIN(N1,N2,6),
1 BIN(N1,N2,7), BIN(N1,N2,8), BIN(N1,N2,9),
1 BIN(N1,N2,10), BIN(N1,N2,11), BIN(N1,N2,12),
1 BIN(N1,N2,13), BIN(N1,N2,14), BIN(N1,N2,15),
1 BIN(N1,N2,16), BIN(N1,N2,17), BIN(N1,N2,18),
1 BIN(N1,N2,19), BIN(N1,N2,20), BIN(N1,N2,21)
ENDDO
ENDDO
C
DO N3=1, 21
WRITE(10,*) 'N3=', N3, 'PANG(N3)=' , PANG(N3)
WRITE(10,*) 'THETA(N3)=' , THETA(N3)
WRITE(10,*) 'PHI(N3)=' , PHI(N3)
ENDDO
C
CALL XSTAR_FMAT
C
C PLOT PHOTON FLUX VERSUS X AND Y
C
C CALL XSTAR_PLOT
C
C
STOP
END
C
C XSTAR.INC
REAL*4 DIV, NDIV, MDIV, RAND
C
REAL*4 MDIV2, NDIV2
C
REAL*4 DELTHETA(50), NUM, DENOM
C
REAL*4 PSI(55), THETA(55), PHI(55)
C
REAL*4 DELTHL(10,55), SLITW(10), SLITW2(10)
C
REAL*4 XPOS, YPOS, XPOS2, YPOS2, XPOS3, YPOS3
C
REAL*4 SHIFT(10), STIF, GRIDW
C
REAL*4 SHIFT2(10), SNUM
C
REAL*4 VX(110,110), VY(110,110)
C
REAL*4 XDET(5,50,30)
C
REAL*4 DTOT(10,55), REM

```



```

C
REAL*4 U(110,110),V(110,110)
C
REAL*4 DANG,DPOS,DETRES,DETANG
C
INTEGER*4 TGRID,MGRID,NGRID,K2
C
INTEGER*4 PTEST, TSLIT
C
INTEGER*4 ISNUM, NSLIT
C
INTEGER*4 KSNUM, PANG(30)
C
INTEGER*4 NTOT,INCR,BIN(5,50,30)
C
INTEGER*4 REM2
C
COMMON/GRID/ MGRID,NGRID,ISEED,SLITW
C
COMMON/GRIDC/ TGRID,TSLIT
C
COMMON/POINT/ THETA3,PHI3,PANG,THETA,PHI
C
COMMON/COORD/ XPOS,YPOS
C
COMMON/LOC/ DELTHL
C
COMMON/PTEST/ PTEST
C
COMMON/XY/ XPOS2,YPOS2
C
COMMON/PEN2/ ISNUM
C
COMMON/XY2/ XPOS3,YPOS3
C
COMMON/FOUR/ VX,VY
C
COMMON/MTX/ BIN,XDET,NTOT,DTOT
C
DATA PI/3.14159/
C
DATA ISEED/1/
REAL*4 FUNCTION RANO(IDUM)
C JUST SET IDUM TO ANY NEGATIVE SEED TO START
DIMENSION V(97)
DATA IFF /0/
IF(IDUM.LT.0.OR.IFF.EQ.0)THEN
  IFF=1
  ISEED=ABS(IDUM)
  IDUM=1
  DO 11 J=1,97

```

```

        DUM=RAN(ISEED)
11      CONTINUE
        DO 12 J=1,97
            V(J)=RAN(ISEED)
12      CONTINUE
        Y=RAN(ISEED)
        ENDIF
        J=1+INT(97.*Y)
        IF(J.GT.97.OR.J.LT.1)PAUSE
        Y=V(J)
        RANO=Y
        V(J)=RAN(ISEED)
        RETURN
        END
        SUBROUTINE XSTAR_COORD
C
C THIS ROUTINE DETERMINES THE RANDOM LOCATION ON THE SURFACE OF
C THE FIRST GRID ON WHICH THE PHOTON FALLS
C
        INCLUDE 'XSTAR.INC/LIST'
C
        TYPE *, 'ENTERING XSTAR_COORD'
C
        RAND=RANO(IDUM)
C   TYPE *, 'RAND=', RAND
C
        XPOS=RAND*10 !IN CM
C
        RAND=RANO(IDUM)
C   TYPE *, 'RAND=', RAND
C
        YPOS=RAND*10 !IN CM
C
C   TYPE *, 'XPOS=', XPOS
C   TYPE *, 'YPOS=', YPOS
C
        RETURN
        END
        SUBROUTINE XSTAR_FLARE
C
C THE PURPOSE OF THIS SUBROUTINE IS TO BUILD A FLARE
C FROM A COLLECTION OF POINT SOURCES, A SIGNIFICANT
C PROBLEM IS WHAT COLLECTION OF POINTS BEST REPRESENT
C A FLARE OF INTEREST.
C
C THIS ATTEMPT AT PAINTING A FLARE WILL BE REPRESENTED
C BY A 100 ARCSECOND LONG SEMICIRCLE WITH 20 POINT
C SOURCES EQUA-SPACED ALONG THE ARC. THIS MEANS THE
C RADIUS OF THE FLARE WILL BE 100/PI.
C
C THE ORIENTATION OF THE FLARE TO THE VERTICAL AXIS

```

```

C OF THE TELESCOPE WILL BE 45 DEGREES. THE FIRST
C POINT WILL BE 0.0 DEGREES OF ROTATION FROM THE
C HORIZONTAL, THE NEXT WILL BE 9.0, THE NEXT
C 9.0+9.0 AND SO FORTH. ESSENTIALLY, DIVIDING
C 180 DEGREE BY 21 PIXELS AND PUTTING THE POINT
C SOURCE IN THE CENTER OF EACH PIXEL.
C
C   INCLUDE 'XSTAR.INC/LIST'
C
C
C   TYPE *, 'ENTERING XSTAR FLARE'
C   WRITE(10,*) 'ENTERING XSTAR FLARE'
C
C LET PSI BE THE ANGLE AROUND THE CIRCLE
C
C   J=0
C   PSI(1) = 0.0
C   TYPE *, 'PSI(1) =', PSI(1)
C   DELPSI=PI/20
C   DO J = 2,21
C     PSI(J)=PSI(J-1)+(DELPSI)
C     TYPE *, 'J=', J, 'PSI(J) =', PSI(J)
C   END DO
C
C DEFINE ANGLES OF FLARE POINT
C
C   ANGLE OF ROTATION ABOUT Z-AXIS OF TELESCOPE
C
C   CENTER FLARE AT 45 DEGREES ABOUT CENTER
C   30 ARCSEC FROM CENTER OF TELESCOPE
C
C LOOP
C
C   J2=0
C
C   DOWHILE (J2.LE.20)
C
C     J2=J2+1
C
C     PHI2=30 !ARCSECONDS FROM CENTER OF TELESCOPE
C     PHI2=60 !ARCSECONDS FROM CENTER OF TELESCOPE
C     PHI2=240 !ARCSECONDS FROM CENTER OF TELESCOPE
C     PHI2=480 !ARCSECONDS FROM CENTER OF TELESCOPE
C     PHI2=960 !ARCSECONDS FROM CENTER OF TELESCOPE
C     PHI2=540 !ARCSECONDS FROM CENTER OF TELESCOPE
C     PHI2=600 !ARCSECONDS FROM CENTER OF TELESCOPE
C     PHI2=700 !ARCSECONDS FROM CENTER OF TELESCOPE
C     PHI2=800 !ARCSECONDS FROM CENTER OF TELESCOPE
C     PHI2=900 !ARCSECONDS FROM CENTER OF TELESCOPE
C     PHI2=1000 !ARCSECONDS FROM CENTER OF TELESCOPE
C

```

```

C   TYPE *, '*****'
C   TYPE *, 'ENTER ARCSECONDS OUT FROM SUN CENTER (INT)'
C   TYPE *, '*****'
C   ACCEPT 1000, PHI2
C1000  FORMAT(I)
C
C   ARCRAD=10.0
C
C   NUM=(ARCRAD)*COS(PSI(J2))  !IN ARCSECONDS
C   TYPE *, 'NUM=', NUM
C   DENOM=((ARCRAD)*(SIN(PSI(J2))))+PHI2  !IN ARCSECONDS
C   TYPE *, 'DENOM=', DENOM
C   DELTHETA(J2)=ATAN(NUM/DENOM)  !IN RADIANS
C
C   THETA(J2)=((45.0)*(PI/180))+DELTHETA(J2)  !IN RADIANS
C
C   TYPE *, 'J2=', J2, ', ', THETA(J2)=', THETA(J2)
C
C   ENDDO
C
C   ANGLE OF ROTATION AWAY FROM Z-AXIS OF TELESCOPE
C
C   LOOP
C
C   J3=0
C
C   TYPE *, 'PSI(1)=', PSI(1)
C
C   DOWHILE (J3.LE.20)
C
C   J3=J3+1
C
C   TYPE *, 'J3=', J3
C   TYPE *, 'PSI(J3)=', PSI(J3)
C   TYPE *, 'PHI2=', PHI2
C   NUM=PHI2+((ARCRAD)*SIN(PSI(J3)))
C   NUM=NUM*(4.848E-6)  !CONVERTING PHI TO RADIANS
C   DENOM=COS(DELTHETA(J3))
C   PHI(J3)=NUM/DENOM
C   TYPE *, 'DELTHETA(J3)=', DELTHETA(J3)
C   TYPE *, 'NUM=', NUM, ', ', 'DENOM=', DENOM
C
C   TYPE *, 'J3=', J3, ', ', 'PHI(J3)=', PHI(J3)
C
C   ENDDO
C
C   TYPE *, 'PHI3=', PHI3, ', ', 'THETA3=', THETA3
C   WRITE(10,*) 'PHI3=', PHI3, ', ', 'THETA3=', THETA3
C
C   RETURN
C   END

```

```

      SUBROUTINE XSTAR_FMAT
C
C THIS ROUTINE WRITES UV FILE FOR AIPS/UVFIL
C
      INCLUDE 'XSTAR.INC/LIST'
C
      TYPE *, 'ENTERING XSTAR_FMAT'
C
      OPEN(UNIT=4, FILE='IN2FIL.DAT', STATUS='NEW')
C
      DO J1=1, TSLIT
        DO J2=1, TGRID
          R1=SLITW(J1)
          R2=520.0 !GRID SEP IN CM
          R3=R2/R1
          U(J1,J2)=R3*(SIN(DELTHL(J1,J2)))
          V(J1,J2)=R3*(COS(DELTHL(J1,J2)))
C
          U(J1,J2)=-U(J1,J2)/(1.0E4*2.0) !10-5-90
C
          U(J1,J2)=U(J1,J2)/(1.0E4*PI) !OLD
C
          V(J1,J2)=+V(J1,J2)/(1.0E4*2.0) !10-5-90
C
          V(J1,J2)=-V(J1,J2)/(1.0E4*PI) !OLD
C
          VX(J1,J2)=-VX(J1,J2) !AIPS CONVENTION
C
          VY(J1,J2)=-VY(J1,J2) !AIPS CONVENTION
C
          WT=DTOT(J1,J2)
          WRITE(4,2001) U(J1,J2), V(J1,J2), VX(J1,J2), VY(J1,J2), WT
2001  FORMAT(2X,F10.6,1X,F10.6,2X,F12.6,1X,F12.6,1X,F10.4)
          ENDDO
        ENDDO
C
      RETURN
      END
      SUBROUTINE XSTAR_FOUR
C
C THIS ROUTINE CALCULATES THE FOURIER COMPONENTS AND WRITES THEM
C TO A FILE IN THE AIPS/UVFIL FORMAT
C
      INCLUDE 'XSTAR.INC/LIST'
C
      TYPE *, 'ENTERING XSTAR_FOUR'
C
C DETECTOR SPATIAL RESOLUTION IS IMPORTANT HERE
C
C
C   DANG=((XPOS3*2*PI)/10)-(PI) !RADIANS
      DANG=(XPOS3*2*PI)/10
C

```

```

M=MGRID
N=NGRID
VX(M,N)=VX(M,N)+COS(DANG)
VY(M,N)=VY(M,N)+SIN(DANG)
C
C  TYPE *,MGRID=',MGRID,NGRID=',NGRID
C  TYPE *,M=',M,N=',N
C  TYPE *,VX(M,N)=',VX(M,N)
C  TYPE *,VY(M,N)=',VY(M,N)
RETURN
END
SUBROUTINE XSTAR_PEN
C
C THIS SUBROUTINE DECIDES WHETHER THE PHOTON SURVIVES STRIKING
C THE FIRST GRID
C
C  INCLUDE 'XSTAR.INC/LIST'
C
C  TYPE *,'ENTERING XSTAR_PEN'
C  WRITE(3,*) 'ENTERING XSTAR_PEN'
C
C SLITW IS GIVEN IN XSTAR_GRID WHEN GRID IS CHOSEN
C
C  M=MGRID
C
C  REM=AMOD(10.0,SLITW(1))
C  SHIFT(1)=REM/2
C  SHIFT(2)=.0125/2
C  TYPE *,REM=',REM
C  TYPE *,SHIFT=',SHIFT
C  TYPE *,ISNUM=',ISNUM
C
C CENTER GRIDS IN 10 CM SQUARE AREA
C
C LOOP
C
C FIND WHICH INTERVAL SLIT OR SLAT THAT THE PHOTON FALLS
C
C  J1=0
C  STIF=0.0
C  DOWHILE (XPOS.GT.STIF)
C  J1=J1+1
C  TYPE *,J1=',J1
C  STIF=(J1*SLITW(M))+SHIFT(M)
C  TYPE *,STIF=',STIF
C  NSLIT=J1
C  ENDDO
C  TYPE *,NSLIT=',NSLIT
C
C DETERMINE IF IT PASSES THROUGH
C

```

```

      REM2=MOD(NSLIT,2)
C   TYPE *,REM2=',REM2
      IF (REM2.GT.0) THEN
        PTEST=7
      ENDIF
C
      RETURN
      END

      SUBROUTINE XSTAR_GRID
C
C   THE PURPOSE OF THE SUBROUTINE IS TO RANDOMLY SELECT A GRID
C   FOR PHOTON PENETRATION
C
C   IN THIS CASE TWO SLITS WIDTHS AT 30 DEGREES SEPARATION LEADS TO
C   24 GRIDS
C
C   INCLUDE 'XSTAR.INC/LIST'
C
C   WRITE(3,*) 'ENTERING XSTAR_GRID'
C   TYPE *, 'ENTERING XSTAR_GRID'
C
      TSLIT=2
      TGRID=24
C
      RAND=RANO(IDUM)
C   TYPE *,RAND=',RAND
C   WRITE(3,*) 'RAND=',RAND
      MDIV=1.0/TSLIT
      NDIV=1.0/TGRID
      K2=0
C
C 1ST INDEX
C
      DOWHILE (K2.LE.100)
        K2=K2+1
C   TYPE *,K2=',K2
        MDIV2=K2*MDIV
C   TYPE *,MDIV2=',MDIV2
        IF (RAND.LE.MDIV2) THEN
          MGRID=K2
          K2=101
        ENDIF
      ENDDO
C
C 2D INDEX
C
      K3=0
      RAND=RANO(IDUM)
C   TYPE *,RAND=',RAND
      DOWHILE (K3.LE.100)

```

```

      K3=K3+1
      NDIV2=K3*NDIV
      IF (RANDE.NDIV2) THEN
        NGRID=K3
        K3=101
      ENDIF
    ENDDO

C
C DETERMINE SLIT WIDTH HERE
C
      SLITW(1)=.0275
      SLITW(2)=.0125
C
C   TYPE *, 'LEAVING XSTAR_GRID'
C
      RETURN
      END
      SUBROUTINE XSTAR_LOCAL
C
C THIS ROUTINE ROTATES THE INCOMING PHOTON ANGLE TO CORRESPOND TO T
C OF THE GRID IN THE TELESCOPE
C
      INCLUDE 'XSTAR.INC/LIST'
C
C THIS ROUTINE MUST ALSO ASSIGN ROTATION ANGLES TO ALL GRIDS
C
      TYPE *, 'ENTERING XSTAR_LOCAL'
C
      DELTHL(1,1)=0.0
      DELTHL(2,1)=0.0
      DO J1=1, TSLIT
        DO J2=2, TGRID
          DELTHL(J1,J2)=DELTHL(J1,J2-1)+(15*(PI/180))
C        TYPE *, 'J1=', J1, ', J2=', J2
C        TYPE *, 'DELTHL(J1,J2)', DELTHL(J1,J2)
        ENDDO
      ENDDO
C
C   TYPE *, 'DELTHL'
C   TYPE *, DELTHL
C
C APPLY LOCAL GRID ANGLE TO INCOMING PHOTON ANGLE ABOUT TELESCOPE A
C
      THETA3=THETA3-DELTHL(MGRID,NGRID)
C
      RETURN
      END

      SUBROUTINE XSTAR_MTX(KK3)
C
C THIS ROUTINE GIVES THE TOTAL NUMBER OF PHOTONS MAKING IT

```



```

C AND THE TOTAL NUMBER MAKING IT TO A DETECTOR
C AND THE NUMBER PER BIN
C
C   INCLUDE 'XSTAR.INC/LIST'
C
C   INCR=21
C   DETRES=10.0/INCR
C   KK3=KK3+1
C
C   J1=0
C   DPOS=0.0
C   DOWHILE(XPOS3.GT.DPOS)
C   J1=J1+1
C   DPOS=J1*DETRES
C   ENDDO
C
C   M=MGRID
C   N=NGRID
C   TYPE *,J1=',J1
C   BIN(M,N,J1)=BIN(M,N,J1)+1
C   XDET(M,N,J1)=DPOS-DETRES/2
C   NTOT=KK3
C   DTOT(M,N)=DTOT(M,N)+1.0
C
C   TYPE *,NTOT=',NTOT
C
C   RETURN
C   END
C   SUBROUTINE XSTAR_PEN2
C
C   THIS SUBROUTINE DECIDES WHETHER THE PHOTON SURVIVES STRIKING
C   THE FIRST GRID
C
C   INCLUDE 'XSTAR.INC/LIST'
C
C   TYPE *,'ENTERING XSTAR_PEN2'
C   WRITE(3,*) 'ENTERING XSTAR_PEN2'
C
C   SLITW IS GIVEN IN XSTAR_GRID WHEN GRID IS CHOSEN
C   CENTER GRIDS IN 10 CM SQUARE AREA
C
C   M=MGRID
C   REM=AMOD(10.0,SLITW(1))
C   SLITW2(1)=(10.0-REM)/(365)
C   SLITW2(2)=(10.0-.0125)/(801)
C   SHIFT2(1)=(REM/2)
C   SHIFT2(2)=.0125/2
C
C   NOTE DIFF HERE FROM FIRST ROUTINE
C
C   TYPE *,REM=',REM

```

```

C  TYPE *, 'SLITW2=', SLITW2
C
C LOOP
C
C FIND WHICH INTERVAL SLIT OR SLAT THAT THE PHOTON FALLS
C
    J1=0
    STIF=0.0
    DOWHILE (XPOS2.GT.STIF)
        J1=J1+1
C     TYPE *, 'J1=', J1
        STIF=(J1*SLITW2(M))+SHIFT2(M)
C     TYPE *, 'STIF=', STIF
        NSLIT=J1
    ENDDO
C
C  TYPE *, 'NSLIT=', NSLIT
C
C DETERMINE IF IT PASSES THROUGH
C
    REM2= MOD(NSLIT,2)
C
C  TYPE *, 'REM2=', REM2
C
    IF (REM2.EQ.0) THEN
        PTEST=7
    ENDIF
C
    RETURN
END
SUBROUTINE XSTAR_POINT
C
    INCLUDE 'XSTAR.INC/LIST'
C
C
    TYPE *, 'ENTERING XSTAR_POINT'
C  TYPE *, 'CONFIRMED'
C  WRITE(10,*) 'ENTERING XSTAR_POINT'
C
C NOW RANDOMLY SELECT ANGLES FOR PHOTON
C
    RAND=RANO(IDUM)
C
C FOR UNIFORM FLARE OF 21 POINT SOURCES
C
    DIV=1.0/21
C
C
C
C  TYPE *, 'RAND=', RAND
C

```

```

C
C LOOP
C
C   J4=0
C   NDIV=0.0
C
C   DOWHILE (RAND.GT.NDIV)
C
C     J4=J4+1
C     TYPE *,J4=',J4
C     NDIV=J4*DIV
C     TYPE *,NDIV=',NDIV
C     PHI3=PHI(J4)
C     TYPE *,PHI3=',PHI3
C     THETA3=THETA(J4)
C     TYPE *,THETA3=',THETA3
C
C   ENDDO
C
C FOR UNIFORM FLARE OF 21 POINT SOURCES
C WITH ENDPOINT 10 TIMES BRIGHTER
C
C   DIV=1.0/39
C
C   P6=DIV*10
C   IF (RAND.LE.P6) THEN
C     PHI3=PHI(1)
C     THETA3=THETA(1)
C     J6=1
C   ENDIF
C
C   P7=DIV*29
C   IF (RAND.GE.P7) THEN
C     PHI3=PHI(21)
C     THETA3=THETA(21)
C     J6=21
C   ENDIF
C
C   I2=0
C   IF (RAND.GT.P6.AND.RAND.LT.P7) THEN
C     DO J5=2,20
C       I2=I2+1
C       P1=((DIV*10)+(I2*DIV))
C       IF (RAND.GT.P6.AND.RAND.LE.P1) THEN
C         PHI3=PHI(J5)
C         THETA3=THETA(J5)
C         J6=J5
C       ENDIF
C     P6=P1
C   ENDDO
C   ENDIF

```



```

C  ENDIF
C  IF (RAND.LT.(2*XNRATA).AND.RAND.GE.XNRATA) THEN
C      PHI3=PHI(2)
C      THETA3=THETA(2)
C      PANG(2)=PANG(2)+1
C      TYPE *,PANG(2)
C  ENDIF
C  IF (RAND.LT.(3*XNRATA).AND.RAND.GE.(2*XNRATA)) THEN
C      PHI3=PHI(3)
C      THETA3=THETA(3)
C      PANG(3)=PANG(3)+1
C      TYPE *,PANG(3)
C  ENDIF
C  IF (RAND.LT.(4*XNRATA).AND.RAND.GE.(3*XNRATA)) THEN
C      PHI3=PHI(4)
C      THETA3=THETA(4)
C      PANG(4)=PANG(4)+1
C      TYPE *,PANG(4)
C  ENDIF
C  IF (RAND.LT.(5*XNRATA).AND.RAND.GE.(4*XNRATA)) THEN
C      PHI3=PHI(5)
C      THETA3=THETA(5)
C      PANG(5)=PANG(5)+1
C      TYPE *,PANG(5)
C  ENDIF
C  XNR1=(5*XNRATA)
C  TYPE *,XNR1=XNR1
C  XNR2=XNR1+XNRATB
C  TYPE *,XNR2=XNR2
C  IF (RAND.LT.XNR2.AND.RAND.GE.XNR1) THEN
C      PHI3=PHI(6)
C      THETA3=THETA(6)
C      PANG(6)=PANG(6)+1
C      TYPE *,PANG(6)
C  ENDIF
C  XNR3=XNR1+(2*XNRATB)
C  TYPE *,XNR3=XNR3
C  IF (RAND.LT.XNR3.AND.RAND.GE.XNR2) THEN
C      PHI3=PHI(7)
C      THETA3=THETA(7)
C      PANG(7)=PANG(7)+1
C      TYPE *,PANG(7)
C  ENDIF
C  XNR4=XNR1+(3*XNRATB)
C  TYPE *,XNR4=XNR4
C  IF (RAND.LT.XNR4.AND.RAND.GE.XNR3) THEN
C      PHI3=PHI(8)
C      THETA3=THETA(8)
C      PANG(8)=PANG(8)+1
C      TYPE *,PANG(8)
C  ENDIF

```

```

C   XNR5=XNR1+(4*XNRATB)
C   TYPE *,XNR5=',XNR5
C   IF (RAND.LT.XNR5.AND.RAND.GE.XNR4) THEN
C       PHI3=PHI(9)
C       THETA3=THETA(9)
CC   PANG(9)=PANG(9)+1
CC   TYPE *,PANG(9)
C   ENDIF
C   XNR6=XNR1+(5*XNRATB)
C   TYPE *,XNR6=',XNR6
C   IF (RAND.LT.XNR6.AND.RAND.GE.XNR5) THEN
C       PHI3=PHI(10)
C       THETA3=THETA(10)
C       PANG(10)=PANG(10)+1
C       TYPE *,PANG(10)
C   ENDIF
C   XNR7=XNR1+(6*XNRATB)
C   TYPE *,XNR7=',XNR7
C   IF (RAND.LT.XNR7.AND.RAND.GE.XNR6) THEN
C       PHI3=PHI(11)
C       THETA3=THETA(11)
C       PANG(11)=PANG(11)+1
C       TYPE *,PANG(11)
C   ENDIF
C   XNR8=XNR1+(7*XNRATB)
C   TYPE *,XNR8=',XNR8
C   IF (RAND.LT.XNR8.AND.RAND.GE.XNR7) THEN
C       PHI3=PHI(12)
C       THETA3=THETA(12)
C       PANG(12)=PANG(12)+1
C       TYPE *,PANG(12)
C   ENDIF
C   XNR9=XNR1+(8*XNRATB)
C   TYPE *,XNR9=',XNR9
C   IF (RAND.LT.XNR9.AND.RAND.GE.XNR8) THEN
C       PHI3=PHI(13)
C       THETA3=THETA(13)
C       PANG(13)=PANG(13)+1
CC   TYPE *,PANG(13)
CC   ENDIF
CC   XNR10=XNR1+(9*XNRATB)
CC   TYPE *,XNR10=',XNR10
CCC   IF (RAND.LT.XNR10.AND.RAND.GE.XNR9) THEN
C       PHI3=PHI(14)
C       THETA3=THETA(14)
C       PANG(14)=PANG(14)+1
C       TYPE *,PANG(14)
C   ENDIF
C   XNR11=XNR1+(10*XNRATB)
C   TYPE *,XNR11=',XNR11
C   IF (RAND.LT.XNR11.AND.RAND.GE.XNR10) THEN

```

```

C     PHI3=PHI(15)
C     THETA3=THETA(15)
CC    PANG(15)=PANG(15)+1
C     TYPE *,PANG(15)
CC    ENDIF
C     XNR12=XNR1+(11*XNRATB)
C     TYPE *,XNR12=XNR12
C     IF (RAND.LT.XNR12.AND.RAND.GE.XNR11) THEN
C         PHI3=PHI(16)
CC        THETA3=THETA(16)
C        PANG(16)=PANG(16)+1
CC        TYPE *,PANG(16)
C    ENDIF
C    XNR13=XNR12+XNRATA
CC    TYPE *,XNR13=XNR13
CC    IF (RAND.LT.XNR13.AND.RAND.GE.XNR12) THEN
C        PHI3=PHI(17)
C        THETA3=THETA(17)
C        PANG(17)=PANG(17)+1
C        TYPE *,PANG(17)
C    ENDIF
C    XNR14=XNR12+(2*XNRATA)
C    TYPE *,XNR14=XNR14
C    IF (RAND.LT.XNR14.AND.RAND.GE.XNR13) THEN
C        PHI3=PHI(18)
C        THETA3=THETA(18)
C        PANG(18)=PANG(18)+1
C        TYPE *,PANG(18)
C    ENDIF
C    XNR15=XNR12+(3*XNRATA)
C    TYPE *,XNR15=XNR15
C    IF (RAND.LT.XNR15.AND.RAND.GE.XNR14) THEN
C        PHI3=PHI(19)
C        THETA3=THETA(19)
C        PANG(19)=PANG(19)+1
C        TYPE *,PANG(19)
C    ENDIF
C    XNR16=XNR12+(4*XNRATA)
C    TYPE *,XNR16=XNR16
C    IF (RAND.LT.XNR16.AND.RAND.GE.XNR15) THEN
C        PHI3=PHI(20)
CC        THETA3=THETA(20)
C        PANG(20)=PANG(20)+1
C        TYPE *,PANG(20)
C    ENDIF
C    XNR17=XNR12+(5*XNRATA)
C    TYPE *,XNR17=XNR17
C    IF (RAND.LT.XNRATA.AND.RAND.GE.0.0) THEN
C        PHI3=PHI(21)
C        THETA3=THETA(21)
C        PANG(21)=PANG(21)+1

```

```

C      TYPE *,PANG(21)
C      ENDIF
C
C*****
C**** THREE POINT "THERMAL FLARE"*****
C*****
C
C      IF (RAND.LE..28) THEN
C          PHI3=PHI(1)
C          THETA3=THETA(1)
C          PANG(1)=PANG(1)+1
C      ENDIF
C      IF (RAND.GT..28.AND.RAND.LE..68) THEN
C          PHI3=PHI(11)
C          THETA3=THETA(11)
C          PANG(11)=PANG(11)+1
C      ENDIF
C      IF (RAND.GT..68) THEN
C          PHI3=PHI(21)
C          THETA3=THETA(21)
C          PANG(21)=PANG(21)+1
C      ENDIF
C
C*****
C      MODEL T AT TIME=0 AT 10 KEV
C*****
C
C          XYZ=9.98E-4
C      IF (RAND.LE.XYZ) THEN
C          PHI3=PHI(1)
C          THETA3=THETA(1)
C          PANG(1)=PANG(1)+1
C      ENDIF
C      IF (RAND.GT.XYZ.AND.RAND.LT.(.999)) THEN
C          PHI3=PHI(11)
C          THETA3=THETA(11)
C          PANG(11)=PANG(11)+1
C      ENDIF
C      IF (RAND.GT.(.999)) THEN
C          PHI3=PHI(21)
C          THETA3=THETA(21)
C          PANG(21)=PANG(21)+1
C      ENDIF
C
C*****
C*****
C      MODEL NT AT 10 KEV AT 40 SEC
C*****
C
C
C      XNTOT=532320.0

```



```

CC  XNRAT1=(144000./XNTOT)
C   XNRAT2=(43200./XNTOT)+XNRAT1
C   XNRAT3=(240./XNTOT)+XNRAT2
C   XNRAT4=(960./XNTOT)+XNRAT3
C   XNRAT5=(1920./XNTOT)+XNRAT4
C   XNRAT6=(2880./XNTOT)+XNRAT5
C   XNRAT7=(3360./XNTOT)+XNRAT6
C   XNRAT8=(14400./XNTOT)+XNRAT7
C   XNRAT9=(19200./XNTOT)+XNRAT8
C   XNRAT10=(24000./XNTOT)+XNRAT9
C   XNRAT11=(24000./XNTOT)+XNRAT10
C   XNRAT12=(24000./XNTOT)+XNRAT11
C   XNRAT13=(19200./XNTOT)+XNRAT12
C   XNRAT14=(14400./XNTOT)+XNRAT13
C   XNRAT15=(3360./XNTOT)+XNRAT14
C   XNRAT16=(2880./XNTOT)+XNRAT15
C   XNRAT17=(1920./XNTOT)+XNRAT16
C   XNRAT18=(960./XNTOT)+XNRAT17
C   XNRAT19=(240./XNTOT)+XNRAT18
C   XNRAT20=(43200./XNTOT)+XNRAT19
C   XNRAT21=(144000./XNTOT)+XNRAT20
C
C   TYPE *,RAND='RAND
C   TYPE *,XNTOT='XNTOT
C   TYPE *,XNRAT1='XNRAT1
C   TYPE *,XNRAT2='XNRAT2
C   TYPE *,XNRAT3='XNRAT3
C   TYPE *,XNRAT4='XNRAT4
C   TYPE *,XNRAT5='XNRAT5
C   TYPE *,XNRAT6='XNRAT6
C   TYPE *,XNRAT7='XNRAT7
C   TYPE *,XNRAT8='XNRAT8
C   TYPE *,XNRAT9='XNRAT9
C   TYPE *,XNRAT10='XNRAT10
C   TYPE *,XNRAT11='XNRAT11
C   TYPE *,XNRAT12='XNRAT12
C   TYPE *,XNRAT13='XNRAT13
C   TYPE *,XNRAT14='XNRAT14
C   TYPE *,XNRAT15='XNRAT15
C   TYPE *,XNRAT16='XNRAT16
C   TYPE *,XNRAT17='XNRAT17
C   TYPE *,XNRAT18='XNRAT18
C   TYPE *,XNRAT19='XNRAT19
C   TYPE *,XNRAT20='XNRAT20
C   TYPE *,XNRAT21='XNRAT21
C
C   IF (RAND.LT.XNRAT1.AND.RAND.GE.0.0) THEN
C
C       PHI3=PHI(1)
C       THETA3=THETA(1)
C       PANG(1)=PANG(1)+1

```

```

C      TYPE *,PANG(1)
C      TYPE *,'FLARE POSITION=',1
C  ENDIF
C  IF (RAND.LT.(XNRAT2).AND.RAND.GE.XNRAT1) THEN
C      PHI3=PHI(2)
C      THETA3=THETA(2)
C      PANG(2)=PANG(2)+1
C      TYPE *,PANG(2)
C      TYPE *,'FLARE POSITION=',2
C  ENDIF
C  IF (RAND.LT.(XNRAT3).AND.RAND.GE.(XNRAT2)) THEN
C      PHI3=PHI(3)
C      THETA3=THETA(3)
C      PANG(3)=PANG(3)+1
C      TYPE *,PANG(3)
C      TYPE *,'FLARE POSITION=',3
C  ENDIF
C  IF (RAND.LT.(XNRAT4).AND.RAND.GE.(XNRAT3)) THEN
C      PHI3=PHI(4)
C      THETA3=THETA(4)
C      PANG(4)=PANG(4)+1
C      TYPE *,PANG(4)
C      TYPE *,'FLARE POSITION=',4
C  ENDIF
C
C  IF (RAND.LT.(XNRAT5).AND.RAND.GE.(XNRAT4)) THEN
C      PHI3=PHI(5)
C      THETA3=THETA(5)
C      PANG(5)=PANG(5)+1
C      TYPE *,PANG(5)
C      TYPE *,'FLARE POSITION=',5
C  ENDIF
C
C  IF (RAND.LT.(XNRAT6).AND.RAND.GE.(XNRAT5)) THEN
C      PHI3=PHI(6)
C      THETA3=THETA(6)
C      PANG(6)=PANG(6)+1
C      TYPE *,PANG(6)
C      TYPE *,'FLARE POSITION=',6
CC  ENDIF
C
C  IF (RAND.LT.(XNRAT7).AND.RAND.GE.(XNRAT6)) THEN
C      PHI3=PHI(7)
C      THETA3=THETA(7)
C      PANG(7)=PANG(7)+1
C      TYPE *,PANG(7)
C      TYPE *,'FLARE POSITION=',7
C  ENDIF
C
C  IF (RAND.LT.(XNRAT8).AND.RAND.GE.(XNRAT7)) THEN
C      PHI3=PHI(8)

```

```

C      THETA3=THETA(8)
C      PANG(8)=PANG(8)+1
C      TYPE *,PANG(8)
C      TYPE *,'FLARE POSITION=',8
C  ENDIF
C
C  IF (RAND.LT.(XNRAT9).AND.RAND.GE.(XNRAT8)) THEN
C      PHI3=PHI(9)
C      THETA3=THETA(9)
C      PANG(9)=PANG(9)+1
C      TYPE *,PANG(9)
C      TYPE *,'FLARE POSITION=',9
C  ENDIF
C
C  IF (RAND.LT.XNRAT10.AND.RAND.GE.XNRAT9) THEN
C      PHI3=PHI(10)
C      THETA3=THETA(10)
C      PANG(10)=PANG(10)+1
C      TYPE *,PANG(10)
C      TYPE *,'FLARE POSITION=',10
C  ENDIF
C
C  IF (RAND.LT.XNRAT11.AND.RAND.GE.XNRAT10) THEN
C      PHI3=PHI(11)
C      THETA3=THETA(11)
C      PANG(11)=PANG(11)+1
C      TYPE *,PANG(11)
C      TYPE *,'FLARE POSITION=',11
C  ENDIF
C
C  IF (RAND.LT.XNRAT12.AND.RAND.GE.XNRAT11) THEN
C      PHI3=PHI(12)
C      THETA3=THETA(12)
C      PANG(12)=PANG(12)+1
C      TYPE *,PANG(12)
C      TYPE *,'FLARE POSITION=',12
C  ENDIF
C
C  IF (RAND.LT.XNRAT13.AND.RAND.GE.XNRAT12) THEN
C      PHI3=PHI(13)
C      THETA3=THETA(13)
C      PANG(13)=PANG(13)+1
C      TYPE *,PANG(13)
C      TYPE *,'FLARE POSITION=',13
C  ENDIF
C
C  IF (RAND.LT.XNRAT14.AND.RAND.GE.XNRAT13) THEN
C      PHI3=PHI(14)
C      THETA3=THETA(14)
C      PANG(14)=PANG(14)+1
C      TYPE *,PANG(14)

```

```

C      TYPE *,FLARE POSITION=',14
C  ENDIF
C
C  IF (RAND.LT.XNRAT15.AND.RAND.GE.XNRAT14) THEN
C      PHI3=PHI(15)
C      THETA3=THETA(15)
C      PANG(15)=PANG(15)+1
C      TYPE *,PANG(15)
C      TYPE *,FLARE POSITION=',15
C  ENDIF
C
C  IF (RAND.LT.XNRAT16.AND.RAND.GE.XNRAT15) THEN
C      PHI3=PHI(16)
C      THETA3=THETA(16)
C      PANG(16)=PANG(16)+1
C      TYPE *,PANG(16)
C      TYPE *,FLARE POSITION=',16
C  ENDIF
C
C  IF (RAND.LT.XNRAT17.AND.RAND.GE.XNRAT16) THEN
C      PHI3=PHI(17)
C      THETA3=THETA(17)
CC      PANG(17)=PANG(17)+1
C      TYPE *,PANG(17)
C      TYPE *,FLARE POSITION=',17
C  ENDIF
CC
C  IF (RAND.LT.XNRAT18.AND.RAND.GE.XNRAT17) THEN
C      PHI3=PHI(18)
C      THETA3=THETA(18)
C      PANG(18)=PANG(18)+1
C      TYPE *,PANG(18)
CC      TYPE *,FLARE POSITION=',18
CC  ENDIF
C
C  IF (RAND.LT.XNRAT19.AND.RAND.GE.XNRAT18) THEN
C      PHI3=PHI(19)
C      THETA3=THETA(19)
C      PANG(19)=PANG(19)+1
C      TYPE *,PANG(19)
CC      TYPE *,FLARE POSITION=',19
C  ENDIF
C
C  IF (RAND.LT.XNRAT20.AND.RAND.GE.XNRAT19) THEN
C      PHI3=PHI(20)
C      THETA3=THETA(20)
C      PANG(20)=PANG(20)+1
C      TYPE *,PANG(20)
C      TYPE *,FLARE POSITION=',20
C  ENDIF
C

```

```

C IF (RAND.LT.XNRAT21.AND.RAND.GE.XNRAT20) THEN
C   PHI3=PHI(21)
C   THETA3=THETA(21)
C   PANG(21)=PANG(21)+1
C   TYPE *,PANG(21)
C   TYPE *,'FLARE POSITION=',21
C   ENDIF
C
C*****
C*****
C*****
C*****
C MODEL T AT 10 KEV AT 10 SEC
C*****
C
C
C   XNRAT1=.0769
C
C IF (RAND.LT.XNRAT1.AND.RAND.GE.0.0) THEN
C
C   PHI3=PHI(1)
C   THETA3=THETA(1)
C   PANG(1)=PANG(1)+1
C   TYPE *,PANG(1)
C   TYPE *,'FLARE POSITION=',1
C   ENDIF
C
C IF (RAND.LT.(2*XNRAT1).AND.RAND.GE.XNRAT1) THEN
C   PHI3=PHI(6)
C   THETA3=THETA(6)
C   PANG(6)=PANG(6)+1
C   TYPE *,PANG(2)
C   TYPE *,'FLARE POSITION=',2
C   ENDIF
C
C IF (RAND.LT.(3*XNRAT1).AND.RAND.GE.(2*XNRAT1)) THEN
C   PHI3=PHI(7)
C   THETA3=THETA(7)
C   PANG(7)=PANG(7)+1
C   TYPE *,PANG(3)
C   TYPE *,'FLARE POSITION=',3
C   ENDIF
C
C IF (RAND.LT.(4*XNRAT1).AND.RAND.GE.(3*XNRAT1)) THEN
C   PHI3=PHI(8)
C   THETA3=THETA(8)
C   PANG(8)=PANG(8)+1
C   TYPE *,PANG(4)
C   TYPE *,'FLARE POSITION=',4
C   ENDIF
C

```

```

      IF (RAND.LT.(5*XNRAT1).AND.RAND.GE.(4*XNRAT1)) THEN
        PHI3=PHI(9)
        THETA3=THETA(9)
        PANG(9)=PANG(9)+1
C      TYPE *,PANG(5)
C      TYPE *,FLARE POSITION=,5
      ENDIF
C
      IF (RAND.LT.(6*XNRAT1).AND.RAND.GE.(5*XNRAT1)) THEN
        PHI3=PHI(10)
        THETA3=THETA(10)
        PANG(10)=PANG(10)+1
C      TYPE *,PANG(6)
C      TYPE *,FLARE POSITION=,6
      ENDIF
C
      IF (RAND.LT.(7*XNRAT1).AND.RAND.GE.(6*XNRAT1)) THEN
        PHI3=PHI(11)
        THETA3=THETA(11)
        PANG(11)=PANG(11)+1
C      TYPE *,PANG(7)
C      TYPE *,FLARE POSITION=,7
      ENDIF
C
      IF (RAND.LT.(8*XNRAT1).AND.RAND.GE.(7*XNRAT1)) THEN
        PHI3=PHI(12)
        THETA3=THETA(12)
        PANG(12)=PANG(12)+1
C      TYPE *,PANG(8)
C      TYPE *,FLARE POSITION=,8
      ENDIF
C
      IF (RAND.LT.(9*XNRAT1).AND.RAND.GE.(8*XNRAT1)) THEN
        PHI3=PHI(13)
        THETA3=THETA(13)
        PANG(13)=PANG(13)+1
C      TYPE *,PANG(9)
C      TYPE *,FLARE POSITION=,9
      ENDIF
C
      IF (RAND.LT.(10*XNRAT1).AND.RAND.GE.(9*XNRAT1)) THEN
        PHI3=PHI(14)
        THETA3=THETA(14)
        PANG(14)=PANG(14)+1
C      TYPE *,PANG(10)
C      TYPE *,FLARE POSITION=,10
      ENDIF
C
      IF (RAND.LT.(11*XNRAT1).AND.RAND.GE.(10*XNRAT1)) THEN
        PHI3=PHI(15)
        THETA3=THETA(15)

```

```

      PANG(15)=PANG(15)+1
C      TYPE *,PANG(11)
C      TYPE *,'FLARE POSITION=',11
      ENDIF
C
      IF (RAND.LT.(12*XNRAT1).AND.RAND.GE.(11*XNRAT1)) THEN
        PHI3=PHI(16)
        THETA3=THETA(16)
        PANG(16)=PANG(16)+1
C        TYPE *,PANG(16)
C        TYPE *,'FLARE POSITION=',16
      ENDIF
C
      IF (RAND.LT.(13*XNRAT1).AND.RAND.GE.(12*XNRAT1)) THEN
        PHI3=PHI(21)
        THETA3=THETA(21)
        PANG(21)=PANG(21)+1
C        TYPE *,PANG(21)
C        TYPE *,'FLARE POSITION=',21
      ENDIF
C
C*****
C*****
C
      RETURN
      END
      SUBROUTINE XSTAR_XY
C
C CALCULATE IMPACT OF PHOTON ON LOWER GRID
C
      INCLUDE 'XSTAR.INC/LIST'
C
      TYPE *,'ENTERING XSTAR_XY'
C      WRITE(3,*) 'ENTERING XSTAR_XY'
C
      GSEP=520 !CM
C
      TYPE *,'THETA3(SUB)=' ,THETA3
      DELX=GSEP*TAN(PHI3)*SIN(THETA3)
      DELY=GSEP*TAN(PHI3)*COS(THETA3)
C
      XPOSX=XPOS-DELX
      YPOSX=YPOS-DELY
      XPOS2=(XPOSX*COS(TWIST))+(YPOSX*SIN(TWIST))
      YPOS2=(YPOSX*COS(TWIST))-(XPOSX*SIN(TWIST))
C
C      WRITE(3,*) 'XPOS2=',XPOS2,'YPOS2=',YPOS2
C
      IF (XPOS2.GT.10.0.OR.YPOS2.GT.10.0) THEN
        PTEST=7
      ENDIF

```

```

C
  IF (XPOS2.LT.0.0.OR.YPOS2.LT.0.0) THEN
    PTEST=7
  ENDIF
C  TYPE *,XPOS2=',XPOS2,YPOS2=',YPOS2
C  TYPE *,PTEST=',PTEST
  RETURN
  END
  SUBROUTINE XSTAR_XY2
C
C CALCULATE IMPACT OF PHOTON ON LOWER GRID
C
  INCLUDE 'XSTAR.INC/LIST'
C
  TYPE *,'ENTERING XSTAR_XY2'
C
  GSEP2=1.0      !CM
C
  DELX=GSEP2*TAN(PHI3)*SIN(THETA3)
  DELY=GSEP2*TAN(PHI3)*COS(THETA3)
C
  XPOS3=XPOS2-DELX
  YPOS3=YPOS2-DELY
C
  IF (XPOS3.GT.10.0.OR.YPOS3.GT.10.0) THEN
    PTEST=7
  ENDIF
C
  IF (XPOS3.LT.0.0.OR.YPOS3.LT.0.0) THEN
    PTEST=7
  ENDIF
C
C  TYPE *,'PHI3=',PHI3,',','THETA3=',THETA3
C  TYPE *,'DELX=',DELX,'DELY=',DELY
C  TYPE *,'XPOS3=',XPOS3,'YPOS3=',YPOS3
  RETURN
  END

```



## APPENDIX D

### RMC Code

This appendix contains an example of the code defining the RMC design described in Chapter VI and its associated end-to-end, random photon counting simulation. The design/simulation provides a data stream of Fourier components which may be used as input for AIPS. This operating system will then provide a final image.

```

PROGRAM XRAYS_MAIN
C
C THIS IS THE MOTHER PROGRAM FOR DETERMINING A TELESCOPE'S RESPONSE
C TO AN INCOMING EXTENDED SOURCE WAVEFRONT USING THE RAY TRACE
C METHOD AND WRITING THE VISIBILITY POINTS TO A U,V FILE FOR INPUT
C INTO AIPS. IN THIS PROGRAM, THE EXTENDED SOURCE IS TREATED AS A
C COMBINATION OF POINT SOURCES WHICH ARE SUPERIMPOSED TO FORM A
C COMPLEX TRACE WHICH IS THEN BROKEN INTO COMPONENTS USING THE BINNI
C METHOD.
C
C   INCLUDE 'FIXESDATA.INC/LIST'
C
C TELESCOPE GEOMETRY LOOP
C
C   DO 1000 NGRID = 1,2
C
C     TYPE *, 'NGRID = ', NGRID
C
C     TYPE *, 'ENTERING FIXES_GEO'
C
C     CALL FIXES_GEO(NGRID)
C     CALL GRID_GEO(NGRID)
C
C FLARE GEOMETRY LOOP
C
C   DO 1000 K5 = 1,20
C
C     TYPE *, 'FLARE GEOMETRY LOOP: ', 'SOURCE POINT # = ', K5
C     TYPE *, 'ENTERING FLARE_GEO'
C
C     CALL FLARE_GEO(K5)
C
C     TYPE *, 'ENTERING XRAYS_BETA'
C
C     CALL XRAYS_BETA
C
C     TYPE *, 'ENTERING XRAYS_THARY'
C
C     CALL XRAYS_THARY
C
C     TYPE *, 'ENTERING XRAYS_THETA'
C
C     CALL XRAYS_THETA
C
C     TYPE *, 'ENTERING XRAYS_SLOPE'
C
C     CALL XRAYS_SLOPE
C

```

```

C      TYPE *, 'ENTERING XRAYs_MVAL'
C      CALL XRAYs_MVAL
C      TYPE *, 'ENTERING XRAYs_PHI'
C      CALL XRAYs_PHI
C      TYPE *, 'ENTERING XRAYs_ALPHA'
C      CALL XRAYs_ALPHA
C      TYPE *, 'ENTERING XRAYs_FALPHA'
C      CALL XRAYs_FALPHA
C      TYPE *, 'ENTERING XRAYs_FALPHA_ROTATE'
C      CALL XRAYs_FALPHA_ROTATE
C      TYPE *, 'ENTERING XRAYs_SAWTH'
C      CALL XRAYs_SAWTH(NGRID,K5)
C
C900  CONTINUE
C      TYPE *, 'ENTERING XRAYs_BIN'
C
C      NOTE: THIS PLOT CALL MUST BE COMMENTED
C      OUT TO USE THE ONE IN SAWTH
C
C      IF (K5.EQ. 1 .OR. 20) THEN
C      CALL PLOT_XRAY (SAWTP,FSAWTP,IB,8,DVAL,LVAL,KI)
C      ENDIF
C
C      CALL XRAYs_BIN(NGRID,K5)
C
C1000 CONTINUE
C
C9999 STOP
C      END
C      FIXESDATA.INC
C
C      REAL*4 THARY(2000),FTHARY(2000),THETA(8100),
1  FTHETA(8100),DTHETA(1200),SLOPE(1200)
C
C      REAL*4 BETA(100),DPHI(1000),PHI(30000)
C
C      REAL*4 SAWT(2,30000),FSAWT(2,30000)
C
C      REAL*4 SAWT1(30000),FSAWT1(30000)

```

```

C
REAL*4 SAWTP(30000),FSAWTP(30000)
C
REAL*4 ALPHA(30000),FALPHA(30000),XPHI(30000),YFALPHA(30000)
C
REAL*4 DVAL,LVAL,PI,NUM(101),DNUM(101)
C
REAL*4 DUM1(30000),DUM2(30000),DUM3(30000),DUM4(30000)
C
REAL*4 BINA(200),BINB(200),BINC(200),BIND(200),SUM(200)
C
REAL*4 U(200),V(200),VX(200),VY(200)
C
REAL*4 REGA(200),SAWTH(40),FSAWD(2,30000),TERVAL
C
INTEGER*4 MVAL,NGRID,KI,XL(8),M
C
CCC DATA DVAL/.0027/,LVAL/40.0/,PI/3.14159/,KI/10/
CCC DATA DVAL/.0349/,LVAL/40.0/,PI/3.14159/,KI/10/
CCC DATA DVAL/.00465/,LVAL/40.0/,PI/3.14159/,KI/10/
CCC DATA DVAL/.0087/,LVAL/40.0/,PI/3.14159/,KI/10/
CCC DATA DVAL/.0175/,LVAL/40.0/,PI/3.14159/,KI/10/
C
DATA LVAL/5.2/,PI/3.14159/,KI/1/
C
COMMON/THET/ THARY,FTHARY,THETA,FTHETA,DTHETA,SLOPE
C
COMMON/BEPH/ BETA,DPHI,PHI
C
COMMON/ALPH/ ALPHA,FALPHA,XPHI,YFALPHA
C
COMMON/RDATA/ DVAL,LVAL,PI,NUM,DNUM
C
COMMON/IDATA/ KI,MVAL
C
COMMON/SAW/ SAWTH,SAWT,FSAWT,SAWTP,FSAWTP
C
COMMON/SAWW/ SAWT1,FSAWT1
C
COMMON/BIN/ BINA,BINB,BINC,BIND,IB,SUM
C
COMMON/DUM/ DUM1,DUM2,DUM3,DUM4,VX,VY,U,V
C
COMMON/REG/ REGA,SAWD
C
C-----
SUBROUTINE FLARE_GEO(K5)
C
C THE PURPOSE OF THIS SUBROUTINE IS TO BUILD A FLARE
C FROM A COLLECTION OF POINT SOURCES, A SIGNIFICANT
C PROBLEM IS WHAT COLLECTION OF POINTS BEST REPRESENT

```

```

C A FLARE OF INTEREST.
C
C THIS ATTEMPT AT PAINTING A FLARE WILL BE REPRESENTED
C BY A 100 ARCSECOND LONG SEMICIRCLE WITH 20 POINT
C SOURCES EQUA-SPACED ALONG THE ARC. THIS MEANS THE
C RADIUS OF THE FLARE WILL BE 100/PI.
C
C THE ORIENTATION OF THE FLARE TO THE VERTICAL AXIS
C OF THE TELESCOPE WILL BE 45 DEGREES. THE FIRST
C POINT WILL BE 4.5 DEGREES OF ROTATION FROM THE
C HORIZONTAL, THE NEXT WILL BE 4.5 + 9.0, THE NEXT
C 4.5+9.0+9.0 AND SO FORTH. ESSENTIALLY, DIVIDING
C 180 DEGRESS BY 20 PIXELS AND PUTTING THE POINT
C SOURCE IN THE CENTER OF EACH PIXEL.
C
C   INCLUDE 'FIXESDATA.INC/LIST'
C
C   DIMENSION PSI(30)
C
C   OPEN(UNIT=3,FILE='FLARE.DAT',STATUS='NEW')
C
C   LET PSI BE THE ANGLE AROUND THE CIRCLE
C   LET DELPSI BE THE ITERATION OR 9.0 DEGREES
C
C     PSI(1) = 4.5*(PI/180.0)
C     DO J = 2,20
C       PSI(J)=PSI(J-1)+(9.0*(PI/180.0))
CCC   TYPE *,J='J',PSI(J)='PSI(J)
C     END DO
C
C   DEFINE ANGLES OF FLARE POINT
C
C   ANGLE FROM AXIS OF ROTATION OF TELESCOPE IN RADIANS
C   DO N=1,20
C
C     WRITE(3,*) 'KI BEFORE ERROR=' ,KI, 'N BEFORE ERROR=' ,N
C     BETA(KI)=BETA(KI)+((SIN(PSI(N)))*(10.0/18.0)
C     1 *(1/3600.0))
C
C
C     WRITE(3,*) 'BETA(KI)=' ,BETA(KI), 'KI=' ,KI
C     WRITE(3,*) 'PSI(N)=' ,PSI(N), 'N=' ,N
C
C
C   ANGLE OF ROTATION OF TELESCOPE ABOUT AXIS OF ROTATION
C   TO COALIGN POINT SOURCE AND VERTICAL AXIS OF TELESCOPE
C
C     SAWTH(N)=((PI/180.0)*45.0)+((COS(PSI(N)))

```

```

1 *(10.0/18.0)*(1/3600.0))
C  WRITE(3,*) 'SAWTH(K5)=' ,SAWTH,K5=' ,K5
C  WRITE(3,*) 'BETA(KI)=' ,BETA(KI),KI=' ,KI
  ENDDO
  RETURN
  END
  SUBROUTINE XRAY5_BETA
C
  INCLUDE 'FIXESDATA.INC/LIST'
C
C-----
C
C THE PURPOSE OF THIS LOOP IS TO SPAN THE TELESCOPE FIELD OF VIEW OF
C APROXIMATELY 10 DEGREES FOR A POINT SOURCE. WE WILL INPUT THE
C ANGLE KI.
C
  DO I=1,100
C
    IF(I.EQ.1) THEN
C
      BETA(I) = PI/1800
C
    ELSE
C
C BETA IS ANGLE OF POINT SOURCE FROM AXIS OF TELESCOPE
C
      BETA(I) = BETA(I-1) + PI/1800
    ENDIF
C
  END DO
C
  RETURN
  END
  SUBROUTINE XRAY5_THARY
C
  INCLUDE 'FIXESDATA.INC/LIST'
C
  I = 0
C
C THIS LOOP IDENTIFIES THE NORMALIZED MAXS AND MINS FOR A POINT
C SOURCE AT AN ANGLE THETA THAT THIS DETECTOR SEES
C
C THARY(I) ARE THE ANGLES AT WHICH ALPHA (THETA) ARE MAXS,MINS
C
C THIS IS TWO DIMENSIONAL PROBLEM WITH POINT SOURCE LYING IN PLANE
C THAT CROSS SECTIONS SLITS AT 90 DEG.
C
C2345678901234567890
C
  DO N=1,800
    M = N-1

```

```

      I = I + 1
C
C THE EQUATION FOR THETA MAX
C
      THARY(I) = ATAN((2 * M * DVAL) / LVAL)
C
      FTHARY(I) = 1.0
C
C DIAGNOSTICS: WRITE THETA MAX VALUES TO 'FOR002.DAT', FOR VIEWING.
C
CCC  WRITE(2,25)I,THARY(I),FTHARY(I)
C
      I = I + 1
C
C THE EQUATION FOR THETA MIN
C
      THARY(I) = ATAN(((2 * M + 1) * DVAL) / LVAL)
C
      FTHARY(I) = 0.0
C
C DIAGNOSTICS: WRITE THETA MIN VALUES TO 'FOR002.DAT', FOR VIEWING.
C
CCC  WRITE(2,25)I,THARY(I),FTHARY(I)
20  FORMAT(1X,F12.6,2X,F12.6)
25  FORMAT(1X,I4,''),'THARY='F12.6,2X,'FTHARY='F12.6)
      END DO
      TYPE *, 'I=',I,'THARY(I)=' ,THARY(I),'FTHARY(I)=' ,FTHARY(I)
9999 RETURN
      END
      SUBROUTINE XRAYS _THETA
C
      INCLUDE 'FIXESDATA.INC/LIST'
C
C-----
C
C NOW WE BUILD A SAWTOOTH CURVE USING THE END POINTS CALCULATED
C BEFORE BUILDING AN FTHETA VS THETA SAWTOOTH
C
      THETA(1) = THARY(1)
      FTHETA(1) = FTHARY(1)
      I = 0
      DO N = 1,800      !500
C
      FTHETA(N*10) = FTHARY(N+1)
      THETA(N*10) = THARY(N+1)
C*** DIAGNOSTICS ***
C
C  WRITE(8,100)N,FTHETA(N),THETA(N)
100  FORMAT(1X,I4,''),'FTHETA='F15.6,2X,'THETA='F15.6)
      END DO

```

```

C
  RETURN
  END

  SUBROUTINE XRAYS_SLOPE
C
  INCLUDE 'FIXESDATA.INC/LIST'
C
C-----
C
C NUMERATOR AND DENOMINATOR DIAGNOSTIC FOR SLOPE
C
  NUM(1) = (FTHETA(10)) - (FTHETA(1))
  DNUM(1) = (THETA(10)) - (THETA(1))
C
C CALCULATING SLOPE OF EACH LINE SEGMENT
C
  SLOPE(1) = NUM(1)/DNUM(1)
  TYPE *, 'SLOPE(1) = ', SLOPE(1)
  II = 0
  DO 10 N = 1, 800
    M = N + 1
    I = (N + 1) * 10
    J = N * 10
C
C FOR 1ST SEGMENT, WE MUST USE 9, FOR 2ND, 10
C
CCC TYPE *, F(I) = ', FTHETA(I), F(J) = ', FTHETA(J),
CCC *      'T(I) = ', THETA(I), T(J) = ', THETA(J)
C
  SLOPE(M) = (FTHETA(I) - FTHETA(J))
1    / (THETA(I) - THETA(J))
C
  IF(N.EQ.1) THEN
    DTHETA(N) = (THETA(N*10) - THETA(N)) / 9
C
  ELSE
    DTHETA(N) = (THETA(N*10) - THETA((N-1)*10)) / 10
C
  END IF
C
  DO L = 1, 9
    II = II + 1
C
    THETA(II+1) = THETA(II) + DTHETA(N)
C
    IF(N.EQ.1) THEN
      FTHETA(II) = SLOPE(N) * THETA(II) + 1.0
C
    ELSE
      IF(SLOPE(N).LT.0.0) FTHETA(II+1) = (SLOPE(N)*(THETA(II+1) - THETA

```



```

1      (10*(N-1)))) +1.0
C
      IF(SLOPE(N).GT.0.0) FTHETA(II+1) = SLOPE(N) * (THETA(II+1) -
1      THETA(10*(N-1)))
      ENDIF
C
      ENDDO
C
      II = (N * 10) -1
C
C SAVE N VALUE IN N1 FOR PLOT PURPOSE
C
10  CONTINUE
      N1 = (N-1)*10
      NN1 = II - (L-1)
      TYPE *,N1=',N1',NN1=',NN1
C
C
C PLOT THETA VS FTHETA
C CALL PLOT ROUTINE
C
C  CALL PLOT_XRAY (THETA,FTHETA,500,1,DVAL,LVAL,KI)
C
C  DO K = 1,1001
CCC  WRITE(7,100)K,THETA(K),FTHETA(K)
100  FORMAT(1X,I4,',',2X,THETA=',F10.6,2X,FTHETA=',F10.6)
C  ENDDO
C
      RETURN
      END
      SUBROUTINE XRAYS_MVAL
C
      INCLUDE 'FIXESDATA.INC/LIST'
C
      REAL*4 RVAL
C LETS CALCULATE MVAL
C
      DOMN = 1,500
C
      RVAL= (2 * MN) * (DVAL/LVAL) * (1.0/(TAN(BETA(KI))))
C
      IF(RVAL.GT. 1.0) GO TO 10
C
      MVAL = MN
C
      RVAL= ((2 * MN) + 1) * (DVAL/LVAL) * (1.0/(TAN(BETA(KI))))
C
      IF(RVAL.GT. 1.0) GO TO 10
C
CCC  WRITE(8,100)MN,MVAL,RVAL
100  FORMAT(1X,I4,',',1X,MVAL=',J4,1X,RVAL=',F13.9)

```

```

      END DO
C
10  CONTINUE
CCC  WRITE(8,101)MN,MVAL,RVAL
101  FORMAT(//,1X,I4,')',1X,MVAL=',I4,1X,RVAL=',F13.9)
      TYPE *, 'MN=',MN,MVAL=',MVAL,RVAL=',RVAL
      RETURN
      END
      SUBROUTINE XRAYS_PHI
C
      INCLUDE 'FIXESDATA.INC/LIST'
C
C THIS LOOP REPRESENTS THE TELESCOPE ROTATION
C DEFINES PHI MAXS & MINS AND DELTA PHI'S
C
      KK = 0
      IT = 0
      M = MVAL
      DO 10 N= 1,550
C
C PHI IS THE ANGLE OF ROTATION OF TELESCOPE
C
C
      IT = IT + 1
C
C GIVES PHI MAX
C
      Y = 1.0/(TAN(BETA(KI)))
      PHI(IT*10)=ACOS((2*M*DVAL)/LVAL*Y)
      FALPHA(IT*10)=1.0
C
      IT = IT + 1
      M = M - 1
      IF(M.LT.0) GO TO 20
C
C
C GIVES PHI MIN
C
      Y = 1.0/(TAN(BETA(KI)))
      PHI(IT*10)=ACOS(((2*M+1)*DVAL)/LVAL*Y)
      FALPHA(IT*10)=0.0
C
C
10  CONTINUE
20  CONTINUE
C
C THIS LOOP IS JUST A DIAGNOSTIC WRITE OF THE FALPHA & PHI ARRAYS
C
CCC  DO J=1,100
CCC  WRITE(8,100)J,FALPHA(J),PHI(J),DPHI(J)
100  FORMAT(1X,I4,')',FALPHA=',F10.6,1X,PHI=',F10.6,1X,

```

```

      1 'DPHI='F12.6)
CCC  ENDDO
C-----
C
C BREAK PHI INTO EQUAL SEGMENTS
C
  DO 30 N = 1,800
    IF(N.EQ.1) THEN
      DPHI(1) = (PHI(10) - PHI(1))/9
    C
    ELSE
      DPHI(N) = (PHI(N*10) - PHI((N-1)*10))/10
    ENDIF
  C
  DO K = 1,9
    KK = KK + 1
  C
    PHI(KK+1) = PHI(KK) + DPHI(N)
  C
  C
    IF(PHI(KK+1) .GE. 1.570796) GO TO 40
    IF(PHI(KK) .GE. 1.570796) GO TO 40
  C
  C
    ENDDO
  C
    KK = (N*10)-1
    KKPTS = KK - (K-1)      !THE # OF POINTS TO PLOT
30  CONTINUE
40  CONTINUE
    TYPE *, 'N='N-1,'KK='KK,'PHI(KK)='PHI(KK)
  C
  C
  C THIS LOOP IS JUST FOR DIAGNOSTIC PURPOSES...PRINT FALPHA & PHI ARRAYS
  C
  CCC  DO M = 1,100
  CCC  WRITE(8,110)M,FALPHA(M),PHI(M),DPHI(M)
110  FORMAT(1X,I4,'),'FALPHA='F10.6,1X,'PHI='F10.6,1X,
      1 'DPHI='F12.6)
  CCC  ENDDO
  C
  C
  C THIS LOOP IS JUST FOR DIAGNOSTIC PURPOSES...PRINT FALPHA & PHI ARRAYS
  C
  CCC  DO M = 2500,3000
  CCC  WRITE(8,120)M,FALPHA(M),PHI(M)
120  FORMAT(1X,I4,'),'FALPHA='F10.6,1X,'PHI='F10.6)
  CCC  ENDDO
      TYPE *, 'KKPTS='KKPTS
  C
  C PLOT PHI VS FALPHA

```

```

C CALL PLOT ROUTINE
C
C   CALL PLOT_XRAY (PHI,FALPHA,KKPTS,2,DVAL,LVAL,KI)
C
  RETURN
  END
  SUBROUTINE XRAYS_ALPHA
C
  INCLUDE 'FIXESDATA.INC/LIST'
C
C PICK ONE VALUE OF I AT THIS POINT ,I-10
C
C
  DO N =1,8000
C
C ALPHA IS EQUIVALENT VIEW ANGLE COMBINING PHI AND BETA AND
C CORRESPONDS TO THETA
C
C
C
    ALPHA(N) =ABS(ATAN(TAN(BETA(KI)) * COS(PHI(N))))
C
CCC  WRITE(7,100)N,ALPHA(N),PHI(N)
100  FORMAT(1X,I4,')',1X,'ALPHA=',F10.6,1X,'PHI=',F10.6)
C
    IF ( ALPHA(N) .LE. 0.0) GO TO 10
C
  END DO
10  CONTINUE
    N3=N-1
C
    TYPE *,N3='N3
C
C PLOT ALPHA VS PHI
C CALL PLOT ROUTINE
C
C   CALL PLOT_XRAY (PHI,ALPHA,N3,3,DVAL,LVAL,KI)
C
  RETURN
  END
  SUBROUTINE XRAYS_FALPHA
C
  INCLUDE 'FIXESDATA.INC/LIST'
C
  REAL*4 EXPK_HARY(8000)
  INTEGER*4 N2
C
C THE PURPOSE OF THIS LOOP IS TO IDENTIFY THE SEGMENTS FTHETA VS THETA
C WHICH ALPHA FALLS AND HENCE CALCULATE FALPHA
CC  WRITE(8,96)
96  FORMAT(1H1)

```

```

C      DO 20 N = 1,8000
C
C      DO 10 K = 1,800
C
C      TYPE *, 'K=', K-1, 'N=', N, 'ALPHA(N) =', ALPHA(N),
C *      THARY(K) =', THARY(K)
C
C
C      IF (ALPHA(N) .GT. THARY(K) .AND.
1      ALPHA(N) .LT. THARY(K+1)) THEN !2ND IF
C
C      EXPK = ((-1.0)**K)
C      IF (EXPK .LT. 0.0) THEN !3RD IF
C      FALPHA(N) = SLOPE(K) * (ALPHA(N) - THARY(K)) + 1.0
C
C      ELSE
C      EXPK = ((-1.0)**K)
C      IF (EXPK .GT. 0.0) THEN !4TH IF
C      FALPHA(N) = SLOPE(K) * (ALPHA(N) - THARY(K))
C      ENDIF !END OF 4TH IF
C      ENDIF !END OF 3RD IF
C
C      IF (FALPHA(N) .GT. 0.999) FALPHA(N) = 1.0
CCC      IF (FALPHA(N) .LT. 0.0006) FALPHA(N) = 0.0
C
C      HARY(N) = THARY(K)
C      GO TO 20
C
C      ENDIF !END OF 2ND IF
C
C
C
10      CONTINUE
C
C-----
C
C
C
20      CONTINUE
C
C      SAVE N VALUE IN N2 FOR PLOT PURPOSE
C
C      N2 = N - 1
C
C      DIAGNOSTICS
C
CCC      DO N = 1, 1200
CCC      WRITE(8, 100) N, ALPHA(N), FALPHA(N), SLOPE(N), THARY(N), HARY(N),
CCC      1 HARY(N+1)

```

```

CCC100 FORMAT(1X,I4,')',1X,'ALPHA='F10.6,1X,'FALPHA='F10.6,1X,
CCC 1 'SLOPE='F17.6,1X,'THARY='F10.6,1X,'HARYN='F10.6,1X,
CCC 2 'HARYN1='F10.6)
C
CCC  END DO
C
CCC  WRITE(8,101)
CCC101 FORMAT(1H1)
C
CCC  DO N =1,1200
CCC  WRITE(8,102)N,THARY(N),HARY(N),HARY(N+1)
CCC102 FORMAT(1X,I4,')',1X,'THARY='F10.6,1X,'HARYN='F10.6,1X,
CCC 2 'HARYN1='F10.6)
C
CCC  END DO
C
      TYPE *,N2='N2
C
C PLOT PHI VS FALPHA
C CALL PLOT ROUTINE
C
C  CALL PLOT_XRAY (PHI,FALPHA,N2,4,DVAL,LVAL,KI)
C
      RETURN
      END
      SUBROUTINE XRAYS_FALPHA_ROTATE
C
      INCLUDE 'FIXESDATA.INC/LIST'
C
      INTEGER*4 K1
C
C THIS PART CALCULATES MIRROR IMAGE OF FIRST 90deg OF ROTATION
C TAKING ADVANTAGE OF SYMMETRY OF PHYSICAL SITUATION.
C
      M = 0
C
      DO N = 1,8000
C
      M = M + 1
      M1 = ((2 * MVAL) + 1) * 10
      M2 = M1 + M
      M3 = M1 - M
C
      PHI(M2) = (PHI(M1) - PHI(M3)) + PHI(M1)
C
      FALPHA(M2) = FALPHA(M3)
C
      IF (PHI(M2) .GE. PI) GO TO 10
C
      END DO
10  CONTINUE

```

```

C
  K1 = M2
  TYPE *, 'M=',M,'N=',N,'M2=',M2,'K1=',K1
C
C THIS LOOP IS JUST A DIAGNOSTIC
C
CCC  WRITE(8,96)
CCC  DO J =1,3000
CC   WRITE(8,100)J,PHI(J),FALPHA(J)
C100 FORMAT(1X,I4,''),PHI='F15.6,1X,FALPHA='F10.6)
CCC  ENDDO
C
C PLOT PHI VS FALPHA... THE FIRST 90deg PORTION
C CALL PLOT ROUTINE
C
C   CALL PLOT_XRAY (PHI,FALPHA,M2,5,DVAL,LVAL,K1)
C
C PASS 'K1' VALUE TO THE FALPHA ROTATION SUBROUTINE. K1 IS THE
C LAST POINT LOCATION IN THE FIRST 90deg PORTION.
C
  CALL XRAYS_PLOT_FAL_PHI(K1)
C
  RETURN
  END
  SUBROUTINE XRAYS_SAWTH(NGRID,K5)
C
C THIS SUBROUTINE ROTATES THE COMPRESSED SAWTOOTH TRACES
C THRU THE APPROPRIATE ANGLE AND THEN ADDS THEM TOGETHER
C ONE SHOULD HAVE SIX SINUSOID CURVES AT THE END, ONE FOR
C EACH GRID, THEN THESE ARE BINNED TO GET FOURIER COMPONENTS
C
  INCLUDE 'FIXESDATA.INC/LIST'
C
C LOOP TO SHIFT SAWTOOTH BY ANGLE SAWTH
C
  M=NGRID
C
C   TYPE *, ' NOTE: INCLUDE FILE: (M,N)=(6,24000)'
C   TYPE *, ' CORRESPONDS TO NGRID = 6'
C
C LOOP
C
  DO N=1,29080
    SAWT1(N)=PHI(N)+SAWTH(K5)
    FSAWT1(N)=FALPHA(N)
  ENDDO
C
C SOME DIAGNOSTICS HERE
C
CCC  DO NO=1,1000
CCC  WRITE(7,*) NO, ' SAWT1(NO)=' ,SAWT1(NO),FSAWT1(NO)=' ,FSAWT1(NO)

```

```

CCC * ,FALPHA(NO)='FALPHA(NO),'SAWTH(K5)='SAWTH(K5)
CCC  END DO
C
C
C 2D LOOP
C
  DO J=1,29080
    IF (SAWT1(J).GE.(2*PI)) THEN
      JA=J
      GO TO 10
    ENDIF
  END DO
C
10  CONTINUE
C  WRITE(7,*) 'JA='JA,' SAWT1(J)='SAWT1(J)
C  WRITE(7,*) 'J='J
C
C 3D LOOP
C
  DO K=1,29080
    KB=JA+K-1
    SAWT(M,K)=SAWT1(KB)-(2*PI)
C
C 4/4/90 CHANGE HERE
C
C   FSAWT(M,K)=FSAWT(M,K)+FSAWT1(KB)
C
C   FSAWT(M,K)=FSAWT1(KB)
C
C   IF(SAWT(M,K).GE.SAWTH(K5)) THEN
C     IA=K
C     GO TO 20
C   ENDIF
C   END DO
C
20  CONTINUE
C  WRITE(7,*) 'IA='IA,' KB='KB
C  WRITE(7,*) 'K='K,'SAWT(M,K)='SAWT(M,K)
C  WRITE(7,*) 'M='M,' SAWTH(K5)='SAWTH(K5)
C
C 4TH LOOP
C
  DO I=1,29080
    IC=I+IA
    SAWT(M,IC)=SAWT1(I)
C
C 4/4/90 CHANGE HERE
C
C   FSAWT(M,IC)=FSAWT(M,IC)+FSAWT1(I)
C
C   FSAWT(M,IC)=FSAWT1(I)

```



```

C      IF (SAWT(M,IC).GE.(2*PI))GO TO 30
      END DO
C
C 30 CONTINUE
C  WRITE(7,*) 'IC=' ,IC,' SAWT(M,IC)=' ,SAWT(M,IC)
C  WRITE(7,*) 'FSAWT(M,IC)=' ,FSAWT(M,IC)
C
C 5TH LOOP
C
      DO IB=1,29080
        SAWTP(IB)=SAWT(M,IB)
        FSAWTP(IB)=FSAWT(M,IB)
        IF (SAWTP(IB).GE.(2*PI))GO TO 40
      END DO
C 40 CONTINUE
C
C
C SOME DIAGNOSTICS HERE
C
      IG=IB
      DO IF=1,10
        IG=IG-1
C  WRITE(7,*) 'NGRID=' ,NGRID,' ' ,M=' ,M,' ' ,N=' ,N
C  WRITE(7,*) 'IB=' ,IB,' IG=' ,IG,' SAWTH(K5)=' ,SAWTH(K5)
C  WRITE(7,*) 'IG-1=' ,IG-1,' SAWTP(IG-1)=' ,SAWTP(IG-1)
C  WRITE(7,*) 'SAWTP(IG-2)=' ,SAWTP(IG-2)
C  WRITE(7,*) 'FSAWTP(IG-1)=' ,FSAWTP(IG-1)
C  WRITE(7,*) 'FSAWTP(IG-2)=' ,FSAWTP(IG-2)
C  WRITE(7,*) 'SAWT(M,IG-1)=' ,SAWT(M,IG-1)
C  WRITE(7,*) 'SAWT(M,IG-2)=' ,SAWT(M,IG-2)
C  WRITE(7,*) 'FSAWT(M,IG-1)=' ,FSAWT(M,IG-1)
C  WRITE(7,*) 'FSAWT(M,IG-2)=' ,FSAWT(M,IG-2)
      END DO
C
C  IF (K5.EQ.20) THEN
C  CALL PLOT_XRAY (SAWTP,FSAWTP,IB,8,DVAL,LVAL,KI)
C  ENDIF
C
C  DIAGNOSTIC WRITE
C
      RETURN
      END

      SUBROUTINE XRAYS_BIN(NGRID,K5)
C
C THE PURPOSE OF THIS SUBROUTINE IS TO BIN THE
C FINAL SINUSOIDAL FUNCTION FOR EACH GRID AND
C PRINT IT OUT TO AN FORTRAN OUTPUT FILE
C
      INCLUDE 'FIXESDATA.INC/LIST'

```

```

C
C  INITIALIZATION
C
  CHK=0.0
  TERVAL4 = 0.0
  J=1
CCCC SUM=0.0
  I=0
C
  M=NGRID
C
C  TYPE *, 'NOTICE HERE THAT XL(NGRID) MAY NEED TO'
C  TYPE *, 'BE VARIED TO OPTIMIZE TELESCOPE'
c
  XL(1)=32    !8
  XL(2)=84    !16
C  XL(3)=32
C  XL(4)=64
C  XL(5)=128
C  XL(6)=128
C
  TERVAL = PI/(4*XL(M))
C
  DUM1(1)=0.0
  DUM2(1)=0.0
  DUM3(1)=0.0
  DUM4(1)=0.0
C
C  IF (K5.EQ.1.AND.NGRID.EQ.1) THEN
C    OPEN(UNIT=4,FILE='IN2FIL.DAT',STATUS='NEW')
C  ENDIF
C
C
C
C
C  LOOP FOR 360 DEGREES
C
  DO WHILE (SAWT(M,J) LE.(2*PI))
C
C    INITIALIZATION
C
    IF (K5.EQ.1) THEN
      BINA(I)=0.0
      BINB(I)=0.0
      BINC(I)=0.0
      BIND(I)=0.0
    ENDIF
C
    I=I+1
C
    TERVAL1 = TERVAL + TERVAL4

```

```

    Terval2 = Terval + Terval1
    Terval3 = Terval + Terval2
    Terval4 = Terval + Terval3
C
    REGA(I)=Terval2
C
CCC  WRITE(4,*)'REGA(I)=' ,REGA(I), 'I=' ,I
CCC  WRITE(4,*)'SAWT(M,J)=' ,SAWT(M,J), ' , 'M=' ,M, 'J=' ,J
    TYPE *,REGA(I)=' ,REGA(I), 'I=' ,I
C
C    TYPE *,'1ST BIN LOOP'
C
C LOOP FOR 1ST BIN
C
    DO WHILE (SAWT(M,J).LE.Terval1)
CCCC  IF (FALPHA(J).EQ.(0.0)) THEN
        BINA(I)=BINA(I)+1.0
CCCC  ENDIF
        J=J+1
    END DO
C
C    TYPE *,'2D BIN LOOP'
C
C LOOP FOR 2D BIN
C
C
    DO WHILE (SAWT(M,J).LE.Terval2)
CCCC  IF (FALPHA(J).EQ.(0.0)) THEN
        BINB(I)=BINB(I)+1.0
CCCC  ENDIF
        J=J+1
    END DO
C
C USE MIDPOINT FOR U,V POINT
C
C    TYPE *,'3D BIN LOOP'
C
C LOOP FOR 3D BIN
C
    DO WHILE (SAWT(M,J).LE.Terval3)
CCCC  IF (FALPHA(J).EQ.(0.0)) THEN
        BINC(I)=BINC(I)+1.0
CCCC  ENDIF
        J=J+1
    END DO
C
C    TYPE *,'4TH BIN LOOP'
C
C
C LOOP FOR 4TH BIN
C

```

```

DO WHILE (SAWT(M,J).LE.TERVAL4)
CCCC  IF (FALPHA(J).EQ.(0.0)) THEN
      BIND(I)=BIND(I)+1.0
CCCC  ENDF
      J=J+1
END DO

C
C
      TYPE *,J='J'
CCC   WRITE(4,*)'M='M,'J='J
CCC   WRITE(4,*)'SAWT='SAWT(M,J),'FSAWT(M,J)='FSAWT(M,J)
C
C CALCULATE U,V
C
CCC   WRITE(4,*)'BINA(I)='BINA(I),'','I='I
CCC   WRITE(4,*)'BINB(I)='BINB(I),'','I='I
CCC   WRITE(4,*)'BINC(I)='BINC(I),'','I='I
CCC   WRITE(4,*)'BIND(I)='BIND(I),'','I='I
C
      VX(I)=BINA(I)-BINB(I)-BINC(I)+BIND(I)
      VY(I)=BINA(I)+BINB(I)-BINC(I)-BIND(I)
      U(I)=COS(REGA(I))/(DVAL/LVAL)
      V(I)=SIN(REGA(I))/(DVAL/LVAL)
C
      WT=1.0
C
C POSSIBLE DIAGNOSTICS
C
      CHK=CHK+BINA(I)-BINB(I)+BINC(I)-BIND(I)
      SUM(I)=BINA(I)+BINB(I)+BINC(I)+BIND(I)
C


---


      TYPE *,U(I),V(I),VX(I),VY(I)
C
C      VX(I)=VX(I)*2.0E1
C      VY(I)=VY(I)*2.0E1
C
C      U(I)=U(I)/2.5E05
C      U(I)=-U(I)/2.5E05
C      U(I)=U(I)/2.5E04
C
C      V(I)=V(I)/2.5E05
C      V(I)=-V(I)/2.5E04
C
      TYPE *,U(I),V(I),VX(I),VY(I)
C
      IF (K5.EQ.20) THEN
        WRITE(4,2001) U(I),V(I),VX(I),VY(I),WT
2001  FORMAT (2X,F10.6,1X,F10.6,2X,F11.6,1X,F10.6,1X,F10.4)
      ENDF
C
END DO

```

```

C      IP=I-1
C      IF (K5 EQ. 20) THEN
C          CALL PLOT_XRAY (REGA,SUM,IP,9,DVAL,LVAL,KI)
C      ENDIF
C      TYPE *, 'NO. OF BINS =', I, ', ', 'CHK=', CHK
C      TYPE *, 'SUM=', SUM
C      RETURN
C      END
X      PROGRAM XROT

C      *****
C      ** THIS PROGRAM WILL CREATE THE DATA FILE FOR THE ROTATING **
C      ***** MODULATION COLLIMATOR *****
C      *****

      DIMENSION ANGLE(4000),U(4000),V(4000),R(4000),XI(4000)
      DIMENSION IPASS(4),xmin(25),xmax(25)

C      ** D=Distance between grids **
      D=500.
      PI=3.14159
      ISEED=3703
C      ** SWID=slit width **
      SWID1=.0125
      SWID2=.0275
C      ** DIV=number of bins **
      DIV=1000.
C      ** XMAXPI=maximum value of theta **
      XMAXPI=2.*PI

      TYPE *, 'Enter angle along x-axis of flare center, in arcseconds'
      READ *, XDELTA
      XDELTA=XDELTA/3600./180.*PI
      TYPE *, 'Enter radius of flare, in arcseconds'
      READ *, XPSI
      XPSI=XPSI/3600./180.*PI
      TYPE *, 'Enter number of initial photons'
      READ *, JTIMES
      TYPE *, 'Enter number of point sources'
      READ *, XFLARE
      TYPE *, 'Enter twist angle, in arcseconds'
      READ *, TWIST
      TWIST=TWIST/3600./180.*PI
      type *, 'Enter number of noise photons'
      read *, noise

C      *****

```

```

C ***** INITIALIZE STUFF *****
C *****

C ** IGRID is the number of the grid set **
C ** IGRID=1 is grid set with slit width=.0125 and not shifted **
C ** IGRID=2 is grid set with slit width=.0125 and shifted pi/2 *
C ** IGRID=3 is grid set with slit width=.0275 and not shifted **
C ** IGRID=4 is grid set with slit width=.0275 and shifted pi/2 *

DO IGRID=1,4
  IF (IGRID.EQ.1 .OR. IGRID.EQ.2) SWID=SWID1
  IF (IGRID.EQ.3 .OR. IGRID.EQ.4) SWID=SWID2
  IF (IGRID.EQ.1 .OR. IGRID.EQ.3) PHASE=0
  IF (IGRID.EQ.2. OR. IGRID.EQ.4) PHASE=SWID*1.5
  DO I=1+DIV*(IGRID-1),DIV*IGRID
    ANGLE(I)=0
    U(I)=0
    V(I)=0
    R(I)=0
    XI(I)=0
  ENDDO

C *****
C ***** MAIN LOOP *****
C *****

DO I=1+ITIMES*(IGRID-1),ITIMES*IGRID

C ***** FINDS COORD. ON GRID 1 *****

  X1=RAN(ISEED)*10.
  Y1=RAN(ISEED)*10.

C ***** CHECKS IF PASSES THRU GRID 1 *****

  PASS=0
  IDUM1=INT(X1/SWID)
  IF (IDUM1/2..NE.INT(IDUM1/2.)) PASS=1

C ***** TRANSFORMATION ONTO GRID 2 *****

C ** deltheta is the angle rotation increment of the collimator *
  IF (PASS.EQ.1) THEN
    DELTHETA=XMAXPI/DIV
    THETA=RAN(ISEED)*XMAXPI
C ** dumm is number between 0 & number of point sources **
    dumm=INT(ran(iseed)*XFLARE)
C ** zeta is # between 0 & pi in increments = # point sources **
    IF (XFLARE.EQ.1) ZETA=0
    IF (XFLARE.NE.1) ZETA=DUMM*PI/(XFLARE-1.)
C ** delta is angle along x-axis of one of the point sources **

```

```

C  ** psi is angle along y-axis of one of the point sources **
    DELTA=XDELTA+XPSI*sin(ZETA)
    PSI=XPSI*cos(ZETA)
C  ** sigma the angle of rotation + displacement of point source **
C  **** due to rotation **
    IF (DELTA.EQ.0) SIGMA=THETA+PI/2.
    IF (DELTA.NE.0) SIGMA=THETA+ATAN(TAN(PSI)/TAN(DELTA))
C  ** alpha is displacement of point source along x-axis **
C  ** beta is displacement of point source along y-axis **
    ALPHA=TAN(SQRT(PSI**2+DELTA**2))*COS(SIGMA)
    BETA=TAN(SQRT(PSI**2+DELTA**2))*SIN(SIGMA)
    X2=X1-D*(ALPHA)
    Y2=Y1-D*BETA

C  ***** TWIST *****

C  ** finds new values of x2 and y2 on grid 2 due to twist **
    aa=atan(y2/x2)
    rr=sqrt(x2**2+y2**2)
    ddd=(tan(aa-twist))**2
    X2=rr/(sqrt(ddd*(1+1/ddd)))
    y2=sqrt(abs(rr**2-x2**2))

C  ***** CHECKS IF PASSES THRU GRID 2 *****

    X2=X2+PHASE
    IF (X2.LE.10 .AND. Y2.LE.10.) THEN
    IF (X2.GE.0 .AND. Y2.GE.0) THEN
        IDUM2=INT(X2/SWID)
        IF (IDUM2/2..NE.INT(IDUM2/2.)) THEN
            DUM=INT(THETA/DELTHETA)
            IF (DUM.NE.0) THEN
                IPASS(IGRID)=IPASS(IGRID)+1

C  ***** ANGLE SUMS PHOTONS THAT PASS *****

                DUMMY=DUM+DIV*(IGRID-1)
                ANGLE(DUMMY)=ANGLE(DUMMY)+1
            ENDIF
        ENDIF
    ENDIF
    ENDIF
    ENDDO

C  ***** NOISE *****

    do in=1,noise/4
        ntheta=int(ran(iseed)*1000)+1+(igrid-1)*1000
        type *, ntheta
        angle(ntheta)=angle(ntheta)+1

```

```

        enddo

C *****
C ***** PREPARES THINGS FOR OUTPUT FILE *****
C *****

C ** CORRECTS FOR MISSING AREA OF DETECTOR AT VARIOUS ANGLES **

    do i=1,div
        theta=(2*pi/div)*i
        dx=abs(D*tan(delta*sin(theta)))
        dy=abs(D*tan(delta*cos(theta)))
        perarea=(10-dx)*(10-dy)/100.
        angle(i+(igrid-1)*div)=angle(i+(igrid-1)*div)/perarea
    enddo

C ***** AVERAGES 20 MAX'S AND 20 MIN'S *****

    do i=1,25
        xmin(i)=100000.
        xmax(i)=0.
    enddo

    DO I=1+DIV*(IGRID-1),DIV*IGRID
        iave=0
        true=1
        dowhile (true.eq.1)
            iave=iave+1
            if (iave.gt.24) true=0
            IF (ANGLE(I).GT.XMAX(iave)) THEN
                XMAX(iave)=ANGLE(I)
            true=0
            endif
        enddo
        iave=0
        true2=1
        dowhile (true2.eq.1)
            iave=iave+1
            if (iave.gt.24) true2=0
            if (angle(I).lt.xmin(iave)) then
                xmin(iave)=angle(i)
            true2=0
            endif
        enddo
    enddo

    smin=0
    smax=0
    do j=2,24
        smin=smin+xmin(j)
        smax=smax+xmax(j)
    enddo

```



```

        enddo

        xave=(smin/24+smax/24)/2

C ***** FINDS U, V, AND REAL VALUES *****

        TH=0
        DO I=1+DIV*(IGRID-1),DIV*IGRID
            TH=TH+DELTHETA
            U(I)=-D/(2.*SWID)*COS(TH)/10000.
            V(I)=D/(2.*SWID)*SIN(TH)/10000.
            R(I)=ANGLE(I)-XAVE
            XI(I)=R(I)
        ENDDO
    ENDDO

C ***** WRITES FILE IN AIPS FORMAT *****

        OPEN(UNIT=1,FILE='XROT.DAT',STATUS='NEW')
        DO I=1,1000
            ANGLE(I)=ABS(R(I))+ABS(XI(I+1000))
            WRITE(1,25) U(I),V(I),R(I),XI(I+1000),ANGLE(I)
        ENDDO
        DO I=2001,3000
            ANGLE(I)=ABS(R(I))+ABS(XI(I+1000))
            WRITE(1,25) U(I),V(I),R(I),XI(I+1000),ANGLE(I)
        ENDDO

C ***** WRITES FILE WITH PARAMETERS *****

        OPEN(UNIT=2,FILE='XROT2.DAT',STATUS='NEW')
        WRITE(2,*)DIV,XMAXPI,ITIMES,XDELTA,XPSI,IPASS(1),IPASS(2),
& IPASS(3),IPASS(4),XFLARE,twist,noise

C ***** WRITES IDL FILE *****

        OPEN(UNIT=3,FILE='XROT3.DAT',STATUS='NEW')
        WRITE(3,*)r

25  FORMAT(2X,F10.6,1X,F10.6,2X,F12.6,1X,F12.6,1X,F10.4)

        CLOSE(1)
        CLOSE(2)
        CLOSE(3)

        CALL EXIT
    END

```

## REFERENCES

- Abels, J.G., 1968, *Proceedings Astronomical Society of Australia*, **1**, 172.
- AIPS Cookbook*, 1986, NRAO, Charlottesville, VA.
- Allen, C. W., 1973, *Astrophysical Quantities*, 3rd Edition, Athlone Press, London.
- Antonucci, E., et al., 1982, *Solar Phys.*, **78**, 107.
- Billings, D.E., 1966, *A Guide to the Solar Corona*, Academic Press, New York.
- Bracewell, R., 1965, *The Fourier Transform and Its Applications*, McGraw-Hill, Inc., New York.
- Bracewell, R. and Riddle, A.T., 1968, *Ap. J.*, **150**, 427.
- Bradt, H., Garmire, G., Oda, M., Spada, G., Sreekantan, B., and Gorenstein, P., 1968, *Space Sci. Rev.*, **8**, 471.
- Brown, J.C., 1971, *Solar Phys.* **18**, 489.
- Brown, J.C., 1974, in *Coronal Disturbances*, Proc. IAU Symp. 57 (G.A. Newkirk, Jr., ed.), p. 105, Reidel, Dordrecht.
- Brown, D.G., and Emslie, A.G., 1987, *Solar Phys.*, **110**, 305.
- Brown, J.C. and Emslie, A.G., 1988, *Ap. J.*, **331**, 554.
- Brown, J.C., Melrose, D.B., and Spicer, D.S., 1979, *Ap. J.*, **228**, 592.

- Campbell, J.W., Davis, J.M., and Emslie, A.G., 1991a, *X-Ray/EUV Optics for Astronomy, Microscopy, Polarimetry, and Projection Lithography*, Proc. SPIE, Vol. 1343 (R.B. Hoover, and A.B.C. Walker, Jr. eds.), 359.
- Campbell, J.W. et al., 1991b, *EUV, X-Ray, and Gamma-Ray Instru. for Astronomy II*, Proc. SPIE, Vol. 1549 (R.B. Hoover, and A.B.C. Walker, Jr. eds.), 155.
- Chen, F.F., 1974, *Introduction to Plasma Physics*, Plenum Press, New York.
- Crannell, C.J., 1988, *Imaging Solar Flares in Hard X-Rays And Gamma-Rays from Balloon-borne Platforms*, NASA, Goddard Space Flight Center.
- Chubb, T.A., Friedman, H. and Kreplin, R.W., 1966, *J. Geophys. Rev.*, **71**, 3611.
- Culhane, J.L. and Acton, L.W., 1970, *Mon. Not. Roy. Astr. Soc.*, **151**, 141.
- Dennis, B. R., 1988, *Solar Phys.*, **118**, 49.
- Dicke, R.H., 1968, *Ap. J. Lett.*, **153**, L101.
- Emslie, A.G., 1981, *Ap. J.*, **245**, 711.
- Emslie, A.G., 1983, *Solar Phys.*, **86**, 133.
- Emslie, A.G., 1987, *Solar Phys.*, **113**, 175.
- Emslie, A.G., 1989, *Solar Phys.*, **121**, 105.
- Emslie, A.G. and Machado, M.E., 1987, *Solar Phys.*, **107**, 263.
- Emslie, A.G., Fennelly, J.A., and Machado, M.E., 1986a, *Adv. Space Res.*, **6**(6), 139.

- Emslie, A.G. and Nagai, F., 1985, *Ap. J.*, **288**, 779.
- Fishman, G.J., et al., 1989, in *Gamma-Ray Observatory Science Workshop* (W. Neil Johnson, ed.) 2.39.
- Fishman, G.J., et al., 1989, in *Gamma-Ray Observatory Science Workshop* (W. Neil Johnson, ed.) 3.47.
- Fomalont, E.B., and Wright, M.C.H., 1974, in *Galactic and Extragalactic Radio Astronomy*, (G.L.Verschuur and K.I. Kellermann, eds.) New York Springer, 256.
- Forrest, D.J. and Chupp, E.L., 1983, *Nature*, **305**, 291.
- Giovanelli, R.G., 1939, *Ap. J.*, **89**, 555.
- Greisen, E., 1986, *The AIPS Cookbook*, NRAO, Charlottesville, VA.
- Greisen, E., and Harten, R., 1981, *Astron. Astrophys. Suppl. Ser.*, **44**, 371-374.
- Hecht, E., and Zajac, A., 1974, *Optics*, Addison-Wesley, Reading, MA.
- Hoyng, P., Brown, J.C., and van Beek, H.F., 1976, *Solar Phys.*, **48**, 197.
- Hoyng, P., Duijveman, A., Machado, M.E., Rust, D.M., Svestka, Z., Boelee, A., deJager, C., Frost, K.J., Lafleur, H., Simnett, G.M., van Beek, H.F., and Woodgate, B.E., 1981, *Ap. J. Lett.*, **246**, L155.
- Hurford, G.J., 1977, *CALTECH Astrophysics Preprint*, BBSO #0167.
- Hurford, G.J., and Hudson, H.S., 1980, *CALTECH Astrophys. Preprint*, BBSO # 0188, UCSD-SP-79-27, U. of California.
- Kahler, S.W., 1971a, *Ap. J.*, **164**, 365.

- Kahler, S.W., 1971b, *Ap. J.*, **168**, 319.
- Kane, S.R., Frost, K.J., and Donnelly, R.F., 1979, *Ap. J.*, **234**, 669.
- Kane, S.R., Kai, K., Kosugi, T., Enome, S., Landecker, P.B., and McKenzie, D.L., 1986, *Ap.J.*, **271**, 376.
- Kosugi, T., Dennis, B.R., and Kai, K., 1988, *Ap. J.* **324**, 1118.
- Krall, N.A. and Trivelpiece, A.W., 1973, *Principles of Plasma Physics*, McGraw-Hill, New York.
- Kramers, H.A., 1923, *Phil. Mag.*, **46**(6), 836.
- LaRosa, T.N., and Emslie, A.G., 1989, *Solar Phys.*, **120**, 343.
- La Rosa, T.N., 1990, *Solar Phys.*, **126**, 153.
- Li, P., and Emslie, A.G., 1990, *Solar Phys.*, **129**, 113.
- Makishima, K., Miyamoto, S., Murakami, T., Nishimura, J., Oda, M., Ogawara, Y., and Tawara, Y., 1978, in *New Instrumentation In Space Astronomy*, (Van Der Hucht, K., and Vaiana, G.S., eds.), New York Pergamon.
- Macdonald, W.M., Rosenbluth, M.N., and Chuck, W., 1957, *Physical Review*, **107**, 350.
- MacKinnon, A.L., Brown, J.C., and Hayward, J., 1985, *Solar Phys.*, **99**, 231.
- Manheimer, W.M., 1977, *Phys. Fluids*, **20**, 265.
- Mariska, J.T., Emslie, A.G., and Li, P., 1989, *Ap. J.*, **342**, 1067.

- Mertz, L., 1965, *Transformations in Optics*, Wiley, New York.
- Mertz, L.N., 1989, in *EUV and  $\gamma$ -Ray Instru. for Astron. and Atomic Physics*, Proc. SPIE, Vol. **1159**, (C.J. Hailey and O.H.W. Siegmund, eds.) 100.
- Mertz, L.N., Nakano, G.H., and Kilner, J.R., 1986, *J. Opt. Soc. Am.*, **3**(12), 86.
- Murphy, M.J., 1990, *Nucl. Instru. Meth.* **55**, 62.
- Nagai, F., and Emslie, A.G., 1984, *Ap. J.*, **244**, 1163.
- Oda, 1965, *Applied Optics*, **4**, 143.
- Paciesas, W.S., et al., 1989, in *Gamma-Ray Observatory Science Workshop*, (W. Neil Johnson, ed.), 2.89.
- Palmer, D., and Prince, T., 1987, *IEEE Trans. Nuc. Sci.*, **NS-34**(1), 71.
- Pendleton, G.N., et al., 1989, in *Gamma-Ray Observatory Science Workshop*, (W. Neil Johnson, ed.), 4.547.
- Peterson, L.E. and Winckler, J.R., 1959, *J. Geophys. Res.*, **64**, 697.
- Smith, D.F., 1980, *Solar Phys.*, **66**, 135.
- Smith, D.F. and Brown, J.C., 1980, *Ap. J.*, **242**, 799.
- Smith, D.G. and Lilliequist, C.G., 1979, *Ap. J.*, **232**, 582.
- Steward, E.G., 1987, *Fourier Optics*, 2nd Ed., John Wiley & Sons, New York.
- Švestka, Z., 1976, *Solar Flares*, Reidel, Dordrecht.

Schnopper, H.W., Thompson, R.J., and Watt, S., 1968, *Space Sci. Rev.*, **8**, 534.

Smithers, R.K., 1991, *Sky & Telescope*, **84**(4), 343.

Spitzer, L., Jr., 1962, *The Physics of Fully Ionized Gases*, 2nd ed., Wiley & Sons, New York.

Tandberg-Hanssen, E., and Emslie, A.G., 1988, *The Physics of Solar Flares*, Cambridge University Press.

Tandberg-Hanssen, E. et al., 1984, *Solar Phys.*, **90**, 41.

van Beek, H.F., Thompson, R.J., and Watt, S., 1968, *Space Sci. Rev.*, **8**, 197.

van Hollebeke, M.A.I., MaSung, L.S., and McDonald, F.B., 1975, *Solar Phys.*, **41**, 189.

Walker, A.B.C., Jr., Barbee, T.W., Jr., Hoover, R., and Lindblom, J.F., 1988, *Science*, **241**, 1781.

Wells, D., Greisen, E., and Harten, R., 1981, *Astron. Astrophys. Suppl. Ser.*, **44**, 363-370.





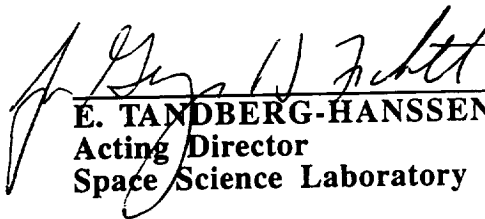
**APPROVAL**

**IMAGING THE SUN IN HARD X-RAYS USING FOURIER TELESCOPES**

**By**

**J. W. Campbell**

**The information in this report has been reviewed for technical content. Review of any information concerning Department of Defense or nuclear energy activities or programs has been made the MSFC Security Classification Officer. This report, in its entirety, has been determined to be unclassified.**

  
\_\_\_\_\_  
**E. TANDBERG-HANSEN**  
**Acting Director**  
**Space Science Laboratory**

